8-2014

Extension and applications of the GVVPT2 method to the study of transition metals

Patrick K. Tamukong

EXTENSION AND APPLICATIONS OF THE GVVPT2 METHOD TO
THE STUDY OF TRANSITION METALS

by

Patrick K. Tamukong

Teachers' Diploma, Advanced Teachers' Training College Bambili, 2002
Bachelor of Science, University of Buea, 2007

A Dissertation

Submitted to the Graduate Faculty

of the

University of North Dakota

In partial fulfillment of the requirements

For the degree of
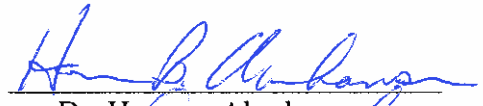
Doctor of Philosophy

Grand Forks, North Dakota
August
2014
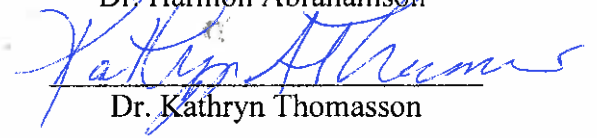
This dissertation, submitted by Patrick K. Tamukong in partial fulfillment of the requirements for the Degree of Doctor of Philosophy from the University of North Dakota, has been read by the Faculty Advisory Committee under whom the work has been done and is hereby approved.

Chairperson: Dr. Mark R. Hoffmann

Dr. Harmon Abrahamson

Dr. Kathryn Thomasson
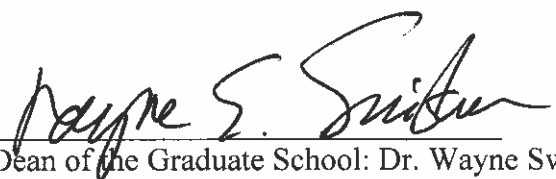
Dr. Jerome Delhommelle
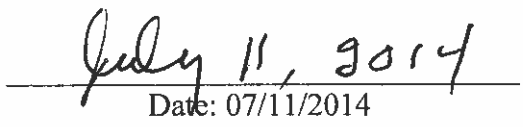
Dr. Ju Kim

This dissertation meets the standards for appearance, conforms to the style and format requirements of the Graduate School of the University of North Dakota, and is hereby approved.

Dean of the Graduate School: Dr. Wayne Swisher

Date: 07/11/2014

PERMISSION

Title   Extension and Applications of the GVVPT2 Method to the Study of Transition Metals

Department   Chemistry

Degree   Doctor of Philosophy

Signature   Patrick Khan Tamukong

Date   July 11, 2014

TABLE OF CONTENTS

LIST OF FIGURES

LIST OF TABLES

ABBREVIATIONS

Abbreviation	Definition
ACPF	Averaged Coupled Pair Functional
AMD	Advanced Micro Device
ANO	Atomic Natural Orbital
ANO-RCC	ANO-Relativistic Correlation Consistent
ANO-RCC VTZP	ANO-RCC Valence Triple Zeta with Polarization Functions
AOs	Atomic Orbitals
AQCC	Averaged Quadratic Coupled Cluster
aug-cc-pV5Z	Augmented Correlation Consistent Polarized Valence Quintuple Zeta
aug-cc-pVQZ	Augmented Correlation Consistent Polarized Valence Quadruple Zeta
aug-cc-pVTZ	Augmented Correlation Consistent Polarized Valence Triple Zeta
aug-cc-pVTZ-DK	aug-cc-pVTZ-Douglas-Kroll
B88	Becke's 1988 Exchange Functional
B95	Becke's τ-Dependent Gradient-Corrected Correlation Functional
B3LYP	Becke's 3 parameter Lee-Yang-Parr Exchange Correlation Functional
B3P86	Becke's 3 Parameter Hybrid Functional with Non-Local Correlation Provided by Perdew 86

B3PW91	Becke's 3 Parameter Hybrid Functional with Non-Local Correlation Provided by PW91
BHandHLYP	Becke-Half-and-Half-LYP
BLYP	Becke-Lee-Yang-Parr Exchange Correlation Functional
BOP	Becke's Exchange Plus One-parameter Progressive Correlation Functional
BP	PW91 and B88 Functionals
BP86	Becke's One Parameter Hybrid Functional with Non-Local Correlation Provided by Perdew 86
BSSE	Basis Set Superposition Error
CAS	Complete Active Space
CASSCF	Complete Active Space Self-Consistent Field
CASPT2	Complete Active Space Second Order Perturbation Theory
CBS	Complete Basis Set
cc-pVQZ	Correlation Consistent Polarized Valence Quadruple Zeta
cc-pVTZ	Correlation Consistent Polarized Valence Triple Zeta
cc-pVTZ-DK	cc-pVTZ-Douglas-Kroll
cc-pwCV5Z	Correlation Consistent Polarized Weighted Core Valence Quintuple Zeta
cc-pwCVQZ	Correlation Consistent Polarized Weighted Core Valence Quadruple Zeta
CCSD	Coupled Cluster with Single and Double Excitations
CCSDT	Coupled Cluster with Single, Double, and Triple Excitations
CCSD(T)	CCSD with pertubative Triple Excitations

CCSDt	CCSD with selected Triple electron excitations
CI	Configuration Interaction
CIPT2	Configuration Interaction Second Order Perturbation Theory
CSF	Configuration State Function
D_e	Equilibrium Dissociation Energy
DFT	Density Functional Theory
DFT-in-DFT	Density Functional Theory-in-Density Functional Theory
DHF	Dirac-Hartree-Fock
DKH	Douglas-Kroll-Hess
DMC	Diffusion Monte Carlo
DMRG-SCF	Density Matrix Renormalization Group SCF
DOE	Density Orbital Embedding
DV-X_α	Discrete Variational X_α Method
EBO	Effective Bond Order
ECP	Effective Core Potential
Emb-OEP	Embedded Optimized Effective Potential
ESR	Electron Spin Resonance
FCI	Full Configuration Interaction
FDE	Frozen Density Embedding
FOCI	First Order CI
FO + MRCISD	Hybrid of FOCI and MRCISD
GGA	Generalized Gradient Approximation

GUGA	Graphical Unitary Group Approach
GVB	Generalized Valence Bond
GVBCI	GVB with Configuration Interaction
GVB-vdw	GVB-van der Waals
GVVPT2	Generalized Van Vleck Second Order Pertubation Theory
HF	Hartree-Fock
IPEA	Ionization Potential-Electron Affinity
KS	Kohn-Sham
KSCED	Kohn-Sham Equations with Constrained Electron Density
KS-DFT	Kohn-Sham Density Functional Theory
LANL2DZ	Los Alamos National Laboratory Double Zeta
LANL08	Uncontracted Los Alamos National Laboratory Basis Set of 2008
LDA	Local Density Approximation
LLP	Lee-Lee-Parr Kinetic Energy Functional
LSDA	Local Spin Density Approximation
LYP	Lee-Yang-Parr Functional
MBPT	Many-Body Pertubation Theory
MBPT4	Fourth Order MBPT
MCQDPT	Multiconfigurational Quasidegenerate Perturbation Theory
MCQDPT2	Second Order MCQDPT
MCSCF	Multi-Configuration Self-Consistent Field
MGVB	Modified GVB
MO	Molecular Orbital

MP2	Second Order Møller-Plesset Pertubation Theory
MP4	Fourth Order Møller-Plesset Pertubation Theory
MP4(SDTQ)	Full MP4 with Single, Double, Triple, and Quadruple Excitations
MPW3LYP	Modified Perdew-Wang 3 Parameter Lee-Yang- Parr Exchange Correlation Functional
mPW91PW91	Barone's Modified PW91 Exchange and PW91 Correlation Functional
MRACPF	Multireference ACPF
MRCI	Multireference Configuration Interaction
MRCI + Q	Multireference Internally Contracted Configuration Interaction Plus Davidson Quadruple Corrections
MRCISD	MRCI Including Single and Double Electron Excitations
MRCISD(T)	MRCISD Including Perturbative Triple Excitations
MRCISD(TQ)	MRCISD Including Perturbative Triple and Qaudruple Excitations
MRCISDTQ	MRCISD Including Triple and Qaudruple Excitations
MR-MP	Multireference Møller-Plesset Perturbation Theory
MRPT	Multireference Pertubation Theory
MRPT2	Second Order MRPT
NEP	Nonlinear Equality-Constrained Problem
NESC	Normalized Elimination of Small Component
NEVPT2	Second Order N-Electron Valence State Perturbation Theory
NEVPT3	Third Order N-Electron Valence State Perturbation Theory
PBE1PBE	Perdew-Burke-Ernzerhof Exchange and Correlation Functional
PC-NEVPT2	Partially Contracted NEVPT2
PDFT	Partition DFT

PECs	Potential Energy Curves
PES	Potential Energy Surface
PFI-ZEKE	Pulsed-Field Ionization-Zero Electron Kinetic Energy
POLSDCI	Polarization Singles and Doubles CI
PW91	Perdew-Wang 1991 Exchange and Correlation Functional
QCAS-SCF	Quasi-Complete Active Space Self-Consistent Field
QCISD(T)	Quadratic CISD(T)
QDPT	Quasi-Degenerate Pertubation Theory
RAS	Restricted Active Space
RASSCF	Restricted Active Space Self-Consistent Field
RASSI-SO	Restricted Active Space State Interaction Spin–Orbit
R_e	Equilibrium Bond Length
RECP	Relativistic ECP
RHF	Restricted Hartree Fock
RKR	Rydberg-Klein-Rees
RMP2	Restricted MP2
ROHF	Restricted Open-Shell HF
RSC	Relativistic Small Core
RTPI	Resonant Two-Photon Ionization
SAC-CI	Symmetry-Adapted-Cluster CI
SA-MCSCF	State-Averaged MCSCF
SCF	Self-Consistent Field
SC-QDPT	Self-consistent Quasi-Degenerate Pertubation Theory

sf-X2C	Spin-Free Exact Two Component
SLYP	Slater Lee-Yang-Parr Exchange Correlation Functional
SOCI	Second Order CI
SOCI + Q	Second Order CI with Davidson Correction for Unlinked Quadruple Clusters
SS-MRPT2	State Specific MRPT2
SVWW	Slater Vosko-Wilk-Nusair Exchange-Correlation Functional
T_e	Vertical Adiabatic Transition Energy
TMs	Transition Metals
VMC	Variational Monte Carlo
VWN	Vosko-Wilk-Nusair Functional I
VWN5	Vosko-Wilk-Nusair Functional V
VWN-BP	BP Functional with the Local Correlation replaced by VWN Functional
UCCSD(T)	Unrestricted CCSD(T)
UNDMOL	University of North Dakota Molecular Electronic Structure Code
ω_e	Harmonic Frequency
WFT	Wave Function Theory
XC	Exchange Correlation

ACKNOWLEDGMENTS

I will gratefully acknowledge the following persons without whom the work reported in this dissertation would be impossible:

1. Prof. Mark R. Hoffmann who accepted me into his research group and patiently molded me in chemical theory and computation up to this moment. He has been there to respond to all questions on the different research projects and sometimes by e-mail when away on a trip.

2. The rest of my Graduate Advisory Committee (Prof. Kathryn Thomasson, Prof. Harmon B. Abrahamson, Prof. Ju Kim, and Dr. Jerome Delhommelle) whose advice, particularly during oral progress reports, helped immensely to shape the work reported herein.

3. Dr. Yury Khait without whom the theory part of this dissertation relating to embedding, in particular, would be nearly impossible.

4. The rest of our research group members, particularly Dr. Daniel P. Theis, Dr. Yvonne Bongfen Mbote, and Dr. Rashel Mokambe Sumpter, who schooled me on how to perform ab initio calculations particularly in my early years in the group.

5. My beloved wife, Delphine N. Banjong; my children, Shekina N. Khan and Pearl Z. Khan; and my enlarged family including siblings and in-laws, whose moral support and prayers kept me riding to the finished line.

6. My dear father, Mbeh Tamukong James Ami, who in his late 70s was able to spend a whole summer with us, helping with our kids while I worked on this

dissertation. Likewise my mother-in-law, Odilia Anong, who spent another summer at our home helping in the same way as my father did.

7. My Church family (particularly the Nfor's family, the Rott's family, and Kimberly Lane) whose prayers and encouragement contributed in no small way to help me realize this dream.

8. God Almighty who has given me life and intelligence and who opened the door for me to study at the prestigious University of North Dakota. He deserves all the glory.

ABSTRACT

The ground and low-lying excited electronic states of molecules of the first (Sc_2, Cr_2, Mn_2, and Ni_2) and second (Y_2, Mo_2, and Tc_2) row of transition elements have been investigated for the first time with the generalized Van Vleck second order multireference perturbation theory (GVVPT2) method, a variant of MRPT. All potential energy curves (PECs) obtained in these studies were smooth and continuous; that is, they are free from wiggles or inflexion points. In order to account for relativistic effects, which become important in heavy elements, the GVVPT2 method was extended to include scalar relativistic effects through the spin-free exact two component (sf-X2C) method and used in the studies of all molecules of second row transition elements and some of those of the first row considered in this present work. GVVPT2 studies of triatomic lithium and beryllium were also done as a first step to studies of small clusters of transition metals. The spectroscopic constants (bond lengths, harmonic frequencies, bond energies, and adiabatic transition energies) obtained for all PECs at the GVVPT2 level were in good agreement with experimental data, where available, and with results from previous studies using other high level ab initio methods. Optimized geometries of the triatomics were also in good agreement with previous findings. The studies included electronic states (e.g., the $2^1\Sigma_g^+$ and $3^1\Sigma_g^+$ states of Y_2 as well as the $1^5\Sigma_g^+$ and $1^9\Sigma_g^+$ states of Tc_2) not previously discussed in the literature.

As a first step to applying GVVPT2 to the study of relatively larger systems, the present work includes the results of efforts on improving DFT-in-DFT embedding theory. New equations were determined which involved an additional constraint of orthogonality of the orbitals of one subsystem to those of the complementary subsystem as warranted by formal arguments based on the formulation of DFT-in-DFT embedding. A computer program was realized using the new embedding equations and test calculations performed. Analyses of electron density deformations in embedding theory, in comparison with conventional Kohn-Sham (KS)-DFT densities, were performed using the new embedding program and a computer code that was also written to compute electron densities of molecules in real space, given reduced one particle density matrices.

The results revealed that whereas the current formulation of DFT-in-DFT embedding theory generally underestimates electron density, at the interface between subsystems in comparison with conventional KS-DFT calculations of the supermolecule, the new DFT-in-DFT embedding scheme with the external orthogonality constraint was found to remedy the situation. Worthy of special note in this new embedding protocol is the fact that the nonadditive kinetic potential (v_T), thought to be a major cause of weaknesses in DFT-in-DFT embedding and to which many previous research efforts have been devoted, can be set exactly to zero.

The present work therefore realized, for the first time, a new DFT-in-DFT embedding theory that neither relies on kinetic functionals nor requires a supermolecular DFT calculation. Test calculations using the new embedding theory and supermolecular basis set expansion of KS orbitals reproduced conventional KS-DFT energies to at least the 7th decimal place (and even exactly at many geometries). A new way of expanding

KS orbitals was also employed in the new embedding protocol, which is intermediate between the usual supermolecular and monomer basis expansions, referred to as the "extended monomer expansion". The monomer basis expansion scheme was inadequate for the new DFT-in-DFT embedding protocol. Test calculations found this novel, computationally cheaper, extended monomer approach to give results quite close to those from supermolecular basis expansions.

CHAPTER I

INTRODUCTION

Electronic structure calculations are a key complement to scientific experimentation. Virtually all properties of molecules and materials are derivable from knowledge of their electronic structures. In particular, electronic structure calculations can provide insight: into reaction pathways and mechanisms; ascertain structures of experimentally inaccessible intermediates; and determine several other properties of materials that help explain experimental results and make useful predictions. Unfortunately, however, the electronic Schrödinger equation that models each system by a Hamiltonian operator and a corresponding wave function describing its electron cloud is exactly soluble only for a single electron system, such as the hydrogen atom. For systems of more than one electron, approximations must be made with regards to describing electron-electron interactions. These interactions are often divided into *static correlation*, used to describe situations in which a single configuration of the electrons is insufficient for describing a system, and *dynamic correlation* when corrections resulting from the instantaneous movement of electrons due to neighboring electrons are warranted in order to afford an accurate description of a system. The former correlation is otherwise known as *long range correlation* and is important when the total wave function is not dominated by a single Slater determinant [1]. Good examples of this scenario would be bond breaking situations and regions of near degeneracy. The latter correlation is also

called *short range correlation* and is due to the need to account for a coulomb hole when describing electronic interactions. The coulomb hole results from the fact that the position of each electron becomes the center of a constantly changing region (the coulomb hole) to be avoided by neighboring electrons due to coulomb repulsions [2]. The Hartree Fock (HF) self-consistent field (SCF) method, the lowest rung in ab initio electronic structure calculation methods, represents the electronic wave function as a single configuration of the electrons and fails to account for the coulomb hole. Thus, electrons are inherently uncorrelated at this level of theory. All post-HF methods seek to overcome these limitations through different approximations with varying degrees of accuracy in results.

The work described in this dissertation is in two main parts: the first part involves GVVPT2 [3, 4] studies of dimers of first (Sc_2, Cr_2, Mn_2, and Ni_2) and second (Y_2, Mo_2, and Tc_2) row transition elements and trimers of Li, and Be; the second part describes the new DFT-in-DFT embedding protocol [5, 6] developed and applied as part of the work for this dissertation. This new protocol involves an additional constraint of external orbital orthogonality. External orthogonality requires a subsystem's orbitals to be orthogonal to those of the complementary subsystem. Neglect of this latter constraint led to poor estimates of electron densities, and hence embedding energies, when compared with reference conventional KS-DFT calculations of the corresponding supermolecules. Figure 1 illustrates how a system may be partitioned into subsystems as is often done in DFT-in-DFT embedding theory.
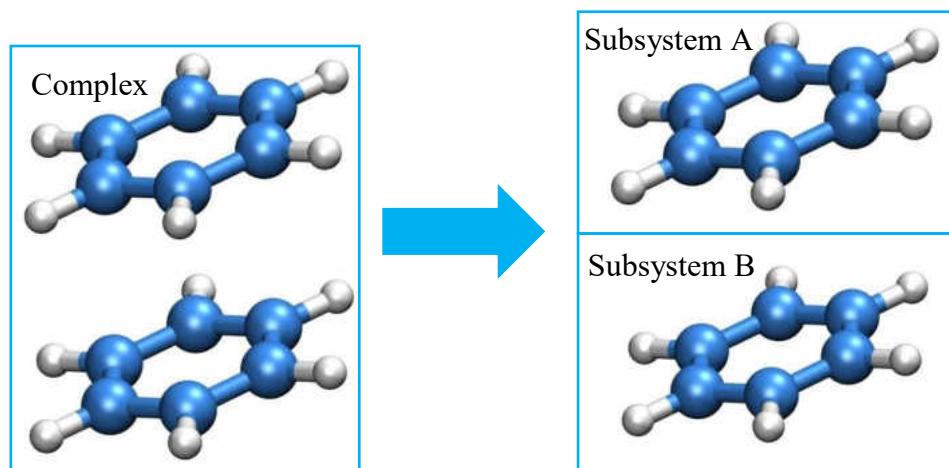
Figure 1. An illustration of the philosophy of embedding theory where a benzene dimer complex is partitioned into subsystems A and B. The new variant of DFT-in-DFT embedding presented herein requires orbitals of subsystem A to be orthogonal to those of subsystem B.

In the paragraphs that follow, the two main parts of this dissertation are briefly introduced.

Theoretical Studies of Transition Metals

Aspects of the transition metal (TM) molecules that have been studied using the GVVPT2 method were previously investigated theoretically using different methods. The present studies, however, considered chemically motivated valence bond style active spaces in the calculations that were not used in previous work. The present work likewise includes electronic states not previously characterized. Moreover, full potential energy curves (PECs) for some of the molecules were generated for the first time.

Studies of transition metals and their derivatives have become increasingly important and attractive, both to experimentalists and theoreticians, due to their many applications; e.g., catalysis, magnetism, medical and engineering applications. Novel

applications of the elements continue to emerge such as recent discoveries of transition metal catalysts for renewable energy; e.g., the synthesis of titanium (IV) oxide nanowires for solar energy capture [7], syntheses of TM catalysts for water splitting [8-11], and TM-derived materials for the emerging field of spintronics [12-14]. These applications are due to the unique characteristics of TM elements including: the formation of compounds whose colors result from *d-d* transitions; the ability to exist in different stable oxidation states which permits the formation of different types of complexes; and the existence of low-lying vacant d-subshells.

However, studies on TM dimers are quite challenging both experimentally and theoretically. Experimentalists are faced with difficulties associated with the very high melting and boiling points of TMs. This often leaves matrix isolation techniques as the best alternatives for experimental studies of TMs, albeit with poor rotational spectra coupled with the fact that matrices can affect ground and low-lying electronic states differently. For example, Infante et al. [15] found low-lying excited uranium (IV) oxide electronic states to lie energetically lower than the supposed ground state when the molecules were trapped in an argon matrix.

On the other hand, theoretical studies of TMs are complicated by the occurrence of multiple electronic states within narrow energy ranges, coupled with the generally multireference nature of the wave functions needed to describe such states, requiring a careful balance between descriptions of short and long range electron correlations. The presence of partially filled d-subshells in these metals results in several possibilities of coupling the spin and orbital angular momenta of their valence electrons in the event of bond formation and, hence, many low-lying molecular states. For example, the

combination of a ground state scandium atom (^2D_g; $4s^23d^1$) with either another ground state atom or one in one of the first three excited states (labeled as a^4F_g: $4s^13d^2$; a^2F_g: $4s^13d^2$; z^4F_u: $4s^14p^13d^1$), at only 1.427, 1.846, and 1.956 eV above the ground atomic term, already results in as many as 270 molecular states [16]. In the case of Ni_2, limited configuration interaction (CI) calculations on the molecule [17] found 84 of its molecular states, corresponding to the $^3F_4$ ($3d^84s^2$) + $^3F_4$ ($3d^84s^2$) dissociation limit, to lie within an energy range of only 300 K (0.026 eV) while 45 other states, correlating with the $^3D_3$ ($3d^94s^1$) + $^3D_3$ ($3d^94s^1$) dissociation asymptote, also lay within a narrow energy gap.

The many different possibilities of electronic arrangements within the partially filled d-subshells of TMs imply that the Hilbert spaces for these systems are generally large. The implication of this is that computational costs for high level methods like MRCISD become quite high for reasonably large one-electron basis sets, leaving multireference perturbation theory (MRPT) techniques as plausible alternatives since they offer a good balance between cost and accuracy, in general, in ab initio quantum chemistry calculations. Unfortunately, the near degeneracy of many low-lying electronic states of TM molecules leads to intruder state problems when simplistic MRPT methods are used in such studies [18]. Intruder state problems have long been known to constitute an "Achilles' heel" for MRPT methods and have generated different attempts to resolve the problem, such as the use of shift techniques or elimination of offending (intruding) states. Moreover, attempts to circumvent the problem by changes in active spaces are commonly used [18]. Unfortunately, these approaches do not work well in all situations, as demonstrated recently by Camacho et al. [18] for the case of Mn_2 and Ruipérez et al.

[19] for the case of Cr_2. The calculations due to Camacho et al. [18] were performed at the MCQDPT and CASPT2 levels of theory and found over 5,000 intruder states, which did not allow for the construction of a smooth PEC. These authors succeeded to construct smooth PECs of states of Mn_2 only after drastic shift parameters were used in MRPT methods. However, their results showed a strong dependence on the value of the parameter used. They therefore concluded MRPT methods to be incapable of describing complicated systems such as transition metals that generally have many quasidegenerate states. One way of overcoming the intruder state problem is to use a Dyall bi-electronic zero-order Hamiltonian, as is done in the NEVPT2 method [20, 21]. This approach appears to deal well with intruder states, albeit with a significant increase in complexity in comparison with one-electron Hamiltonians.

For the work described in this dissertation, the generalized Van Vleck second order multireference perturbation theory (GVVPT2) method was used to study the low-lying electronic states of the Sc_2, Cr_2, Mn_2, Ni_2, Y_2, Mo_2, and Tc_2 molecules as well as the geometries of Li_3 and Be_3 and the symmetric dissociation of linear Be_3. The GVVPT2 method based on an MCSCF reference [3, 4] was realized in the Hoffmann research group at the University of North Dakota (UND). The technique, a variant of MRPT, is parameter free and is guaranteed to give smooth and continuous potential energy curves (PECs) based on formal arguments. Moreover, the flexibility of the GVVPT2 method allows it to support both complete and incomplete model spaces. It is additionally an intermediate effective Hamiltonian approach and is subspace-specific. It is computationally realized using spin-adapted many-electron functions. These advantages, coupled with the fact that GVVPT2 uses the macroconfiguration technique

[22], also developed in the Hoffmann Group at UND, have been exploited in the present studies.

The Importance of Relativistic Effects

Relativistic effects are known to affect the properties of atoms and molecules. Several anomalies observed during experimental studies on atoms and molecules are explicable only in terms of relativity. For example, ionization energies, as well as electron affinities, of elements are generally known to decrease down a period in the Periodic Table of elements. For the coinage metals, for example, this pattern is not observed. The experimental ionization energy of gold is known [23] to be the highest in this group of metals (Au = 9.225 eV versus 7.726 eV for Cu and 7.576 eV for Ag). Likewise the experimental value of its electron affinity is larger [24] than that of copper or silver (Au = 2.309 versus 1.226 for Cu and 1.303 for Ag). This large electron affinity allows gold to accept electrons and form ionic compounds such as Rb^+Au^- and Cs^+Au^- [25, 26]. Nonrelativistic calculations on the coinage metals do not reproduce this pattern of experimental ionization potentials and electron affinities. For example, a nonrelativistic MRCI calculation [27] on Cu found an electron affinity value of only 1.06. On the other hand, a QCISD(T) calculation [28] that used a relativistic pseudopotential basis set already came close to predicting the correct ionization potentials and electron affinities; giving the former as 7.695 eV, 7.431 eV, 8.898 eV and the latter as 1.199, 1.199, 2.073 for Cu, Ag, and Au, respectively. A CCSD(T) study [29] that incorporated the relativistic spin-averaged Douglas-Kroll no-pair method [30, 31] came even closer to predicting the correct values of these quantities; giving ionization potentials and electron affinities as 7.733, 7.461, 9.123, and 1.236, 1.254, 2.229 for Cu, Ag, and Au,

respectively. The authors of this latter study also performed calculations at the restricted open shell Hartree-Fock (ROHF) and coupled cluster with single and double electron excitations (CCSD) levels of theory and found less accurate results. In their study, the correlation of semi-core $(n\text{-}1)s^2(n\text{-}1)p^6$ electrons was found to improve accuracy. The data reported here for Au were obtained with only the $(n\text{-}1)p^6$ electrons correlated and the $(n\text{-}1)s^2$ frozen whereas for Cu and Ag, all 8 semi-core electrons were correlated. It can be seen that the accuracy drops in the case of Au, in comparison with reference experimental data. These studies clearly indicate that the unusually high ionization potential or electron affinity of Au is due to relativistic effects.

Many other anomalous properties of atoms and molecules are attributable to relativistic effects. The yellow color of gold can only be explained using relativity [32]. The relativistic stabilizing contraction of the outer 6s subshell of gold together with a destabilizing expansion of the 5d subshell narrows the energy gap between these two subshells. An absorption at 2.40 eV measured for fine gold was assigned [33] to a transition from a filled 5d band to a largely 6s Fermi level. No such transition was observable in the cases of copper and silver. Furthermore, the liquid state of mercury at room temperature also owes its explanation to a relativistic contraction of the outer 6s subshell [25, 34]. Desclaux and Kim [35] verified this contraction at the relativistic Dirac-Hartree-Fock (DHF) level of theory. In his review on relativistic effects in structural chemistry, Pyykkö [36] noted that for very precise calculations, relativistic effects are needed even for the simplest systems such as H_2 and H_2^+. The review noted several abnormal observations in the Periodic Table of the elements that are due to relativistic effects such as: the occurrence of lead (Pb) in a faced centered cubic (fcc)

crystal structure rather than the diamond structure in carbon (C); the chemical similarity between zirconium (Zr) and hafnium (Hf) due to the cancellation of relativistic and shell structure effects; lanthanide contraction; d-block contraction; and the occurrence of high valencies for the actinide series.

Although relativistic effects are often neglected in many theoretical studies on light elements (typically those of the first, second, and maybe third rows of the Periodic Table of elements), these effects have been found to improve accuracies in theoretical descriptions when taken into account. On the other hand, their inclusion in calculations of heavier elements is more dramatic. For example, nonrelativistic MRCISD calculations [37] on atomic iron (Fe) underestimated the $^5F\left(3d^7 4s^1\right) \leftarrow {}^5D\left(3d^6 4s^2\right)$ excitation energy by as large as 0.185 eV whereas a scalar relativistic treatment, through the DKH Hamiltonian, at the same level of theory predicted a value close to the reference experimental value, only 0.055 eV larger. A full relativistic treatment [38] that included spin-orbit coupling effects at the RASSI-SO level of theory overestimated the $^5F\left(3d^7 4s^1\right) \leftarrow {}^5D\left(3d^6 4s^2\right)$ excitation energy by only 0.031 eV. Such studies, among many others (including those to be reported in this dissertation), underscore the importance of considering relativistic effects in the theoretical description of virtually all quantum systems. In a recent review on the effects of relativity on atomic and molecular properties [39], the authors stated "real life of molecules is a relativistic quantum mechanical life. This holds for all atoms and molecules throughout the Periodic Table". Even for very light elements, effects of relativity are visible in the fine structures of their atomic spectra.

Indeed, relativistic effects are to be expected for all atoms based on formal arguments. Einstein [40] suggested that the mass of a fast-moving particle increases with its speed according to the relation

$$m = \frac{m_0}{\sqrt{1 - \left(\dfrac{v}{c}\right)^2}} \quad , \tag{1.1}$$

where m_0 is the rest mass of the particle, c is the speed of light in vacuum, and v is the speed of the particle. From this expression, in the limit of $v \ll c$, $m \approx m_0$, and relativistic effects are minimal. Based on Bohr's description of the atom [41], the angular momentum of an electron revolving around a nucleus is quantized and defined as

$$mvr = n\hbar \quad , \tag{1.2}$$

where m is the electron's mass, r is the radius of its orbit, v is its speed, n is the principal quantum number, while $\hbar$ is the reduced Planck's Constant. Again from Bohr's description of the atom [41], the radius, r, is

$$r = \frac{n^2 4\pi\varepsilon_0 \hbar^2}{mZe^2} \quad , \tag{1.3}$$

where ε_0 is the vacuum permittivity, Z is the nuclear charge, while e is the electronic charge. Substituting Eq. (1.3) in Eq. (1.2) and assuming atomic units ($e = m_0 = \hbar = 4\pi\varepsilon_0 = 1$) leads to

$$v = \frac{Z}{n} \tag{1.4}$$

This implies that the speed of an electron increases proportionately with nuclear charge and the mass accordingly, following Eq. (1.1). Even for the 1s electron of hydrogen for which v = 1 a.u. from Eq. (1.4) (compared with c ≈ 137.026 a.u.), an increase in the

electronic mass of only $\left[1-\left(\dfrac{1}{137.036}\right)^2\right]^{-\frac{1}{2}} = 2.66 \times 10^{-5}$ already shows up in the fine

structure of the spectrum of atomic hydrogen (of course, there is no spin-orbit coupling effect for a 1s electron). As will be shown in this dissertation, wherever they were considered, relativistic effects were shown to improve the accuracy of GVVPT2 results for all the systems studied. Such effects were included in all calculations of molecules of second row transition elements considered in this work.

The Need for Embedding Theory

Despite the growth in recent years in terms of computer power and the development of more computationally efficient post HF ab initio methods, key bottlenecks persist in the field of quantum computation. Paramount among these challenges is the steep scaling of several quantum chemistry methods with system size. Even the least computationally intensive methods, Hartree-Fock (HF) and density functional theory (DFT), scale, respectively, as N^4 and N^3 with system size. More precise methods like the CCSD(T) variant of coupled cluster scales as N^7 while full configuration interaction (FCI), that delivers the most accurate results, scales as N! with system size [42]. Imagining a FCI calculation on a system of only 20 electrons is already beyond present computability. The steep scaling of many quantum chemistry methods curtails their applicability to the study of systems of only a few atoms. In the present work, the method of choice for studies on transition metal molecules, the GVVPT2 method, scales

as N^5 compared to MRCISD which scales as N^6 with system size (where N is a measure of the system size e.g., the number of basis functions). Attempting a GVVPT2 calculation on a gold crystal of only 10 gold atoms will already be a tedious calculation due to computational cost and memory requirement. Yet, a nanoparticle of gold with a radius of only 13 nm already contains about 542,940 gold atoms.

There is a need to modify existing or to develop new quantum chemistry methods that can be used to study large realistic systems rather than just isolated atoms and molecules in the gas phase. Several recent research efforts in the field of quantum chemistry have sought to address this concern. Some of such efforts have been impressive. Examples include: the development of fast matrix diagonalization algorithms [43, 44]; parallelization [45-48] of computational chemistry methods to run either on single computers with multiple processors or on an arbitrary number of computers connected by a network; the development of local methods such as finite element methods [49, 50]; and the development of stochastic versions of deterministic ab initio methods [51-55]. Such innovations have led to increased computational speed and enabled calculations on reasonably *large* systems to be realized. However, the complexity of many quantum chemistry algorithms makes partitioning into independent tasks that can run in parallel quite challenging.

Other attempts at applying high level ab initio methods to the study of large systems include linear and quadratic scaling; that is, the so-called *O(N)* and *O(N²)* methods [56-61].   These approaches are either based on a so-called density fitting scheme, in which the four-index two electron interaction terms are replaced with either two- or three-index integrals, which reduces scaling with basis set size [56], or on a local

approximation framework where the molecular orbitals are first localized by a unitary transformation and interactions of distant pairs of localized orbitals are subsequently neglected [62]. Whereas these methods have substantially reduced computational cost and allowed consideration of relatively larger systems, such recipes also introduce new sources of error; e.g., convergence problems accompany local approximation methods while scaling to multiple computer processors within the inherent limits of accuracy of the methods remains a challenge [60].

Embedding schemes, which are based on the principle of "divide-and-conquer" [63-65], appear to be propitious approaches to electronic structure calculations on large systems. In such approaches, a system gets partitioned into a small region of interest, called the embedded subsystem (hereafter designated as subsystem A), and a larger region of peripheral interest referred to as the environment (hereafter, referred to as subsystem B). The environment may be further subdivided [66]. Embedding theories seek to achieve high accuracy within the localized, generally complex, embedded subsystem by describing it at a high level of theory while the effect of the environment is approximated. A key bottleneck in these approaches is in the description of the often artificial boundary between subsystems. In DFT-in-DFT embedding theory [66-75], each subsystem is treated at the DFT level and subsystem interactions are dependent on their electron densities plus non-additive terms resulting from the non-additive nature of the exchange-correlation (XC) and kinetic energy potentials. In the so-called wave function theory (WFT)-in-DFT embedding scheme [67, 68, 76, 77], the environment subsystem is treated at the DFT level, generating an embedding potential which is then included as an external potential in WFT calculations on the embedded subsystem.

In this dissertation, we present a new variant of DFT-in-DFT embedding theory. Previous formulations of DFT-in-DFT [71, 72], partitioned the total electron density of a supersystem into a sum of subsystems' densities,

$$\rho_{tot}(\vec{r}) = \rho_A(\vec{r}) + \rho_B(\vec{r}) \, , \qquad (1.5)$$

following the ideas of Cortona [73], Senatore and Subbaswamy [74, 75], where $\rho_{tot}(\vec{r})$ is the total density while $\rho_A(\vec{r})$ and $\rho_B(\vec{r})$ are electron densities of the respective subsystems. The total energy functional is then minimized under the constraint of fixed electron number in each subsystem and without requiring that a subsystem's orbitals be orthogonal to those of the complementary subsystem (that is, external orbital orthogonality is ignored). In Chapter VII of this dissertation where the new embedding scheme is described, it is shown that such neglect of external orthogonality leads to poor estimates of electron densities and hence, energies within embedding theory. Moreover, Eq. (1.5) is exactly true only if the external orthogonality condition holds. The new scheme incorporates this constraint and is shown in Chapter IX to lead to more accurate results compared to those from previous DFT-in-DFT embedding schemes.

Organization and Structure

The work described in this dissertation has been grouped into 10 Chapters. This first Chapter introduces the transition metals that were investigated at the GVVPT2 level of theory. It also includes the raison d'être for including relativistic effects in the GVVPT2 description of the molecules studied, and lastly, the motivation for pursuing an embedding theory scheme.

Chapter II contains a review of the methods used in the studies on transition metals and the triatoms of Li and Be. Chapters III to VI detail the studies done on low-lying electronic states of dimers of: Sc and Y; Cr and Mo; Mn and Tc; and Ni, respectively. But for Ni_2, molecules of first row transition elements were intentionally placed with their isovalent counterparts of the second row in order to permit easy comparisons and analyses of the effects of relativity particularly on molecules of second row transition elements.

Chapter VII contains a full description of a new approach to DFT-in-DFT embedding theory and its practical implementation. Chapter VIII provides test results that were obtained by applying the new embedding protocol to different types of chemical systems with varying degrees of interaction strength between the subsystems. The results in Chapter VIII span interaction energies between subsystems and PECs that were obtained for the separation of supermolecules into fragments as defined in embedding theory. Also included are electron density deformation contour and relief maps that were obtained using the new embedding method and a computer program that was also written to compute electron densities of molecules in real space given reduced density matrices. Worthy of special note is that the non-additive kinetic energy potential, v_T, that could be termed the bête noire of DFT-in-DFT embedding and that has since been blamed for weaknesses in the theory, can be set to exactly zero in the new embedding protocol.

Chapter IX reports GVVPT2 studies of triatoms of Li and Be. The purpose of those studies was to assess the capability of GVVPT2 for describing systems of more atoms in anticipation of embedding GVVPT2 calculations. Chapter X contains an overview of the work reported in this dissertation together with proposals for future work.

CHAPTER II

THEORETICAL METHODS

Introduction

This Chapter describes the methods used in the studies on transition metal dimers and triatoms of Li and Be that will be discussed in Chapters III to VI and then Chapter IX. Before discussing the specific methods, it is useful to state the electronic structure problem and the mathematical principles often applied in its solution. As mentioned in the introduction, due to electron-electron interactions, the electronic structure problem can be solved only approximately for any system with more than one electron.

The Electronic Structure Problem

Most methods of computational chemistry are developed to solve the time-independent Schrödinger equation [78]

$$\hat{H}|\Psi\rangle = E|\Psi\rangle \, , \tag{2.1}$$

where $|\Psi\rangle$ is the wave function sought for and E is its corresponding eigenvalue or energy. $\hat{H}$ is the Hamiltonian operator describing particle motions and their interactions, and is most commonly taken in the non-relativistic limit. For a system of N electrons and M nuclei, $\hat{H}$ is defined [79] in atomic units as

$$\hat{H} = -\underbrace{\sum_{i=1}^{N} \frac{1}{2} \nabla_i^2}_{T_e} - \underbrace{\sum_{A=1}^{M} \frac{1}{2M_A} \nabla_A^2}_{T_n} - \underbrace{\sum_{i=1}^{N} \sum_{A=1}^{M} \frac{Z_A}{r_{iA}}}_{V_{en}} + \underbrace{\sum_{i=1}^{N} \sum_{j>i}^{N} \frac{1}{r_{ij}}}_{V_{ee}} + \underbrace{\sum_{A=1}^{M} \sum_{B>A}^{M} \frac{Z_A Z_B}{R_{AB}}}_{V_{nn}} \, , \tag{2.2}$$

where the first two terms (T_e and T_n) are the kinetic energy operators of the electrons and nuclei, respectively; the third term (V_{en}) is the electron-nuclei attraction potential; while the last two terms (V_{ee} and V_{nn}) describe electron-electron and nuclei-nuclei repulsion potentials, respectively. The symbols r_{iA}, r_{ii} and R_{AB} define electron-nuclei, electron-electron, and nuclei-nuclei interaction distances as defined in Eq. (2.3) and illustrated in Figure 2 for a two electron, two nuclei system

$$r_{iA} = \left|\vec{r}_{iA}\right| = \left|\vec{r}_i - \vec{R}_A\right|, \quad r_{ij} = \left|\vec{r}_{ij}\right| = \left|\vec{r}_i - \vec{r}_j\right|, \quad R_{AB} = \left|\vec{R}_{AB}\right| = \left|\vec{R}_A - \vec{R}_B\right| \qquad (2.3)$$
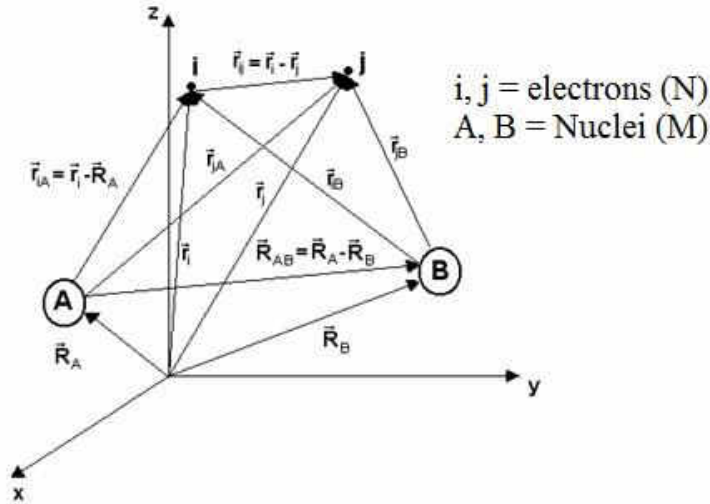
Figure 2. Interactions in a two nuclei (A, B)-two electron (i, j) system shown in the cartesian coordinate system (Image taken from Szabo and Ostlund, [79]).

Eq. (2.1) is often solved within the Born-Oppenheimer approximation [80] where the kinetic energy of the nuclei (T_n) is assumed to be negligible compared to electronic motion (hence, $T_n = 0$) and the nuclei-nuclei coulomb repulsion potential (V_{nn}) is assumed to be a constant that adds to the Hamiltonian eigenvalues. These two approximations lead to an electronic Hamiltonian obtained from Eq. (2.2) as

$$\hat{H}_{elec} = -\underbrace{\sum_{i=1}^{N}\frac{1}{2}\nabla_i^2}_{T_e} - \underbrace{\sum_{i=1}^{N}\sum_{A=1}^{M}\frac{Z_A}{r_{iA}}}_{V_{en}} + \underbrace{\sum_{i=1}^{N}\sum_{j>i}^{N}\frac{1}{r_{ij}}}_{V_{ee}} , \qquad (2.4)$$

where the quantities retain their previously defined meanings. The corresponding wave function for $\hat{H}_{elec}$, the electronic wave function ($|\Psi_{elec}\rangle$), describes electronic motion and interactions in a potential due to the nuclei at fixed positions in space. In this way, $|\Psi_{elec}\rangle$ is an explicit function of electronic coordinates (r_i) but an implicit function of nuclear coordinates (R_A); $|\Psi_{elec}\rangle = |\Psi_{elec}\rangle(\{r_i\};\{R_A\})$. The electronic Schrödinger equation,

$$\hat{H}_{elec}|\Psi_{elec}\rangle = E_{elec}|\Psi_{elec}\rangle, \qquad (2.5)$$

is then solved to obtain the eigenvectors, $|\Psi_{elec}\rangle$, and corresponding eigenvalues, $E_{elec} = E_{elec}(R_A)$, which are functions of nuclear positions. This approximation decouples the total wave function in Eq. (2.1) into a product of purely an electronic and a nuclear wave function ($|\Psi\rangle = |\Psi_{elec}\rangle|\Psi_{nucl}\rangle$). The total energy of the system is obtained as a sum of the electronic energy from Eq. (2.5) and the constant nuclei-nuclei coulombic potential

$$E_{tot} = E_{elec} + V_{nn} \qquad (2.6)$$

In order to describe the dynamics of molecules or the motion of their nuclei within the Born-Oppenheimer approximation, a nuclear Hamiltonian is defined from Eq. (2.2) by approximating the electronic coordinates by their average values over the electronic wave function [79],

$$\hat{H}_{nucl} = -\sum_{A=1}^{M} \frac{1}{2M_A} \nabla_A^2 + \left\langle -\sum_{i=1}^{N} \frac{1}{2} \nabla_i^2 - \sum_{i=1}^{N} \sum_{A=1}^{M} \frac{Z_A}{r_{iA}} + \sum_{i=1}^{N} \sum_{j>i}^{N} \frac{1}{r_{ij}} \right\rangle + \sum_{A=1}^{M} \sum_{B>A}^{M} \frac{Z_A Z_B}{R_{AB}}$$

$$= -\sum_{A=1}^{M} \frac{1}{2M_A} \nabla_A^2 + E_{elec}\left(\{R_A\}\right) + \sum_{A=1}^{M} \sum_{B>A}^{M} \frac{Z_A Z_B}{R_{AB}} \tag{2.7}$$

$$= -\sum_{A=1}^{M} \frac{1}{2M_A} \nabla_A^2 + E_{tot}\left(\{R_A\}\right)$$

Having averaged out the electronic degrees of freedom, the total energy (E_{tot}) then serves just as a potential term that adds to the nuclear kinetic energy operator to constitute the nuclear Hamiltonian operator that describes the motion of the nuclei on the potential energy surface obtained by solving Eq. (2.5) within the Born-Oppenheimer approximation. The solution of the nuclear eigenvalue problem

$$\hat{H}_{nucl} |\Psi_{nucl}\rangle = E |\Psi_{nucl}\rangle \tag{2.8}$$

describes the vibrational, translational, and rotational degrees of freedom of the molecule. The eigenvalue in Eq. (2.8) is the total energy of the system, as in Eq. (2.1), and is different from $E_{elec}(R_A)$ in Eq. (2.5) which is only the electronic energy for some fixed geometry of the molecule.

The Variational Principle and Method of Lagrange Multipliers

The variational principle and Lagrange's method of undetermined multipliers are ubiquitously applied in quantum physics and chemistry. The eigenvalue problems that are solved in quantum chemistry often result from applying these techniques to the Schrödinger equation, subject to given constraints. It is therefore important to review these mathematical approaches here.

In the variational method [79, 81], it is assumed that any function that satisfies the same boundary conditions as the eigenvectors of a given Hamiltonian, such as that in Eq.

(2.1), can be expressed as a linear combination of those eigenvectors with coefficients to be determined. The eigenvalue problem

$$\hat{H}\left|\Phi_\alpha\right\rangle = \varepsilon_\alpha \left|\Phi_\alpha\right\rangle, \ \alpha = 0,\ 1,\ 2,\ \dots \ , \tag{2.9}$$

in general, has an infinite number of solutions that constitute a complete orthonormal set of vectors, $\left|\Phi_\alpha\right\rangle$. Since the solutions $\left|\Phi_\alpha\right\rangle$ are not known (i.e., otherwise there would be no problem to solve), the variational principle supposes that there are approximate solutions, $\left|\tilde{\Phi}\right\rangle$, that can be expressed as linear combinations of the true solutions

$$\left|\tilde{\Phi}\right\rangle = \sum_\alpha \left|\Phi_\alpha\right\rangle C_\alpha \tag{2.10}$$

As many approximate solutions ($\left|\tilde{\Phi}\right\rangle$) as are true ones ($\left|\Phi_\alpha\right\rangle$) can be constructed in this manner and are themselves, approximate eigenvectors of the Hamiltonian. The lowest eigenvalue of such approximate states is an upper bound to the exact ground state energy, ε_0,

$$\left\langle\tilde{\Phi}\left|\hat{H}\right|\tilde{\Phi}\right\rangle \geq \varepsilon_0 \tag{2.11}$$

The general task in quantum chemistry methods is often that of determination of an optimal set of some expansion coefficients, such as the C_α coefficients in Eq. (2.10). These coefficients are generally coefficients of Slater determinants or coefficients of configuration state functions constituting the many-particle Hilbert space of a quantum system. Moreover, the coefficients of basis functions spanning molecular orbitals, i.e., eigenfunctions of a one-electron Hamiltonian related to the true system, are thus determined. Obtaining an optimal set of expansion coefficients, C_α, often also relies on Lagrange's method of undetermined multipliers.

20

In the Lagrangian method, a function (or functional) is minimized subject to given equality constraints [82]. The function or functional could otherwise be maximized. In wave function methods, these constraints are generally related to a requirement that the functions (molecular orbitals or total wave functions) be orthonormal. In DFT, a functional of the electron density is minimized subject to the number conservation constraint (i.e., the requirement that the density integrates to give the total number of electrons in the system, $\int \rho(\bar{r})d\bar{r} = N$). To illustrate this, suppose that the maxima of the function $f(x, y) = x^2 y$ are to be obtained subject to the constraint equation $x^2 + y^2 = 3$. In Lagrange's method of undetermined multipliers, a lagrangian (Λ) is constructed as a sum of the function to be maximized and the constraint equation multiplied by a lagrange multiplier (λ). If there are multiple constraints, then each constraint equation is added with some λ coefficient. In the present example, one writes

$$\Lambda(x, y, \lambda) = x^2 y + \lambda(x^2 + y^2 - 3) \qquad (2.12)$$

Variations of Λ with respect to the independent variables x, y, and λ give zero at the critical points of Λ. That is,

$$\frac{\partial\Lambda(x, y, \lambda)}{\partial x} = \frac{\partial\Lambda(x, y, \lambda)}{\partial y} = \frac{\partial\Lambda(x, y, \lambda)}{\partial \lambda} = 0$$
$$\updownarrow \qquad\qquad (2.13)$$
$$2xy + 2x\lambda = x^2 + 2y\lambda = x^2 + y^2 - 3 = 0$$

Eq. (2.13) leads to $x = \pm\sqrt{2}$ and $y = \pm1$ or $x = 0$ and $y = \pm\sqrt{3}$, yielding a maximum for f(x, y) of 2 when $x = \pm\sqrt{2}$ and $y = 1$. This example is shown diagrammatically in Figure 3, together with the minima of f(x, y) which occur at $x = \pm\sqrt{2}$ and $y = -1$.
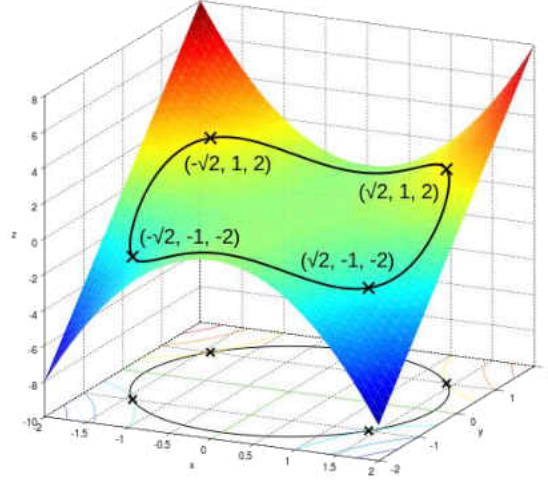
Figure 3. Constrained optimization of f(x, y) = x²y (Image taken from Ref. [83]).

In the variational methods of quantum chemistry, the task is to minimize the left hand side of Eq. (2.11) in order to obtain a value as close to the true ground state energy as possible. The constraint is the requirement that the approximate $\left|\tilde{\Phi}\right\rangle$ function be normalized to unity, that is

$$\left\langle\tilde{\Phi}\middle|\tilde{\Phi}\right\rangle=1=\sum_{\beta}\sum_{\alpha}\left\langle\Phi_{\beta}\middle|\Phi_{\alpha}\right\rangle C_{\beta}^{*}C_{\alpha}\ , \tag{2.14}$$

where the definition of $\left|\tilde{\Phi}\right\rangle$ from Eq. (2.10) has been used and the asterisk in C_{β}^{*} denotes the complex conjugate of C_{β}. In general, C_{β} is real ($C_{\beta} = C_{\beta}^{*}$). Thus, one constructs the following lagrangian

$$\begin{aligned}\Lambda\left(C_{1},C_{2},\cdots,C_{N},E\right)&=\left\langle\tilde{\Phi}\middle|\hat{H}\middle|\tilde{\Phi}\right\rangle-E\left(\left\langle\tilde{\Phi}\middle|\tilde{\Phi}\right\rangle-1\right)\\&=\sum_{\alpha\beta}C_{\alpha}C_{\beta}\left\langle\Phi_{\alpha}\middle|\hat{H}\middle|\Phi_{\beta}\right\rangle-E\sum_{\alpha\beta}\left(\left\langle\Phi_{\alpha}\middle|\Phi_{\beta}\right\rangle C_{\alpha}C_{\beta}-1\right)\end{aligned} \tag{2.15}$$

Considering variations of $\Lambda(C_1, C_2, \cdots, C_N, E)$ with respect to the coefficients (C_α or C_β) to be zero leads to

$$\sum_\beta H_{\alpha\beta} C_\beta = E \sum_\beta S_{\alpha\beta} C_\beta \,, \qquad (2.16)$$

where $H_{\alpha\beta} = \langle \Phi_\alpha | \hat{H} | \Phi_\beta \rangle$ and $S_{\alpha\beta} = \langle \Phi_\alpha | \Phi_\beta \rangle$ (N.B. the basis set of $|\Phi_\alpha\rangle$ many-electron functions is generally orthogonal, but in the corresponding one-electron problem, they are not). In matrix form, Eq. (2.16) is written as

$$\mathbf{HC} = \mathbf{ESC}, \qquad (2.17)$$

where $\mathbf{H}$ is the matrix of the Hamiltonian operator ($\hat{H}$); $\mathbf{E}$ is the (diagonal) matrix of eigenvectors; $\mathbf{S}$ is the overlap matrix; while $\mathbf{C}$ is the matrix of the expansion coefficients (all in the basis of $|\Phi_\alpha\rangle$ functions). Thus, the variational principle and Lagrange's method of undetermined multipliers reduce the problem of solving the many body Schrödinger equation to a generalized eigenvalue problem, which becomes an ordinary eigenvalue problem in the case of an orthonormal basis (where $\mathbf{S} = \mathbf{I}$).

The Hartree-Fock Self-Consistent Field Approximation

The Hartree-Fock (HF) self-consistent field (SCF) approximation [79, 81, 82, 84-86] is often the starting point for most ab initio electronic structure calculations, including those performed on the molecules discussed in this dissertation. At the HF level of theory [84-86], the many-electron Hamiltonian is approximated as a sum of one electron operators called Fock operators

$$\hat{H}_0 = \sum_i f_i \ , \tag{2.18}$$

where

$$f_i = -\frac{1}{2}\nabla_i^2 - \sum_{A=1}^{M}\frac{Z_A}{r_{iA}} + v_i^{HF} \tag{2.19}$$

is the Fock operator for the ith electron. The first term in the definition of f_i is the kinetic energy operator for the ith electron; the second term is its attraction potential to all nuclei; while the last term is the repulsion potential it experiences due to the averaged presence of all other electrons in the system. Thus, the complex many-electron problem has essentially been reduced to a one-electron problem in which electron-electron interactions are only treated by their mean, hence HF is a mean field solution. As will be seen subsequently, such an approach falls short of being able to describe complicated systems such as the transition metal molecules described in this dissertation. Nonetheless, the HF approximation provides a starting molecular orbital guess for high level calculations, or for determination of better one-electron functions.

With the Fock operator thus defined as in Eq. (2.19), the task then is to compute the eigenvectors and eigenvalues of the different Fock operators that add up to give the total approximate Hamiltonian,

$$f_i|\chi(x_i)\rangle = \varepsilon|\chi(x_i)\rangle \tag{2.20}$$

These eigenvectors or spin orbitals, $|\chi(x_i)\rangle$, are used to construct the wave function for the system, where x_i denotes both spin and spatial coordinates of the ith electron. At the

HF level of theory, the wave function is approximated as a single Slater determinant [87] defined in terms of the first N spin orbitals, $\left|\chi(x_i)\right\rangle$, with the lowest eigenvalues,

$$\left|\Psi(x_1, x_2, \cdots, x_N)\right\rangle = \frac{1}{\sqrt{N!}} \begin{vmatrix} \left|\chi_1(x_1)\right\rangle & \left|\chi_2(x_1)\right\rangle & \cdots & \left|\chi_N(x_1)\right\rangle \\ \left|\chi_1(x_2)\right\rangle & \left|\chi_2(x_2)\right\rangle & \cdots & \left|\chi_N(x_2)\right\rangle \\ \vdots & \vdots & \ddots & \vdots \\ \left|\chi_1(x_N)\right\rangle & \left|\chi_2(x_N)\right\rangle & \cdots & \left|\chi_N(x_N)\right\rangle \end{vmatrix}, \qquad (2.21)$$

where N is the number of electrons in the system and the pre-factor, $\frac{1}{\sqrt{N!}}$, is a normalization factor.

The terms "restricted" and "unrestricted" are often used as prefixes to HF (and other techniques) to specify that the spatial part is the same for an alpha and a beta spin orbital in the case of "restricted" or different in the case of "unrestricted". Thus, in restricted HF (RHF) theory, a spin orbital could be expressed as

$$\left|\chi(x_i)\right\rangle = \begin{cases} \left|\psi_i(\vec{r})\right\rangle \alpha(\omega) \\ \left|\psi_i(\vec{r})\right\rangle \beta(\omega) \end{cases}, \qquad (2.22)$$

where $\vec{r}$ and ω denote the spatial and spin coordinates of the electrons, respectively; $\left|\psi_i(\vec{r})\right\rangle$ is the spatial part while $\alpha(\omega)$ and $\beta(\omega)$ are the spin parts of the spin orbital. Eq. (2.22) implies that each spatial orbital $\left|\psi_i(\vec{r})\right\rangle$ gives rise to two spin orbitals.

In solving the eigenvalue problem in Eq. (2.20), the spin part of the orbitals can be integrated out (i.e., $\left\langle \tau_i \middle| \tau_j \right\rangle = \delta_{ij}$ where $\tau = \alpha(\omega)$ or $\beta(\omega)$) and the equations are solved for the spatial orbitals. As introduced by Roothaan [88], the approach is to approximate

the spatial functions as linear combinations of a finite set of known spatial basis functions, $|\varphi_i\rangle$,

$$|\psi_i\rangle = \sum_{v=1}^{K} |\varphi_v\rangle C_v^i \qquad (2.23)$$

This approximation leads to spatial molecular orbitals (MOs) that are exact only in the space spanned by the set of K basis functions. Rewriting Eq. (2.20) in terms of spatial orbitals using the definition in Eq. (2.23) gives

$$f_i \sum_{v=1}^{K} |\varphi_v\rangle C_v^i = \varepsilon \sum_{v=1}^{K} |\varphi_v\rangle C_v^i \qquad (2.24)$$

Multiplying Eq. (2.24) by $\langle\varphi_\mu|$ leads to the so-called nonlinear Roothaan matrix equation [88] solved iteratively in HF theory (i.e, Eq. (2.17))

$$\mathbf{FC} = \mathbf{SC\varepsilon}, \qquad (2.25)$$

where $\mathbf{F}$ is the matrix of the Fock operator in terms of a finite set of spatial basis functions; $\mathbf{C}$ is the matrix of the expansion coefficients in Eq. (2.23); $\mathbf{S}$ is the overlap matrix between basis functions; while $\boldsymbol{\varepsilon}$ is a diagonal matrix of the corresponding eigenvalues of the eigenvectors of the Fock operator. In practical calculations, Eq. (2.25) is first transformed into a matrix eigenvalue problem by orthonormalizing the set of basis functions, $|\varphi_v\rangle$, in order to render the overlap matrix, $\mathbf{S} \equiv \mathbf{I}$ (where $\mathbf{I}$ is the identity matrix). The procedure frequently used is the symmetric (Löwdin) orthonormalization [89] in which the coefficient matrix $\mathbf{C}$ is recast as

$$\mathbf{C} = \mathbf{S}^{-\frac{1}{2}}\mathbf{C}' \qquad\qquad (2.26)$$

Substituting this definition into Eq. (2.25) and left multiplying by the adjoint of $\mathbf{S}^{-\frac{1}{2}}$ gives

$$\left(\mathbf{S}^{-\frac{1}{2}}\right)^{\dagger}\mathbf{F}\mathbf{S}^{-\frac{1}{2}}\mathbf{C}' = \left(\mathbf{S}^{-\frac{1}{2}}\right)^{\dagger}\mathbf{S}\mathbf{S}^{-\frac{1}{2}}\mathbf{C}'\boldsymbol{\varepsilon} \iff \mathbf{F}'\mathbf{C}' = \mathbf{C}'\boldsymbol{\varepsilon} \qquad (2.27)$$

where $\left(\mathbf{S}^{-\frac{1}{2}}\right)^{\dagger}\mathbf{S}\mathbf{S}^{-\frac{1}{2}} = \mathbf{I}$. The matrix eigenvalue Eq. (2.27) is then solved for $\mathbf{C}'$ by

diagonalizing $\mathbf{F}'$ and $\mathbf{C}$ is subsequently obtained through Eq. (2.26).

As already noted in Chapter I, the HF method is inadequate for the majority of quantum mechanical systems due to its failure to explicitly treat electron-electron interactions. Although the correlation energy associated with such interactions is only about 1% of the total energy of quantum systems [82], yet it is critical for accurate descriptions of chemical bonding. In the present work, the RHF method was used to generate starting orbital guesses for more accurate descriptions of the systems studied.

Second Order Möller-Plesset Perturbation Theory

In the HF method, only occupied orbitals are physically meaningful for the original N-electron problem [90]. One way of approximately accounting for correlation effects beyond the HF method is through the (nondegenerate) second order Möller-Plesset perturbation theory (MP2) method [91] that scales less steeply than CI.

In perturbation theory, it is assumed that the exact many-electron Hamiltonian with a complicated solution can be partitioned into a part that is exactly soluble and a small perturbation as follows

$$\hat{H} = \hat{H}_0 + \lambda V, \tag{2.28}$$

where $V << \hat{H}_0$ and $0 \le \lambda \le 1$. $\hat{H}$ in Eq. (2.28) is the actual Hamiltonian whose eigenfunctions and eigenvalues are needed; $\hat{H}_0$ is the Hamiltonian of a closely related system with known eigenfunctions, $\left| \Psi_n^{(0)} \right\rangle$, and eigenvalues, $E_n^{(0)}$; V is a perturbation term; λ is a parameter that determines the strength of the perturbation. The success of this approach depends on the way $\hat{H}$ is partitioned into $\hat{H}_0$ and V. Perturbation theory works well if the main features of $\hat{H}$ are contained in $\hat{H}_0$ (that is, $V << \hat{H}_0$). The MP2 method considers as $\hat{H}_0$ the HF Hamiltonian defined in Eq. (2.18). The difference between the HF Hamiltonian and the exact Hamiltonian for any system lies in the approximate treatment of electron-electron interactions within the HF theory as opposed to the exact treatment of such interactions. The perturbation potential in MP2 is just this difference, that is

$$V = \sum_{i=1}^{N} \left(\sum_{j>i}^{N} \vec{r}_{ij}^{-1} - V_i^{HF} \right), \tag{2.29}$$

where V_i^{HF} is the average potential in HF theory defined in Eq. (2.19) while $\vec{r}_{ij}^{-1}$ is the electron-electron interaction distance defined in Eq. (2.3). MP2 is a particular realization of the Rayleigh-Schrödinger perturbation theory (RSPT) described in Ref. [79, 82]. The approach is to expand the eigenvectors, $\left| \Psi_n \right\rangle$, and eigenvalues, E_n, of the exact Hamiltonian ($\hat{H}$) as power series in λ,

$$\left|\Psi_n\right\rangle = \left|\Psi_n^{(0)}\right\rangle + \lambda\left|\Psi_n^{(1)}\right\rangle + \lambda^2\left|\Psi_n^{(2)}\right\rangle + \cdots$$

$$E_n = E_n^{(0)} + \lambda E_n^{(1)} + \lambda^2 E_n^{(2)} + \cdots$$

(2.30)

Substituting these expressions into the eigenvalue problem, Eq. (2.5), and writing $\hat{H}$ as in Eq. (2.28) gives

$$\left(\hat{H}_0 + \lambda V\right)\left(\left|\Psi_n^{(0)}\right\rangle + \lambda\left|\Psi_n^{(1)}\right\rangle + \lambda^2\left|\Psi_n^{(2)}\right\rangle + \cdots\right)$$

$$= \left(E_n^{(0)} + \lambda E_n^{(1)} + \lambda^2 E_n^{(2)} + \cdots\right)\left(\left|\Psi_n^{(0)}\right\rangle + \lambda\left|\Psi_n^{(1)}\right\rangle + \lambda^2\left|\Psi_n^{(2)}\right\rangle + \cdots\right)$$

(2.31)

The next step is to collect terms with equal powers of λ and set $\lambda = 1$. This gives

$$\hat{H}_0\left|\Psi_n^{(0)}\right\rangle = E_n^{(0)}\left|\Psi_n^{(0)}\right\rangle$$

$$\hat{H}_0\left|\Psi_n^{(1)}\right\rangle + V\left|\Psi_n^{(0)}\right\rangle = E_n^{(0)}\left|\Psi_n^{(1)}\right\rangle + E_n^{(1)}\left|\Psi_n^{(0)}\right\rangle$$

$$\hat{H}_0\left|\Psi_n^{(2)}\right\rangle + V\left|\Psi_n^{(1)}\right\rangle = E_n^{(0)}\left|\Psi_n^{(2)}\right\rangle + E_n^{(1)}\left|\Psi_n^{(1)}\right\rangle + E_n^{(2)}\left|\Psi_n^{(0)}\right\rangle$$

$$\vdots$$

(2.31)

Left multiplying each equation in (2.31) by $\left\langle\Psi_n^{(0)}\right|$ and assuming $\left\langle\Psi_n^{(0)}\middle|\Psi_n^{(m)}\right\rangle = \delta_{0m}$ (intermediate normalization condition where δ_{0m} is the Kronecker delta) leads to the relations

$$E_n^{(0)} = \left\langle\Psi_n^{(0)}\middle|\hat{H}_0\middle|\Psi_n^{(0)}\right\rangle$$

$$E_n^{(1)} = \left\langle\Psi_n^{(0)}\middle|V\middle|\Psi_n^{(0)}\right\rangle$$

$$E_n^{(2)} = \left\langle\Psi_n^{(0)}\middle|V\middle|\Psi_n^{(1)}\right\rangle$$

$$\vdots$$

(2.32)

Eq. (2.32) indicates that a first order correction ($\left|\Psi_n^{(1)}\right\rangle$) to the wave function determines a second order correction to the energy (third equation in (2.32)). The HF energy of the exact Hamiltonian, $\hat{H}$, is determined as

$$E_0^{HF} = \left\langle \Psi_n^{(0)}\left|\hat{H}\right|\Psi_n^{(0)}\right\rangle = \left\langle \Psi_n^{(0)}\left|\hat{H}_0 + V\right|\Psi_n^{(0)}\right\rangle = E_n^{(0)} + E_n^{(1)} \qquad (2.33)$$

using Eq. (2.32). Therefore the first correction to the HF energy comes at the second order in the perturbative expansion. To solve Eq. (2.31) and (2.32), the higher order corrections to the wave function are expanded in terms of eigenfunctions of the reference Hamiltonian, $\hat{H}_0$, but for the ground state eigenfunction, $\left|\Psi_0^{(0)}\right\rangle$. In HF theory, such eigenfunctions are single Slater determinants that differ from the ground state determinant by the occupation of one or more orbitals considered as virtual in the description of the ground state wave function ($\left|\Psi_0^{(0)}\right\rangle$). Brillouin's theorem [79] dictates that such excited determinants used to span $\left|\Psi_n^{(1)}\right\rangle$, for example, should be related to $\left|\Psi_0^{(0)}\right\rangle$ by double electron excitations from occupied orbitals (a and b) to virtual orbitals (r and s). Thus

$$\left|\Psi_n^{(1)}\right\rangle = \sum_{a>b;r>s}\left|\Psi_{ab}^{rs}\right\rangle\left\langle\Psi_{ab}^{rs}\left|\Psi_n^{(1)}\right\rangle = \sum_{a>b;r>s}\left|\Psi_{ab}^{rs}\right\rangle C_{n,abrs}^{(1)}, \qquad (2.34)$$

where $C_{n,abrs}^{(1)} = \left\langle\Psi_{ab}^{rs}\left|\Psi_n^{(1)}\right\rangle$ and $\left|\Psi_{ab}^{rs}\right\rangle$ denotes an excited determinant. The second equation in (2.31) can be rearranged to

$$\left(E_n^{(0)} - \hat{H}_0\right)\left|\Psi_n^{(1)}\right\rangle = \left(V - E_n^{(1)}\right)\left|\Psi_n^{(0)}\right\rangle$$

$$\Updownarrow$$

$$\left(E_n^{(0)} - \hat{H}_0\right)\sum_{a>b;r>s}\left|\Psi_{ab}^{rs}\right\rangle\left\langle\Psi_{ab}^{rs}\left|\Psi_n^{(1)}\right.\right\rangle = \left[V - \left(\left\langle\Psi_n^{(0)}\left|V\right|\Psi_n^{(0)}\right\rangle\right)\right]\left|\Psi_n^{(0)}\right\rangle \qquad (2.35)$$

where the definitions for $\left|\Psi_n^{(1)}\right\rangle$ in Eq. (2.34) and $E_n^{(1)}$ in Eq. (2.32) have been used. Left multiplying Eq. (2.35) by $\left\langle\Psi_{ab}^{rs}\right|$ and assuming that the eigenfunctions of $\hat{H}_0$ are all orthonormal (hence, $\left\langle\Psi_{ab}^{rs}\left|\Psi_n^{(0)}\right.\right\rangle = 0$ and $\left\langle\Psi_{ab}^{rs}\left|\Psi_{ab}^{rs}\right.\right\rangle = 1$) gives

$$\left(E_n^{(0)} - E_k^{(0)}\right)\left\langle\Psi_{ab}^{rs}\left|\Psi_n^{(1)}\right.\right\rangle = \left\langle\Psi_{ab}^{rs}\left|V\right|\Psi_n^{(0)}\right\rangle \Leftrightarrow \left\langle\Psi_{ab}^{rs}\left|\Psi_n^{(1)}\right.\right\rangle = C_{n,abrs}^{(1)} = \frac{\left\langle\Psi_{ab}^{rs}\left|V\right|\Psi_n^{(0)}\right\rangle}{E_n^{(0)} - E_k^{(0)}} \qquad (2.36)$$

where $E_k^{(0)}$ is the eigenvalue of $\left|\Psi_{ab}^{rs}\right\rangle$ (that is, $\hat{H}_0\left|\Psi_{ab}^{rs}\right\rangle = E_k^{(0)}\left|\Psi_{ab}^{rs}\right\rangle$). The second order energy correction becomes

$$E_n^{(2)} = \left\langle\Psi_n^{(0)}\left|V\right|\Psi_n^{(1)}\right\rangle = \left\langle\Psi_n^{(0)}\left|V\sum_{a>b;r>s}\right|\Psi_{ab}^{rs}\right\rangle C_{n,abrs}^{(1)} = \left\langle\Psi_n^{(0)}\left|V\right|\Psi_{ab}^{rs}\right\rangle\frac{\left\langle\Psi_{ab}^{rs}\left|V\right|\Psi_n^{(0)}\right\rangle}{E_n^{(0)} - E_k^{(0)}}$$

$$= \frac{\left|\left\langle\Psi_n^{(0)}\left|V\right|\Psi_k^{(0)}\right\rangle\right|^2}{E_n^{(0)} - E_k^{(0)}} \qquad , \qquad (2.37)$$

where $\left|\Psi_k^{(0)}\right\rangle = \left|\Psi_{ab}^{rs}\right\rangle$. The MP2 total energy is then

$$E^{MP2} = E_0^{HF} + E_n^{(2)} = E_n^{(0)} + E_n^{(1)} + E_n^{(2)} \qquad (2.38)$$

As stated previously, the term "restricted" implies that the spatial parts of alpha spin orbitals were constrained to be equal to those of beta spin orbitals. Such calculations capture only about half of the dynamic correlation energy but can be used to generate

initial guesses of molecular orbitals (MOs) (through orbital rotation) for the next level of calculations which is the MCSCF method and is briefly described in the next subsection.

The Multiconfiguration Self-Consistent Field (MCSCF) Method

The purpose of MCSCF calculations in the present work was to account for static or long range electron correlation, which can be very important for transition metal systems. Such systems warrant a multiconfigurational treatment. That is, their wave functions are dominated by more than one configuration of the electrons, which must be accounted for in an accurate description of those wave functions. Single reference methods like the RHF and RMP2 methods described above fall short of being able to adequately describe such systems. As will be seen in the subsequent Chapters discussing studies on transition metal molecules, several of the computed electronic states were found to have more than one leading electron configuration (some occurring with nearly equal amplitudes, cf. Eq. (2.16)) contributing to the total wave function. MCSCF accounts for this multiconfigurational character of the wave function by considering not one determinant but a set of model space configuration state functions (CSFs) in determining the molecular orbitals.

Choice of Active Space

The most challenging problem in MCSCF [92-94], as well as particular choices as CASSCF and RASSCF [95-98], is the choice of the configuration space or model space. A poor model space often leads to difficult and slow or even no convergence. It could even lead to convergence to a state other than the desired state. The strategy often used is to partition the molecular orbitals into three main groups: (1) the core or inactive orbitals which are the energetically lowest lying orbitals that are doubly occupied in all

configurations; (2) the active orbitals which are used to generate the many-electron functions spanning the valence or model space and have variable occupancies; and (3) the virtual orbitals which are energetically high lying orbitals and are unoccupied in any model space function. In the CASSCF method, all possible electron configurations are considered that can be generated from the active orbitals in the description of the wave function. That is, full configuration interaction (FCI) is performed within the active or model space. This can be quite expensive for large systems. For example, distributing m electrons in n active orbitals without any restriction leads to N configurations where

$$N = \frac{n!(n+1)!}{\left(\frac{m}{2}\right)!\left(\frac{m}{2}+1\right)!\left(n-\frac{m}{2}\right)!\left(n-\frac{m}{2}+1\right)!} \tag{2.39}$$

In the RASSCF method, the active orbitals are further partitioned into three subspaces: (a) restricted active space 1 (RAS1); (b) restricted active space 2 (RAS2); and (c) restricted active space 3 (RAS3). In RASSCF calculations, the RAS1 set of orbitals is restricted to no more than two holes while RAS3 is restricted to no more than two electrons. These restrictions significantly reduce the configuration space and permit calculations on relatively larger systems for which CASSCF is too expensive.

The difficulty with these calculations is to determine which orbitals should be considered active. This is not immediately obvious by observing, say, natural orbitals obtained from RMP2 calculations. The biggest problem often faced is which of the virtual orbitals from HF or RMP2 calculations should be included in the active space at the CASSCF, RASSCF, or MCSCF levels. Getting around this depends on the questions being addressed in the specific problem. For example, if calculations are being performed

on a system involving bond breaking, then at least all the bonding and antibonding orbitals involved in the process should be included in the active space; if a calculation is performed on a π-system such as on two parallel π-stacked benzene rings (as illustrated in Figure 1), it would be desirable to include the π orbitals derived from the valence shells of the atoms. In the present calculations, besides using these strategies, natural occupation numbers of RMP2 orbitals were often analyzed to provide a clue to what orbitals should be considered active. Sometimes, initial calculations relied on trial and error, simply driven by physical and/or chemical intuition.

Preliminary diagnostic calculations are often essential to assess the accuracy of choice of the active space. Such diagnosis involves, e.g., the ability of the chosen active space to correctly dissociate a covalent bond. This is crucial because some active spaces work well around equilibrium geometries but are inadequate for describing bond dissociation. There are many published studies in which the authors focused calculations only at short bond lengths around the equilibrium geometries. The usefulness of such calculations is questionable since it is not clear if the active spaces used were sufficient for the description of the entire potential energy curves (PECs) or even the bond breaking regions. The quality of CASSCF, RASSCF, and MCSCF results is dependent on the quality of the active space and wrong active spaces can lead to meaningless/unphysical results at some geometries or even to discontinuities. If the wrong active space is chosen at these levels, high level methods, like GVVPT2, will be unable to correct for the lapse and deliver accurate results. In the present work, narrowing down on the most advantageous active space for the transition metal molecules was challenging and involved a lot of experimentation. Each system seemed to pose unique challenges. For

example, the active space used to compute the electronic states of Mn_2 was insufficient for some of the electronic states of its isovalent counterpart, Tc_2.

Lastly, because GVVPT2 is mathematically and computationally robust [3, 4] (i.e., there will always be a solution to the equations, even when the accuracy is diminished), wave function amplitudes are often analyzed for the presence of any large individual contributions from the external space, which signal the need to include additional orbitals in the model space. Obviously, obtaining such a result after a significant portion of the potential energy surface has been studied is disappointing and a waste of computational resources. Consequently, assessments of model space adequacy are optimally made for a few selected points across the potential energy surface of interest prior to extensive calculations. However, in the situation that convergence of the underlying MCSCF calculations is nontrivial, and use is made of the availability of orbitals from adjacent geometries, one can encounter problems with the model space only after a significant number of calculations with an inadequate model space have been made.

The Macroconfiguration Approach

The technique of macroconfigurations introduced by Khait et al. [22] was used in the MCSCF and GVVPT2 calculations reported in this dissertation. This approach is similar, but not equivalent, to the orbital partitioning scheme of RASSCF. In fact, a RASSCF model space is a special case of the use of macroconfigurations. In the macroconfiguration method, active orbitals are partitioned into groups and the active electrons are distributed into those groups. Unlike RASSCF which considers three groups within the set of active orbitals, the macroconfiguration method allows more than three

groups and additionally, the active electrons could be placed in those groups in any manner. There are no particular constraints on the number of electrons per orbital subgroup provided $n_a \leq 2m_a$ where n_a is the number of electrons and m_a is the number of orbitals in the subgroup. There are also no constraints as to the number of orbitals allowed in a given subgroup. Thus, the macroconfiguration approach entails essentially unlimited flexibility, only subject to computational resource constraints. [N.B. Henceforth, a macroconfiguration is represented by the symbol $\kappa(\mathbf{n})$ where $\mathbf{n}$ specifies the number of active electrons distributed among active orbital subgroups].

Suppose that the active orbitals of a system are partitioned into g orbital subgroups. A macroconfiguration, $\kappa(\mathbf{n})$, is then a specific distribution of its $\mathbf{n}$ active electrons among those subgroups,

$$\kappa(\mathbf{n}) = A_1^{n_1} A_2^{n_2} \ldots A_g^{n_g}, \qquad (2.40)$$

where $A_1, A_2, \cdots, A_g$ denote the active orbital subgroups while the superscripts represent integer numbers of electrons in each subgroup. The electron numbers ($n_1, n_2, \cdots, n_g$) can be varied subject to the constraints

$$0 \leq n_a \leq 2m_a, \quad a \in [1, g], \qquad (2.41)$$

$$n_1 + n_2 + \cdots + n_g = \mathbf{n}, \qquad (2.42)$$

where n_a is the number of electrons in active orbital subgroup A_a; m_a is the number of orbitals in A_a; while Eq. (2.42) requires that the sum of electrons in the subgroups must give the number of active electrons, $\mathbf{n}$. Each unique specification of the active electrons as in Eq. (2.40) defines a reference $\kappa(\mathbf{n})$. The flexibility of the macroconfiguration method [22] allows it to support complete active space (CAS) type calculations (when the

active orbitals are all in one group) as well as incomplete active spaces. The user specifies the number of orbitals considered active and decides on how to partition those orbitals. Next, the user determines how to distribute the active electrons defining the reference macroconfigurations ($\kappa(\mathbf{n})$s). In preliminary calculations on some of the molecules in the present work, some of the reference $\kappa(\mathbf{n})$s specified in the input file were found not to lead to configurations of correct spin and point group symmetry for the investigated states. Such $\kappa(\mathbf{n})$s were therefore removed from the list of reference $\kappa(\mathbf{n})$s. In general, when distributing active electrons among the orbital subgroups, symmetry constraints should be considered. For a specified molecular term, there are obviously some electronic distributions that would not generate configurations with the desired symmetry. For example, a $\kappa(\mathbf{n})$ such as the following

$$\kappa(\mathbf{n}) = \left(\pi_u \pi_u\right)^3 \left(\sigma_g \sigma_g\right)^2 \left(\delta_g \delta_g\right)^2 \tag{2.43}$$

cannot describe a gerade (g) molecular term such as Γ_g in the $D_{\infty h}$ symmetry point group (since all configurations derived from this macroconfiguration would rather have ungerade (u) parity: $u \times u \times u \times g \times g \times g \times g = u$).

Once the $\kappa(\mathbf{n})$s have been specified, each $\kappa(\mathbf{n})$ generates a unique set of configurations and consequently configuration state functions (CSFs). CSFs are spin-adapted linear combinations of Slater determinants constructed to be eigenfunctions of the total spin squared ($\hat{S}^2$) operator and its z-projection ($\hat{S}_z$). CSFs constitute the basis for the expansion of the many-electron wave function. Since they are linear combinations of Slater determinants, they automatically obey the Pauli principle and lead to the correct spin symmetry of the molecule. Moreover, CSFs possess the symmetry properties of the $U(2n)$ and S_N groups [99-102]. In the MCSCF and GVVPT2 programs used in the

present studies, CSFs were generated from κ(**n**)s and their configurations using the graphical unitary group approach (GUGA) [103]. Details as to how the configuration-driven codes in UNDMOL work are available in Ref. [104].

The set of configurations, and hence CSFs, of each κ(**n**) are orthogonal to those of other κ(**n**)s. The fact that each κ(**n**) creates a set of configurations (and CSFs) that is disjoint with respect to configurations generated from all other κ(**n**)s allows a large number of noninteracting electronic configuration pairs to be screened (i.e., without actual calculation) and, also, provides an efficient way of generating excited configurations. All orbital rotations within a given subgroup of active orbitals are redundant whereas orbital rotations among subgroups are non-redundant. This latter point is critical in performing orbital optimization calculations using κ(**n**)s. Its implication is that the user must analyze the molecular orbitals to ensure that the right orbitals are in the right positions before performing calculations. Any orbital flips would lead to a different MCSCF or GVVPT2 solution. In the UNDMOL electronic structure software package developed by the Hoffmann group at the University of North Dakota [N.B. The structure of UNDMOL is described in Ref. [104]], the molecular orbital file is named *orbitals.dat*. In this file, molecular orbitals are listed in order of symmetry type (that is, the irreducible representations beginning with the first in the given point group); and orbitals of a given symmetry are listed in order of increasing energy. Orbital flips involve a core orbital replacing an active orbital or a virtual orbital replacing an active orbital or an active orbital expected to be higher in energy replacing one that is expected to lie energetically lower.

To illustrate this, consider a molecule in D_{2h} symmetry (the highest Abelian group supported by UNDMOL). The D_{2h} point group has the following irreducible representations $\{A_g, B_{1g}, B_{2g}, B_{3g}, A_u, B_{1u}, B_{2u}, B_{3u}\}$. In the orbitals.dat file, molecular orbitals would be listed beginning with A_g type orbitals to those of B_{3u} irreducible representation; and for each symmetry type, orbitals would be listed in order of increasing energy, with special consideration for multiple active orbital groups. Occasionally, however, molecular orbitals may not be in their rightful positions in the orbitals.dat file. For example, an orbital that is expected to be the sixth A_g type may appear as the eighth A_g type orbital. If the orbitals are not identified and manually switched back to their rightful positions, a different MCSCF or GVVPT2 solution would be obtained in calculations provided those orbitals belong to different valence subspaces. To further clarify this, consider the Cr_2 molecule. Suppose an active space for Cr_2 is assumed, consisting of twelve molecular orbitals derived from the 3d and 4s subshells of the Cr atoms. Suppose also that the orbital splitting in Figure 4 is assumed for these orbitals. In the D_{2h} point group, these orbitals are associated with the irreducible representations $3d_{z^2}\sigma_g = A_g$, $3d_{z^2}\sigma_u^* = B_{1u}$, $3d_{xz}\pi_u = B_{3u}$, $3d_{xz}\pi_g^* = B_{2g}$, $3d_{yz}\pi_u = B_{2u}$, $3d_{yz}\pi_g^* = B_{3g}$, $3d_{x^2-y^2}\delta_g = A_g$, $3d_{x^2-y^2}\delta_u^* = B_{1u}$, $3d_{xy}\delta_g = B_{1g}$, $3d_{xy}\delta_u^* = A_u$, $4s\sigma_g = A_g$, and $4s\sigma_u^* = B_{1u}$. This gives a total of three A_g type orbitals, three B_{1u} type orbitals, and one orbital for all other symmetry types.
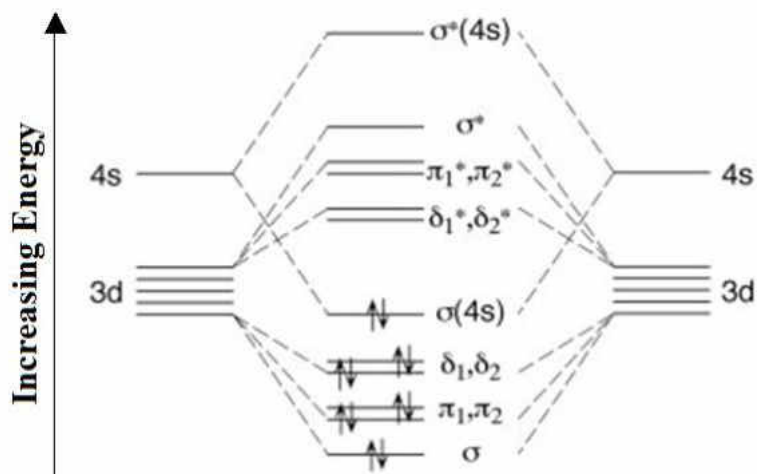
Figure 4. Molecular orbital splitting for the Cr_2 molecule.

If a valence bond style description of the bonding in the partitioning of the active space is considered such that each bonding orbital is paired with its corresponding antibonding counterpart to constitute an active subspace and then two of the twelve active electrons are assigned to each subspace, this would lead to the following reference $\kappa(\mathbf{n})$

$$\left(3d_{z^2}\sigma_g\, 3d_{z^2}\sigma_u^*\right)^2 \left(3d_{xz}\pi_u\, 3d_{xz}\pi_g^*\right)^2 \left(3d_{yz}\pi_u\, 3d_{yz}\pi_g^*\right)^2 \times$$
$$\left(3d_{x^2-y^2}\delta_g\, 3d_{x^2-y^2}\delta_u^*\right)^2 \left(3d_{xy}\delta_g\, 3d_{xy}\delta_u^*\right)^2 \left(4s\sigma_g\, 4s\sigma_u^*\right)^2 \quad , \tag{2.44}$$

where the superscripts indicate the number of electrons per subspace (this is, indeed, what was done in the calculations of this molecule). The positions of the subspaces in the reference $\kappa(\mathbf{n})$ are immaterial as long as the orbitals in each group correspond to different irreducible representations of the point group. For example, the π orbitals derived from $3d_{xz}$ correspond to different irreducible representations than those from $3d_{yz}$. Therefore, the π subspaces could be placed anywhere (and in any order) in reference $\kappa(\mathbf{n})$ (2.44) such as at the first or last positions. If, however, active orbitals within different subspaces correspond to the same irreducible representations of the point group, careful

examination of the orbitals in the orbitals.dat file must be done to ensure that the orbitals are in their rightful positions. If the orbital diagram in Figure 4 is indeed the correct ordering in the orbitals.dat file and the orbital groups are defined using an energy ordering, then the bonding a_g orbitals lie energetically in the order $3d_{z^2}\sigma_g \leq 3d_{x^2-y^2}\delta_g \leq 4s\sigma_g$. However, their antibonding counterparts of b_{1u} symmetry are rather in the order $3d_{x^2-y^2}\delta_u^* \leq 3d_{z^2}\sigma_u^* \leq 4s\sigma_u^*$. Thus, the positions of the $3d_{x^2-y^2}\delta_u^*$ and $3d_{z^2}\sigma_u^*$ must be interchanged to reflect the same ordering in the bonding orbitals and, thus, guarantee that each of the bonding orbitals is actually paired with the corresponding antibonding one. Without manually performing this switch in orbitals.dat, the user would specify reference $\kappa(\mathbf{n})$ in the input file whereas the first orbital subspace in that reference $\kappa(\mathbf{n})$ is not $\left(3d_{z^2}\sigma_g 3d_{z^2}\sigma_u^*\right)^2$ as expected but rather $\left(3d_{z^2}\sigma_g 3d_{x^2-y^2}\delta_u^*\right)^2$. This will, in general, affect the calculations and lead to a different solution. One way of avoiding orbital flips is to place all active orbitals corresponding to the same irreducible representations of the point group in the same valence subspace. Since orbital rotations related to a given subspace are redundant, any orbital flips within a valence subspace would likewise be redundant.

All things being equal, the macroconfiguration approach provides a very efficient way of evaluating Hamiltonian matrix elements. Some matrix elements are determined to be zero *a priori*. Any Hamiltonian matrix element that couples CSFs resulting from configurations (and hence, macroconfigurations) that differ by more than two electrons are automatically zero. Details on how Hamiltonian matrix elements are evaluated using the macroconfiguation and GUGA techniques are provided in Ref. [105].

The Multiconfigurational Self-Consistent Field Wave function

In order to account for static or long range electron correlation, the MCSCF method [92-94] constructs the total wave function as a linear combination of CSFs from a user-specified model space generated from active orbitals that are known (or suspected, on chemical grounds) to have partial occupancy. Once the correct model space has been specified and generated from $\kappa(\mathbf{n})$s as discussed above, orthonormal sets of CSFs are generated from those $\kappa(\mathbf{n})$s by appropriate antisymmetrization and spin combinations, and used to span the wave function in a manner similar to CI methods,

$$\left|\Psi_I^{MC}\right\rangle = \left|\Phi_M\right\rangle C_{MI} = \sum_{m \in L_M} \left|\Phi_m\right\rangle C_{mI} , \tag{2.45}$$

where $\left|\Psi_I^{MC}\right\rangle$ is the MCSCF wave function sought for; $\left|\Phi_m\right\rangle$ is a set of CSFs belonging to the model space of dimension L_M. The MCSCF eigenstates, $\left|\Psi_I^{MC}\right\rangle$, solve the eigenvalue problem within the model space,

$$\hat{H}\left|\Psi_I^{MC}\right\rangle = E_I^{MC}\left|\Psi_I^{MC}\right\rangle, \tag{2.46}$$

where E_I^{MC} is the Ith-lowest eigenvalue of the model space MCSCF wave function,

$$E_I^{MC} = \left\langle \Psi_I^{MC} \left|\hat{H}\right| \Psi_I^{MC} \right\rangle \tag{2.47}$$

Using Eq. (2.45), the matrix form of Eq. (2.46) is

$$\mathbf{H}_{MM}\mathbf{C}_{MI} = \mathbf{E}_I^{MC}\mathbf{C}_{MI} \qquad\qquad \left(\mathbf{C}_{IM}^+\mathbf{C}_{MI} = \mathbf{I}\right), \tag{2.48}$$

where $\mathbf{H}_{MM} = \left\langle \Phi_M \left|H\right| \Phi_M \right\rangle$ is the matrix of the model space block of the total Hamiltonian ($\mathbf{H}_{TT}$), $\mathbf{C}_{MI}$ is the matrix of the CI coefficients in Eq. (2.45) (N.B. The orthogonality of the basis CSFs, $\left|\Phi_m\right\rangle$, in Eq. (2.45) is guaranteed by construction), and $\mathbf{E}_I^{MC}$ is a diagonal matrix of MCSCF eigenvalues. The Hamiltonian operator in Eq. (2.47)

may be written more explicitly, in terms of the molecular orbitals that determine each

CSF, as

$$\hat{H} = \sum_{ij}^{MOs} h_{ij} E_{ij} + \tfrac{1}{2} \sum_{ijkl}^{MOs} g_{ijkl} e_{ijkl} \,, \qquad (2.49)$$

where h_{ij} and g_{ijkl} are the one- and two-electron molecular orbital integrals while E_{ij} and

e_{ijkl} are the generators of the unitary group, defined as

$$
\begin{aligned}
E_{ij} &= a_{i\alpha}^{\dagger} a_{j\alpha} + a_{i\beta}^{\dagger} a_{j\beta} \\
e_{ijkl} &= E_{ij} E_{kl} - \delta_{jk} E_{il}
\end{aligned}
\qquad (2.50)
$$

Whereas CI methods optimize only the CI coefficients, the MCSCF variationally

determines the optimal sets of both the CI expansion coefficients in Eq. (2.45) and the

molecular orbital expansion coefficients in terms of basis functions. Since the HF

molecular orbitals were determined self-consistently in the average field of a single

electron configuration, they must be reoptimized at the MCSCF level; similarly, MP2

natural orbitals are not self-consistent for the model space. As noted before, only the

occupied orbitals within the single determinant HF wave function make physical sense

for an N-electron system. And, while MP2 MOs are superior to SCF orbitals (relative to

MCSCF orbitals) they too need modification. In order to describe a multiconfigurational

situation at the MCSCF level of theory, both the atomic basis function coefficients

describing molecular orbitals as in Eq. (2.23) and the CI coefficients in Eq. (2.45) are

simultaneously optimized variationally. This is a nontrivial and highly nonlinear problem.

MCSCF optimization is one of the most challenging of ab initio quantum

chemistry tasks due to the coupling of the CI coefficients to the one-electron space. This

implies that difficulties faced in the HF iterative scheme are compounded at the MCSCF

level of theory [82]. Such problems are intensified when incomplete model spaces are used or when multiple states of the same symmetry are optimized in a state-averaged calculation. In the event that multiple low-lying electronic states are found to have the same spin and irreducible representation, the matrix Eq. (2.48) may be used to determine both the MCSCF eigenvectors and eigenvalues for all such states. This is called a state-averaged MCSCF (SA-MCSCF) calculation, leading to state-averaged eigenvalues, E_{SA}^{MC}, where

$$E_{SA}^{MC} = \sum_{I=1}^{N_P} w_I E_I^{MC} = \sum_{I=1}^{N_P} w_I \left\langle \Psi_I^{MC} \left| H \right| \Psi_I^{MC} \right\rangle, \tag{2.51}$$

where N_P is the number of MCSCF states of the same spin and irreducible representation included in the state-averaged calculation and $\left(w_I \geq 0 \right)$ are geometry independent weights, whose sum is constrained to be unity $\left(\sum_{I=1}^{N_P} w_I = 1 \right)$, that specify the influence of each of the N_P states on the MOs and CI coefficients being optimized. E_I^{MC} in Eq. (2.51) is the energy of the Ith state.

Obtaining MCSCF solutions is a nontrivial task and as noted previously, success of the procedure largely depends on the quality of the active space and the nature of the starting orbitals. However, the development of direct minimization methods [106-109], based on the Newton-Raphson algorithm, enabled rapid convergence within the MCSCF iterative scheme, provided that one is in the local region of the final MCSCF solution. Nonetheless, those approaches require explicit evaluation of the hessian matrix involving the transformation of two electron integrals that are not used in the construction of the Fockian matrices [109]. Moreover, MCSCF iterative schemes based on the Newton-

Raphson method can sometimes converge to incorrect roots [110]. The technique that was used to circumvent such problems is outlined in Ref. [111]. The approach uses directions of negative curvature, based on a step-length algorithm, to minimize the MCSCF energies of both ground and excited states on a manifold that can be described topologically as a nonlinear equality-constrained problem (NEP). The technique was demonstrated: to be applicable to general MCSCF wave functions; to support both complete and incomplete model spaces; and to work with Newton and quasi-Newton methods for the determination of descent directions.

A problem often encountered in MCSCF iterations is identifying and dealing with redundancies [112]. At the MCSCF level of theory, it can be hard to distinguish between low-occupancy occupied and unoccupied (virtual) orbitals (and also between high-occupancy active orbitals and core orbitals) since the one-electron energies of the various spaces can be misleading. In the present work, advantage was taken of orbital invariances guaranteed by macroconfigurations [22].

<p style="text-align:center">The Generalized Van Vleck Second Order Perturbation Theory</p>

Besides entailing a computationally intensive iterative procedure whose success highly depends on the quality of the model space, the MCSCF method fails to adequately capture dynamic electron correlation energy. Although this short range energy is usually only about 1% of the total energies of quantum systems, it is critical to the understanding of the physics of such systems. For example, in this work, in studies of the $X^1\Sigma_g^+$ state of Cr_2, MCSCF calculations using different basis sets, including all-electron and effective core potential (ECP) basis sets, could not give even qualitatively correct potential energy curves (PECs). The method for complete recovery of electron correlation energy is the

full configuration interaction (FCI) method in which all possible configurations of electrons are considered in the total Hilbert space. However, this approach is prohibitively expensive (scaling as N! with system size, where N is a measure of the size of a system in terms of the number of atoms or basis functions) even for systems of a few atoms. Truncated MRCI methods, like MRCISD, provide accurate descriptions of complex systems for which both short and long range electron correlations are important. However, configuration interaction (CI) methods diagonalize the entire Hamiltonian matrix in the space of the specified truncation, which can be quite huge. This curtails the applicability of such methods to the study of model systems or small molecules. The MRCISD(TQ) method [113] partitions the total configuration space (L) into a model (L_M) subspace of reference configurations, and two external subspaces (L_{Q1} and L_{Q2}). L_{Q1} is related to the reference configurations by single and double excitations (i.e., as in MRCISD) and L_{Q2} by triple and quadruple excitations. Eventually, an eigenvalue problem, involving an effective Hamiltonian, is solved within a subspace of $L_M \oplus L_{Q1}$. Such procedures significantly reduce computational costs relative to MRCISDTQ but L_{Q1} could still be quite large compared to L_M and so the size restrictions of MRCISD apply.

Due to the high cost of computation for most high level quantum chemistry methods that account for static and dynamic electron correlation effects, multireference perturbation theory (MRPT) methods are often better alternatives since such methods consider the vast majority of electron excitations perturbatively. Second order MRPT methods scale an order of magnitude less than MRCISD (approximately N^5 for MRPT

versus N^6 for MRCISD, where N is a measure of system size). However, as was mentioned in Chapter I, many MRPT methods suffer from intruder state problems. Although various shift parameters are often used to overcome such problems, results tend to depend on the nature of such parameters [18]. On the other hand, a recent study [114] that compared three relatively new MRPT schemes: the GVVPT2 method used in the present studies; the second order state-specific multireference perturbation theory (SS-MRPT2); and the second order multiconfiguration perturbation theory (MCPT2), using both Møller-Plesset [91] and Epstein-Nesbet [115, 116] partition schemes for the Hamiltonian, found that GVVPT2 (and SS-MRPT2) gave smooth PECs for all systems tested whereas MCPT2 suffered from instabilities in the solutions at some points. Since interest in the present studies is in multiple states, and SS-MRPT2 by construction is state-specific (SS), GVVPT2 was clearly desirable for the studies in this dissertation. A key feature of the GVVPT2 method is its ability to produce smooth PECs of any system including those that could be a challenge to other MRPT techniques and especially to older MRPTs. The salient features of GVVPT2 are briefly reviewed in the next paragraphs.

GVVPT2 [3, 4] is a variant of quasidegenerate perturbation theory (QDPT) [117]. More precisely, its mathematical foundation is the self-consistent quasidegenerate perturbation theory (SC-QDPT) method [118], which was constructed to: obviate any instabilities resulting from the presence of intruder states; guarantee size-consistency; ensure that the projection of the correlated wave functions on the model space coincided with the optimal primary subspace within which the lowest states of interest are sought; and moreover, guarantee that the energies of the primary states sought are upper bounds

to the full CI limit. In order to understand the formulation of GVVPT2, it behooves us therefore to begin with a brief review of the SC-QDPT method.

In SC-QDPT, the total Hilbert space, spanned by N orthonormal CSFs ($\left|\Phi_n\right\rangle$)

$$L = span\left\{\left|\Phi_n\right\rangle\right\}_{n=1}^{N} \, , \tag{2.52}$$

is partitioned into a model space, L_M, in which the N_p lowest states are sought, and an external space L_Q, whose configurations are related to those of L_M through electron excitations,

$$L_M = span\left\{\left|\Phi_m\right\rangle\right\}_{m=1}^{N_m} \; ; \; L_Q = span\left\{\left|\Phi_q\right\rangle\right\}_{q=1}^{N_q} \, , \tag{2.53}$$

where $\left|\Phi_m\right\rangle$ and $\left|\Phi_q\right\rangle$ denote CSFs in L_M and L_Q, respectively. SC-QDPT is constructed to completely avoid quasideneracy problems by further partitioning the model space into a primary subspace, L_P, which contains the N_p lowest states sought, and an orthogonal complement, called the secondary subspace (L_S),

$$L_P = span\left\{\left|\Psi_p^{(0)}\right\rangle\right\}_{p=1}^{N_P} \; ; \; L_S = span\left\{\left|\Psi_s^{(0)}\right\rangle\right\}_{s=1}^{N_s} \; ; \; N_p + N_s = N_m \; ; \; L_S \oplus L_P = L_M \tag{2.54}$$

whose interactions with the perturbed primary subspace are described variationally rather than perturbatively. $\left|\Psi_p^{(0)}\right\rangle$ and $\left|\Psi_s^{(0)}\right\rangle$ are the unperturbed primary and secondary states, respectively. It is clear that, all things being equal, states in the secondary subspace are the ones whose energies are closest to those of primary states and hence, these secondary states are the ones most likely to cause intruder state problems. By considering perturbed primary-unperturbed secondary (P-S) interactions variationally, the intruder state problem is avoided and the secondary subspace then serves as an "energy buffer" that

separates the primary and external subspaces well enough to permit primary-external (P-Q) interactions to be described in a strongly convergent perturbative manner.

GVVPT2 follows the above partitioning of the total Hilbert space such that the total effective Hamiltonian matrix ($\mathbf{H}^{\text{eff}}$) has the following form,

$$\mathbf{H}^{\text{eff}} = \left(\begin{array}{c|c|c} \mathbf{H}^{\text{eff}}_{PP} & \mathbf{H}^{\text{eff}}_{PS} & \mathbf{H}^{\text{eff}}_{PQ} \\ \hline \mathbf{H}^{\text{eff}}_{SP} & \mathbf{H}^{\text{eff}}_{SS} & \mathbf{H}^{\text{eff}}_{SQ} \\ \hline \mathbf{H}^{\text{eff}}_{QP} & \mathbf{H}^{\text{eff}}_{QS} & \mathbf{H}^{\text{eff}}_{QQ} \end{array} \right) \tag{2.55}$$

where subscripts P, S, and Q denote primary, secondary, and external subspaces, respectively, and the matrix elements are described in terms of states in these subspaces; e.g., $\mathbf{H}^{\text{eff}}_{PP}$ is a block of the effective Hamiltonian matrix involving primary state vectors. [N.B. Henceforth in this subsection, bold symbols are used to denote matrices of operators or a set of vectors, e.g., $|\mathbf{\Phi}_P\rangle$ denotes a set of many-electron functions within the primary subspace]. The projection operators unto the L_P, L_S, and L_Q subspaces are defined as

$$P_P = |\mathbf{\Phi}_P\rangle\langle\mathbf{\Phi}_P| = \sum_{i=1}^{N_p} |\Psi_i^{(0)}\rangle\langle\Psi_i^{(0)}|$$

$$P_S = |\mathbf{\Phi}_S\rangle\langle\mathbf{\Phi}_S| = \sum_{j=1}^{N_s} |\Psi_j^{(0)}\rangle\langle\Psi_j^{(0)}| \tag{2.56}$$

$$P_Q = |\mathbf{\Phi}_Q\rangle\langle\mathbf{\Phi}_Q| = \sum_{\mu=1}^{N_q} |\Phi_\mu\rangle\langle\Phi_\mu|$$

where $|\Psi_P^{(0)}\rangle = |\Psi_i^{(0)}\rangle$ and $|\Psi_S^{(0)}\rangle = |\Psi_j^{(0)}\rangle$ are the unperturbed primary and secondary states, respectively, and $|\mathbf{\Phi}_Q\rangle$ is a set of external space CSFs. The $|\Psi_P^{(0)}\rangle$ states constitute the N_p lowest orthonormal eigenstates of the effective Hamiltonian in the model space

$$\langle\mathbf{\Psi}_P^{(0)}|\hat{H}|\mathbf{\Psi}_P^{(0)}\rangle = \mathbf{E}_P^{(0)}, \tag{2.57}$$

where $\mathbf{E}_p^{(0)} = diag\left\{E_1^{(0)}, E_2^{(0)}, \cdots, E_{N_p}^{(0)}\right\}$ denotes the diagonal matrix of eigenvalues of the N_p states, $\left|\mathbf{\Psi}_p^{(0)}\right\rangle$. To obtain the perturbed primary states of interest, a unitary wave-like operator [114] is defined as

$$\Omega(x) = e^X = P_S + (P_P + P_Q)e^X(P_P + P_Q),\qquad(2.58)$$

where X denotes a skew-Hermitian operator ($X^\dagger = -X$) that describes primary-external rotations. It is related to the primary (P_P) and external (P_Q) space projectors as follows

$$X = P_Q X P_P - P_P X^\dagger P_Q = \sum_p \sum_{q \in L_Q}^{N_p} X_{qp}\left(\left|\Phi_q\right\rangle\left\langle\Psi_p^{(0)}\right| - \left|\Psi_p^{(0)}\right\rangle\left\langle\Phi_q\right|\right)\qquad(2.59)$$

The effective Hamiltonian whose matrix is shown in Eq. (2.55) is constructed to satisfy the Bloch equation

$$\hat{H}\Omega P_p = \Omega P_p \hat{H}^{eff} P_p \quad\Leftrightarrow\quad \hat{H}^{eff} = \Omega^\dagger \hat{H} \Omega\qquad(2.60)$$

The wave-like operator in Eq. (2.58) is constructed as a product of parts that act on different subspaces. In infinite precision, this leads to the following decoupling equations relating to primary-secondary (P-S) and primary-external (P-Q) subspace interactions

$$P_Q \hat{H}^{eff} P_P = 0\qquad(2.61)$$

and

$$P_S \hat{H}^{eff} P_P = 0\qquad(2.62)$$

The matrix elements of operator X are nominally defined as

$$X_{qi} = \frac{\left\langle\Phi_q\left|H\right|\Psi_i^{(0)}\right\rangle}{\varepsilon_i^{(0)} - \varepsilon_q^i}, \quad (i \in P, q \in Q)\qquad(2.63)$$

where $\varepsilon_i^{(0)}$ and ε_q^i are Møller–Plesset-type energies, which are computed from the state-specific one-particle reduced density matrix $\mathbf{D}^i$, with elements

$$D_{ab}^i = \left\langle \Psi_i^{(0)} \middle| E_{ab} \middle| \Psi_i^{(0)} \right\rangle = \sum_{m,n \in L_M} C_{mi} C_{ni} \left\langle \Phi_m \middle| E_{ab} \middle| \Phi_n \right\rangle, \quad \left(i \in L_P; a, b = \text{occupied orbitals}\right) \quad (2.64)$$

and state-dependent averaged Fock operator for state i, f_c^i,

$$f_c^i = h_{cc} + \sum_{a \geq b} D_{ab}^i [(cc \mid ab) - \frac{1}{2}(ca \mid cb)], \quad \left(i \in L_P\right), \quad (2.65)$$

where a and b index occupied orbitals while c represents any orbital. The Møller–Plesset-type energies, $\varepsilon_i^{(0)}$ and ε_q^i, are obtained as follows

$$\varepsilon_i^{(0)} = \sum_a f_a^i D_{aa}^i, \quad (2.66)$$

$$\varepsilon_q^i = \sum_c f_c^i N_c^q, \quad (2.67)$$

where $\varepsilon_i^{(0)}$ is the reference Møller-Plesset-type energy while ε_q^i is the state-specific zeroth-order energy of external CSF q, and N_c^q is the occupation number of orbital c in CSF q. The energy ε_q^i is the same for all external CSFs belonging to a given external configuration (**e**) ($\varepsilon_q^i = \varepsilon_e^i$, where ε_e^i is the average energy for CSFs of external configuration **e**).

The disadvantage of using $\varepsilon_i^{(0)}$ and ε_q^i in Eq. (2.63) is the possibility of singularities occurring when $\varepsilon_i^{(0)} \approx \varepsilon_q^i$ or even negative values in the event that $\varepsilon_i^{(0)} < \varepsilon_q^i$. To circumvent such problems, GVVPT2 uses a nonlinear energy shift (Δ_i) together with a hyperbolic tangent function which provides a meaningful bound when Δ_i is negligible. The hyperbolic tangent plays the role of a switching function between degenerate and

nondegenerate regimes such that the elements of the rotation matrix, X_{qi}, in Eq. (2.66) are defined as

$$X_{qi} = \frac{\tanh(\Delta_i)}{\Delta_i} H_{qi} = \frac{\tanh(\Delta_i)}{\Delta_i} \sum_{m \in L_M} H_{qm} C_{mi} , \qquad (2.68)$$

where the C_{mi} denote eigenvectors of the unperturbed model Hamiltonian matrix and Δ_i is defined as

$$\Delta_i = \frac{1}{2}(\varepsilon_q^i - \varepsilon_i^{(0)}) + \frac{1}{2}\sqrt{(\varepsilon_q^i - \varepsilon_i^{(0)})^2 + 4\sum_{q \in e} H_{qi}^2} \qquad (2.69)$$

Eq. (2.69) incorporates the quasidegeneracy of the CSFs within each external configuration (**e**). Unlike in SC-QDPT, there are not any iterations of the external state vectors as these were found to be unnecessary for accuracies at the GVVPT2 level.

The effective Hamiltonian is represented in the basis of model space CSFs as follows

$$\begin{aligned} P_M \hat{H}^{\text{eff}} P_M &= p_P \hat{H}^{\text{eff}} P_P + P_P \hat{H}^{\text{eff}} P_S + P_S \hat{H}^{\text{eff}} P_P + P_S \hat{H}^{\text{eff}} P_S \\ &= P_M \hat{H} P_M + P_P X^\dagger \hat{H} P_M + P_M \hat{H} X P_P - \frac{1}{2} P_P \left[\hat{H} X + X^\dagger \hat{H} \right] P_P \end{aligned} , \qquad (2.70)$$

where P_M is the projector onto the model space ($P_M = P_P + P_S$). In matrix form, Eq. (2.70) becomes

$$\mathbf{H}_{MM}^{\text{eff}} = \mathbf{H}_{MM} + (\mathbf{HX})_{MP} \mathbf{C}_{PM}^\dagger + \mathbf{C}_{MP} (\mathbf{HX})_{PM}^\dagger - \mathbf{C}_{MP} (\mathbf{CHX})_{PP} \mathbf{C}_{PM}^\dagger , \qquad (2.71)$$

where $\mathbf{C}_{MP}$ is the matrix of $C_{mp} = C_{mi}$ in Eq. (2.68), while

$$(\mathbf{HX})_{MP} = \mathbf{H}_{MQ} \mathbf{X}_{QP} , \qquad (2.72)$$

and

$$(\mathbf{CHX})_{PP} = \frac{1}{2} \left[\mathbf{C}_{PM}^\dagger (\mathbf{HX})_{MP} + (\mathbf{HX})_{PM}^\dagger \mathbf{C}_{MP} \right] \qquad (2.73)$$

Ultimately, GVVPT2 diagonalizes an effective Hamiltonian matrix whose size is the same as the model space Hamiltonian (that is, the same dimension as the Hamiltonian diagonalized at the MCSCF level of theory). This effective Hamiltonian (represented here as $\mathbf{H}_{MM}^{eff,X}$) has four blocks (see Eq. (2.70)) defined as

$$\mathbf{H}_{PP}^{eff,X} = \mathbf{H}_{PP} + \frac{1}{2}\left(\mathbf{H}_{PQ}\mathbf{X}_{qp} + \mathbf{X}_{QP}^{\dagger}\mathbf{H}_{QP}\right), \tag{2.74}$$

$$\mathbf{H}_{SP}^{eff,X} = \mathbf{H}_{SQ}\mathbf{X}_{QP} \quad , \qquad (\mathbf{H}_{SP}^{eff,X} = \mathbf{H}_{PS}^{eff,X}), \tag{2.75}$$

and

$$\mathbf{H}_{SS}^{eff,X} = \mathbf{H}_{SS} \tag{2.76}$$

An advantage of the rotation matrix, $\mathbf{X}$, is that it provides wave function corrections that are analytically differentiable with respect to nuclear displacements.

The Spin-Free Exact Two Component (sf-X2C) Method

The significance of relativistic effects was first mentioned in Chapter I of this dissertation. In the present subsection, salient features of the specific approach of including scalar relativistic effects within GVVPT2 are reviewed. The relativistic technique used here is due to Liu et al. [119-124], often referred to as the spin-free exact two component (sf-X2C) method. The sf-X2C Hamiltonian is written, in second quantization, as follows

$$H = \sum_{pq}\left[\mathbf{h}_{+,sf}^{X2C}\right]_{pq}a_{p}^{+}a_{q} + \frac{1}{2}\sum_{pqrs}(pr|qs)a_{p}^{+}a_{q}^{+}a_{s}a_{r}, \tag{2.77}$$

where the first term is the one-electron spin-free (sf) part of the exact two-component (X2C) Hamiltonian [119] while the second term describes columbic two-electron

interactions. To arrive at the sf-X2C Hamiltonian for positive energy states, $\mathbf{h}_{+,sf}^{X2C}$, the modified Dirac Hamiltonian, $\mathbf{h}^D$, which satisfies the one-electron Dirac equation

$$\mathbf{h}^D \mathbf{C} = \mathbf{MCE} \ , \tag{2.78}$$

is separated into spin-free (sf) and spin-dependent (sd) parts as follows [122]

$$\mathbf{h}^D = \mathbf{h}_{sf}^D + \mathbf{h}_{sd}^D = \begin{pmatrix} \mathbf{V} & \mathbf{T} \\ \mathbf{T} & \dfrac{\alpha^2}{4}\mathbf{W}_{sf} - \mathbf{T} \end{pmatrix} + \begin{pmatrix} 0 & 0 \\ 0 & \dfrac{\alpha^2}{4}\mathbf{W}_{sd} \end{pmatrix} \tag{2.79}$$

$\mathbf{V}$ is the matrix of the external nuclear attraction potential operator, $\hat{V} = -\dfrac{Z}{\vec{r}}$; $\mathbf{T}$ is the matrix of the kinetic energy operator, $\hat{T} = \dfrac{\vec{p}^2}{2}$; $\mathbf{C}$ is the matrix of the large ($\mathbf{A}$) and small ($\mathbf{B}$) component coefficients of the bispinor, $\mathbf{C} = \begin{pmatrix} \mathbf{A} \\ \mathbf{B} \end{pmatrix}$; while $\mathbf{W}$ is the matrix of the operator

$$\hat{W} = (\vec{\sigma}.\vec{p})\hat{V}(\vec{\sigma}.\vec{p}) = \vec{p}.\hat{V}\vec{p} + i\vec{\sigma}.\left(\vec{p}\hat{V} \times \vec{p}\right) = \hat{W}_{sf} + \hat{W}_{sd} \tag{2.80}$$

The Dirac identity has been invoked in Eq. (2.80). The spin-free (sf) part of $\hat{W}$, that is $\hat{W}_{sf}$, describes scalar relativistic effects whereas the spin-dependent (sd) part, $\hat{W}_{sd}$, incorporates spin-orbit coupling effects. The non-relativistic metric $\mathbf{M}$ is defined as [122]

$$\mathbf{M} = \begin{pmatrix} \mathbf{S} & 0 \\ 0 & \dfrac{\alpha^2}{2}\mathbf{T} \end{pmatrix}, \tag{2.81}$$

where α is the fine-structure constant and $\mathbf{S}$ is the overlap matrix in the kinetically balanced basis, $\{g_\mu\}$; $S_{\mu\nu} = \langle g_\mu | g_\nu \rangle$. Ignoring spin-orbit coupling effects, Eq. (2.78) becomes

$$\mathbf{h}_{sf}^D \mathbf{C} = \mathbf{MCE} \tag{2.82}$$

which is then diagonalized. The sf-X2C Hamiltonian, $\mathbf{h}^{X2C}_{+,sf}$, is related to the normalized elimination of small component (NESC) Hamiltonian, $\mathbf{L}^{NESC}_{+,sf}$, through the picture-change transformation $\mathbf{R}$ as follows [119]

$$\mathbf{h}^{X2C}_{+,sf} = \mathbf{R}^{\dagger}_{+}\mathbf{L}^{NESC}_{+,sf}\mathbf{R}_{+} ,$$ (2.83)

where

$$\mathbf{R} = \left(\mathbf{S}^{-1}\widetilde{\mathbf{S}}_{+}\right)^{-\frac{1}{2}} = \mathbf{S}^{-\frac{1}{2}}\left(\mathbf{S}^{-\frac{1}{2}}\widetilde{\mathbf{S}}_{+}\mathbf{S}^{-\frac{1}{2}}\right)^{-\frac{1}{2}}\mathbf{S}^{\frac{1}{2}} ,$$ (2.84)

and the spin-free normalized elimination of small component (NESC) Hamiltonian $(\mathbf{L}^{NESC}_{+,sf})$ is defined [123] as

$$\mathbf{L}^{NESC}_{+,sf} = \mathbf{V} + \mathbf{T}\mathbf{X} + \mathbf{X}^{\dagger}\mathbf{T} + \mathbf{X}^{\dagger}\left[\frac{\alpha^2}{4}\mathbf{W}_{sf} - \mathbf{T}\right]\mathbf{X}$$ (2.85)

The metric $\mathbf{X}$ defines the ratio of small to large component coefficients of positive energy states,

$$\mathbf{X} = \mathbf{B}_{+}\mathbf{A}^{-1}_{+}$$ (2.86)

It should be noted that in Eq. (2.83), $\mathbf{h}^{X2C}_{+,sf}$ is in the Schrödinger picture (that is, $\mathbf{h}^{X2C}_{+,sf}\mathbf{C}_{+} = \mathbf{S}\mathbf{C}_{+}\mathbf{E}$ with the non-relativistic metric $\mathbf{S}$) whereas $\mathbf{L}^{NESC}_{+,sf}$ is in the Dirac picture (that is, $\mathbf{L}^{NESC}_{+}\mathbf{A}_{+} = \widetilde{\mathbf{S}}_{+}\mathbf{A}_{+}\mathbf{E}$) with the relativistic metric $\widetilde{\mathbf{S}}_{+} = \left(\mathbf{S} + \left(\frac{\alpha^2}{4}\right)\mathbf{X}^{\dagger}\mathbf{T}\mathbf{X}\right)$.

Conclusions

In this Chapter, the methods used in studies on transition metal molecules and triatoms of Li and Be have been described. The methods were presented in the order in which the calculations were done. All calculations started at the RHF level of theory to generate a starting molecular orbital guess. RMP2 calculations were subsequently

performed to obtain starting orbitals for MCSCF; finally, GVVPT2 calculations were performed using converged MCSCF wave functions. The advantages of macroconfigurations were exploited in the MCSCF and GVVPT2 calculations.

For complete specification of procedures, it is worth commenting briefly here on the diagonalization and integral evaluation schemes in UNDMOL. Whereas several matrix diagonalization schemes exist such as the Arnoldi method [125], Lanczos method [126], Davidson [127], and Jacobi [128] methods, the latter three are the more widely used ones because of the symmetry of the matrices. In the present studies, Davidson's method [127] was used in MCSCF and GVVPT2 calculations, while the Jacobi method [128] was one of two alternatives used within the RHF method. The second alternative within RHF for matrix diagonalization involved a two-step procedure in which a matrix was first reduced to tridiagonal form using the Householder scheme by a routine referred to in Ref. [129] (and us) as tred2. Another routine (tqli) subsequently reduces the tridiagonal matrix to diagonal form as described also in Ref. [129]. Integral evaluation was performed using a local implementation of the Obara-Saika recursive scheme [130] and made use of Pople-Head-Gordon [131] and Hamilton-Schaefer [132] schemes to transfer angular momentum.

CHAPTER III

GVVPT2 STUDIES OF LOW-LYING ELECTRONIC STATES OF SCANDIUM AND
YTTRIUM DIMERS

Introduction

Scandium (Sc) and yttrium (Y) are the first elements of the first and second series of transition elements, respectively. These elements have been the subject of a number of previous theoretical studies. Interest in Sc and Y has been partly due to their applications. For example, oxides of Y are used in television tubes and in ceramics and glass whereas some yttrium compounds have medical applications e.g., complexes of Y-90 isotope are used in radioimmunotherapy [133-135]. Another motivation for studies of Sc and Y is the fact that they appear to be among the simplest of transition elements to study. With only six valence electrons, dimers of Sc and Y would appear simple to describe at first sight, but this observation is deceptive. Available experimental data for these molecules are quite fragmentary and disputable, while data from many past theoretical studies are not less contradictory.

By electron spin resonance (ESR) experiments, Knight et al. [136] established the ground state of Sc_2 as $X^5\Sigma_u^-$, which was later confirmed by Singer and Grinter [137] through magnetic measurements. Using data obtained from Raman vibrational spectroscopy, Moskovits et al. [138] determined the harmonic frequency (ω_e) and anharmonic constant ($\omega_e x_e$) of the ground state of Sc_2 as $\omega_e = 238.9$ cm^{-1} and $\omega_e x_e = $

0.93 cm^{-1}. The equilibrium bond length of ground state Sc$_2$ has not been experimentally determined. By assuming a harmonic frequency of 230 cm^{-1}, Verhaegen et al. [139] evaluated the bond length (R$_e$) of Sc$_2$ to be 2.70 Å for the supposed ground state. Based on mass spectrometric measurements, Verhaegen et al. [139] showed that the Sc$_2$ molecule is strongly bound and determined its binding energy with respect to ground state atoms (D_0^0) as 25.9 ± 5 kcal/mol (1.12 eV). Later, however, Verhaegen et al. revised this value as 38.0 ± 2.3 kcal/mol (1.65 eV) (see discussion in Ref. [16]). Although these values for D_0^0 are still disputable [16], the avoided crossing rule strictly ensures that the lowest $^5\Sigma_u^-$ state of Sc$_2$ correlates with the first excited asymptote Sc(^{2}D$_g$) + Sc(a^{4}F$_g$), and hence the dissociation energy (D_0) of ground state Sc$_2$ is equal to $D_0^0 + 1.427$ eV.

Although many theoretical studies of Sc$_2$ have been performed and $1^5\Sigma_u^-$ is generally accepted as the ground state (see the review in Ref. [16]), it has recently been disputed by Matxain et al. [140]. Using the quantum diffusion Monte Carlo (DMC) method with Stuttgart relativistic pseudopotentials and basis sets (ECP10MDF), Matxain et al. [140] found the triplet state, $1^3\Sigma_u^-$, to lie 0.17 eV below the quintet $1^5\Sigma_u^-$ term. Although this ordering of states was corroborated by CASPT2 calculations (0.16 eV) performed by the same authors, they referred to these results as quite doubtful in their brief erratum [141]. More recent calculations of states of Sc$_2$, performed by Kalemos et al. [16] at the valence multireference internally contracted configuration interaction plus Davidson quadruple corrections (MRCI+Q) level with correlation consistent quadruple (cc-pVQZ) and quintuple zeta (cc-pV5Z) basis sets, agreed with the earlier result that

$1^5\Sigma_u^-$ is the ground state and $1^3\Sigma_u^-$ is located (just 0.04 eV) above. The most recent calculations for ground state Sc_2 at the same level of theory, and using C_{2v} symmetry, but with extrapolation to the complete basis set (CBS) limit, have been performed by Kaplan and Miranda [142]. Thus, from both the experimental and theoretical standpoints, studies on Sc_2 have been inconclusive, although many previous theoretical studies have tended to favor a $1^5\Sigma_u^-$ ground term for the molecule.

Results from previous studies of the yttrium dimer (Y_2) are also quite conflicting. The exact nature of the ground electronic state of Y_2 is not fully resolved. Whereas the contention for the ground state for Sc_2 is between the states $^5\Sigma_u^-$ and $^3\Sigma_u^-$, for its isovalent Y_2 counterpart, it is between the states $^5\Sigma_u^-$ and $^1\Sigma_g^+$. Experimental efforts to characterize the Y_2 ground electronic state have yielded conflicting results. The binding energy of the supposed ground state of Y_2 was determined by Verhaegen et al. [139] as 1.62 ± 0.22 eV, using the third law method [143], but this method is unreliable due to inherent limitations due to a requirement of a knowledge of the unknown electronic structure. Knight et al. [144] observed the electron spin resonance (ESR) spectra of Y_3 in a matrix isolation technique but failed to obtain the same for Y_2. Yang et al. [145] determined the Y_2 ground state as $^5\Sigma_u^-$ with a harmonic frequency, $\omega_e = 185 \pm 0.2$ cm^{-1} in a one-photon pulsed-field ionization-zero electron kinetic energy (PFI-ZEKE) photoelectron spectroscopic study. On the other hand, Fang et al. [146] obtained $\omega_e = 184.4 \pm 0.4$ cm^{-1} and $D_e = 3.5 \pm 0.4$ eV in a mass-selected resonance Raman matrix isolation study of Y_2 and computed $R_e = 2.65$ Å using Badger's rule [147]. These authors

assigned the ground state of Y_2 as $^1\Sigma_g^+$. Thus, the nature of the ground term for Y_2 is uncertain from the experimental stand point.

Theoretical results on Y_2 in the literature are not less contradictory. Walch and Bauschlicher [148], using the complete active space self-consistent field configuration interaction (CASSCF-CI) method, found the ground state of Y_2 to be $^5\Sigma_u^-$ (with a dominant configuration of $5s\sigma_g^2 5s\sigma_u^{*1} 4d_{z^2}\sigma_g^1 4d_{xz}\pi_u^1 4d_{yz}\pi_u^1$, similar to that for the $^5\Sigma_u^-$ ground state of Sc_2, and dissociating to $5s^2 4d^1 + 5s^1 4d^2$ atomic configurations; the first excited state atom lying at 1.36 eV above the ground state atom) with R_e = 3.03 Å, ω_e = 171 cm^{-1}, and D_e = 2.44 eV. These authors noted that the $^1\Sigma_g^+$ state of Y_2 was in competition with the supposed quintet ground state and suggested that higher order electron correlations could stabilize the former relative to the latter. For the $^1\Sigma_g^+$ state, they obtained R_e = 2.74 Å, D_e = 2.93 eV, ω_e = 206.0 cm^{-1}. This state was 0.87 eV less stable than the quintet at the vicinity of R_e and had a dominant configuration of $5s\sigma_g^2 4d_{xz}\pi_u^2 4d_{yz}\pi_u^2$, resulting from two excited state atoms with configuration $5s^1 4d^2$. This warrants further consideration because a $^1\Sigma_g^+$ state can also result from the coupling of two doublet ground state Y atoms ($5s^2 4d^1$: ^2D_g) and is expected to lie lower in energy. The PEC of Walch and Bauschlicher for the lowest $^1\Sigma_g^+$ state of Y_2 therefore violates the noncrossing rule. In fact, since Y_2 is isovalent with Sc_2, following the analysis of Kalemos et al. [16] on the molecular states of Sc_2, the combination of two doublet ground state atoms of Y should result in a total of 30 molecular terms, 3 of which are of

$^1\Sigma_g^+$ symmetry. The noncrossing rule therefore implies that the first three lowest $^1\Sigma_g^+$ states should correlate with the $5s^24d^1 + 5s^24d^1$ dissociation asymptote. This is indeed what was observed in the present work as will be seen below. Balasubramanian and Dai [149] employed second order CI with Davidson correction for unlinked quadruple clusters (SOCI + Q) method on a CASSCF wave function using D_{2h} symmetry and with a relativistic effective core potential (RECP) basis set [150], in which the $4s^24p^64d^15s^2$ shells were included in the valence space, and obtained a $^5\Sigma_u^-$ ground state with $R_e = 3.03$ Å, $\omega_e = 172$ cm^{-1}, $D_e = 2.6$ eV (relative to the $Y(4d^15s^2) + Y(4d^25s^1)$ dissociation limit). These authors also found the lowest $^1\Sigma_g^+$ state to be 0.87 eV less stable than the quintet ground state at the CASSCF/SOCI + Q level (and 0.55 eV less stable at the MRSDCI level) with $R_e = 2.76$ Å, $\omega_e = 180$ cm^{-1}, and $D_e = 3.09$ eV (with respect to the Y $(4d^25s^1) + Y (4d^25s^1)$ dissociation asymptote) and $D_e = 0.37$ eV (relative to the Y $(4d^15s^2)$ + Y $(4d^15s^2)$ dissociation limit). In the present work, the first three lowest $^1\Sigma_g^+$ states of Y_2 were found to correlate with the ground state atoms' dissociation limit as expected.

Previous DFT results of both Sc_2 and Y_2 molecules have tended to favor a quintet ground state. For example, Gutsev and Bauschlicher [151] found the ground term of Sc_2 to be $^5\Sigma_u^-$, using different DFT functionals, while Yang et al. [145] also obtained a $^5\Sigma_u^-$ ground state for Y_2 at the DFT level. Yang et al. also found the lowest $^1\Sigma_g^+$ state of Y_2 to lie at 0.29 eV above the quintet ground state, with the same leading configuration as had been reported by Walch and Bauschlicher [148]. Yanagisawa et al. [152] likewise obtained a $^5\Sigma_u^-$ ground term for Y_2 at the DFT level.

In this work, the low-lying electronic states of Sc_2 and Y_2 were reinvestigated at the GVVPT2 level of theory. The purpose of these studies was to resolve controversies on the low-lying electronic states of these molecules and to ascertain whether the PECs of their ground and excited states are free from artificial inflection points; i.e., "wiggles". The rest of this Chapter is organized as follows. The next subsection describes details as to how the calculations were done; the results are presented and discussed in the third subsection; while a final subsection concludes the Chapter.

Computational Details

The technique of macroconfigurations [22] was used within MCSCF and GVVPT2 calculations of the Sc_2 and Y_2 molecules. The advantages of using macroconfigurations ($\kappa(\mathbf{n})$s) were reviewed in Chapter II. The active space used to construct reference $\kappa(\mathbf{n})$s consisted of molecular orbitals (MOs) derived from the 3d and 4s subshells in the case of Sc_2 and 4d and 5s subshells in the case of Y_2. Calculations on the three lowest $^1\Sigma_g^+$ states of Y_2 also investigated the effects of including $5p_z$-derived MOs into the active space.

For Sc_2, two sets of reference $\kappa(\mathbf{n})$s were used in separate calculations. In the first set, each active MO and its corresponding antibonding counterpart constituted a group except that the four sigma MOs dominated by $3d_{z^2}$ and 4s were placed in one subspace. Two reference $\kappa(\mathbf{n})$s (labeled CASE 1 in Figure 5 and Table 1 in the Results and Discussion section) were defined from this grouping (and used to compute the $X^5\Sigma_u^-$ state), viz.

$$\kappa(\mathbf{n}) = \left(3d_{xz}\pi_u\,3d_{xz}\pi_g^*\right)^1\left(3d_{yz}\pi_u\,3d_{yz}\pi_g^*\right)^1\left(3d_{z^2}\sigma_g\,3d_{z^2}\sigma_u^*\,4s\sigma_g\,4s\sigma_u^*\right)^4 \times$$
$$\left(3d_{x^2-y^2}\delta_g\,3d_{x^2-y^2}\delta_u^*\right)^0\left(3d_{xy}\delta_g\,3d_{xy}\delta_u^*\right)^0 \tag{3.1}$$

$$\kappa(\mathbf{n}) = \left(3d_{xz}\pi_u\,3d_{xz}\pi_g^*\right)^1\left(3d_{yz}\pi_u\,3d_{yz}\pi_g^*\right)^1\left(3d_{z^2}\sigma_g\,3d_{z^2}\sigma_u^*\,4s\sigma_g\,4s\sigma_u^*\right)^2 \times$$
$$\left(3d_{x^2-y^2}\delta_g\,3d_{x^2-y^2}\delta_u^*\right)^1\left(3d_{xy}\delta_g\,3d_{xy}\delta_u^*\right)^1 \tag{3.2}$$

The superscripts denote the number of electrons assigned to each group of MOs. This set of reference $\kappa(\mathbf{n})$s led to 34 model space and 261,936,074 all space CSFs for the $X^5\Sigma_u^-$ state of Sc_2, using the cc-pVTZ basis set. For the second set of reference $\kappa(\mathbf{n})$s (labeled CASE 2 in Figure 6 and Table 1 in the Results and Discussion section), the MOs were grouped according to orbital type (pi, sigma, and delta) and six active electrons were distributed among the three orbital groups resulting in five reference $\kappa(\mathbf{n})$s, viz.

$$\kappa(\mathbf{n}) = \left(3d_{xz}\pi_u\,3d_{xz}\pi_g^*\,3d_{yz}\pi_u\,3d_{yz}\pi_g^*\right)^2\left(3d_{z^2}\sigma_g\,3d_{z^2}\sigma_u^*\,4s\sigma_g\,4s\sigma_u^*\right)^4 \times$$
$$\left(3d_{x^2-y^2}\delta_g\,3d_{x^2-y^2}\delta_u^*\,3d_{xy}\delta_g\,3d_{xy}\delta_u^*\right)^0 \tag{3.3}$$

$$\kappa(\mathbf{n}) = \left(3d_{xz}\pi_u\,3d_{xz}\pi_g^*\,3d_{yz}\pi_u\,3d_{yz}\pi_g^*\right)^1\left(3d_{z^2}\sigma_g\,3d_{z^2}\sigma_u^*\,4s\sigma_g\,4s\sigma_u^*\right)^4 \times$$
$$\left(3d_{x^2-y^2}\delta_g\,3d_{x^2-y^2}\delta_u^*\,3d_{xy}\delta_g\,3d_{xy}\delta_u^*\right)^1 \tag{3.4}$$

$$\kappa(\mathbf{n}) = \left(3d_{xz}\pi_u\,3d_{xz}\pi_g^*\,3d_{yz}\pi_u\,3d_{yz}\pi_g^*\right)^2\left(3d_{z^2}\sigma_g\,3d_{z^2}\sigma_u^*\,4s\sigma_g\,4s\sigma_u^*\right)^3 \times$$
$$\left(3d_{x^2-y^2}\delta_g\,3d_{x^2-y^2}\delta_u^*\,3d_{xy}\delta_g\,3d_{xy}\delta_u^*\right)^1 \tag{3.5}$$

$$\kappa(\mathbf{n}) = \left(3d_{xz}\pi_u\,3d_{xz}\pi_g^*\,3d_{yz}\pi_u\,3d_{yz}\pi_g^*\right)^1\left(3d_{z^2}\sigma_g\,3d_{z^2}\sigma_u^*\,4s\sigma_g\,4s\sigma_u^*\right)^3 \times$$
$$\left(3d_{x^2-y^2}\delta_g\,3d_{x^2-y^2}\delta_u^*\,3d_{xy}\delta_g\,3d_{xy}\delta_u^*\right)^2 \tag{3.6}$$

$$\kappa(\mathbf{n}) = \left(3d_{xz}\pi_u\,3d_{xz}\pi_g^*\,3d_{yz}\pi_u\,3d_{yz}\pi_g^*\right)^2\left(3d_{z^2}\sigma_g\,3d_{z^2}\sigma_u^*\,4s\sigma_g\,4s\sigma_u^*\right)^2 \times$$
$$\left(3d_{x^2-y^2}\delta_g\,3d_{x^2-y^2}\delta_u^*\,3d_{xy}\delta_g\,3d_{xy}\delta_u^*\right)^2 \tag{3.7}$$

This set of five reference $\kappa(\mathbf{n})$s was used to construct the PECs for the $X^5\Sigma_u^-$, $1^3\Sigma_u^-$, and $1^3\Sigma_g^-$ electronic states of Sc_2. The set generated 610 model space and 1,048,717,820 total space CSFs in the case of the $X^5\Sigma_u^-$ state; and 1510 model space and 2,070,199,828 all space CSFs in the case of the $1^3\Sigma_u^-$ and $1^3\Sigma_g^-$ states; all using the cc-pVTZ basis set.

For the investigated electronic states of Y_2, the model space consisted of 4d (σ and π) and 5s-derived MOs grouped into two orbital subspaces from which three reference $\kappa(\mathbf{n})$s were constructed as follows

$$\kappa(\mathbf{n}) \;=\; \left(4d_{xz}\pi_u\,4d_{xz}\pi_g^*\,4d_{yz}\pi_u\,4d_{yz}\pi_g^*\right)^0\left(4d_{z^2}\sigma_g\,4d_{z^2}\sigma_u^*\,5s\sigma_g\,5s\sigma_u^*\right)^6 \tag{3.8}$$

$$\kappa(\mathbf{n}) \;=\; \left(4d_{xz}\pi_u\,4d_{xz}\pi_g^*\,4d_{yz}\pi_u\,4d_{yz}\pi_g^*\right)^2\left(4d_{z^2}\sigma_g\,4d_{z^2}\sigma_u^*\,5s\sigma_g\,5s\sigma_u^*\right)^4 \tag{3.9}$$

$$\kappa(\mathbf{n}) \;=\; \left(4d_{xz}\pi_u\,4d_{xz}\pi_g^*\,4d_{yz}\pi_u\,4d_{yz}\pi_g^*\right)^4\left(4d_{z^2}\sigma_g\,4d_{z^2}\sigma_u^*\,5s\sigma_g\,5s\sigma_u^*\right)^2 \tag{3.10}$$

This partitioning of the model space gave rise to 172 model space and 1,012,046,286 total space CSFs used to span the wave functions for the $1^1\Sigma_g^+$, $2^1\Sigma_g^+$ and $3^1\Sigma_g^+$ states of Y_2, using the aug-cc-pVTZ-DK basis set. Meanwhile, the $^5\Sigma_u^-$ ground state generated 58 model space and 1,320,147,234 all space CSFs. Additional calculation of the $1^1\Sigma_g^+$, $2^1\Sigma_g^+$ and $3^1\Sigma_g^+$ states of Y_2 considered a larger active space that involved $5p_z$-dominated MOs. These extra orbitals were added to the sigma subspace in the set of three reference $\kappa(\mathbf{n})$s (3.8) to (3.10). This led to 710 model space and 2,108,403,566 all space CSFs for the singlet states, using the cc-pVTZ-DK basis set. Preliminary calculations showed that

the 4d-derived delta MOs were not important in describing the investigated Y_2 states and were thus excluded from the active space.

All calculations were performed in D_{2h} symmetry. For all calculated states of Sc_2, the correlation consistent triple zeta (cc-pVTZ) basis set [153], consisting of 151 Gaussian primitives contracted to [7s6p4d2f1g], was employed. Calculations of states of Y_2 used the aug-cc-pVTZ-DK basis set [154], constructed from the primitive set (20s16p8d2f1g) contracted to [7s6p4d2f1g] for elements Sc to Zn, and the set (25s20p13d3f2g) contracted to [9s8p6d3f2g] for elements Y to Cd. Calculations on the enlarged active space for Y_2 that included $5p_z$-dominated MOs utilized the cc-pVTZ-DK basis set [154] derived from the primitive set (25s20p13d2f1g) contracted to [8s7p5d2f1g]. Multiconfigurational self-consistent field (MCSCF) calculations were performed using the above reference $\kappa(\mathbf{n})$s to account for static electron correlation. The initial MOs to begin such calculations were obtained from approximate natural orbitals of second-order restricted Møller−Plesset perturbation (RMP2) calculations from a closed-shell Hartree−Fock (HF) reference. Dynamic electron correlation energy was recovered through the GVVPT2 method. Calculations of states of Y_2 included scalar relativistic effects through the spin-free exact two-component (sf-X2C) method that was described in Chapter II.

Where reported, the effective bond order (EBO) was determined using the expression

$$\eta = \frac{\sum_i \chi_i c_i^2}{\sum_i c_i^2} \ , \qquad (3.11)$$

where η is the EBO, χ_i is the EBO for the *i*-th configuration (CSF) while c_i^2 is its corresponding contributing weight to the total wavefunction. The EBO for each important configuration considered in the determination of EBO was calculated using the well-known formula

$$\chi_i = \frac{1}{2}\left(n_b - n_{ab}\right),\qquad (3.12)$$

where n_b denotes the number of bonding while n_{ab} is the number of antibonding electrons.

Results and Discussion

The $X^5\Sigma_u^-$, $1^3\Sigma_u^-$, *and* $1^3\Sigma_g^-$ *electronic states of* Sc_2

The PECs obtained for the lowest quintet state ($X^5\Sigma_u^-$) of Sc_2 at the GVVPT2 level of theory and two different active spaces (CASE 1 and CASE 2) are shown in Figure 6 together with the curves for the two triplets also investigated ($1^3\Sigma_u^-$ and $1^3\Sigma_g^-$). Corresponding spectroscopic constants characterizing the curves in Figure 5 are displayed in Table 1. In Figure 6, two curves are shown for the quintet state resulting from the different partitioning schemes of the active space (CASES 1 and 2, described above). The two results are similar at short bond lengths, with the only difference being that at long bond lengths, CASE 1 partitioning predicts a somewhat higher binding energy (D_e = 2.36 eV versus 2.25 eV). The GVVPT2 part took 28.65 s for CASE 1 and 53.42 s for CASE 2 reference spaces (on a dual-core AMD opteron ™ processor 2212 model 65). The leading configuration in both cases was found to be $3d_{xz}\pi_u^1 3d_{yz}\pi_u^1 4s\sigma_g^2 3d_{z^2}\sigma_g^1 4s\sigma_u^1$, contributing approximately 0.74 by weight to the total ground electronic state wave function in CASE 1 partitioning and about 0.81 by weight in

CASE 2 partitioning near the minimum (2.57 Å). The EBO for the quintet ground state, determined from the CASE 2 reference space using 7 important CSFs (the least with an amplitude of 0.101 and the largest with an amplitude of 0.902), was 1.83.
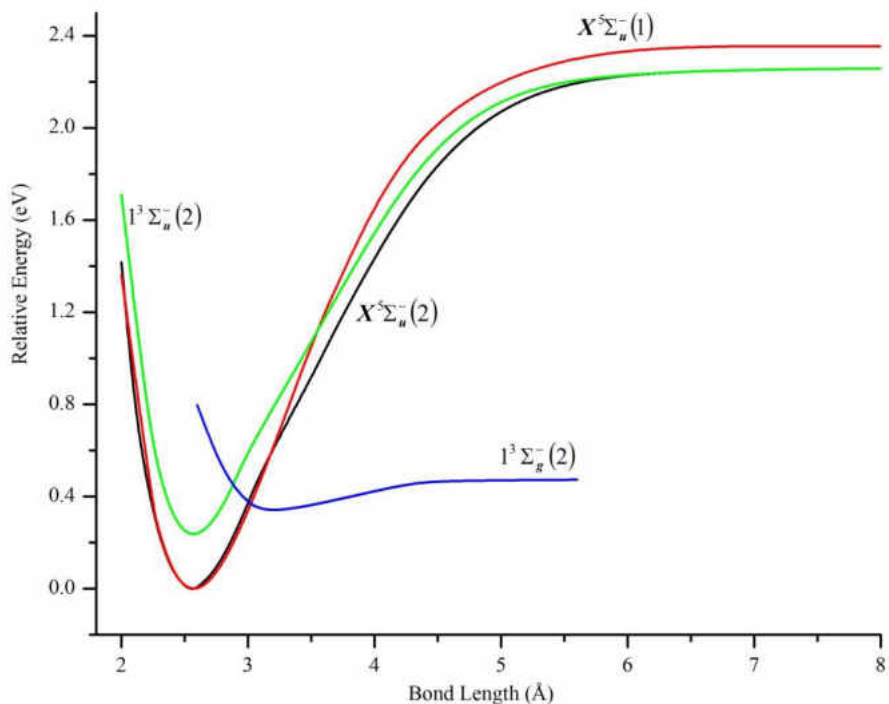
Figure 5. PECs of the $X^5\Sigma_u^-$, $1^3\Sigma_u^-$, and $1^3\Sigma_g^-$ electronic states of Sc_2 obtained at the GVVPT2 level of theory using the cc-pVTZ basis set. The energies of the two triplet states are plotted relative to the lowest energy value of the quintet ground state obtained from CASE 2 partitioning of the active space. The numbers 1 and 2 in parentheses following the molecular term symbols indicate that either CASE 1 or CASE 2 sets of reference $\kappa(\mathbf{n})$s were used in the calculations, respectively.

CASE 2 partitioning scheme was used to investigate the triplet excited states. The wave function used to generate the curve shown in Figure 5 for the $1^3\Sigma_u^-$ state was verified to obey the true $D_{\infty h}$ symmetry of the molecule. This curve lies at some 0.23 eV above the quintet ground state and has the same dissociation channel and about the same

bond length as does the ground state ($R_e \approx 1.56$ Å). The $1^3\Sigma_u^-$ state of Sc_2 competes with the $1^5\Sigma_u^-$ state for being the ground state, as previous theoretical studies have shown. In preliminary calculations of the $1^3\Sigma_u^-$ state in the present work, this state was found to have two MCSCF solutions at bond lengths ≤ 3.7 Å: one with broken symmetry (i.e., D_{2h} but not $D_{\infty h}$) and another with proper $D_{\infty h}$ symmetry. At the GVVPT2 level, the former solution was found to be 0.18 eV more stable whereas the latter solution was 0.23 eV less stable than the $1^5\Sigma_u^-$ at the vicinity of the equilibrium geometry (see Figure 6). This observation underscored the importance of carefully assessing calculations of electronic states of transition metal molecules for possible symmetry breaking.
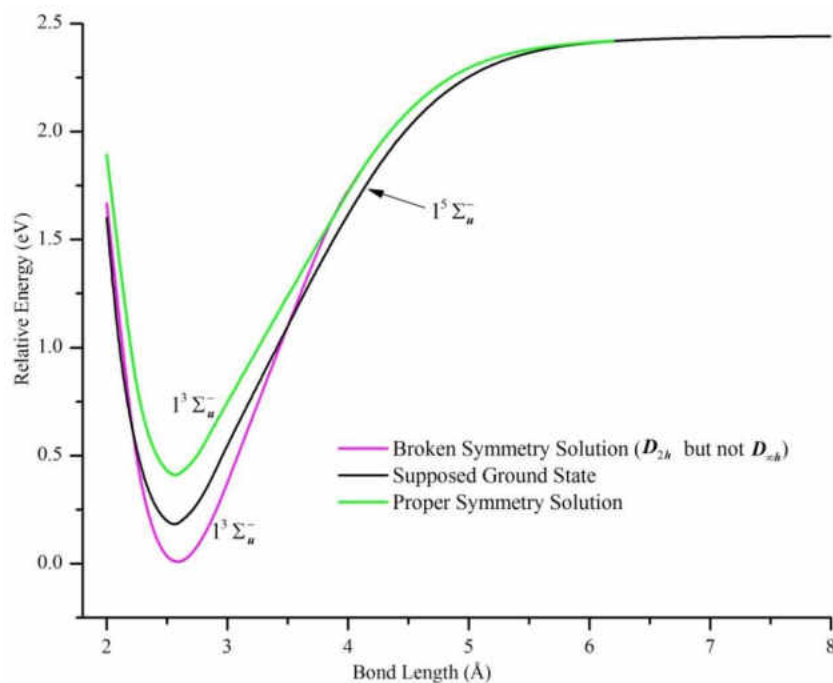
Figure 6. PECs of the $1^5\Sigma_u^-$ and $1^3\Sigma_u^-$ electronic states of Sc_2 obtained at the GVVPT2 level of theory using the cc-pVTZ basis set. All energies are plotted relative to the lowest energy value of the broken symmetry solution of $1^3\Sigma_u^-$. The $1^3\Sigma_u^-$ state shows two solutions at shorter bond lengths: one with proper symmetry and another with broken symmetry.

Table 1. Equilibrium distances (R_e), binding energies (D_e), and harmonic frequencies (ω_e) of three electronic states of Sc_2 calculated at the GVVPT2 level of theory compared with results by other methods.

Method	Basis Set	R_e(Å)	D_e(eV)	ω_e(cm^{-1})
		$X^5\Sigma_u^-$		
MRCI + Q[a]	cc-pV5Z	2.75	2.17	224.0
PC-NEVPT2[b]	(21s15p10d6f4g2h)	2.58	1.74	257.5
GVVPT2[c]	cc-pVTZ	2.57	2.36	255.9
GVVPT2[d]	cc-pVTZ	2.57	2.25	258.1
Experiment				238.9[g]
		$1^3\Sigma_u^-$		
MRCI + Q[a]	cc-pV5Z	2.74	2.13	234.0
PC-NEVPT2[b]	(21s15p10d6f4g2h)	2.60	1.65	260.1
GVVPT2[d1]	cc-pVTZ	2.57	2.03	264.0
GVVPT2[d2]	cc-pVTZ	2.60	2.44	503.8
		$1^3\Sigma_g^-$		
MRCI + Q[a]	cc-pV5Z	3.45	0.23	93.4
GVVPT2[d]	cc-pVTZ	3.19	0.13	114.8

[a]Ref. [16], [b]Ref. [155], [c]This work (CASE 1), [d]This work (CASE 2), [e]Ref. [139], [f]Ref. [156], [g]Ref. [138], [d1]This work (CASE 2, proper symmetry solution), [d2]This work (CASE 2, broken symmetry solution).

As shown in Figure 5, the $1^3\Sigma_g^-$ state, which dissociates to ground state atoms, is van der Waals-like (R_e = 3.19 Å, D_e = 0.13 eV, and ω_e = 114.8 cm^{-1}). The energy gap between the dissociation asymptotes for this state and the quintet ground state was found to be about 1.78 eV, which is 0.35 eV larger than the experimental value of 1.427 eV for the Sc from its $3d^1 4s^2$ ground to a $3d^2 4s^1$ excited atomic state. The $X^5\Sigma_u^-$ state of Sc_2

has a dissociation limit with one Sc atom in its ground state and another in an excited state.

The $X^5\Sigma_u^-$, $1^1\Sigma_g^+$, $2^1\Sigma_g^+$ and $3^1\Sigma_g^+$ states of Y_2

The PECs for the $X^5\Sigma_u^-$ and $1^1\Sigma_g^+$ states of Y_2 are shown in Figure 7 and the data characterizing the curves are shown in Table 2.
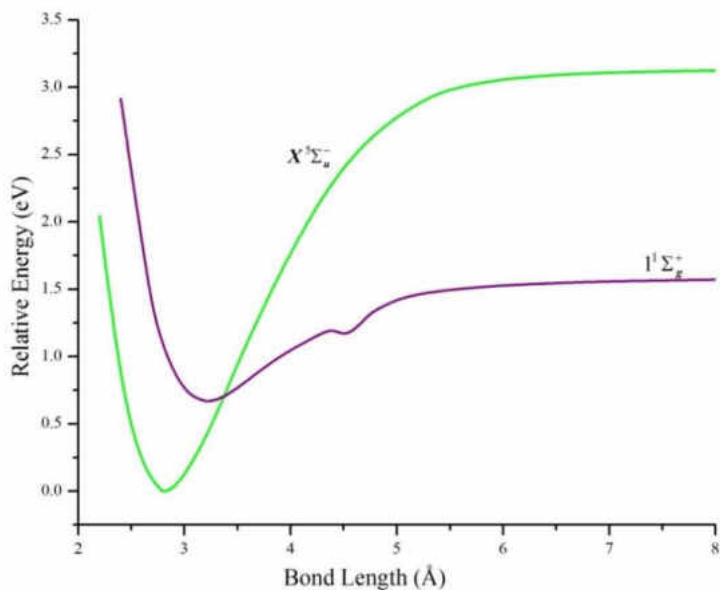
Figure 7. PECs of the $X^5\Sigma_u^-$ and $1^1\Sigma_g^+$ states of Y_2 computed at the relativistic GVVPT2 level of theory using the aug-cc-pVTZ-DK basis set. All energies are plotted relative to the lowest energy value of the quintet ground state.

Similar to the situation in isovalent Sc_2, where two low-lying electronic states ($^5\Sigma_u^-$ and $^3\Sigma_u^-$) are relevant to determination of the ground state, for Y_2, the lowest $^5\Sigma_u^-$ and $^1\Sigma_g^+$ states should be considered.

Table 2. Equilibrium distances (R_e), binding energies (D_e), adiabatic transition energies (T_e), and harmonic frequencies (ω_e) of electronic states of Y_2 calculated at the relativistic GVVPT2 level of theory compared with results from other methods.

Method	Basis Set	R_e(Å)	D_e(eV)	ω_e(cm⁻¹)	Te (eV)
		$X^5\Sigma_u^-$			
CASSCF-CI[a]		3.03	2.44	171.0	
CASSCF/SOCI + Q[b]	RECP	3.03	2.60	172.0	
DFT(VWN-BP)[c]	slater-type triple ζ	2.94		173.0	
DFT(B3P86)[c]	LANL2DZ	2.73		214.0	
DFT (BOP)[d]	(23s18p15d4f/9s5p6d2f)	2.96	2.14	173.3	
DFT(B3LYP)[e]	CEP-121G	2.76	0.22	204.4	
DFT(BLYP)[e]	CEP-121G	2.79	0.56	193.5	
DFT(B3PW91)[e]	CEP-121G	2.75	0.68	206.9	
DFT(BHLYP)[e]	CEP-121G	2.74	0.47	213.9	
DFT(BP86)[e]	CEP-121G	2.76	1.03	198.7	
DFT(B3P86)[e]	CEP-121G	2.73	0.72	208.9	
DFT(SVWN)[e]	CEP-121G	2.72	1.73	206.8	
DFT(mPW1PW91)[e]	CEP-121G	2.74	0.64	208.8	
DFT(PBE1PBE)[e]	CEP-121G	2.74	0.66	209.2	
GVVPT2	Aug-cc-pVTZ-DK	2.80	3.12	287.2	
Experiment			1.62 ± 0.22[f]	185 ± 0.2[c]	
		2.65[g]	3.5 ± 0.4[g]	184.4 ± 0.4[g]	
		$1^1\Sigma_g^+$			
CASSCF-CI[a]		2.74	2.93[h]	206.0	0.87
CASSCF/SOCI + Q[b]	RECP	2.76	3.09[h] (0.37)[i]	180.0	0.87
DFT(VWN-BP)[c]	slater-type triple ζ	2.59		207.0	0.29
DFT(B3P86)[c]	LANL2DZ	2.76		225.0	0.96
GVVPT2	Aug-cc-pVTZ-DK	3.21	0.91	140.0	0.67
		$2^1\Sigma_g^+$			
GVVPT2	Aug-cc-pVTZ-DK	3.27	0.75	122.9	0.83
		$3^1\Sigma_g^+$			
GVVPT2	Aug-cc-pVTZ-DK	3.36	0.09	118.3	1.49
		(4.27)	(0.10)	(113.9)	(1.48)

[a]Ref. [148], [b]Ref. [149], [c]Ref. [145], [d]Ref.[152], [e]Ref. [157], [f]Ref. [139] (Third law method), [g]Ref. [146] (Reported a $^1\Sigma_g^+$ ground state), [h]Dissociation to excited state atoms (Y: $4d^25s^1$), [i]Dissociation to ground state atoms (Y: $4d^15s^2$).

As was mentioned in the Introduction, experimental determination of the symmetry of the Y_2 ground state has not been unambiguous, although a $^5\Sigma_u^-$ ground state seems the more likely. In this study, the ground state of the Y_2 molecule was found to be $X^5\Sigma_u^-$ in agreement with most previous theoretical studies (see Table 2).

In agreement with the Walch and Bauschlicher study [148], the major configuration of the $X^5\Sigma_u^-$ state was found to be

$$4d_{xz}\pi_u^1 4d_{yz}\pi_u^1 5s\sigma_g^2 4d_{z^2}\sigma_g^1 5s\sigma_u^{*1} \tag{3.13}$$

For this configuration, a weight of 0.800 was found at 2.80 Å (i.e., at the minimum) which decreased to 0.548 at 4.4 Å. This configuration is quite similar to that often reported for the Sc_2 $X^5\Sigma_u^-$ state. Using formulas (3.11) and (3.12), an EBO of 1.87 was obtained for the ground state of Y_2 at 2.81 Å (using 8 important configurations), which dropped to 1.15 at 4.4 Å. Spectroscopic constants obtained by the GVVPT2 study were in reasonable agreement with the CASSCF/SOCI + Q study [149] and with experiment [146] (i.e., R_e = 2.80 Å vs 3.03 Å vs 2.65 Å; D_e = 3.12 eV vs 2.6 eV vs 3.5 ± 0.4 eV), although the harmonic frequency was less so (ω_e = 287 cm^{-1} vs 172 cm^{-1} vs 184 cm^{-1}).

The $1^1\Sigma_g^+$ state of Y_2 was found to lie at 0.67 eV above the $X^5\Sigma_u^-$ state around the equilibrium geometry. Walch and Bauschlicher [148] and Dai and Balasubramanian [149] had found the $1^1\Sigma_g^+$ state of Y_2, which had

$$4d_{xz}\pi_u^2 4d_{yz}\pi_u^2 5s\sigma_g^2 \tag{3.14}$$

as the major configuration, to lie at 0.87 eV above a quintet ground state. They also reported a dissociation asymptote for the singlet state that involved excited Y atoms. In

this study, a state averaged calculation was performed on the first three lowest $^1\Sigma_g^+$ states of Y_2 with equal weighting and found all three states to correlate with the ground state atoms' dissociation channel. In fact, near degeneracy at certain geometries did not permit even a *qualitatively* correct curve for the $1^1\Sigma_g^+$ state to be computed in a one state calculation.
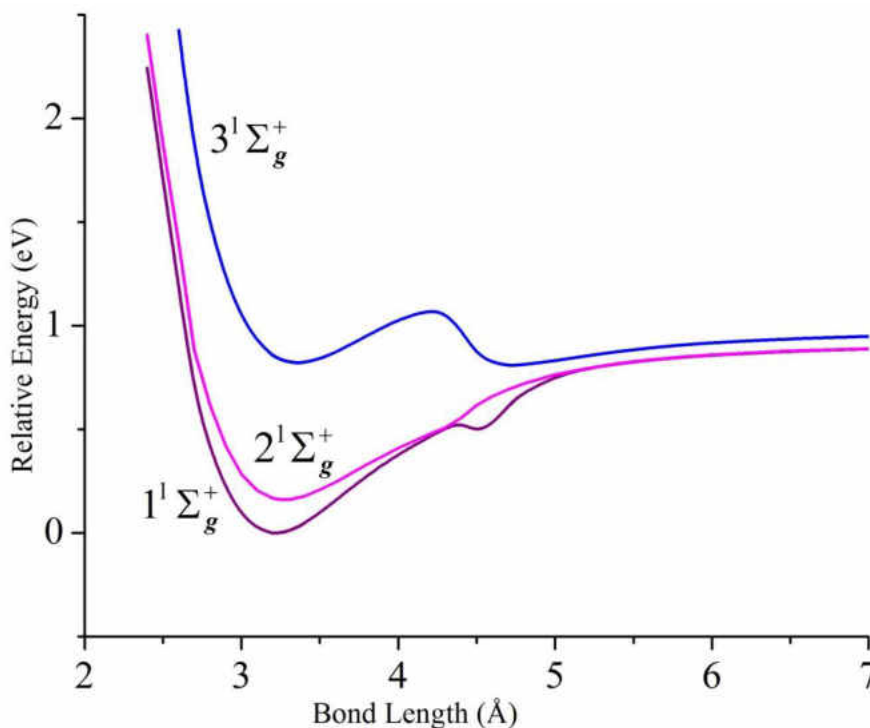
Figure 8. PECs of the $1^1\Sigma_g^+$, $2^1\Sigma_g^+$, and $3^1\Sigma_g^+$ states of Y_2 computed at the relativistic GVVPT2 level of theory using the aug-cc-pVTZ-DK basis set. All energies are plotted relative to the lowest energy value of the $1^1\Sigma_g^+$ state.

In contrast with the earlier studies, the present work obtained

$$4d_{xz}\pi_u^2 5s\sigma_g^2 5s\sigma_u^{*2} \text{ and } 4d_{yz}\pi_u^2 5s\sigma_g^2 5s\sigma_u^{*2} \tag{3.15}$$

as the major configurations in the state-averaged calculation near the equilibrium bond length. As with the $X^5\Sigma_u^-$ state, spectroscopic constants were in reasonable agreement

with the CASSCF/SOCI + Q study [149] (i.e., R_e = 3.21 Å vs 2.76 Å; D_e = 0.91 eV vs 0.37 eV; ω_e = 140 cm^{-1} vs 180 cm^{-1}; T_e = 0.67 eV vs 0.87 eV); there are no available experimental data for the $1^1\Sigma_g^+$ state. Figure 8 shows the PECs of the three lowest $^1\Sigma_g^+$ states of Y_2 obtained in the state-averaged calculation.

The shallow bump around a bond length of 4.6 Å on the $1^1\Sigma_g^+$ PEC shown in Figures 7 is not an artifact but is a consequence of what is suspected to be an avoided crossing. This curve is shown with two other low lying $^1\Sigma_g^+$ states of Y_2 in Figure 8 and the corresponding data describing them are included in Table 2. In particular, the results on the $2^1\Sigma_g^+$ and $3^1\Sigma_g^+$ states of the Y_2 species are the first to be reported, to the best of my knowledge. As can be seen, the PEC for the $3^1\Sigma_g^+$ state has two shallow minima: an inner minimum at R_e = 3.36 Å with D_e = 0.09 eV, ω_e = 118.3 cm^{-1}, and T_e = 0.82 eV (with respect to the $1^1\Sigma_g^+$ state) and an outer very slightly deeper minimum at R_e = 4.72 Å with D_e = 0.10 eV, ω_e = 113.9 cm^{-1} and T_e = 0.81 eV.

To corroborate the PEC-based hypothesis that the bump in the $1^1\Sigma_g^+$ PEC around 4.6 Å is an avoided crossing, the important configurations of the $1^1\Sigma_g^+$ and $2^1\Sigma_g^+$ states were analyzed just before the bump (at 4.3 Å) and at the bump (4.6 Å). As shown in Table 3, the leading configurations of the $1^1\Sigma_g^+$ state at 4.3 Å (i.e., 1, 4, 7, and 9) become the leading configurations of the $2^1\Sigma_g^+$ state at 4.6 Å (i.e., 1, 2, 3, and 4, respectively) whereas the major configurations of the $2^1\Sigma_g^+$ state at 4.3 Å also become those of the $1^1\Sigma_g^+$ state at 4.6 Å.

Table 3. Important configurations of the $1^1\Sigma_g^+$ and $2^1\Sigma_g^+$ states of Y_2 indicative of a switch in the two states on going from 4.3 to 4.6 Å bond length[a].

CSF No.	Amplitudes	Configurations
$1^1\Sigma_g^+$ (R = 4.3 Å)		
1	**0.34157**	**3 0 0 0 3 0 3 0**
2	-0.03741	1 0 0 1 3 2 2 0
3	0.04777	1 0 0 2 3 1 2 0
4	**-0.34157**	**0 3 0 0 3 0 3 0**
5	-0.03741	0 1 1 0 3 2 2 0
6	0.04777	0 1 2 0 3 1 2 0
7	**0.54083**	**0 0 3 0 3 0 3 0**
8	-0.05873	0 0 3 0 0 3 3 0
9	**-0.54083**	**0 0 0 3 3 0 3 0**
10	0.05873	0 0 0 3 0 3 3 0
$2^1\Sigma_g^+$ (R = 4.3 Å)		
1	**-0.28202**	**0 0 0 0 3 3 3 0**
2	**0.07568**	**0 0 0 0 3 0 3 3**
3	**-0.33449**	**3 0 0 0 3 0 3 0**
4	**-0.33449**	**0 3 0 0 3 0 3 0**
5	**0.50751**	**0 0 3 0 3 0 3 0**
6	**0.50751**	**0 0 0 3 3 0 3 0**
7	-0.06378	0 0 3 3 0 0 3 0
$1^1\Sigma_g^+$ (R = 4.6 Å)		
1	**0.65995**	**0 0 0 0 3 3 3 0**
2	-0.05299	0 0 0 0 3 3 1 2
3	**-0.39146**	**0 0 0 0 3 0 3 3**
4	0.06181	0 0 0 0 1 2 3 3
5	**0.22319**	**3 0 0 0 3 0 3 0**
6	**0.22319**	**0 3 0 0 3 0 3 0**
7	**-0.27683**	**0 0 3 0 3 0 3 0**
8	**-0.27683**	**0 0 0 3 3 0 3 0**
$2^1\Sigma_g^+$ (R = 4.6 Å)		
1	**0.39767**	**3 0 0 0 3 0 3 0**
2	**-0.39767**	**0 3 0 0 3 0 3 0**
3	**0.51141**	**0 0 3 0 3 0 3 0**
4	**-0.51141**	**0 0 0 3 3 0 3 0**

[a]Active core orbitals are fully occupied in all listed configurations and are therefore not included. Configurations of the states that get exchanged are shown in bold (e.g., configurations 1, 4, 7, and 9 of the $1^1\Sigma_g^+$ state at 4.3 Å become configurations 1, 2, 3, and 4, respectively of state $2^1\Sigma_g^+$ at 4.6 Å).

The configurations shown in Table 3 are represented using step vector notation: the number 0 corresponds to zero orbital occupancy; 1 to single occupancy, spin coupled to increase spin; 2 to single occupancy with a reduction in spin; and 3 to double orbital occupancy. The orbital symmetries (in D_{2h} point group) are {0 0 0 0 1 2 2 3 3 4 5 5 5 5 6 6 7 7 | 2 3 6 7 0 0 5 5} where 0 to 7 denote irreps A_g to B_{3u} with the active core orbitals lexically preceding the valence orbitals.

Obtaining the correct initial orbitals for the characterization of the $1^1\Sigma_g^+$, $2^1\Sigma_g^+$, and $3^1\Sigma_g^+$ states of Y_2 was difficult. In preliminary state averaged calculations in which the $5p_z$-derived σ MOs replaced the $4d_{z^2}-$ dominated MOs, the $3^1\Sigma_g^+$ state to was found correlate with the Y $(4d^2 5s^1)$ + Y $(4d^2 5s^1)$ dissociation asymptote in violation of the non-crossing rule.

With the use of formulas (3.11) and (3.12), the EBO for the $1^1\Sigma_g^+$ state was 0.90 (using 10 important configurations), for $2^1\Sigma_g^+$ 0.94 (using 12 important configurations), and for $3^1\Sigma_g^+$ 0.94 (using 10 important configurations) at 3.24 Å. At this geometry, two leading configurations for the $1^1\Sigma_g^+$ state, each contributing 0.381 by weight to the wave function, were those shown in (3.15).The same configurations were dominant in the $2^1\Sigma_g^+$ state, contributing 0.353 by weight each to the overall wave function. The leading configuration for the $3^1\Sigma_g^+$ state was rather $5s\sigma_g^2 4d_{z^2}\sigma_g^2 5s\sigma_u^{*2}$, contributing 0.756 by weight to the wave function at 3.24 Å. It is important to note that all these configurations suggest the coupling of two ground Y atoms (Y: $4d^1 5s^2$).

When the $5p_z$-derived MOs were included in the active space and the enlarged model space used to compute the three lowest $^1\Sigma_g^+$ states of Y_2, the bump in the $1^1\Sigma_g^+$ curve was seen to be shifted inward to around 3.0 Å bond length whereas the inner minimum in the $3^1\Sigma_g^+$ curve now lay around 2.9 Å (Figure 9). A few calculations were performed involving four $^1\Sigma_g^+$ states of Y_2 around the bump in the $3^1\Sigma_g^+$ curve and the latter curve was found to be energetically quite close to the $4^1\Sigma_g^+$ curve, indicating a likely avoided crossing that might explain the double minimum in the $3^1\Sigma_g^+$ curve.
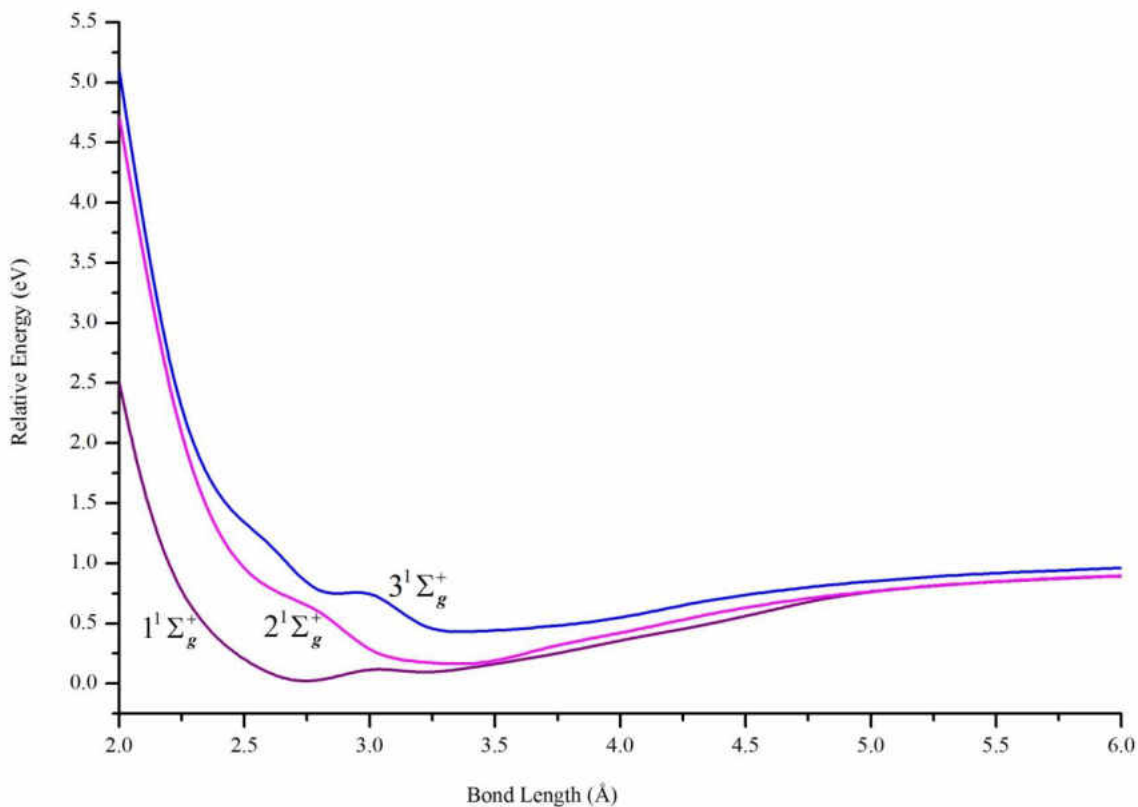
Figure 9. PECs of the $1^1\Sigma_g^+$, $2^1\Sigma_g^+$, and $3^1\Sigma_g^+$ states of Y_2 computed at the relativistic GVVPT2 level of theory using the aug-cc-pVTZ-DK basis set and an active space that included $5p_z$-derived MOs. The energies are plotted relative to the lowest energy value of the $1^1\Sigma_g^+$ state.

Conclusions

This Chapter described the ground electronic states of Sc_2 and Y_2, and some of their low lying excited states, as were obtained at the GVVPT2 level of theory with scalar relativistic effects included via the spin-free exact two-component (sf-X2C) method in the case of Y_2. In test calculations of Sc_2 that included scalar relativistic effects, relativity was not found to significantly impact the states of Sc_2. Hence, such calculations were discontinued. Although Sc_2 and Y_2 have the same ground state ($X^5\Sigma_u^-$), the effects of scalar relativity are evident when the EBOs of these states are compared. In Sc_2, the EBO was 1.83 whereas in Y_2, it was 2.81 (both determined in the vicinity of the equilibrium bond length). A plausible explanation for the higher EBO in Y_2 is that the relativistic contraction of the outer 5s subshell of atomic Y accompanied by a slight destabilizing expansion of its 4d-subshell orbitals leads to 4d and 5s orbitals of Y being averagely of the same spatial extent and hence, contributing fairly strongly to bonding at the same region in space. Such expansion and contraction are minimal in Sc.

Noteworthy in the present studies is the use of simple valence bond-type active spaces. Such model spaces have been successfully used in GVVPT2 studies on other transition metal molecules besides the ones reported here (see Ref. [158, 159]). In all those studies, the PECs obtained at the GVVPT2 level were all smooth and continuous. The present studies support the generally held view that the ground state of Sc_2 is $X^5\Sigma_u^-$. Spectroscopic constants are in good agreement with MRCISD + Q/cc-pV5Z [16] and experimental results. Notably, D_e at the MRCISD + Q/cc-pV5Z is 2.17 eV, while GVVPT2/cc-pVTZ obtains 2.25 eV; experiment [134] obtained 239 cm^{-1} for ω_e, with

MRCISD + Q/cc-pV5Z [16] being 15 cm^{-1} lower and GVVPT2/cc-pVTZ being 19 cm^{-1} higher.

The results on the Y_2 states are quite revealing of how complicated this seemingly simple species with only 6 active electrons is; hence the need for a careful choice of an active space. Whereas previous theoretical studies considered the $1^1\Sigma_g^+$ state of Y_2, only Dai and Balasubramanian[149] reported a dissociation assymptote involving two ground Y atoms for this state (in addition to a dissociation channel involving excited state atoms) but did not provide a full PEC for the said state. This study is the first to find that the lowest three $^1\Sigma_g^+$ states of Y_2 correlate with the ground state atoms' dissociation limit, as expected theoretically. Moreover, this study is the first to obtain full PECs of the $2^1\Sigma_g^+$ and $3^1\Sigma_g^+$ states of Y_2, which prove to be critical in understanding the dissociation channels. Although the lowest two $^1\Sigma_g^+$ states were described reasonably well with an active orbital space of 4d (σ and π) and 5s-derived MOs, inclusion of $5p_z$-derived orbitals provides better curves. In contrast, computational artifacts remain for $3^1\Sigma_g^+$, which suggests that the states originating from the first excited dissociation limit should be included for quantitative studies of that state. Overall, even though the ground term for the Y_2 molecule has not been experimentally ascertained unambiguously, many theoretical studies have tended to favor a $^5\Sigma_u^-$ ground state and the present work lends further support in this regard. Comparison of GVVPT2 results with those from CASSCF/SOCI + Q and experiment, where available, corroborate the general correctness

of the present results, but also suggest that more accurate calculations are needed especially for the purpose of spectroscopic studies.

CHAPTER IV

GVVPT2 STUDIES OF LOW-LYING ELECTRONIC STATES OF CHROMIUM AND
MOLYBDENUM DIMERS

Introduction

This Chapter discusses studies carried out on some of the electronic states of Cr

and Mo diatoms. These studies were the first to have been done using the GVVPT2

method that was extended to include scalar relativistic effects through the spin-free exact

two component (sf-X2C) method as was described in Chapter II. Cr and Mo are isovalent

and, contrary to the Aufbau Principle, preferably exist in the more stable ^7S atomic state

with configuration $(n-1)d^5ns^1$ as opposed to the ^5D atomic state with configuration

$(n-1)d^4ns^2$ (where n = 4 for Cr and 5 for Mo). The $^7S_{J=3}$ term of Cr lies 0.961 eV lower

that the $^5D_{J=0}$ state [160]. In Mo, this energy difference is even larger (1.360 eV) [161].

The $(n-1)d^5ns^1$ ground configuration of Cr and Mo is quite amenable to bond formation.

In fact, the group VI elements (Cr, Mo, W, and Sg) are expected to form metal-metal

bonds with the highest multiplicity among transition elements. Strong multiple metal-

metal bonds in Tungsten (W) may lend credence to the fact that W has the highest

melting point of all metals. Moreover, Roos et al. [162] reported sextuple bonds in Mo_2

and W_2, based on relativistic CASPT2 calculations.

This Chapter is organized as follows. The present subsection provides a brief

discourse of previous theoretical and experimental efforts on Cr_2 and Mo_2; the next

subsection will discuss computational details; the results are presented and discussed in the third subsection; while a final subsection concludes the chapter.

Previous Studies of Cr_2

Cr_2 is perhaps one of the most challenging small molecules in the world of quantum chemistry and has since served as the species with which the capability of newly developed ab initio methods in quantum chemistry is assessed. Despite having been first identified over four decades ago [163, 164], the bonding in this molecule remains a formidable challenge to theoretical chemists. Over fifty different computational treatments have been made on Cr_2 in an effort to elucidate its bonding. Early attempts did not lead to useful characterizations and resulted in published statements such as that by Salahub in 1987 [165] that labeled Cr_2 as "a bête noire". Bauschlicher and Partridge in 1994 [166] declared that "obtaining a quantitative description of Cr_2 has so far proven to be impossible", while in as late as 1999 Thomas et al. [167] stated about Cr_2 that "it has been found repeatedly that improving the computational level did not necessarily improve the results".

Cr_2 has been the subject of many experimental studies. By resonant two-photon ionization (R2PI) spectroscopy, Michalopoulos et al. [168] determined the bond length of Cr_2 to be $R_e = 1.68 \pm 0.01$ Å and its ground state as $X^1\Sigma_g^+$. By laser-induced fluorescence spectroscopy, Bondybey et al. [169] determined the equilibrium bond length to be $R_e = 1.679$ Å with a harmonic frequency of $\omega_e = 470$ cm^{-1}. From photoionization spectroscopy Simard et al. [170] obtained the dissociation energy $D_e = 1.56 \pm 0.06$ eV, while the mass spectrometric experiment by Hilpert and Ruthardt [171] led to $D_e = 1.473 \pm 0.056$ eV and

Su et al. [172] reported $D_e = 1.45 \pm 0.10$ eV. By negative ion photoelectron spectroscopy, Casey and Leopold [173] determined the ground state harmonic frequency of Cr_2 to be approximately $\omega_e = 481$ cm^{-1}. In this experiment, they obtained transition energies from 29 vibrational levels and, using the Rydberg-Klein-Rees (RKR) method [174-176], obtained a RKR potential energy curve for the ground state of Cr_2 that clearly showed a shelf region from around 2.5 Å to 3.0 Å.

Theoretical efforts on ground state Cr_2 are assessed relative to the RKR PEC obtained in the Casey and Leopold [173] study. Early attempts in this regard led to disappointing results. Coupled cluster with single and double excitations (CCSD) calculations [177] with the (14s11p6d2f1g)/[10s8p3d2f1g] basis set gave a too short bond length ($R_e = 1.46$ Å) and a too large harmonic frequency ($\omega_e = 1161$ cm^{-1}). At the unrestricted CCSD level with perturbative inclusion of triples [UCCSD(T)], Bauschlicher and Partridge [166], using the (20s15p10d6f4g)/[9s8p7d5f2g] basis set, obtained $R_e = 2.54$ Å and $D_e = 0.89$ eV. With a CASSCF reference function and then an Epstein-Nesbet second-order perturbation correction using the [10s8p3d2f] basis set [178], a reasonably good ($R_e = 1.6258$ Å) bond length was obtained but the potential function could not dissociate properly ($D_e = 2.786$ eV). With the multireference ACPF (MRACPF) formalism using the (20s15p10d6f)/[9s8p7d5f] basis set [166], Dachsel et al. [179] obtained $R_e = 1.72$ Å, $D_e = 1.09$ eV, and $\omega_e = 338.7$ cm^{-1}. In contrast to earlier disappointing CASPT2 studies [180, 181], Roos [182] performed very large CASPT2 calculations that considered an expanded active space of 12 electrons and 16 molecular orbitals (derived from the 3d and 4s subshells plus all bonding MOs from 4p and the corresponding anti-bonding sigma type), used the modified (g1) zero-order Hamiltonian

of Andersson [183], a large ANO basis set, relativistic corrections, and level shifts, and obtained good values for the bond length, $R_e = 1.66$ Å, and harmonic frequency, $\omega_e = 450$ cm^{-1}, but somewhat overestimated the dissociation energy, $D_e = 1.68$ eV. Calculations done later at the CIPT2 [184] level (N.B. a hybrid of multireference configuration interaction and second order multireference perturbation theory), using the [9s8p7d7f5g3h] basis set, gave values of $R_e = 1.756$ Å, $D_e = 1.18$ eV, and $\omega_e = 322$ cm^{-1}. The same authors performed calculations at the CASPT2 and MRCI+Q levels with the same basis set and reported $R_e = 1.678$ Å, $D_e = 1.84$ eV, and $\omega_e = 565$ cm^{-1} for CASPT2 and $R_e = 1.664$ Å, $D_e = 1.01$ eV, and $\omega_e = 511$ cm^{-1} for MRCI+Q. Notably, none of these three studies gave the correct dissociation energy. Essentially more accurate (though very costly) results were obtained by Müller [185] at the fully uncontracted multireference averaged quadratic coupled cluster (MR-AQCC) level. With the use of a large flexible basis set (including h and i functions), with 28 correlated electrons (3s, 3p, 3d, and 4s electrons) generating up to 2.8 billion configuration state functions (CSFs) and by accounting for scalar relativistic effects through the use of the Douglas-Kroll-Hess (DKH) Hamiltonian [31, 186], he obtained $R_e = 1.685$ Å, $D_e = 1.48$ eV, and $\omega_e = 459$ cm^{-1} after extrapolation to the complete basis set (CBS) limit. Surprisingly, his results are poor with the use of a triple-zeta basis set (TZP), giving two shallow minima at 1.758 Å and 2.5 Å with almost the same energy (-0.078 eV).

The most recent calculations of Cr_2 were performed by Hongo and Maezono [187], Ruipérez et al. [19], and Kurashige and Yanai [188]. Calculations at the variational Monte Carlo (VMC) and DMC levels [187] overestimated R_e by over 25% and underestimated D_e by some 40%. Ruipérez et al. [19] performed calculations at the

restricted active space second order perturbation theory (RASPT2) and CASPT2 levels using the (21s15p10d6f4g)/[10s10p8d6f4g] basis set of Roos [182] and exploiting two different zero-order Hamiltonians. The RASPT2 PEC proved to be seriously deficient at long distances, and the CASPT2 calculations with the g1 zero-order Hamiltonian overestimated D_e by 0.6 eV. In the case of using a zero-order Hamiltonian with the ionization potential-electron affinity (IPEA) shift, these authors observed a strong dependence of the CASPT2 PEC on the IPEA shift parameter and no value was found that consistently gave the best results in terms of shape of the PEC and spectroscopic constants. Whereas the best estimate for IPEA giving a PEC with a shape that agreed well with experiment was 0.45, the best IPEA value for predicting the right R_e was 0.50; for D_e, it was 0.45; and for $\Delta G_{1/2}$, it was 0.40. Kurashige and Yanai [188] performed analogous CASPT2 calculations but with a density matrix renormalization group SCF (DMRG-SCF) reference function, constructed within the active space (12e, 28o) derived from the 3d, 4s, 4p, and 4d subshells, and using the cc-pwCV5Z basis set. After a linear extrapolation to infinite size of the renormalized basis sets, Kurashige and Yanai [188], using a zero-order Hamiltonian with an IPEA shift of 0.25 a.u., obtained the very good results: $R_e = 1.682$ Å, $D_e = 1.551$ eV, and $\omega_e = 471$ cm^{-1}. However, the same calculations without any shift led to unreasonable results: $R_e = 1.719$ Å, $D_e = 1.337$ eV, and $\omega_e = 361$ cm^{-1}, which corroborates the previously noted sensitivity to shift parameters.

<center><i>Previous Studies of</i> Mo$_2$</center>

Information in the literature suggests that the Cr$_2$ molecule has probably been more studied than its isovalent Mo$_2$ counterpart. Whereas Cr$_2$ and Mo$_2$ have both been found to have $X^1\Sigma_g^+$ ground atomic terms, a key difference exists in their PECs: the

<center>85</center>

ground PEC of Cr_2 contains an inner minimum thought to be dominated by 3d-3d bonding interaction and an outer shelf in the range $2.5 - 3.0$ Å believed to be dominated by 4s-4s bonding interaction [162], whereas no such outer shelf is visible in the ground PEC of isovalent Mo_2. As was found in the present studies, at the GVVPT2 level, the $1\,^3\Sigma_u^+$ excited state of Cr_2 also has an outer shelf in its PEC (similar to the ground PEC) whereas the corresponding state of Mo_2 does not possess such a shelf. These observations suggest that the 4d and 5s atomic orbitals of Mo are of similar spatial extents and contribute to bonding at the same interatomic separation whereas the 3d and 4s orbitals of Cr have different spatial extents.

Experimental studies of the ground state of Mo_2 have reported a binding energy that is much larger than that of Cr_2 (roughly 4.47 eV vs 1.56 eV), a longer bond length than that of Cr_2 (about 1.94 Å vs 1.68 Å), but a frequency that averagely the same as that of Cr_2 (about 484.9 cm^{-1} vs 481 cm^{-1}). One of the earliest experimental studies of Mo_2 is due to Efremov et al. [189] who obtained the emission spectra of Mo_2 based on flash photolysis of the $Mo(CO)_2$ molecule. Vibrational analyses of the data obtained led to a bond length of $R_e = 1.929$ Å, a harmonic frequency of $\omega_e = 477.1\,\text{cm}^{-1}$, and a bond energy of $D_0 = 4.12$ eV for the $X\,^1\Sigma_g^+$ state of Mo_2. In the same year (1978), Gupta et al. [190] used a Knudsen effusion mass spectrometric method to study the dissociation of Mo_2 into atoms at a high temperature range of 2,772-2,963 K. They subsequently used the second law method to determine a bond energy (D_0°) of 4.34 ± 0.35 eV, whereas the third law method gave $D_0^\circ = 4.43 \pm 0.02$ eV (assuming $R_e = 1.94$ Å and $\omega_e = 477.1\,\text{cm}^{-1}$)

for ground state Mo_2. Meanwhile Pellin et al. [191] later studied Mo_2 in argon and krypton matrices. From matrix isolation fluorescence spectra, they obtained the same ω_e and R_e values as did Efremov et al. Hopkins et al. [192] carried out resonant two-photon ionization studies of supersonic jet-cooled Mo_2 from which a bond length of $R_e = 1.937$ Å was deduced for the ground state. Simard et al. [170] found $D_0 = 4.476 \pm 0.010$ eV for ground state Mo_2 using photoionization spectra of laser vaporized Mo_2. Kraus et al. [193] used Fourier transform spectrometry to study Mo_2 trapped in solid Ne at cryogenic conditions (about 7 K), from whence a harmonic frequency of $\omega_e = 484.9\,cm^{-1}$ was established for the ground state of Mo_2. The most recent experimental investigation of Mo_2 is due to Feng et al. [194] who obtained resonance Raman spectra of mass-selected Mo_2 in Ar matrices, from whence a harmonic frequency of $\omega_e = 473.3\,cm^{-1}$ was determined for the Mo_2 ground state.

Mo_2 has been the subject of a number of theoretical studies. One of the earliest of these combined local spin density methods with a model potential representation of the inner core electrons of Mo [195] and found $D_e = 4.80$ eV, $R_e = 1.98$ Å, and $\omega_e = 479.0\,cm^{-1}$ for the ground state of Mo_2. On the other hand, calculations at the configuration interaction (CI) level of theory [196] gave $R_e = 2.01$ Å, $\omega_e = 388.0\,cm^{-1}$ and a bond energy (D_0) of only 0.86 eV whereas MRCI [197] gave $R_e = 1.97$ Å and $\omega_e = 475.0\,cm^{-1}$ for ground state Mo_2. A study by Goodgame and Goddard [198] that employed the generalized valence bond-van der Waals (GVB-vdw) method led to $D_0 =$

1.41 eV, $R_e = 1.93$ Å, and $\omega_e = 455.0 \, \text{cm}^{-1}$ for the ground state of Mo_2. A later study by the same authors [199] gave $D_0 = 3.94$ eV and $R_e = 1.92$ Å.

More recent studies of Mo_2 have focused not only on its ground electronic state but also on some low-lying states as has been done also in the work reported in this dissertation. Balasubramanian and Zhu [200] used MRCISD, FOCI, MRCISD + Q, and FO + MRCISD methods and RECP basis sets [150] to study up to 37 low-lying electronic states of Mo_2. For the ground state, they found $R_e = 1.993$ Å and $\omega_e = 447.5 \, \text{cm}^{-1}$ at the MRCISD + Q level, $R_e = 2.044$ Å and $\omega_e = 497.0 \, \text{cm}^{-1}$ at the FOCI level, and $R_e = 2.050$ Å and $\omega_e = 486.0 \, \text{cm}^{-1}$ at the FO + MRCISD level of theory. The authors did not report the dissociation energy of the ground state or for any of the excited states included in their study. One of the most recent studies of Mo_2 is due to Borin et al. [201] who used CASSCF/MS-CASPT2 together with a quadruple-ζ atomic ANO-RCC basis set [202] and found the spectroscopic constants for ground state Mo_2 to be $D_0 = 4.41$ eV, $R_e = 1.950$ Å, and $\omega_e = 459.0 \, \text{cm}^{-1}$.

In general, many ab initio methods have tended to predict spectroscopic constants for Mo_2 that are more in agreement with reference values than for Cr_2. DFT studies, however, lead to spectroscopic data for these molecules that depend largely on the DFT functional used (see, for example, Ref. [157]). Here, the low-lying states of Cr_2 and Mo_2 have been reinvestigated using GVVPT2, partly to assess the capability of GVVPT2 for describing such complicated systems and also to assess the importance of relativistic effects in the Cr system in comparison with Mo. In the next subsection, details of how the calculations were done are provided.

Computational Details

The advantages of macroconfigurations ($\kappa(\mathbf{n})$s) [22] were again used within the MCSCF and GVVPT2 codes to investigate electronic states of Cr_2 and Mo_2. For both molecules, a single valence bond-style reference $\kappa(\mathbf{n})$ was defined by distributing twelve active electrons among six active orbital groups, with each group consisting of a bonding MO and its corresponding antibonding counterpart. The active orbitals were derived from the valence $(n-1)d$ and ns subshells of the atoms. Each valence subspace of two active orbitals was assigned two active electrons in the reference $\kappa(\mathbf{n})$. Thus, for the case of Cr_2, the reference $\kappa(\mathbf{n})$ was the following

$$\kappa(\mathbf{n}) = \frac{\left(3d_{xz}\pi_u 3d_{xz}\pi_g^*\right)^2 \left(3d_{yz}\pi_u 3d_{yz}\pi_g^*\right)^2 \left(3d_{z^2}\sigma_g 3d_{z^2}\sigma_u^*\right)^2 \times}{\left(3d_{x^2-y^2}\delta_g 3d_{x^2-y^2}\delta_u^*\right)^2 \left(3d_{xy}\delta_g 3d_{xy}\delta_u^*\right)^2 \left(4s\sigma_g 4s\sigma_u^*\right)^2} \tag{4.1}$$

This reference $\kappa(\mathbf{n})$ was used to construct the PECs of the $X^1\Sigma_g^+$, $1\,^3\Sigma_u^+$, $1\,^5\Sigma_g^+$, and $1\,^7\Sigma_u^+$ electronic states of Cr_2. The reference $\kappa(\mathbf{n})$ for Mo_2 was the same as (4.1) using its 4d- and 5s-derived MOs. The same states were investigated for Mo_2 as for Cr_2.

With the one reference $\kappa(\mathbf{n})$ described above, MCSCF calculations were first performed to account for static electron correlation. The initial molecular orbital (MO) guesses for one geometry were obtained from approximate natural orbitals of second order restricted Møller-Plesset perturbation (RMP2) calculations from a closed-shell Hartree Fock (HF) reference; subsequent MCSCF calculations used orbitals from adjacent geometries. Dynamic electron correlation energy was accounted for through GVVPT2 calculations. In addition to all active space electrons, high-lying core orbitals (i.e., 3s and 3p electrons in the case of Cr_2, and 4s and 4p in the case of Mo_2) were all

correlated at the GVVPT2 level of theory. All calculations were done using the D_{2h} point group (i.e., the largest point group available in the UNDMOL 1.2 suite of programs: an electronic structure software suite developed and maintained at the University of North Dakota. For details on the structure and operation of UNDMOL 1.2, see Ref. [104]). All calculations of states of Mo_2 included relativistic effects at the GVVPT2 level of theory whereas only studies of the ground state of Cr_2 considered such effects. All studies of excited states of Mo_2 employed the aug-cc-PVTZ-DK basis set [154], derived from the primitive set (25s20p13d3f2g) contracted to [9s8p6d3f2g], while studies of its ground state used this basis set and also the polarized valence triple-ζ quality ANO-RCC basis set [202].

All calculations of excited states of Cr_2 used the cc-pVTZ basis set [153], consisting of 151 Gaussian primitives contracted to [7s6p4d2f1g]. Calculations of the ground state of Cr_2 were done with the cc-pVTZ basis set, but a number of other basis sets were explored as well. These included the correlation consistent quadruple zeta (cc-pVQZ) basis [153] built from 202 primitive Gaussians and contracted to [8s7p5d3f2g] (N.B. The h-functions were neglected in all calculations employing this basis set), the aug-cc-pVTZ basis [153] consisting of 186 primitive Gaussians contracted to [8s7p5d3f2g], Roos Augmented Triple Zeta ANO [37], the ANO-L VTZP basis set [37], and several effective core potential (ECP) basis sets: Stuttgart Relativistic Small Core (RSC) 1997 ECP [203-205], Los Alamos National Laboratory double and triple zeta ECPs, that is, LANL2DZ [206] and LANL08 [207, 208], respectively. The Bauschlicher ANO basis set [209] contracted from the primitive set (19s14p10d6f4g) to [7s6p4d3f2g] was also tested after the Roos aug-TZ ANO gave encouraging results. The performance

of these basis sets on the Cr_2 ground state PEC is shown in Figures 10 to 13 in the Results and Discussion section. Relativistic effects were only considered in calculations of the ground state of Cr_2. This was either done indirectly through use of ECP basis sets or explicitly included in all electron basis sets through the sf-X2C method. Such calculations used the cc-pVTZ or aug-cc-pVTZ-DK basis sets [153] , or the the ANO-RCC VTZP basis set [202]. A new basis set was constructed and tested on the Cr_2 ground state. The construction was done by replacing all contraction coefficients of primitives in the cc-pVTZ-DK basis set [153] with molecular orbital-atomic orbital (MOAO) expansion coefficients (as defined in Eq. (2.23)) obtained from the lowest occupied orbitals of the Cr atom resulting from a restricted open shell Hartree Fock (ROHF) calculation.

Basis set extrapolation was done using the cc-pVTZ and cc-pVQZ results of the ground states of Cr_2. In this process, the total GVVPT2 energy ($E_{tot, GVVPT2}$) was separated into an MCSCF part (E_{MCSCF}) and a dynamic correlation part (E_{dy}). That is

$$E_{dy} = E_{tot,GVVPT2} - E_{MCSCF} \qquad (4.2)$$

The MCSCF part was extrapolated following the exponential extrapolation scheme originally suggested by Feller [210, 211], for SCF thus

$$E_{\infty, MCSCF} = E_{x,MCSCF} - A\exp(-Bx), \qquad (4.3)$$

where $E_{\infty, MCSCF}$ refers to the expected asymptotic limit of the MCSCF energy at the complete basis set (CBS) limit, $E_{x, MCSCF}$ is the calculated MCSCF energy, x is the cardinal number of the basis set (x = 3 for cc-pVTZ, x = 4 for cc-pVQZ) while A and B are fitting parameters. A value of 1.63 for the B parameter has been shown to give good results for SCF extrapolation for many molecules (e.g., see Ref. [212, 213]). In this

work, the values B = 1.63 and B = 1 (which gave good results in previous MCSCF/GVVPT2 studies on NO⁻, [214]) were used. With the value of B defined, a two-point extrapolation expression can easily be obtained from Equation 2. The dynamic correlation part of the total energy was extrapolated following the two-point linear fit of Helgaker et al. [215] and of Halkier et al. [216] built upon the ideas of Schwartz [217]; i.e.,

$$E_{\infty, dy} = E_{x, dy} - Cx^{-3},$$ (4.4)

where $E_{\infty, dy}$ is the dynamic correlation energy at the CBS limit, $E_{x, dy}$ is the computed value, with x again being the cardinal number of the basis set, while C is an undetermined parameter. Substituting x = 3 for the triple zeta basis and x = 4 for the quadruple zeta basis set into Equation 4 to obtain two equations and then eliminating C results in a two-point extrapolation expression for the dynamic correlation energy. The total energy at the CBS limit is calculated as the sum of the extrapolated static (MCSCF) and dynamic correlation energies

$$E_{\infty, total} = E_{\infty, MCSCF} + E_{\infty, dy}$$ (4.5)

Where indicated, effective bond orders were determined using Eqs. (3.11) and (3.12) given in Chapter III.

Results and Discussion

Electronic States of Cr_2

The PECs for the singlet $X^1\Sigma_g^+$ ground state of Cr_2 obtained at the MCSCF and GVVPT2 levels of theory, using some of the basis sets listed above, are shown in Figures 11 and 12, respectively. The MCSCF curves shown in Figure 11 all look similar

(irrespective of basis set) and have no resemblance with the experimental curve (e.g., no outer shelf is seen and all curves predict the ground state to be almost unbound, De ≈ 0.12 eV only).
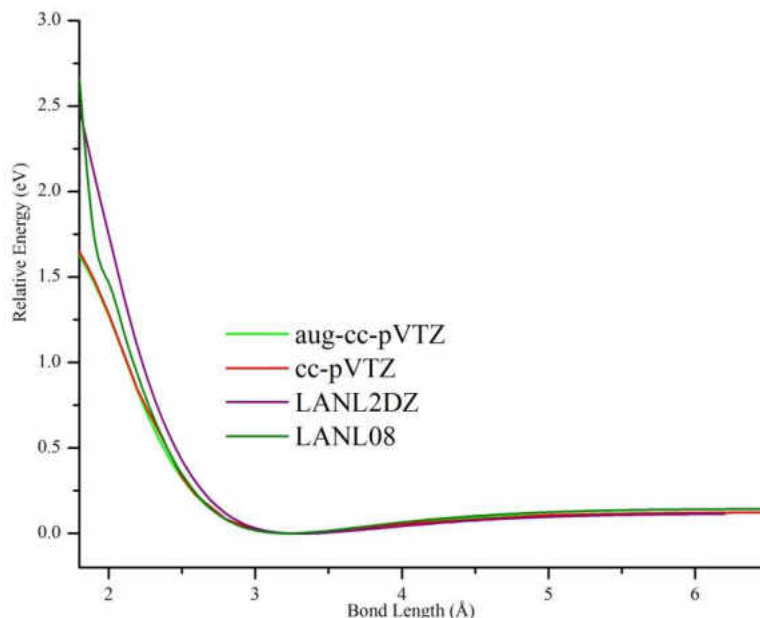
Figure 10. PECs of the singlet ground electronic state, $X^1\Sigma_g^+$, of Cr_2 obtained at the MCSCF level of theory using the basis sets indicated in the inset.

The effect of dynamic electron correlation is profound, as can be seen on comparison of Figures 11 and 12. GVVPT2 adds dynamic correlation energy of about 1.0 Hartree to an MCSCF energy of roughly 2,086.7 Hartrees (considering the cc-pVTZ basis set), yet qualitatively changes the curves. The RKR experimental curve for the ground $X^1\Sigma_g^+$ state of Cr_2 has been included in Figure 12 for comparison with GVVPT2 curves. Observing Figure 12, it appears that the ECP basis sets investigated (Stuttgart RSC 1997, LANL2DZ and LANL08) do not satisfactorily describe the bonding in the ground state of Cr_2. This corroborates the recent work that showed ECP basis sets to perform poorly

[218] on transition metal systems in comparison with all-electron basis sets, predicting

binding energies with deviations from correct values of up to 5.8 kcal/mol or 0.25 eV (in

the case of Sc_2) at the DFT level of theory. On the other hand, Dunning type basis sets

(cc-pVTZ, aug-cc-pVTZ, cc-pVQZ) reproduce essential characteristics of the RKR

experimental curve as can be seen in Figure 12. The spectroscopic constants

characterizing these curves are given in Table 4 while additional curves are provided in

Figure 13.
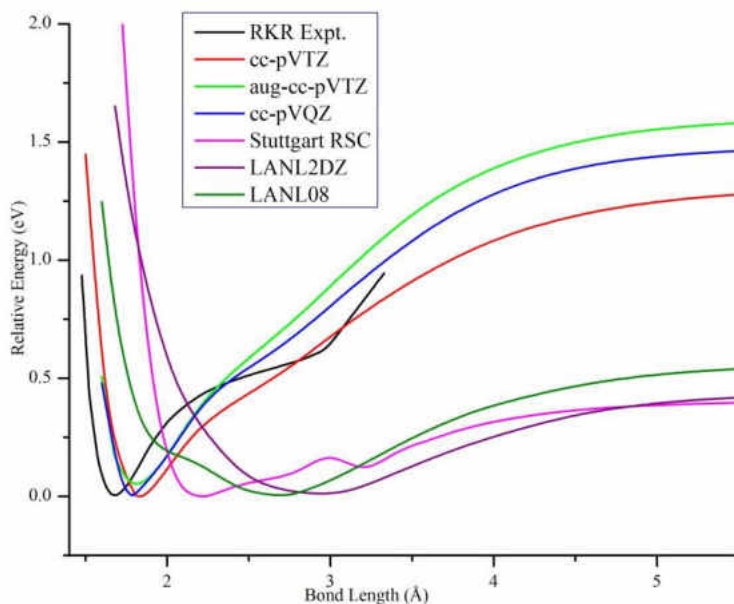
Figure 11. PECs of the $X^1\Sigma_g^+$ state of Cr_2 obtained at the GVVPT2 level of theory using
the basis sets indicated in the inset.

The best results were obtained in relativistic calculations using cc-pVTZ (shown

as cc-pVTZ(R) in Table 4 and Figure 11) where a bond length of R_e = 1.73 Å and

harmonic frequency of $\omega_e = 442.9\,cm^{-1}$ were obtained in comparison with experimental

values of 1.68 Å and $481.0\,cm^{-1}$, respectively. However, the obtained curve is over

bound by about 0.21 eV compared with experiment.

Table 4. Basis set effect on the equilibrium bond length, R_e (Å), dissociation energy, D_e (eV), and the harmonic frequency, ω_e (cm^{-1}) for Cr_2 in its ground state, $X^1\Sigma_g^+$

Basis Set	GVVPT2			MCSCF	
	R_e	D_e	ω_e	R_e	D_e
cc-pVTZ	1.83	1.30	346.4	3.30	0.12
aug-cc-pVTZ	1.81	1.60	412.6	3.30	0.12
cc-pVQZ	1.80	1.47	364.4	-	-
LANL2DZ	3.00	0.56	-	3.40	0.11
LANL08	2.70	0.43	-	3.20	0.14
Stuttgart RSC 1997 ECP	2.22	0.41	-	-	-
Roos Aug-TZ ANO	1.80	1.60	378.9		
Bauschlicher ANO	1.80	1.65	377.1		
New Basis (R)*	1.81	1.45	716.7		
cc-pVTZ (R)	1.73	1.77	442.9		
Expt.	1.68[a]	1.472 ± 0.056[b] 1.56 ± 0.06[c] 1.45 ± 0.1[d]	481[e]		

[a]Ref. [169]. [b]Ref. [171]. [c]Ref. [170]. [d]Ref. [172]. [e]Ref. [173].
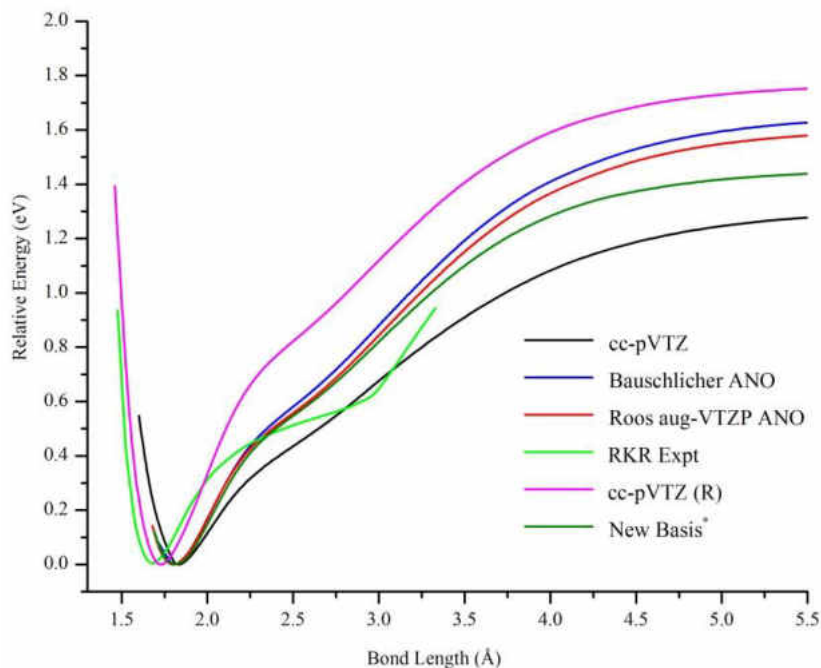
Figure 12. PECs of the $X^1\Sigma_g^+$ state of Cr_2 obtained at the GVVPT2 level of theory using the basis sets indicated in the inset. "R" in parentheses designates that relativistic effects were included. The PEC obtained with the newly constructed basis set (New Basis*) is also included.

The Roos aug-TZ ANO, Bauschlicher ANO, and cc-pVQZ basis sets also led to fairly good results; predicting a bond length that was 0.12 Å too long and harmonic frequencies that were at least $102\,\mathrm{cm}^{-1}$ less than the expected value, whereas aug-cc-pVTZ led to a slightly better frequency. The binding energy of 1.47 eV obtained with cc-pVQZ is in good agreement with the experimental value of 1.472 ± 0.056 eV obtained by Hilpert and Ruthardt [171]. The newly constructed basis set that was used to perform GVVPT2 calculations that included relativistic effects (denoted as "New Basis*" in Figure 12 and "New Basis (R)*" in Table 4) also gave fairly good results; predicting a bond length that was 0.13 Å too long compared with experiment whereas a binding energy of 1.45 eV obtained with this basis set was in good agreement with the experimental value of 1.45 ± 0.1 eV obtained by Su et al. [172]. Calculations with the new basis set led to a sharp minimum in the PEC that resulted in a too high harmonic frequency.

Near the minimum (1.84 Å), the leading configuration in the GVVPT2 wave function for the Cr_2 ground state was

$$3d_{xz}\pi_u^2 3d_{yz}\pi_u^2 3d_{z^2}\sigma_g^2 3d_{x^2-y^2}\delta_g^2 3d_{xy}\delta_g^2 4s\sigma_g^2 \tag{4.6}$$

This configuration had an amplitude of 0.401. Three other important configurations were

$$3d_{xz}\pi_u^2 3d_{yz}\pi_u^2 3d_{z^2}\sigma_g^2 3d_{x^2-y^2}\delta_g^1 3d_{x^2-y^2}\delta_u^{*1} 3d_{xy}\delta_g^1 3d_{xy}\delta_u^{*1} 4s\sigma_g^2 \tag{4.7}$$

$$3d_{xz}\pi_u^2 3d_{yz}\pi_u^2 3d_{z^2}\sigma_g^2 3d_{x^2-y^2}\delta_u^{*2} 3d_{xy}\delta_g^2 4s\sigma_g^2 \tag{4.8}$$

$$3d_{xz}\pi_u^2 3d_{yz}\pi_u^2 3d_{z^2}\sigma_g^2 3d_{x^2-y^2}\delta_g^2 3d_{xy}\delta_u^{*2} 4s\sigma_g^2 \tag{4.9}$$

with amplitudes of 0.237, 0.235 and 0.235, respectively. Using 22 CSFs with amplitudes in the range [0.0811, 0.4011], an EBO of 4.37 (compared with 4.51 at the CASPT2 level [162, 219]) was obtained. The amplitudes of these configurations decrease towards the shelf region so that, at 2.80 Å, the amplitude of the first configuration is only 0.082 (with cc-pVTZ basis). Using 119 CSFs at 2.8 Å with amplitudes in the range [0.0581, 0.0902] gave an EBO of only 1.37.

As was shown above, the GVVPT2 results on ground state Cr_2 reproduced the essential features of the reference experimental curve and gave spectroscopic constants close to expected experimental results. Possible ways of improving on the accuracy of these results were sought. One of such efforts was to account for scalar relativistic effects which, in the case of using the cc-pVTZ basis set, led to better results (but for the binding energy) compared with larger basis set calculations such as those with cc-pVQZ. Preliminary relativistic calculations on ground state Cr_2 in which Douglas-Kroll basis sets, such as aug-cc-pVTZ-DK, that are optimized for use with the DKH Hamiltonian [30, 31], did not lead to improvements in results similar to those reported here with the cc-pVTZ basis. Since the cc-pVTZ and cc-pVTZ-DK basis sets, for example, differ only in contraction coefficients of Gaussian primitives, it is likely that such coefficients are not the optimal set for use with a sf-X2C Hamiltonian as is done in relativistic GVVPT2. It remains to be verified what effects those coefficients have on relativistic GVVPT2 calculations. Such investigation would possibly require calculations in which Gaussian primitives are not contracted for comparison with the cases where they are contracted in e.g., cc-pVTZ versus cc-pVTZ-DK.

Another way of seeking to improve on the results of ground state Cr_2 was to investigate errors connected with basis set truncation by performing basis set extrapolation. In such extrapolations, the energies obtained with the cc-pVTZ and cc-pVQZ basis sets were used in formulas (4.3) to (4.5) to approximate the corresponding total energies at the complete basis set (CBS) limit. Shown in Figure 13 are two PECs plotted with extrapolated energies where the parameter (B) in Eq. (4.3) was set to 1 in one case and to 1.63 in the other case.
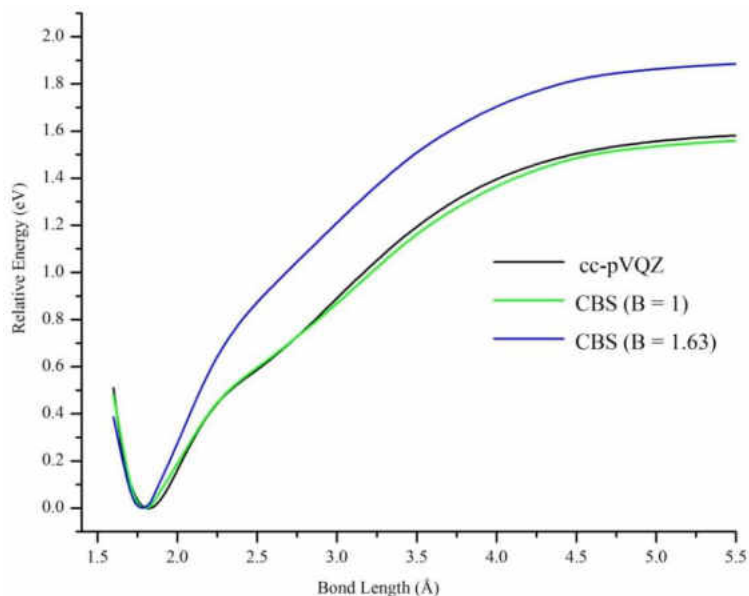
Figure 13. PECs of the $X^1\Sigma_g^+$ state of Cr_2 obtained at the GVVPT2 level and extrapolated to the complete basis set (CBS) limit, using parameters B =1 and B = 1.63 in Eq. (4.3). Energies obtained using the cc-pVTZ and cc-pVQZ basis sets were used in the extrapolation. The cc-pVQZ PEC is included for comparison.

As can be seen in Figure 13, the extrapolation of the MCSCF part of the total energy using B = 1 in Equation (4.3) resulted in a PEC virtually the same as the cc-pVQZ curve at all geometries (only 0.01 Å shorter in bond length), while using B = 1.63 led to a 0.02 Å decrease in bond length at the CBS limit. These results suggest that the basis set

effect on the somewhat long bond length obtained in nonrelativistic GVVPT2 calculations of ground state Cr_2 may be minimal. Moreover, it is seen that the parameter B affects the quality of results. For example, with B = 1.63, the binding energy was overestimated by some 0.30 eV whereas setting B = 1 did not result in such overestimation of the bond energy at the CBS limit.

Finally, the lowest triplet, $1^3\Sigma_u^+$, quintet, $1^5\Sigma_g^+$, and septet, $1^7\Sigma_u^+$, excited states of Cr_2 were investigated at the GVVPT2 level of theory, using the cc-pVTZ basis set. The PECs for these states are shown in Figure 14 together with the ground state and RKR experimental curves. The spectroscopic constants characterizing the curves for the excited electronic states of Cr_2 are shown in Table 5 and compared with the CASPT2 results obtained by Andersson [220]. There are not available experimental data to compare the present results with. As can be seen in Table 5, the present results compare well with the previous CASPT2 data for the investigated states. For example, GVVPT2 predicts a bond length (R_e) of 2. 65 Å and an adiabatic transition energy (T_e), relative to the ground state, of 0.70 eV for the $1^7\Sigma_u^+$ state while CASPT2 gave R_e = 2.67 Å and T_e = 0.88 eV. The interested reader is referred to Figure 1 of Ref. [220] for a comparison of the topologies of GVVPT2 PECs of the $1^3\Sigma_u^+$, $1^5\Sigma_g^+$, and $1^7\Sigma_u^+$ excited states of Cr_2 with those obtained at the CASPT2 level of theory.
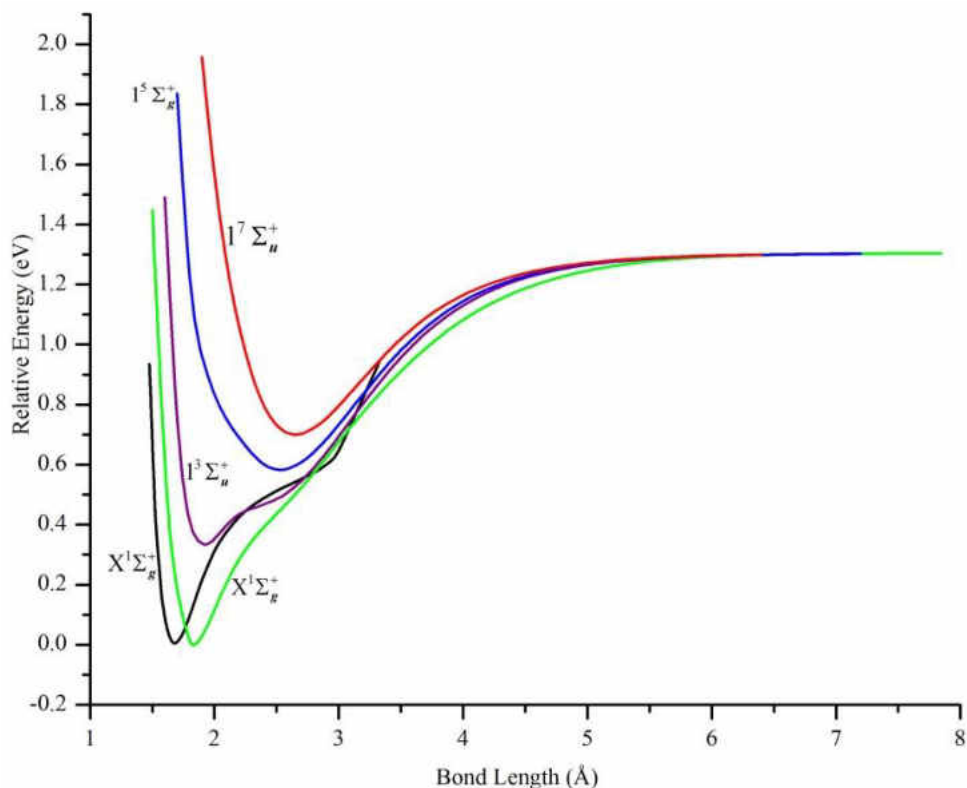
Figure 14. PECs of the $1^3\Sigma_u^+$, $1^5\Sigma_g^+$, and $1^7\Sigma_u^+$ excited states of Cr_2 obtained at the GVVPT2 level of theory using the cc-pVTZ basis set. Also included are the PECs of the ground $X^1\Sigma_g^+$ state of Cr_2 obtained with cc-pVTZ at the GVVPT2 level (green curve) and the RKR experimental PEC (black curve).

Table 5. Spectroscopic constants for excited electronic states of Cr_2, obtained at the GVVPT2 level with the cc-pVTZ basis set, compared with those of Ref. [220] calculated at the CASPT2 level of theory.

Electronic State	GVVPT2				CASPT2[a]		
	$R_e(Å)$	$D_e(eV)$	$\omega_e(cm^{-1})$	$T_e(eV)$	$R_e(Å)$	$\omega_e(cm^{-1})$	$T_e(eV)$
$1\ ^3\Sigma_u^+$	1.93	0.97	307.0	0.33	1.86	410	0.56
$1\ ^5\Sigma_g^+$	2.53	0.72	140.9	0.58	2.58	148	0.78
$1\ ^7\Sigma_u^+$	2.65	0.60	155.9	0.70	2.67	-	0.88

[a]Ref. [220].

PECs of the ground $X^1\Sigma_g^+$ state of Mo_2 as well as those of its $1^3\Sigma_u^+$, $1^5\Sigma_g^+$, and $1^7\Sigma_u^+$ excited states are shown in Figure 15, computed with the basis sets shown in the inset.
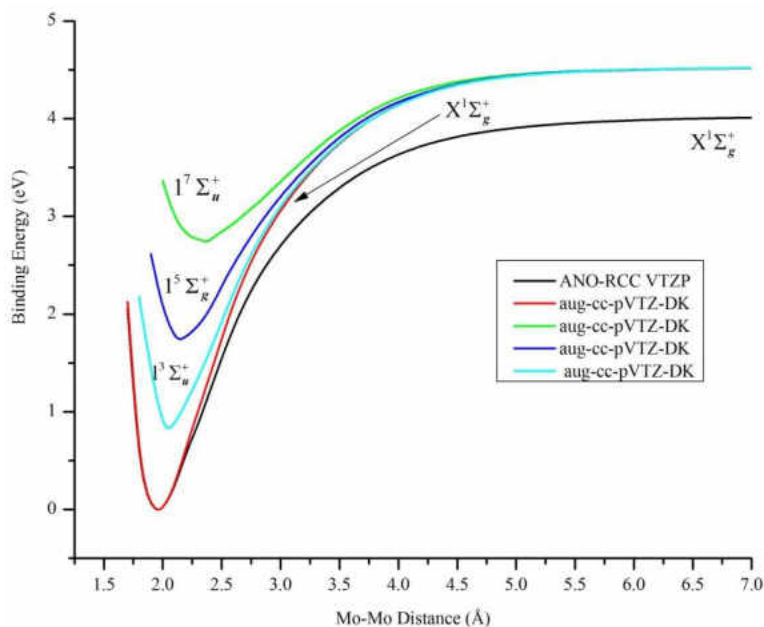
Figure 15. PECs of the $X^1\Sigma_g^+$, $1^3\Sigma_u^+$, $1^5\Sigma_g^+$, and $1^7\Sigma_u^+$ states of Mo_2 obtained at the relativistic GVVPT2 level of theory using the basis sets shown in the inset. All excited state energies were plotted relative to the lowest energy value of the aug-cc-pVTZ-DK PEC of the $X^1\Sigma_g^+$ ground state.

Relativistic effects can be seen by comparing the Mo_2 PECs in Figure 15 to those of Cr_2 provided in Figure 14 (note that PECs of the same electronic states were constructed for the two molecules). As can be seen, the outer shelf shown in the ground $X^1\Sigma_g^+$ and excited $1^3\Sigma_u^+$ state PECs of Cr_2 (Figure 14) are absent in the corresponding curves for Mo_2 (Figure 15). This observation is possibly due to relativistic effects. Relativistic effects tend to contract s and p atomic orbitals while simultaneously slightly

destabilizing the d and f orbitals. Since such effects are weak in Cr, the spatial extents of the 3d and 4s atomic orbitals of Cr are different. In the $3d^5 4s^1$ ground state of Cr, the average expectation value of the 3d orbitals is 1.37 a_0 whereas that of the 4s is more than twice this value (3.52 a_0) [221]. This would give a ratio of $\langle r_{4s} \rangle / \langle r_{3d} \rangle = 2.57$ which is even 0.12 more than the ratio reported by Morse [222]. As a result, the 3d and 4s orbitals of Cr contribute to bonding at different internuclear separations in the Cr_2 molecule. This leads to a shelf region that is dominated by 4s-4s bonding interactions whereas the inner minimum corresponds largely to 3d-3d bonding interaction. For Mo, however, the stronger relativistic contraction of the outer 5s orbital and expansion of the 4d subshell leads to the 5s and 4d orbitals having similar spatial extents. For example, Morse [222] reported a $\langle r_{5s} \rangle / \langle r_{4d} \rangle$ ratio of 2.05 for Mo in its ground state (which is was 0.64 less than the value reported for Cr in the same paper). Due to the smaller difference in the radial extents of the 5s and 4d orbitals, they tend to contribute to bonding averagely at the same interatomic distance in the Mo_2 molecule. This is a plausible explanation on the absence of a shelf in the $X^1\Sigma_g^+$ and excited $1^3\Sigma_u^+$ state PECs of Mo_2.

The data describing the PECs in Figure 15 are in Table 6, compared with data obtained from previous theoretical studies and experimental data for the $X^1\Sigma_g^+$ ground state of Mo_2.

Table 6. Equilibrium distances (R_e), binding energies (D_e), adiabatic transition energies (T_e), and harmonic frequencies (ω_e) of electronic states of Mo_2 calculated at the relativistic GVVPT2 level of theory compared with results from other methods.

Method	Basis Set	R_e(Å)	D_e(eV)	ω_e(cm^{-1})	T_e (cm^{-1})
		$X^1\Sigma_g^+$			
MCSCF-CI[a]		2.01	0.86	388.0	
MRCI[b]	[10s6p5d]	1.97		475.0	
GVB-vdw[c]	[5s5p4d + f set]	1.93	1.41	455.0	
MGVB	[5s5p4d + f set]	1.92	3.94		
CASSCF/MS-CASPT2[e]	ANO-RCC [8s7p5d3f2g1h]	1.95	4.41	459.0	
MRCISD + Q[f]	RECP	1.993		447.5	
(FO + MR)CI[f]	RECP	2.050		486	
FOCI[f]	RECP	2.044		497.0	
PNOF5[g]	ECP	2.10	3.26	368.0	
CASSCF[g]	ECP	2.10	0.55	306.0	
CASPT2[g]	ECP	2.09	2.14	358.0	
CASSCF[h]	ANO-RCC [10s9p9d6f4g2h]	1.96	1.49	430.0	
SC-NEVPT2[h]	ANO-RCC [10s9p9d6f4g2h]	1.92	4.88	507.6	
PC-NEVPT2[h]	ANO-RCC [10s9p9d6f4g2h]	1.92	4.95	506.3	
GVVPT2	Aug-cc-pVTZ-DK	1.96	4.52	444.47	
Experiment		1.929[i]	4.12[i]	477.1[i]	
		1.940[j]	4.21[k]	484.9[l]	
			4.474[m]		
		$1^3\Sigma_u^+$			
CASSCF/MS-CASPT2[e]	ANO-RCC [8s7p5d3f2g1h]	2.063		393.0	8912
(FO + MR)CI[f]	RECP	2.118		458.0	5499
FOCI[f]	RECP	2.118		452.0	6751
GVVPT2	Aug-cc-pVTZ-DK	2.05	3.69	402.4	6719
		$1^5\Sigma_g^+$			
(FO + MR)CI[f]	RECP	2.164		456.0	12234
FOCI[f]	RECP	2.178		423.0	14221
GVVPT2	Aug-cc-pVTZ-DK	2.15	2.78	326.7	14071
		$1^7\Sigma_u^+$			
FOCI[f]	RECP	2.484		268.0	25004
GVVPT2	Aug-cc-pVTZ-DK	2.37	1.78	442.5	22128

[a]Ref. [196], [b]Ref. [197], [c]Ref. [198], [d]Ref. [199], [e]Ref. [201], [f]Ref. [200], [g]Ref. [223], [h]Ref. [224], [i]Ref. [189], [j]Ref. [192], [k]Ref. [190], [l]Ref. [193], [m]Ref. [170].

From Table 6, it can be seen that GVVPT2 results on the investigated states of Mo_2 are in good agreement with those from previous studies that used other high level methods. The ground state bond length of 1.96 Å and bond energy of 4.52 eV obtained at the GVVPT2 level when using the aug-cc-pVTZ-DK basis set are in good agreement with the experimental values of 1.94 Å and 4.47 eV obtained by Hopkins et al. [192] and Simard et al. [170], respectively. Moreover, comparing with experiment, the GVVPT2 ground state bond length is in better agreement than the values obtained at the (FO + MR)CI and MRCISD +Q levels of theory by Balasubramanian and Zhu [200] and at the CASPT2 level of theory [223]. The (FO + MR)CI harmonic frequency is, however, in better agreement than the GVVPT2 value. It should be noted that the experimental binding energies cited in Table 6 represent D_0^o values whereas theoretical methods (including GVVPT2) generally compute D_e (which is greater than D_0^o by the zero point energy). The GVVPT2 harmonic frequency of 444.47 cm^{-1} for ground state Mo_2 is also in good agreement with the experimental value of 477.1 cm^{-1} due to Efremov et al. [189]. GVVPT2 data for the excited states are also in agreement with data listed from other sources for comparison. The GVVPT2 adiabatic transition energies for all three excited states investigated are in agreement with values obtained by Balasubramanian and Zhu [200] at the FOCI level of theory. Differences between GVVPT2 and the Ref. [200] results are seen mostly in the harmonic frequencies. There are not available experimental data of these excited states for comparison.

The data listed for the ground state, obtained using different methods, reveals the importance of electron correlation effects in the description of these molecules. For example, the CASSCF method used by Ruipérez et al. [223] found the ground state of the

Mo_2 molecule to be nearly unbound (De = 0.55 eV only). The CASSCF method (like the MCSCF) accounts for static correlation but fails to capture essential dynamic correlation effects. The CASSCF bond energy of Angeli et al. [224] was also too low (1.49 eV compared to 4.47 eV from experiment).

Conclusions

This Chapter discussed low-lying electronic states of Cr_2 and Mo_2 as were investigated at the GVVPT2 level of theory. The literature cited on previous experimental and theoretical work on these molecules revealed the challenges involved in their description. The GVVPT2 method was shown to be capable of describing their ground and low-lying excited electronic states, using chemically intuitive valence orbitals. Even when using a simple zero-order Hamiltonian, it was shown that the GVVPT2 method gives PECs and spectroscopic constants that are close to experimental results using model spaces derived from valence bond models. Particularly noteworthy is the fact that the curves, in addition to being smooth and continuous, are free of artifactual inflections for both ground and excited states.

This study revealed that a proper description of several of the low-lying electronic states of Cr_2 and Mo_2 can be made using a simple model space consisting of only (*n*-1)d and *n*s-derived MOs (*n* = 4 for Cr and 5 for Mo). In the case of Cr_2 when using the cc-pVTZ basis set, a valence bond style partitioning of these active orbitals as was done in this study resulted in model space dimensions of 1,516, 2,712, and 580 CSFs, and total space dimensions of 998,024,048, 2,141,100,436, and 920,000,422 CSFs for the $X^1\Sigma_g^+$,

$1 {}^3 \Sigma_u^+$, and $1 {}^7 \Sigma_u^+$ electronic states, respectively. This study found that both valence

double zeta and valence triple zeta ECP basis sets perform poorly for Cr_2 .

CHAPTER V

GVVPT2 STUDIES OF LOW-LYING ELECTRONIC STATES OF MANGANESE
AND TECHNETIUM DIMERS

Introduction

Although manganese (Mn) and technetium (Tc) are both in group 7 of the Periodic Table with valence electron configuration $(n-1)\mathrm{d}^5 n\mathrm{s}^2$, corresponding to a $^6\mathrm{S}$ ground atomic term, there are many contrasts between these two elements. For example, whereas Mn constitutes the third most abundant transition element in the earth's crust (about 1060 ppm) (and is commonly obtained from pyrolusite for use in diverse applications such as steel manufacture and glassmaking), Tc is a trace element, constituting as little as 0.0007 ppm of the earth's crustal rocks [225]. Additionally, Mn is known to have only one stable naturally occurring isotope whereas Tc has thirty four known isotopes, all of which are radioactive, with masses ranging from 85 to 118; the most abundant being Tc-99 which is largely present in spent nuclear fuel and has a half-life of 2.1 × 10^5 years [226]. Moreover, Tc is the lightest radioactive and first artificial element to be discovered in 1925, by Noddack-Tacke et al. [227], from the analysis of platinum ores and columbite minerals, who named it masurium; and later by Perrier and Segrè (see Ref. [228, 229]) from the analysis of molybdenum bombarded by deuterium nuclei.

In studies of low-lying electronic states of Mn_2 and Tc_2, isotope Tc-98 was used, which has the longest half-life (4.2 million years) of any isotope. Unlike Cr_2 and Mo_2 that are known to have the same ground state symmetry ($X^1\Sigma_g^+$), the ground electronic states of Mn_2 and Tc_2 are quite different: the established ground state of Tc_2 is $X^3\Sigma_g^-$ with a bond energy of at least 2.13 eV whereas Mn_2 is a van der Waals molecule that has the same ground state symmetry as does Cr_2 and Mo_2, with a binding energy of about 0.10 eV [159]. These differences between Mn_2 and Tc_2 may be explained in terms of the factors that govern metal-metal bonding in transition metals: the relative sizes of the (n - 1)d and ns orbitals and the ns $\rightarrow$ ($n-1$)d excitation energy. For the group 7 metals, the relative sizes of the ($n-1$)d and ns orbitals become similar in spatial extent on going from Mn to Re (probably due to relativistic effects tending to contract the outer ns and slightly expand the inner ($n-1$)d orbitals) such that for ground state atoms, the ratio $\left(\left\langle r_{(n+1)s}\right\rangle / \left\langle r_{nd}\right\rangle\right)$ is 2.99 for Mn, 2.27 for Tc, and 2.11 for Re [148]. The ns $\rightarrow$ ($n-1$)d excited energy decreases somewhat in this order: for Mn = 2.14 eV, Tc = 0.41 eV, Re = 1.76 eV [222]. This decrease favors s-d hybridization, hence d-d bonds. Mn_2 is a van der Waals species due to the high s-d promotion energy and differences in the spatial extents of the 3d and 4s orbitals whereas its isovalent counterparts, Tc_2 and Re_2, exhibit multiple bonds [230].

This Chapter is organized as follows. The present subsection briefly reviews previous theoretical and experimental characterization of low-lying electronic states of Mn_2 and Tc_2; the next subsection will provide details on how the calculations were

performed; the results are presented and discussed in the third subsection; while a final subsection concludes the Chapter.

Previous Studies of Mn_2

As with other transition metal elements, Mn has many low-lying electronic states. The interaction of two ground state Mn atoms gives rise to 36 molecular states with multiplicities ranging from 1 to 11 [231]. Of these 36 states, the ground state was established as $X^1\Sigma_g^+$ from electron spin resonance (ESR) measurements [232, 233]. A singlet ground state was also confirmed by resonance Raman spectra in rare gas matrices [234]. From Raman studies, Kirkwood et al.[235] reported a $X^1\Sigma_g^+$ ground state with constants $\omega_e = 68.10\,\text{cm}^{-1}$ and $\omega_e x_e = 1.05\,\text{cm}^{-1}$. Various spectroscopic analyses gave dissociation energies in the range 0.02 to 0.15 eV [236], and a bond length of 3.4 Å for the $X^1\Sigma_g^+$ ground state [237].

Theoretical studies on electronic states of Mn_2, using MRPT methods, have encountered numerous problems varying from the *discontinuity problem* (also known as intruder state problem) in constructing PECs [18, 238, 239] to poor convergence of perturbative expansions [232]. When applying the MCQDPT method to the study of Mn_2, Camacho et al. [18] observed over 5000 intruders between 1.9 and 4.0 Å and a strong dependence of both the ground state PEC and spectroscopic constants on the shift parameters, required to overcome the problem. This led to the authors questioning the adequacy of MRPT in tackling difficult systems like the Mn_2 dimer. Second order MCQDPT [239] that used the [7s6p4d4f2g] basis set constructed from the primitive set (18s12p8d) due to Koga et al. [240] augmented with the p-type primitives of Takewaki et

al. [241] plus 4f2g polarization functions of Sekiya et al. [242], led to $R_e = 3.29$ Å, $D_e = 0.14$ eV, and $\omega_e = 53.46$ cm^{-1} for the $X^1\Sigma_g^+$ ground state of Mn_2. Using second and third order n-electron valence state perturbation theory (NEVPT2 and NEVPT3) and the atomic natural orbitals (ANO) relativistic correlation consistent basis set developed by Roos et al. [202] and with the inclusion of scalar relativistic corrections through the Douglas–Kroll–Hess Hamiltonian, Angeli and co-workers [243] obtained $R_e = 3.71$ Å, $D_e = 0.08$ eV, and $\omega_e = 41.0$ cm^{-1} in the case of NEVPT2, and $R_e = 3.82$ Å, $D_e = 0.07$ eV, and $\omega_e = 43.0$ cm^{-1} with NEVPT3. At the MRCI level with the use of the aug-cc-pVQZ basis set, Buchachenko et al. [231] obtained $R_e = 3.82$ Å, $D_e = 0.05$ eV, and $\omega_e = 33.7$ cm^{-1}, while Tzeli et al. [250], obtained $R_e = 3.80$ Å, $D_e = 0.05$ eV, $\omega_e = 36$ cm^{-1}, and $R_e = 3.64$ Å, $D_e = 0.06$ eV, $\omega_e = 42$ cm^{-1} at the MRCI+Q and average coupled pair functional (ACPF) levels with the same basis, respectively. DFT studies of Mn_2 gave contradictory results [244-249], most of which favor, in contrast to ab initio wave function methods, a high spin (S = 5) ground state.

Previous Studies of Tc_2

Information on Tc_2 is quite sparse in the literature. Much more is known about Tc derivatives which are useful primarily in radiopharmaceuticals and corrosion protection. Many complexes with a Tc_2 nucleus have been reported in the literature e.g., $Tc_2[O_2CC(CH_3)_3]_4Cl_2$ with a Tc-Tc bond length of 2.19 Å [251], $Tc_2Cl_8^{3-}$ with a Tc-Tc bond length of 2.12 Å [252], and α- and $\beta-TcCl_3$ which are polymorphs of triangular Tc_3Cl_9 units with Tc-Tc bond lengths of 2.44 Å and 2.86 Å, respectively [253]. These complexes all showed evidence of multiple d-d bonding in the Tc_2 moiety. This is

contrary to isovalent Mn which is not known to form compounds with ligated Mn_2 species [254].

Since all 34 known isotopes of Tc are radioactive, little experimental work has been carried out on this element and limited to spectroscopic studies on the atom (e.g., see Ref. [255, 256] and references therein). There are not available experimental data on Tc_2 in the literature apart from values of the binding energy of the supposed ground term of Tc_2 computed from thermodynamic relations by Miedema and Gingerich [257] and by Brewer and Winn [258]. Based on three different expressions relating the dissociation enthalpy to the enthalpy of vaporization and the metal surface enthalpy, Miedema and Gingerich [257] computed D_0 values of 3.49 eV, 3.45 eV and 3.33 eV for Tc_2. Brewer and Winn [258] computed $D_0 = 2.93$ eV for ground state Tc_2 (0.40 eV less than the lowest value obtained be Miedema and Gingerich).

The Tc_2 molecule is better known theoretically than experimentally. Klyagina et al. [259] obtained $R_e = 1.92$ Å for Tc_2 using the discrete variational X_α (DV-X_α) method and reported the dominant electronic configuration for the molecule as

$$5s\sigma_g^2 4d_{z^2}\sigma_g^2 4d_{xz}\pi_u^2 4d_{yz}\pi_u^2 4d_{x^2-y^2}\delta_g^2 4d_{xy}\delta_g^2 4d_{x^2-y^2}\delta_u^{*1} 4d_{xy}\delta_u^{*1} \qquad (5.1)$$

in the vicinity of the equilibrium bond length, suggesting a pentuple bond. Yanagisawa et al. [152] studied second row transition metal dimers at the DFT level, employing different functionals, and also at the MP2 level. They found the ground state of Tc_2 to be $^3\Sigma_g^-$ with $R_e = 1.97$ Å, $D_e = 4.75$ eV, and $\omega_e = 512.0$ cm^{-1} with the BOP exchange-

correlation functional; R_e = 1.93 Å, D_e = 3.15 eV, and ω_e = 557.6 cm^{-1} with the B3LYP

hybrid functional; and R_e = 1.99 Å, D_e = 1.46 eV, and ω_e = 483.5 cm^{-1} with the B88

exchange functional, all predicting the same major configuration around the minimum as

was observed by Klyagina et al. [259]. Most DFT functionals used by them and others

[260] gave comparable equilibrium bond lengths, but binding energies that varied by over

3 eV. In contrast, the MP2 calculations by Yanagisawa et al. [152] found the $^3\Sigma_g^-$ state to

be unbound and instead predicted a ground $^7\Pi_u$ state with R_e = 2.18 Å, D_e = 3.97 eV,

and ω_e = 349.3 cm^{-1} and with dominant configuration

$$5s\sigma_g^2 4d_{z^2}\sigma_g^2 4d_{z^2}\sigma_u^{*1} 4d_{xz}\pi_u^2 4d_{yz}\pi_u^2 4d\pi_g^{*1} 4d_{x^2-y^2}\delta_g^1 4d_{xy}\delta_g^1 4d_{x^2-y^2}\delta_u^{*1} 4d_{xy}\delta_u^{*1} \qquad (5.2)$$

around the minimum, suggesting a triple bond. Even more exotic, Yan and Zhu [261]

optimized the structure of Tc_2 with the B3P86 functional and found the ground state to

be $^{11}\Sigma_g^-$ with R_e = 2.84 Å, D_e = 2.27 eV, and ω_e = 178.52 cm^{-1}. It appears the most

recent calculations on Tc_2 are due to Borin et al. [230]. By applying CASPT2 on a

CASSCF reference wave function and accounting for scalar relativity via the Douglas-

Kroll-Hess (DKH) Hamiltonian [30, 31, 186], and using a quadruple-ζ atomic ANO-RCC

basis set [202], these authors obtained a $^3\Sigma_g^-$ ground state for the Tc_2 molecule with R_e

= 1.94 Å, and ω_e = 492.0 cm^{-1} and with an effective bond order (EBO) of 4.4

(interpretable as a pentuple bond). The same authors found the lowest excited Tc_2 state

to be $1^1\Gamma_g$ (lying at 1285 cm^{-1} or 0.16 eV above the ground state) with R_e = 1.96 Å, and

ω_e = 458.0 cm^{-1} and with a configuration similar to that for the ground state and an EBO

of 4.3. The lowest $^1\Sigma_g^+$ state, which is the reported ground state symmetry for isovalent

counterparts Mn_2 and Re_2, was found to lie at some 1797 cm^{-1} or 0.22 eV above the Tc_2 ground state and had R_e = 1.97 Å, and ω_e = 450.0 cm^{-1} and an EBO of 4.3. After the inclusion of spin-orbit coupling, these authors observed a strong interaction between the $^3\Sigma_g^-$ and $^1\Sigma_g^+$ states that led to a 0_g^+ ground state with composition = $(0.75)^3\Sigma_g^- + (0.25)^1\Sigma_g^+$ and with R_e = 1.94 Å, D_e = 3.30 eV, and ω_e = 490.0 cm^{-1}.

Computational Details

The active spaces used in calculations of Mn_2 and Tc_2 consisted of MOs derived from valence atomic orbitals of the $(n-1)d^5$ and ns^2 subshells. This set of 12 active orbitals was partitioned into orbitals groups from which reference macroconfigurations ($\kappa(\mathbf{n})$s) were derived through different distributions of the active electrons among the valence orbital subspaces as follows.

For Mn_2, four reference model spaces, each consisting of a single reference $\kappa(\mathbf{n})$, were used in separate calculations. Results obtained by using the four different partitioning schemes are labeled CASE A to D in Figures 16 to 18 and Table 8 in the Results and Discussion subsection. These $\kappa(\mathbf{n})$s are

$$\text{CASE A: } \kappa(\mathbf{n}) = \frac{\left(3d_{xz}\pi_u 3d_{xz}\pi_g^*\right)^2\left(3d_{yz}\pi_u 3d_{yz}\pi_g^*\right)^2\left(3d_{x^2-y^2}\delta_g 3d_{x^2-y^2}\delta_u^*\right)^2 \times}{\left(3d_{xy}\delta_g 3d_{xy}\delta_u^*\right)^2\left(3d_{z^2}\sigma_g 3d_{z^2}\sigma_u^* 4s\sigma_g 4s\sigma_u^*\right)^6} \tag{5.3}$$

$$\text{CASE B: } \kappa(\mathbf{n}) = \frac{\left(3d_{xz}\pi_u 3d_{xz}\pi_g^* 3d_{yz}\pi_u 3d_{yz}\pi_g^*\right)^4\left(3d_{x^2-y^2}\delta_g 3d_{x^2-y^2}\delta_u^*\right)^2 \times}{\left(3d_{xy}\delta_g 3d_{xy}\delta_u^*\right)^2\left(3d_{z^2}\sigma_g 3d_{z^2}\sigma_u^* 4s\sigma_g 4s\sigma_u^*\right)^6} \tag{5.4}$$

$$\text{CASE C: } \kappa(\mathbf{n}) = \frac{\left(3d_{xz}\pi_u 3d_{xz}\pi_g^* 3d_{yz}\pi_u 3d_{yz}\pi_g^*\right)^4\left(3d_{x^2-y^2}\delta_g 3d_{x^2-y^2}\delta_u^*\right)^2 \times}{\left(3d_{xy}\delta_g 3d_{xy}\delta_u^*\right)^2\left(3p_z\sigma_g 3p_z\sigma_u^* 3d_{z^2}\sigma_g 3d_{z^2}\sigma_u^* 4s\sigma_g 4s\sigma_u^*\right)^{10}} \tag{5.5}$$

$$\text{CASE D: } \kappa(\mathbf{n}) = \frac{\left(3d_{xz}\pi_u 3d_{xz}\pi_g^*\right)^2 \left(3d_{yz}\pi_u 3d_{yz}\pi_g^*\right)^2 \left(3d_{x^2-y^2}\delta_g 3d_{x^2-y^2}\delta_u^*\right)^2}{\left(3d_{xy}\delta_g 3d_{xy}\delta_u^*\right)^2 \left(3d_{z^2}\sigma_g 3d_{z^2}\sigma_u^*\right)^2} \times \tag{5.6}$$

It should be noted that the CASE C active space also included $3p_z-$derived sigma orbitals while CASE D excluded the 4s-derived MOs (which were included with the 3s- and 3p-derived MOs in the active core). The first reference model space (CASE A) was tested only with the $X^1\Sigma_g^+$ state while CASE B to D were used for all three computed states of Mn_2 ($X^1\Sigma_g^+$, $1^5\Sigma_g^+$ and $1^9\Sigma_g^+$). The total number of CSFs generated within the model and full spaces for these states when using the cc-pVTZ basis set and CASE A to D reference $\kappa(\mathbf{n})$s are shown in Table 7.

Table 7. Model and full space configuration state functions (CSFs) generated when the indicated states of Mn_2 were computed using reference $\kappa(\mathbf{n})$s CASE A to D and the cc-pVTZ basis set.

	Space	$X^1\Sigma_g^+$	$1^5\Sigma_g^+$	$1^9\Sigma_g^+$
CASE A	Model	1372		
	Full	911297138		
CASE B	Model	1520	1394	54
	Full	1689129410	2838795978	354240126
CASE C	Model	3444	3306	132
	Full	3005460208	5079354870	638444152
CASE D	Model	332	280	10
	Full	263365024	433537990	54181732

Whereas calculations of the excited states of Mn_2 used only the cc-pVTZ basis set and did not include relativistic corrections, those of the $X^1\Sigma_g^+$ ground state additionally used the cc-pVQZ [153], ANO-L VTZP [37], and ANO-RCC VTZP [202] basis sets. In the case of ANO-RCC VTZP, relativistic calculations were also performed. These additional basis sets were used only within the CASE D reference $\kappa(\mathbf{n})$ while the

cc-pVTZ basis set was used in all four cases. The cc-pVTZ and cc-pVQZ data on the ground state were used for extrapolation to the CBS limit using formulas (4.3) to (4.5) provided in Chapter IV.

For the $1^1\Sigma_g^+$, $1^5\Sigma_g^+$, and $1^9\Sigma_g^+$ states of Tc_2, a single reference $\kappa(\mathbf{n})$ was constructed, consisting of 5 orbital subspaces; each with a bonding and a corresponding antibonding MO,

$$\kappa(\mathbf{n}) = \frac{\left(4d_{xz}\pi_u 4d_{xz}\pi_g^*\right)^2 \left(4d_{yz}\pi_u 4d_{yz}\pi_g^*\right)^2 \left(4d_{x^2-y^2}\delta_g 4d_{x^2-y^2}\delta_u^*\right)^2 \times}{\left(4d_{xy}\delta_g 4d_{xy}\delta_u^*\right)^2 \left(5s\sigma_g 5s\sigma_u^*\right)^2} \tag{5.7}$$

This active space excluded the $4d_{z^2}$ – derived MOs (which were added to the 4s- and 4p-dominated MOs in the active core) and led to 332 model space and 1886186600 total space CSFs for the $1^1\Sigma_g^+$ state, 280 model space and 3192157814 total CSFs for the $1^5\Sigma_g^+$ state, and 10 model space and 423682756 all space CSFs for the $1^9\Sigma_g^+$ state, when using the aug-cc-pVTZ-DK basis set.

For the $X^3\Sigma_g^-$ and $1^{11}\Sigma_g^-$ states of Tc_2, the active space included all 4d and 5s-derived MOs grouped as follows

$$\kappa(\mathbf{n}) = \frac{\left(4d_{z^2}\sigma_g 4d_{z^2}\sigma_u^* 4d_{x^2-y^2}\delta_g 4d_{x^2-y^2}\delta_u^* 5s\sigma_g 5s\sigma_u^*\right)^6 \times}{\left(4d_{xz}\pi_u 4d_{xz}\pi_g^* 4d_{yz}\pi_u 4d_{yz}\pi_g^*\right)^6 \left(4d_{xy}\delta_g 4d_{xy}\delta_u^*\right)^2} \tag{5.8}$$

This partitioning of the model space resulted in 5,952 model space and 65,230,481,060 all space CSFs for the $X^3\Sigma_g^-$ state, and 2 model space and 975,015,732 total CSFs for the

115

$1\,^{11}\Sigma_g^-$ state when using the aug-cc-pVTZ-DK basis set. Reference $\kappa(\mathbf{n})$ (5.8) could be used to construct the Σ_g^+ states of Tc_2 but is obviously more expensive without leading to qualitatively different PECs. For the lowest $^1\Sigma_g^+$ state, the single point energy difference from results obtained from the use of reference $\kappa(\mathbf{n})$ (5.7) and $\kappa(\mathbf{n})$ (5.8) was only about 0.006 eV at 2.18 Å ($R_e = 2.17$ Å for this state). On the other hand, reference $\kappa(\mathbf{n})$ (5.7) was insufficient for describing the Σ_g^- states of Tc_2. All GVVPT2 calculations of Tc_2 states included scalar relativistic effects (accounted for through the sf-X2C method) and correlated the active electrons of the 4s, 4p, and $4d_{z^2}$ – derived MOs in the case of reference $\kappa(\mathbf{n})$ (5.7) or the 4s and 4p-derived MOs in the case of reference $\kappa(\mathbf{n})$ (5.8) . All calculations of states of Mn_2 and Tc_2 used D_{2h} symmetry.

Results and Discussion

Electronic States of Mn_2

The PECs obtained at the GVVPT2 level for the electronic states of Mn_2 are shown in Figures 16 to 18 for CASE A to D reference $\kappa(\mathbf{n})$s. It can be seen that the results depend fairly strongly on the nature of partitioning of the active space. CASE A partitioning (where the four sigma MOs derived from $3d_{z^2}$ and 4s were grouped together in one valence subspace in order to allow for some bonding involving the 4s-dominated MOs), when used to investigate the singlet ground state gave a bond length that was incorrect ($R_e = 4.58$ Å compared with the experimental value of 3.40 Å), although a binding energy of $D_e = 0.069$ eV was quite good. This reference model space (CASE A) was not used to investigate excited states due to this rather poor R_e value. CASE B

partitioning was derived from CASE A by further increasing the active space within the 3d/4s manifold (by grouping the four 3d-derived pi orbitals in one valence subspace), and yielded a PEC with good characteristics for the singlet ground state. The spectroscopic constants of $R_e = 3.37$ Å, $D_e = 0.11$ eV, and $\omega_e = 83.35$ cm^{-1} obtained with CASE B model space are close to the experimental values of 3.40 Å, 0.10 eV, and 68.1 cm^{-1}, respectively (see Figure 16 and Table 8). Unfortunately with this partitioning, the quintet, $^5\Sigma_g^+$, and nonet, $^9\Sigma_g^+$, electronic states that should have the same dissociation channel as the singlet ground state do not (cf. Figure 16). Moreover, these excited states appear to be slightly more stable (i.e., 0.02 eV) than the ground state in the vicinity of the equilibrium bond length. Yet, analysis of the orbitals did not reveal significant changes in their nature for any of the three electronic states. It is seen that this active space (CASE B) is again insufficient for describing the Mn_2 system.
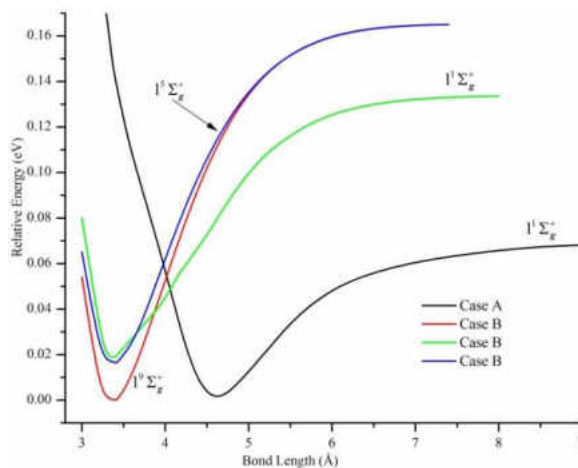
Figure 16. PECs of the $1^1\Sigma_g^+$, $1^5\Sigma_g^+$, and $1^9\Sigma_g^+$ states of Mn_2 obtained at the GVVPT2 level of theory using the cc-pVTZ basis set. All energies from CASE B calculations are plotted relative to the lowest energy value of the lowest lying curve (the nonet state).

Detailed orbital analysis indicated that the sixth b_{1u} MO in D_{2h} symmetry (expected to be 4s-dominated) was exchanged with the fifth b_{1u} MO (3p$_z$-dominated). This observation supports the argument of Camacho et al. [238] that the $3p_z-$ derived antibonding MO is important for an adequate description of the bonding in ground state Mn_2. Therefore, the $3p_z-$ dominated antibonding MO (and also its bonding counterpart in order to permit good dissociation into equivalent fragments), were included into the sigma subspace of CASE B to obtain the reference model space labeled CASE C.
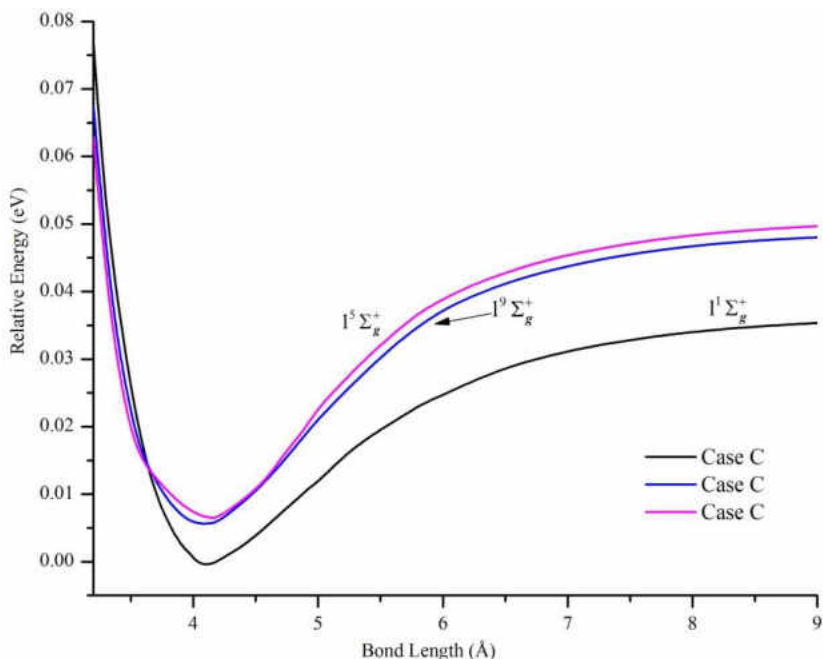
Figure 17. PECs of the $1^1\Sigma_g^+$, $1^5\Sigma_g^+$, and $1^9\Sigma_g^+$ states of Mn_2 obtained at the GVVPT2 level of theory using the cc-pVTZ basis set within CASE C partitioning of the active space. All energies are plotted relative to the lowest energy value of the $1^1\Sigma_g^+$ state.

The PECs for the three electronic states obtained with the CASE C active space of 14 MOs and 18 electrons (14, 18) at the GVVPT2 level using the cc-pVTZ basis set are shown in Figure 17. All three states have $R_e \approx 4.10$ Å but rather than have the same dissociation asymptote, as should be the case, the quintet and nonet states (which appear

to be quasidegenerate) are separated from the singlet ground state by about 0.015 eV at a bond length of 16.0 Å. Difficulties in describing the bonding in Mn_2 when involving the 4s-derived MOs in the active space were first observed by Yamamoto et al. [239]. Without state averaging, these authors obtained three kinds of CASSCF solutions at intermediate bond lengths, which did not permit the construction of a smooth PEC at the second order multiconfigurational quasidegenerate perturbation theory (MCQDPT2) level of theory. This problem of discontinuities in the PECs of Mn_2 due to multiple CASSCF (or MCSCF) solutions, rather than intruder state problems, was also observed by Camacho et al. [238] in their multireference Møller-Plesset perturbation theory (MRMP) study. In calculations with CASE C model space, when beginning from long bond lengths and gradually decreasing the Mn-Mn bond distance, a sharp discontinuity in the MCSCF energy was observed between 4.4 to 4.3 Å for all three electronic states investigated. However, when calculations were resumed with the lower energy orbitals as the initial orbitals at the points where the discontinuities were observed (i.e., performing single point energy calculations inwards to shorter bond lengths and outwards to longer bond lengths), no discontinuities were observed and the smooth curves reported in Figure 17 were constructed from such calculations. State averaging was not necessary at the MCSCF level for convergence.

Analysis of the important configuration state functions (CSFs) contributing to the wave functions for the studied electronic states (using the CASE C active space) revealed that the $3p_z-$ and 4s-derived MOs were doubly occupied in all dominant CSFs, implying inactivity. In retrospect, it is not surprising that the 4s orbitals do not seem to play an important role in the bonding in Mn_2.

Table 8. Equilibrium distances (R_e), binding energies (D_e), and harmonic frequencies (ω_e) of electronic states of Mn_2 calculated at the GVVPT2 level of theory compared with results from other methods.

Electronic State	Method	Basis Set	R_e(Å)	D_e(eV)	ω_e(cm^{-1})
$X^1\Sigma_g^+$	MRCI[a]	aug-cc-pVQZ	4.13	0.03	24.3
	MRCI + Q[a]	aug-cc-pVQZ	3.80	0.05	36
	ACPF[a]	aug-cc-pVQZ	3.64	0.06	42
	CASPT2[b]	ANO-RCC 6s5p4d3f2g1h	3.19	0.28	-
	NEVPT2/SC + s[c]	ANO-RCC 6s5p4d3f2g1h	3.70	0.08	-
	GVVPT2[d]	cc-pVTZ	3.37	0.11	83.4
	GVVPT2[e]	cc-pVQZ	3.83	0.05	30.7
	Experiment		3.40[f]	0.02-0.15[g]	68.1[h]
$^5\Sigma_g^+$					
	MRCI[a]	aug-cc-pVQZ	4.13	0.03	24.6
	MRCI + Q[a]	aug-cc-pVQZ	3.81	0.05	34
	ACPF[a]	aug-cc-pVQZ	3.67	0.06	41
	CASPT2[b]	ANO-RCC 6s5p4d3f2g1h	3.23	0.27	-
	GVVPT2[d]	cc-pVTZ	4.09	0.04	26.4
$^9\Sigma_g^+$					
	MRCI[a]	aug-cc-pVQZ	4.14	0.03	24.5
	MRCI + Q[a]	aug-cc-pVQZ	3.84	0.05	35
	ACPF[a]	aug-cc-pVQZ	3.72	0.05	38
	CASPT2[b]	ANO-RCC 6s5p4d3f2g1h	3.30	0.25	-
	AQCC/LC[C]	aug-cc-pV5Z	3.85	0.04	-
	GVVPT2[d]	cc-pVTZ	4.08	0.04	27.0

[a]Ref. [250], [b]Reference [263], [c]Ref. [231] (SC + s designation implies that all 3s3p3d4s electrons were correlated, SC stands for "small core"), [d]This work (CASE B), [e]This work (CASE D), [f]Ref. [237], [g]Ref. [236], [h]Ref. [235].

The large difference between the average radii of the 3d and 4s subshells of the Mn atom (1.13 vs. 3.38 a_0) [262] indicates that their spatial extents are quite different and, as in chromium, these orbitals cannot simultaneously contribute to bonding at the same internuclear distance. However, no outer shelf is observed in contrast to the situation in Cr_2. Whereas there is strong bonding in Cr_2, there is only weak van der

Waals-like interaction (i.e., weak binding, D_e = 0.1 eV only, and long inter-nuclear distance of 3.4 Å) in Cr_2 that has been ascribed to the shielding effect of the doubly occupied 4s orbitals on the 3d subshells [250].

The results of the fourth tested reference model space (CASE D) are shown in Figure 18 and Table 8.
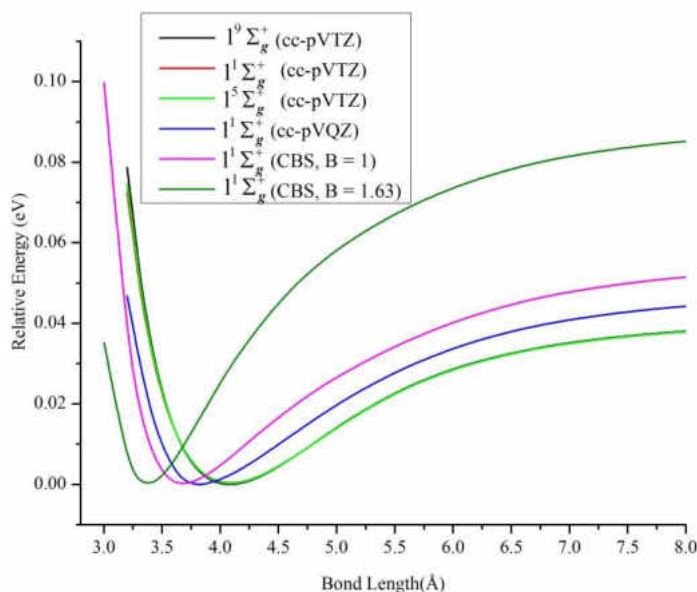
Figure 18. PECs of the $1^1\Sigma_g^+$, $1^5\Sigma_g^+$, and $1^9\Sigma_g^+$ states of Mn_2 obtained at the GVVPT2 level of theory using the basis sets indicated in the inset within CASE D partitioning of the active space. PECs of the $1^1\Sigma_g^+$ state obtained at the complete basis set (CBS) limit using Eqs. (4.3) to (4.5) in Chapter IV and setting parameter B to 1 and to 1.63 are also included.

With the $3p_z-$ and 4s-derived MOs moved from the active space into the active core, the $1^1\Sigma_g^+$, $1^5\Sigma_g^+$, and $1^9\Sigma_g^+$ states are all degenerate with $R_e \approx 4.09$ Å, D_e = 0.04 eV, and $\omega_e \approx$ 27 cm^{-1} using the cc-pVTZ basis set. Analysis of the configuration structure of these states' wave functions did not show any dominant electron configurations. For the ground electronic state, 132 CSFs were used at 4.08 Å with amplitudes in the range [0.0698, 0.0944] and obtained an EBO of only 0.01. The ground state PEC with cc-

pVQZ has a somewhat shorter bond length (R_e = 3.83 Å), higher binding energy (D_e = 0.05 eV) and harmonic frequency (ω_e = 30.7 cm^{-1}).

Extrapolation of the ground state PEC to the complete basis set (CBS) limit, using B = 1.63 in Eq. (4.3), gives R_e = 3.40 Å and D_e = 0.09 eV, which are in very good agreement with experiment. However, when B = 1 is used, which proved efficacious for Cr_2 as it did in previous GVVPT2/MCSCF studies [214], the results were only slightly improved (e.g., R_e = 3.7 Å and D_e = 0.06 eV) from the cc-pVQZ values. Although a detailed analysis of extrapolation of GVVPT2/MCSCF energies was not done, additional insight can be gained by a closer examination of the variation in correlation energy with geometry between Cr_2 and Mn_2. Although neither the full CI curves nor restricted Hartree Fock curves are available for Cr_2 and Mn_2, because of computational expense and complete failure of a single determinant function, respectively, and consequently a partitioning of total correlation energy into nondynamic and dynamic contributions cannot be made, it is possible to plot the dynamic correlation energy as a function of internuclear distance (cf. Figure 19). It can be seen that the dynamic correlation energy recovered by GVVPT2 is almost independent of bond length for Mn_2 but varies significantly with changing bond length for Cr_2. Recognizing that correlation is not cleanly divided into dynamic and nondynamic contributions, and that MCSCF includes some correlation that is more appropriately considered dynamic than nondyanmic, Figure 19 supports the supposition that Cr_2 has significantly greater variation in nondynamic correlation than does Mn_2. Considering that Eq. (4.3), describing CBS extrapolation for nondynamic correlation, was initially developed for extrapolation of Hartree Fock (HF)

energies [210, 211], and that one should expect HF-type extrapolation to work best if the fraction of correlation energy within the MCSCF function is roughly independent of internuclear distance, one should expect that Eq. (4.3) will be more efficacious for Mn_2 and that the constant developed for HF (B = 1.63) is reasonable.
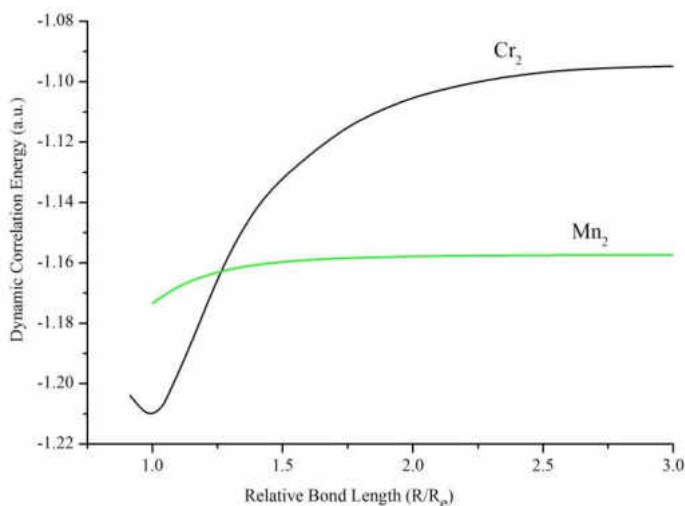
Figure 19. Variation of dynamic correlation energy as a function of relative bond length (R/R_e) for diatomic Cr and Mn. R_e in this case is the bond length at which the dynamic correlation energy is a minimum.

CASE D reference $\kappa(\mathbf{n})$ gave the best results on the investigated states of Mn_2. This model space was verified to allow for coupling of lowest electronic states in a multistate treatment (results of such multistate calculations are not shown here). It seems that inclusion of the $3p_z-$ and/or 4s-derived MOs into the active space for Mn_2 creates more problems than it solves. In CASE D calculations, no discontinuities whatsoever, due to multiple MCSCF solutions, were observed at any geometry. The somewhat long bond lengths (both for Cr_2 and Mn_2) may be due to a choice of a simple zero order Hamiltonian, and possibly that the highest angular momentum functions that could be used were g functions (i.e., $\ell = 4$; N.B. for calculations with cc-pVQZ, the h-functions

123

were neglected). Figure 19 contains PECs of the $X^1\Sigma_g^+$ state of Mn_2 computed using CASE D reference $\kappa(\mathbf{n})$ with ANO-type basis sets (the cc-pVQZ PEC is included for comparison). The data describing the curves are given in Table 9 together with reference experimental values.
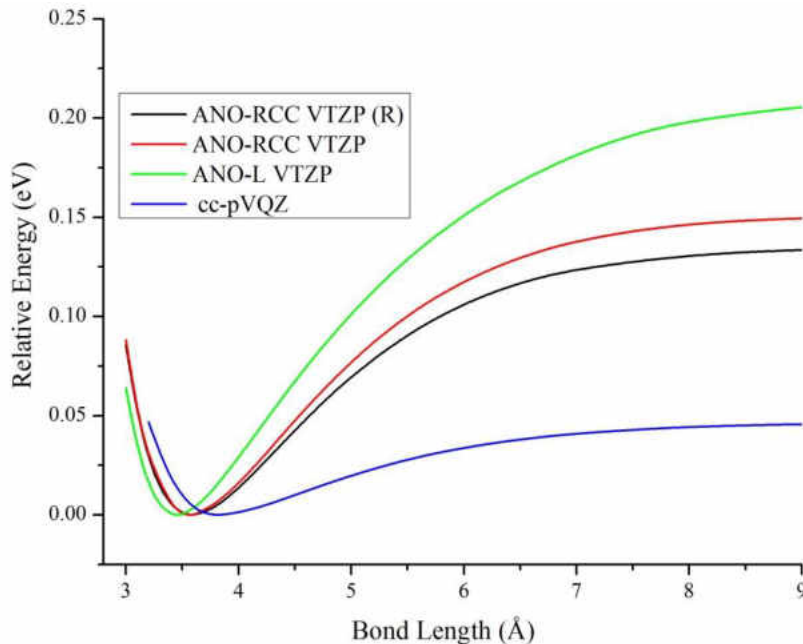
Figure 20. PECs of the $X^1\Sigma_g^+$ state of Mn_2 computed with the basis sets shown in the inset using CASE D partitioning of the active space. ANO-RCC VTZP (R) refers to a relativistic calculation using ANO-RCC VTZP.

Table 9. Equilibrium distances (R_e), binding energies (D_e), and harmonic frequencies (ω_e) of the $X^1\Sigma_g^+$ state of Mn_2 calculated at the GVVPT2 level of theory, using the indicated basis sets, compared with experimental results.

Method	Basis set	R_e (Å)	D_e (eV)	ω_e(cm^{-1})
GVVPT2	cc-pVQZ	3.83	0.05	30.7
GVVPT2	ANO-L VTZP	3.45	0.21	31.4
GVVPT2	ANO-RCC VTZP	3.57	0.15	27.2
GVVPT2	ANO-RCC VTZP (R)	3.59	0.13	25.7
Experiment		3.40[a]	0.02-0.15[b]	68.10[c]

[a]Ref. [237], [b]Ref. [236], [c]Ref. [235].

As shown in Figure 20 and Table 9, the ANO-type basis sets lead to better bond lengths and bond energies than the cc-pVQZ basis (which gave the best results when Dunning-type basis sets were used). It is seen that when relativistic effects were included in the calculations that used the ANO-RCC VTZP basis set, a slight elongation in the bond length was observed (0.02 Å). This slight increase in bond length may be explained by noting that the antiferromagnetic coupling in ground state Mn_2 involves mainly 3d electrons while the 4s electrons are essentially nonbonding. Since relativistic effects expand d and f orbitals, it seems plausible that including such effects in the calculations of the $X^1\Sigma_g^+$ state of Mn_2 should extend the bond length (which is described mainly in terms of d-orbital couplings). However, the present results suggest that relativistic effects are minimal in the Mn_2 molecule.

Electronic States of Tc_2

The PECs obtained for the $X^3\Sigma_g^-$, $1^{11}\Sigma_g^-$, $1^1\Sigma_g^+$, $1^5\Sigma_g^+$ and $1^9\Sigma_g^+$ states of Tc_2 are shown in Figures 21 and 22 and the data describing the curves feature in Table 10. Relativistic GVVPT2 results are therein compared with results from other methods where available. Unlike Mn_2 with a $X^1\Sigma_g^+$ ground state, the ground state of Tc_2 was found to be $^3\Sigma_g^-$ as was observed also by e.g., Yanagisawa et al. [152] and Borin et al. [230]. This state was found to be strongly bound, with a binding energy (De = 3.50 eV) comparable to experimental results (i.e., 2.93-3.49 eV).
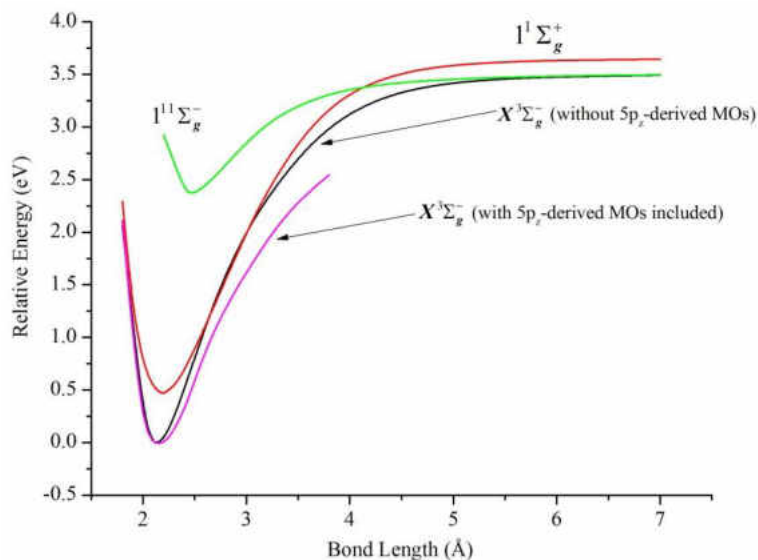
Figure 21. PECs of the $X^3\Sigma_g^-$, $1^{11}\Sigma_g^-$, and $1^1\Sigma_g^+$ states of Tc_2 computed at the sf-X2C relativistic GVVPT2 level of theory using the aug-cc-pVTZ-DK basis set. $5p_z-$ dominated MOs were included in the active space only in the case of the partial $X^3\Sigma_g^-$ curve (magenta curve). But for this magenta curve, all other energies were plotted relative to the lowest energy value of the $X^3\Sigma_g^-$ ground state.

At the equilibrium geometry (2.13 Å), the leading configuration for the $X^3\Sigma_g^-$ term was found to be

$$4d_{xz}\pi_u^2\,4d_{xz}\pi_g^{*1}\,4d_{yz}\pi_u^2\,4d_{yz}\pi_g^{*1}\,4d_{z^2}\sigma_g^2\,5s\sigma_g^2\,4d_{x^2-y^2}\delta_g^2\,4d_{xy}\delta_g^2 \qquad (5.9)$$

Which is similar to that obtained by Klyagina et al. [259] (see (5.1)) and to the average orbital occupations by Borin et al. [230]

$$8\sigma_g(d\sigma)^{1.89}2\delta_g(d\delta)^{3.79}9\sigma_g(5s)^{1.91}5\pi_u(d\pi)^{3.78}8\sigma_u^*(d\sigma)^{0.12}\ \times$$
$$2\delta_u^*(d\delta)^{2.19}9\sigma_u^*(5s)^{0.09}5\pi_g^*(d\pi)^{0.23} \qquad (5.10)$$

all suggesting a quintuple bond. At Re = 2.13 Å, 61 CSFs were used with weights in the range [0.001, 0.306] to compute an EBO of 3.65 for the $X^3\Sigma_g^-$ state of Tc_2. Relativistic

effects, which are expected to slightly contract the s and p while expanding the d and f atomic orbitals, imply that the 4d and 5s orbitals of Tc could have about the same spatial extent and could both be involved in bonding (N.B. the $5s \rightarrow 5d$ excitation energy is only 0.41 eV [222]). At the (scalar relativistic) CASSCF/CASPT2 level [230], the $X^3\Sigma_g^-$ state had R_e = 1.94 Å and $\omega_e = 492.0\,\text{cm}^{-1}$. At the GVVPT2 level, the values R_e = 2.13 Å and $\omega_e = 336.6\,\text{cm}^{-1}$ were obtained.

Consideration of a larger active space including $5p_z$−dominated MOs did not appear to change the PEC of the $X^3\Sigma_g^-$ state qualitatively in the chemically important region of the curve (Figure 21). Such expensive calculations involved a total space dimension of as large as 232,091,673,238 CSFs.

The $1^1\Sigma_g^+$ state of Tc_2 was found in the GVVPT2 study to be 0.47 eV less stable than the $X^3\Sigma_g^-$ state around the equilibrium geometry and had R_e = 2.21 Å, ω_e = 244.07 cm^{-1} and D_e = 2.82 eV with the cc-pVTZ-DK basis set and R_e 2.19 Å, ω_e = 253.92 cm^{-1} and D_e = 3.18 eV with the aug-cc-pVTZ-DK basis. The configurational structure of the $1^1\Sigma_g^+$ state was found to be extremely mixed to the extent that the leading configuration (at 2.18 Å),

$$4d_{xz}\pi_u^2\, 4d_{yz}\pi_u^2\, 4d_{z^2}\sigma_g^2\, 4d_{z^2}\sigma_u^{*2}\, 5s\sigma_g^2\, 4d_{x^2-y^2}\delta_g^2\, 4d_{xy}\delta_g^2\,, \qquad (5.11)$$

contributed only 0.209 by weight to the overall wave function.

Table 10. Equilibrium distances (R_e), binding energies (D_e), adiabatic transition energies (T_e), and harmonic frequencies (ω_e) of electronic states of Tc_2 calculated using sf-X2C relativistic GVVPT2 compared with results from other methods and from experiment.

Method	Basis Set	R_e(Å)	D_e(eV)	ω_e(cm^{-1})	T_e (eV)
		$X^3\Sigma_g^-$			
DV-X$_\alpha$[a]		1.92			
DFT (BOP)[b]	(23s18p15d4f/9s5p6d2f)	1.97	4.75	512.0	
DFT (B3LYP)[b]	(23s18p15d4f/9s5p6d2f)	1.93	3.15	557.6	
DFT(B88)[b]	(23s18p15d4f/9s5p6d2f)	1.99	1.46	483.5	
MP2[b]	(23s18p15d4f/9s5p6d2f)	Unbound[c]	unbound	unbound	
DFT[d]	slater-type triple ζ	2.01			
CASSCF/CASPT2[e]	ANO-RCC VTZP	1.94	3.30[f]	492.0	
GVVPT2	Aug-cc-pVTZ-DK	2.13	3.50	336.6	
Experiment[i]			3.49[g], 3.45[g], 3.33[g], 2.93[h]		
		$1^{11}\Sigma_g^-$			
DFT (B3LYP)[j]		2.84	2.27	178.52	
GVVPT2	Aug-cc-pVTZ-DK	2.47	1.13	225.1	2.38
		$1^1\Sigma_g^+$			
CASSCF/CASPT2[e]	ANO-RCC VTZP	1.97		450.0	0.22
GVVPT2	cc-pVTZ-DK	2.21	2.82	244.1	
GVVPT2	Aug-cc-pVTZ-DK	2.19	3.18	253.9	0.47
		$1^5\Sigma_g^+$			
GVVPT2	Aug-cc-pVTZ-DK	2.31	2.49	246.9	0.70
		$1^9\Sigma_g^+$			
GVVPT2	Aug-cc-pVTZ-DK	2.69	1.35	235.0	1.84

[a]Ref. [259], [b]Ref. [152], [c]This method rather predicted a ground $^7\Pi_u$ state with R_e = 2.18 Å, D_e = 3.97 eV, and ω_e = 349.3 cm^{-1}, [d]Ref. [260], [e]Ref. [230], [f]After considering spin-orbit coupling effects, [g]Ref. [258], [h]Ref. [259], [i]Values computed from thermodynamic relations using dissociation, vaporization and metal surface enthalpies, [j]Ref. [261].

The weight of this configuration decreased to 0.009 at 4.1 Å, where the leading configuration became

$$4d_{xz}\pi_u^1 \, 4d_{xz}\pi_g^{*1} \, 4d_{yz}\pi_u^1 \, 4d_{yz}\pi_g^{*1} \, 4d_{z^2}\sigma_g^2 \, 4d_{z^2}\sigma_u^{*2} \quad \times$$
$$5s\sigma_g^2 \, 4d_{x^2-y^2}\delta_g^1 \, 4d_{x^2-y^2}\delta_u^{*1} \, 4d_{xy}\delta_g^1 \, 4d_{xy}\delta_u^{*1} \tag{5.12}$$

with a weight of 0.014 only. At 2.18 Å, 67 important CSFs were used to compute the

EBO of the $1^1\Sigma_g^+$ state of Tc_2 and obtained 3.17. This state was also computed using a

larger active space that included $5p_z-$ dominated MOs. As can be seen in Figure 22, the

two PECs, with and without the inclusion of $5p_z-$ dominated MOs into the active space,

are quite similar whereas the larger active space increased the total space dimension from

881,588,512 to 3,704,894,420 CSFs (when using cc-pVTZ-DK).
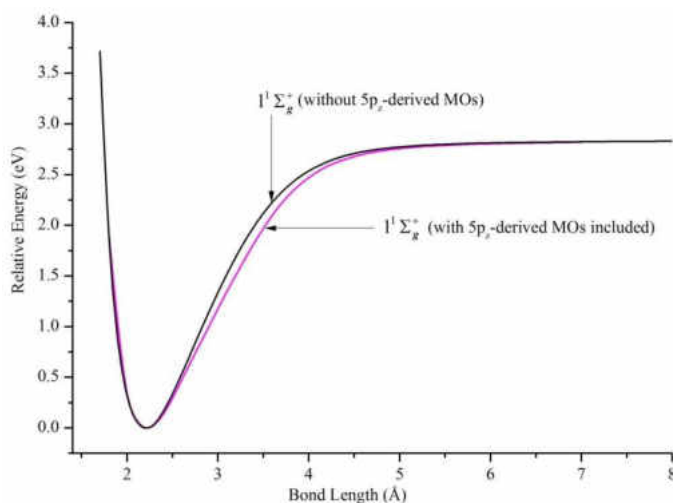
Figure 22. PECs of the $1^1\Sigma_g^+$ state of Tc_2 computed at the sf-X2C relativistic GVVPT2
level of theory using the cc-pVTZ-DK basis set with and without the inclusion
of $5p_z-$ dominated MOs into the active.

Relativistic effects can be seen when not just the binding strengths of Mn_2 and

Tc_2 but also their bond lengths are compared. Taking into account that the atomic radii

of Mn and Tc are close (i.e., 1.40 Å and 1.35 Å, respectively), it is remarkable that the

bond length of the $1^1\Sigma_g^+$ state of Tc_2 is dramatically different (i.e., at least 1.0 Å less)

than that of the $X^1\Sigma_g^+$ state of Mn_2 (Tables 9 and 10).

One DFT study [261] found the spin polarized $1^{11}\Sigma_g^-$ state of Tc_2 to be the ground

term with R_e 2.84 Å, $\omega_e = 178.5$ cm^{-1} and $D_e = 2.27$ eV. In the present calculations, this

state was found to lie as far as 2.38 eV above the ground state (at the equilibrium

geometry) and had R_e 2.47 Å, $\omega_e = 225.1$ cm^{-1} and $D_e = 1.13$ eV. At a bond length of 2.48

Å, this state was described by two leading configurations:

$$
\begin{aligned}
&4d_{xz}\pi_u^2\,4d_{xz}\pi_g^{*1}\,4d_{yz}\pi_u^2\,4d_{yz}\pi_g^{*1}\,4d_{z^2}\sigma_g^1\,4d_{z^2}\sigma_u^{*1}\ \times\\
&5s\sigma_g^1\,5s\sigma_u^{*1}\,4d_{x^2-y^2}\delta_g^1\,4d_{x^2-y^2}\delta_u^{*1}\,4d_{xy}\delta_g^1\,4d_{xy}\delta_u^{*1}
\end{aligned}
\tag{5.13}
$$

and

$$
\begin{aligned}
&4d_{xz}\pi_u^1\,4d_{xz}\pi_g^{*2}\,4d_{yz}\pi_u^1\,4d_{yz}\pi_g^{*2}\,4d_{z^2}\sigma_g^1\,4d_{z^2}\sigma_u^{*1}\ \times\\
&5s\sigma_g^1\,5s\sigma_u^{*1}\,4d_{x^2-y^2}\delta_g^1\,4d_{x^2-y^2}\delta_u^{*1}\,4d_{xy}\delta_g^1\,4d_{xy}\delta_u^{*1}
\end{aligned}
\tag{5.14}
$$

with weights of 0.669 and 0.121, respectively. At this geometry, the EBO was 0.694.

These configurations continued to be the leading ones with their weights becoming equal

at elongated bond lengths.

Figure 23 contains the PECs of the $1^1\Sigma_g^+$, $1^5\Sigma_g^+$, and $1^9\Sigma_g^+$ states of Tc_2 obtained

at the sf-X2C relativistic GVVPT2 level of theory. Though the same states are virtually

degenerate in the case of Mn_2 (see Figure 18), a relativistic treatment of Tc_2 shows

them to be significantly nondegenerate, the $1^5\Sigma_g^+$ and $1^9\Sigma_g^+$ states being found to be 0.70

eV and 1.84 eV less stable than the $1^1\Sigma_g^+$ state, respectively.

The calculations performed on $1^5\Sigma_g^+$ and $1^9\Sigma_g^+$ states of Tc_2 seem to be the first reported. The leading configuration of the $1^5\Sigma_g^+$ state is

$$4d_{xz}\pi_u^2\,4d_{yz}\pi_u^2\,4d_{z^2}\sigma_g^2\,4d_{z^2}\sigma_u^{*2}\,5s\sigma_g^2\,4d_{x^2-y^2}\delta_g^1\,4d_{x^2-y^2}\delta_u^{*1}\,4d_{xy}\delta_g^1\,4d_{xy}\delta_u^{*1}, \qquad (5.15)$$

with a weight of 0.257 at 2.31 Å. This weight decreased to 0.009 at 5.0 Å where the leading configuration was the same as that reported at 4.10 Å for the $1^1\Sigma_g^+$ state (i.e., (5.12)) and had a weight of only 0.012. Using 99 CSFs with amplitudes in the range [0.100, 0.507], an EBO of 0.87 was computed at 2.68 Å for the $1^5\Sigma_g^+$ state of Tc_2.
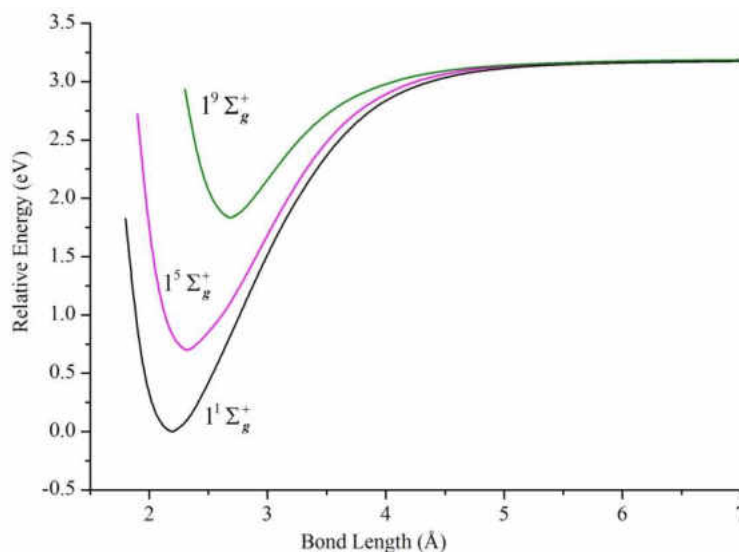
Figure 23. PECs of the $1^1\Sigma_g^+$, $1^5\Sigma_g^+$, and $1^9\Sigma_g^+$ states of Tc_2 computed at the sf-X2C relativistic GVVPT2 level of theory using the aug-cc-pVTZ-DK basis set. The energies are plotted relative to the lowest energy value of the $1^1\Sigma_g^+$ state.

The leading configuration for the $1^9\Sigma_g^+$ state of Tc_2 was again configuration (5.12) reported above for the $1^1\Sigma_g^+$ state at 4.10 Å. This configuration had a weight of 0.694 for the $1^9\Sigma_g^+$ state at 2.68 Å. This weight decreased to only 0.114 at 4.7 Å where 10 important configurations were found to be of nearly equal weights. At 2.68 Å and using

10 CSFs with amplitudes in the range [0.081, 0.833], the EBO was computed to be 0.87 for the $1^9\Sigma_g^+$ state of Tc_2.

Conclusions

This Chapter discussed studies done on the low-lying electronic states of the Mn_2 and Tc_2 molecules using the GVVPT2 method. Only calculations of the ground state ($X^1\Sigma_g^+$) of Mn_2, using the ANO-RCC VTZP, considered scalar relativistic corrections through the sf-X2C method which was described in Chapter II. Since such corrections did not prove to be important for this state of Mn_2, they were ignored in subsequent calculations of its excited states. On the other hand, all calculations of states of Tc_2 included relativistic corrections. The study revealed that although Mn_2 and Tc_2 are isovalent, there are significant differences in their chemistry. For example, the ground states of these molecules are different not only in terms of symmetry ($X^1\Sigma_g^+$ versus $X^3\Sigma_g^-$) but also in terms of bond strength ($D_e \approx 0.10$ eV versus 3.45 eV) and bond length ($R_e \approx 3.5$ Å versus 2.1 Å). Moreover, whereas the $1^1\Sigma_g^+$, $1^5\Sigma_g^+$, and $1^9\Sigma_g^+$ states of Mn_2 were found to be quasidegenerate (Figure 18), the same states were significantly nondegerate in the case of Tc_2 (Figure 23). These differences may be explicable in terms of relativistic effects which are stronger in Tc than in Mn. Such effects contract the 5s orbitals of Tc and simultaneously expand the 4d orbitals such that these orbital sets become of similar spatial extents and possibly contribute together to form strong bonds. Contrarily, weak relativistic effects in Mn do not lead to such changes. Moreover, the $3d \leftarrow 4s$ electron excitation energy in Mn is too high (2.14 eV whereas in Tc, it is only

0.14 eV [222]) such that the 4s orbitals remain virtually doubly occupied in the Mn_2

molecule. Since these outer doubly occupied orbitals are repulsive, the bonds in Mn_2 are

consequently very weak. Despite having different spatial extents of its 3d and 4s orbitals

just as in Cr_2, the Mn_2 PECs do not have an outer shelf as was the case with the $1\,^1\Sigma_g^+$

and $1\,^3\Sigma_u^+$ states of Cr_2, possibly due to the lack of full participation of the 4s orbitals of

Mn_2 in bond formation.

The calculations of states of Mn_2 emphasized the importance of selecting the

right set of MOs to define the active space and properly partitioning these MOs to give

correct reference $\kappa(\mathbf{n})$s. Including either $3p_z -$ or 4s-derived MOs into the active space

of Mn_2 unnecessarily increased the dimension of the active space and, more importantly,

introduced multiple MCSCF solutions at certain geometries. Moreover, obtaining correct

dissociation degeneracies required the use of proper reference spaces. The study revealed

that a good description of the interaction of Mn atoms in Mn_2 can be achieved with an

active space of ten 3d-derived MOs with ten active electrons while correlating the 3s, 3p

and 4s electrons at the GVVPT2 level of theory.

In contrast to a 2001 MP2 study [152] that predicted the ground state of Tc_2 to

be $^7\Pi_u$, a 2004 DFT study [261] that found a $1\,^{11}\Sigma_g^-$ ground state, and in corroboration of

a 2009 CASPT2 study [230] that predicted a $^3\Sigma_g^-$ ground state, sf-X2C GVVPT2

calculations predict a $^3\Sigma_g^-$ ground state (R_e = 2.13 Å, D_e = 3.50 eV, and ω_e = 336.6 cm^{-1})

with a low-lying (0.47 eV) $^1\Sigma_g^+$ state (R_e = 2.19 Å, D_e = 3.18 eV, and ω_e = 253.9 cm^{-1}).

Although the 2009 CASPT2 study showed strong spin-orbit induced mixing between the

$^3\Sigma_g^-$ and $^1\Sigma_g^+$ states, the spectroscopic constants they obtained from the spin-free PECs did not change much with inclusion of spin-orbit coupling corrections. On comparison of spin-free PECs, the present calculations suggest a somewhat longer (ca. 0.15 Å) and broader (ca. 100 cm^{-1}) minimum. Whether this is due to treatment of correlation (including choice of H_0) or some other effect remains to be determined. The energy ordering that was found for the $^3\Sigma_g^-$ and $^1\Sigma_g^+$ states of Tc_2 is the same as that reported in the 2009 CASPT2 study [230].

The calculations of the $1^5\Sigma_g^+$ and $1^9\Sigma_g^+$ states of Tc_2 are apparently the first studies of these states. The states were found to be strongly bound ($D_e = 2.49$ eV and 1.35 eV), with the quintet state being more strongly bound than Cr_2 in its ground state ($De \approx$ 1.56 eV). In all, it is expected that GVVPT2 characterization of the low-lying electronic states of Tc_2 will facilitate the up-to-now unknown experimental results and assist with identifying potentially interesting targets for more computationally intensive methods such as MRCISD and CCSD(T).

CHAPTER VI

GVVPT2 STUDIES OF LOW-LYING ELECTRONIC STATES OF NICKEL DIMER

Introduction

This Chapter reports studies of low-lying electronic states of Ni_2, obtained with the generalized Van Vleck second order multireference perturbation theory (GVVPT2) method. These studies were the first to be performed using GVVPT2. Nickel has a ground atomic term of $^3F_4 (3d^8 4s^2)$ and an excitation energy of only 0.025 eV to the first excited $^3D_3 (3d^9 4s^1)$ term, which is the least in the first row of transition elements [221]. Moreover, the $^3F_4 (3d^8 4s^2) \rightarrow {}^3D_3 (3d^9 4s^1)$ excitation energy has been determined by at least one experimental study [264] to be negative (-0.029 eV). This negative value has been corroborated by ab initio wave function and density functional theory (DFT) calculations [265, 266]. A recent study [267] that employed several functionals at all five rungs of Jacob's ladder of DFT functionals predicted the ground state configuration of the Ni atom as $3d^9 4s^1$ ($^3D_3$) with most of the functionals when using a triple-ζ quality basis set. On the other hand, other theoretical studies [268, 269] have predicted a $3d^8 4s^2$ ($^3F_4$) ground state configuration for the Ni atom while Upton and Goddard III [270] stated that averaging over J components (where J is the sum of spin and orbital angular momenta of the atom) of each state does place the $^3D_3 (3d^9 4s^1)$ state slightly lower energetically than the $^3F_4 (3d^8 4s^2)$ state.

These analyses suggest complications involved in studies of low-lying electronic states of Ni compounds. The low excitation energy between the $^3F_4(3d^84s^2)$ and $^3D_3$ $(3d^94s^1)$ atomic terms indicates the likelihood of the importance of several electronic states of the Ni_2 dimer that result from the $^3F_4 + {}^3F_4$, $^3F_4 + {}^3D_3$, and $^3D_3 + {}^3D_3$ atomic combinations. However, since the fully filled 4s-subshell of the $^3F_4(3d^84s^2)$ ground state of Ni possibly discourages significant bonding interaction (just as was the case with Mn), it seems plausible that bonding in low-lying states of Ni_2 should result largely from the coupling of excited state $(^3D_3)$ Ni atoms. In particular, the lowest states of the Ni_2 molecule might be expected to correlate with the $^3D_3(3d^94s^1)$ + $^3D_3(3d^94s^1)$ dissociation channel. The present studies of Ni_2 considered the different couplings of the Ni atoms $(^3F_4 + {}^3F_4$, $^3F_4 + {}^3D_3$, and $^3D_3 + {}^3D_3$). Before getting to GVVPT2 studies, a brief review of previous experimental and theoretical work on this molecule would be provided in the reminder of the present subsection. The subsequent subsection discusses details on how calculations were done; a third subsection presents and discusses results; while a final subsection summarizes the current findings.

Previous Studies of Ni_2

As already noted above, theoretical studies of the electronic states of Ni_2 are complicated by the presence of many low-lying quasidegenerate electronic states. For example, limited configuration interaction (CI) calculations [17] found 84 states of Ni_2, corresponding to the $^3F_4 + {}^3F_4$ dissociation limit, to lie within an energy range of only 300 K (0.026 eV) and 45 states within a narrow energy gap to correlate with the $^3D_3 +$

$^3D_3$ dissociate asymptote. At the generalized valence bond (GVB) and polarization CI (POL-CI) level of theory [270], 30 of these 45 states of the $^3D_3 + {}^3D_3$ dissociation channel were found to be singlets and triplets ordered energetically as

$$\delta\delta(6 \text{ states}) < \pi\delta(8 \text{ states}) < \delta\sigma(4 \text{ states}) < \pi\pi(6 \text{ states}) < \pi\sigma(4 \text{ states}) < \sigma\sigma(2 \text{ states}) \quad (6.1)$$

with the six lowest states ($^1\Gamma_g$, $^1\Sigma_g^+$, $^3\Sigma_g^-$, $^1\Sigma_u^-$, $^3\Gamma_u$, $^3\Sigma_u^+$) being virtually degenerate and having an average equilibrium bond length, R_e, of 2.04 Å, and binding energy, D_e, of 2.29 eV (N. B. The designations $\delta\delta$, $\pi\delta$, etc., in (6.1) define the positions of the holes in the 3d-orbitals at each atomic center with $3d^9 4s^1$ configuration). Melius et al. [271] also noted that the manifold of electronic states within 0.50 eV of the ground state of Ni_2 was dense and complex.

Being an electron rich system, one would expect theoretical studies on Ni_2 to be less complicated than for other first row transition metal dimers like Cr_2 where there are many more possibilities of distributing 12 electrons in 12 orbitals. Information in the literature on Ni_2, however, proves the contrary. For example, the exact symmetry of the ground electronic state of Ni_2 is uncertain. Different studies have reported different space and spin symmetries for the molecule's ground term. One of the earliest theoretical studies [272] on Ni_2 employed the extended Hückel molecular orbital method and found a $^3\Sigma_g^-$ ground state with configuration

$$3d_{x^2-y^2}\delta_g^2 3d_{x^2-y^2}\delta_u^{*2} 3d_{xy}\delta_g^2 3d_{xy}\delta_u^{*2} 3d_{xz}\pi_u^2 3d_{xz}\pi_g^{*1} 3d_{yz}\pi_u^2 3d_{yz}\pi_g^{*1} 3d_{z^2}\sigma_g^2 3d_{z^2}\sigma_u^{*2} 4s\sigma_g^2 \quad (6.2)$$

and with $R_e = 2.21$ Å, $\omega_e = 370$ cm^{-1}, and $D_e = 2.45$ eV. Meanwhile a self-consistent field (SCF) scattered-wave (X_α -sw) study [273] found a $^1\Sigma_g^+$ ground term with configuration

$$3d_{x^2-y^2}\delta_g^2 3d_{x^2-y^2}\delta_u^{*2} 3d_{xy}\delta_g^2 3d_{xy}\delta_u^{*2} 3d_{xz}\pi_u^2 3d_{xz}\pi_g^{*2} 3d_{yz}\pi_u^2 3d_{yz}\pi_g^{*2} 3d_{z^2}\sigma_g^2 4s\sigma_g^2 \qquad (6.3)$$

whereas the generalized valence bond (GVB) method [271] also predicted a $^1\Sigma_g^+$ ground state for Ni_2 but with configuration

$$3d_{x^2-y^2}\delta_g^2 3d_{x^2-y^2}\delta_u^{*1} 3d_{xy}\delta_g^2 3d_{xy}\delta_u^{*1} 3d_{xz}\pi_u^2 3d_{xz}\pi_g^{*2} 3d_{yz}\pi_u^2 3d_{yz}\pi_g^{*2} 3d_{z^2}\sigma_g^2 3d_{z^2}\sigma_u^{*2} 4s\sigma_g^2 \qquad (6.4)$$

A limited CI study [17], which explored a variety of states of Ni_2 resulting from the $^3F_4 + {}^3F_4$ and $^3D_3 + {}^3D_3$ atomic combinations, found the ground term to be $^1\Sigma_g^+$ with the same configuration as was reported in Ref. [271]. The states $^1\Gamma_g$ and $^1\Sigma_u^-$ were reported to be in close proximity to the $^1\Sigma_g^+$ state in the CI study. Different theoretical studies found the six lowest $\delta\delta-$hole states ($^1\Gamma_g$, $^1\Sigma_g^+$, $^3\Sigma_g^-$, $^1\Sigma_u^-$, $^3\Gamma_u$, $^3\Sigma_u^+$) of Ni_2, resulting from the $^3D_3 + {}^3D_3$ atomic coupling, to be quasidegenerate [274-276]. Using an effective core potential basis set specifically optimized for the Ni atom in the $^3D_3$ state, Noell et al. [275] found the splitting of the six $\delta-$hole states of Ni_2 to be quite small (≤ 0.1 eV) using the generalized valence bond CI (GVBCI) method; the lowest states being $^1\Gamma_g$ and $^1\Sigma_g^+$. However, inclusion of polarization configurations involving single and double excitations to the virtual space (POLSDCI) placed the triplet states ($^3\Sigma_g^-$, $^3\Gamma_u$, $^3\Sigma_u^+$) at approximately 0.07 eV below the singlets. At the singles and doubles CI (SDCI) level of theory, these authors found the energy splitting of the six lowest $\delta\delta-$hole states

138

of Ni_2 to be less than 0.009 eV with an average bond length of 2.26 Å and binding

energy of 1.88 eV. With a basis set similar to that used by Noell et al. [275], a $^3\Sigma_u^+$

ground state was predicted for Ni_2 at the RHF and CISD levels of theory, with the CISD

result giving spectroscopic data: R_e = 2.33 Å, ω_e = 211 cm^{-1}, and D_e = 1.43 eV [276].

Calculations by these authors at the same levels of theory using an all electron basis set

maintained the ground state symmetry as $^3\Sigma_u^+$. On the other hand, a local spin density

method [277] predicted a $^3\Sigma_g^-$ ground state with R_e = 2.18 Å, ω_e = 320 cm^{-1}, and D_e =

2.70 eV. A CASSCF/CASPT2 study [278], that used an atomic natural orbital (ANO)

type contraction of the primitive (21s15p10d6f4g) basis to give [6s5p4d3f2g] for

calculations without the correlation of the semi core 3s3p electrons and [10s9p8d3f2g]

for calculations involving the correlation of 3s3p electrons, also concluded the six lowest

$\delta\delta-$hole states of Ni_2 to lie within a narrow energy gap (0.04 eV) with the triplet states

higher in energy than the singlets. After inclusion of scalar relativistic effects in the

CASPT2 study, the ground term was found to be $^1\Gamma_g$, with the $^1\Sigma_g^+$ term lying only 0.01

eV higher at the equilibrium geometry. Correlating the 3s3p electrons in these

calculations slightly improved the bond lengths and binding energies of the six lowest

$\delta\delta-$hole states, whereas the competing $^1\Gamma_g$ and $^1\Sigma_g^+$ lowest states became degenerate

with spectroscopic constants: R_e = 2.23 Å, D_e = 2.06 eV, and ω_e = 293 cm^{-1} compared

with experimental values of R_e = 2.1545 ± 0.0004 Å [279], D_0^o = 2.042 ± 0.002 eV

[279], and ω_e = 280 ± 20 cm^{-1} [280]. Some of the most recent wave function based

calculations of Ni_2 include those due to Dong et al. [281], using the symmetry-adapted-

cluster configuration interaction (SAC-CI) method, and Cheskidov et al. [282], using the

average coupled pair functional (ACPF), average quadratic coupled cluster (AQCC), internally contracted single and double multireference configuration interaction (MRCI or MRCI + Q with Davidson corrections), and N-electron valence state second-order perturbation theory (NEVPT2) methods. The study by Dong et al. [281] predicted a B_{1u} ground state (with R_e = 2.56 Å) for Ni_2 in D_{2h} symmetry which corresponds to $^3\Sigma_u^+$, $^3\Delta_u$, or $^3\Gamma_u$ in $D_{\infty h}$. The study by Cheskidov et al. [282] used the Dunning-type quadruple-ζ quality basis set, cc-pVQZ-DK (22s18p11d3f2g1h/[8s7p6d3f2g1h]) [283], and found the $^1\Gamma_g$ and $^1\Sigma_g^+$ $\delta\delta-$ hole states of Ni_2 to be quasidegenerate for all five methods, with the $^1\Sigma_g^+$ state lying lower when using AQCC, MRCI + Q, and MRCI methods and the two states fully degenerate at the ACPF and NEVPT2 levels. At the ACPF level, the predicted ground state was rather $^1\Sigma_u^-$ while inclusion of spin-orbit relativistic corrections led to an 0_g^+ ground term ($^1\Sigma_g^+$ + $^3\Sigma_g^-$ $\delta\delta-$ states) whereas the 0_u^- term $\left(^1\Sigma_u^- + \,^3\Sigma_u^+ \, \delta\delta-\text{states}\right)$ lay at only 0.009 ± 0.004 eV above the ground term.

DFT studies of Ni_2 have been inconclusive. Yanagisawa et al. [284] used different DFT functionals to study the triplet ($^3\Sigma_g^-$ and $^3\Sigma_u^+$) states of Ni_2 and found most of the functionals to predict a $^3\Sigma_g^-$ ground term whereas B3LYP rather predicted $^3\Sigma_u^+$. However, the $^3\Sigma_g^-$ state that they found had a configuration that corresponded to the $\pi\pi-$ holes manifold within the $^3D_3 + \,^3D_3$ atomic combination rather than $\delta\delta$-hole states as most of the reported results from studies by wave function methods. Gutsev et al. [151] also found a $^3\Sigma_g^-$ ground state with the same configuration as did Yanagisawa et al.

[284] when using different hybrid functionals. Contrarily, Diaconu et al. [285] found a singlet $\delta\delta-$hole ground state (a mixture of $^1\Gamma_g$ and $^1\Sigma_g^+$) for Ni_2 when using B3LYP with the basis set (14s11p6d3f)/[8s6p4d1f] whereas the Stuttgart RSC ECP basis set [286] with the same functional gave a triplet $\pi\delta-$state (mixture of $^3\Sigma_g^-$ and $^3\Gamma_u$) that lay 0.001 eV lower than the singlet $\delta\delta-$hole term at the equilibrium geometry. The Perdew-Burke-Ernzerhof (PBE) exchange correlation (XC) functional also predicted [287] a $^3\Sigma_g^-$ ground state for Ni_2 with spectroscopic constants that showed significant deviations from experimental values (R_e = 2.93 Å, D_e = 3.09 eV, and ω_e = 334.08 cm^{-1} compared to experimental values of R_e = 2.1545 ± 0.0004 Å [279], D_0° = 2.042 ± 0.002 eV [279], and ω_e = 280 ± 20 cm^{-1} [280]). Using functionals at all levels of Jacob's ladder of DFT functionals, Schultz et al. [268] found different functionals to predict different ground state symmetries for Ni_2; all local spin density approximation (LSDA) functionals predicted a $^3\Sigma_g^-$ ground state, all generalized gradient approximation (GGA) and meta GGA functionals predicted a $^3\Pi_u$ ground term, whereas the hybrid GGA and hybrid meta GGA functionals tested found either the $^3\Sigma_u^+$ or $^3\Sigma_g^-$ term to be the ground term. Meanwhile Du et al. [288] also used different functionals to study low-lying states of Ni_2. Their best results were obtained when using BLYP that predicted a triplet $\sigma\delta-$hole $\left(3d_{z^2}\sigma_u^{*1}3d_{x^2-y^2}\delta_u^{*1}\right)$ ground term. The space symmetry of this state was not reported. With the B3P86 functional, a quintet ground state was predicted for Ni_2 without specifying the space symmetry [289].

Experimental data on Ni_2 is sparse and the true ground term of the molecule is not unequivocally known experimentally. From the analysis of electronic absorption bands of Ni_2 in the visible spectral region in argon matrices, De Vore et al. [290] determined $\omega_e = 192$ cm^{-1} whereas a frequency of 380.9 cm^{-1} was found in solid argon matrix [291]. The latter result was later criticized by Rasanen et al. [292]. In photoelectron spectroscopic studies of Ni_2^-, $\omega_e = 280 \pm 20$ cm^{-1} was determined for the lowest electronic state of Ni_2 [280]. Second and third law analyses of information derived from a combination of Knudsen effusion and mass-spectrometric techniques led to a binding energy of $D_0^o = 2.03 \pm 0.30$ eV (second law result) and $D_0^o = 2.36 \pm 0.22$ eV (third law result) for ground state Ni_2 [293]. By using time-delayed resonant two-photon ionization, Morse et al. [294] determined $D_0^o = 2.068 \pm 0.010$ eV and $R_e = 2.200 \pm 0.007$ Å for the lowest state of Ni_2, assigned as either $^3\Gamma_u$ or $^1\Gamma_g$. Also from two-photon ionization studies on supersonic jet-cooled Ni_2 in argon carrier gas, Pinegar et al. [279] determined $D_0^o = 2.042 \pm 0.002$ eV and $R_e = 2.1545 \pm 0.0004$ Å for the lowest state of Ni_2 but were unable to ascertain the symmetry of this state.

The above analysis of previous work on Ni_2 reveals challenges involved in studies of electronic states of the molecule. The reviewed literature clearly shows conflicting results on the low-lying electronic states of Ni_2. Although many wave function methods have tended to favor $\delta\delta-$hole states ($^1\Gamma_g$, $^1\Sigma_g^+$, $^3\Sigma_g^-$, $^1\Sigma_u^-$, $^3\Gamma_u$, $^3\Sigma_u^+$) as lying lowest energetically, those methods predicted different ground state symmetries with some finding all six states to be degenerate. As shown, spectroscopic data have been

obtained experimentally for Ni_2 but most of the experimental studies could not ascertain the ground state symmetry of the molecule. Due to these uncertainties and given that the GVVPT2 method demonstrated remarkable success at describing electronic states of other complicated transition metal molecules, such as Cr_2 and Y_2, the low-lying states of Ni_2 have been studied using GVVPT2. It should be noted that of all previous theoretical work cited above on electronic states of Ni_2, less than seven of the articles reported full PECs of the states they investigated. This Chapter reports full PECs of 21 states of Ni_2 constructed at the GVVPT2 level of theory. The curves are smooth and void of wiggles. The next subsection presents details on how the calculations were done.

Computational Details

Macroconfigurations ($\kappa(\mathbf{n})$s) [22] were used in the construction of MCSCF and then GVVPT2 wave functions. The active space used to specify reference $\kappa(\mathbf{n})$s consisted of 3d and 4s-derived molecular orbitals (MOs) of Ni. Depending on the specific state being investigated, some of the 3d-derived MOs and/or 4s-derived MOs that were restricted to be doubly occupied were included with the 3s- and 3p-derived MOs in the active core and their electrons only correlated at the GVVPT2 level of theory. For example, in all calculations of $\delta\delta-hole$ states, the $3d\sigma$ and $3d\pi$ MOs were placed in the active core and only correlated at the GVVPT2 level. Similarly, the $3d\sigma$ and $3d\delta$ electrons were frozen in MCSCF calculations of $\pi\pi-hole$ states while only the $3d\sigma$ electrons were frozen in MCSCF calculations of $\delta\pi-hole$ states, whereas the $4s\sigma$ or $4s\sigma+3d\pi$ or $4s\sigma+3d\sigma$ electrons were frozen in MCSCF calculations on states within the $^3F_4(3d^8 4s^2) + {}^3F_4(3d^8 4s^2)$ dissociation channel. The remaining orbitals in the active

space were partitioned into reference $\kappa(\mathbf{n})$s leading to configurations that describe $\delta\delta-$, $\delta\pi-, \delta\sigma-, \pi\pi-, \pi\sigma-, \text{or } \sigma\sigma-\text{states}$ from the $^3D_3(3d^94s^1)+{}^3D_3(3d^94s^1)$ atomic combination or configurations that describe $^3D_3(3d^94s^1)+{}^3F_4(3d^84s^2)$ and $^3F_4(3d^84s^2)+{}^3F_4(3d^84s^2)$ atomic couplings (N.B. $\delta\delta-, \delta\pi-, \delta\sigma-, \pi\pi-, \pi\sigma-, \text{or } \sigma\sigma-$ specifies the positions of the holes within the manifold of 3d-derived MOs for the studied states).

All $\delta\delta-\text{states}$ were computed using one reference $\kappa(\mathbf{n})$

$$\left(3d_{x^2-y^2}\delta_g 3d_{x^2-y^2}\delta_u^* 3d_{xy}\delta_g 3d_{xy}\delta_u^*\right)^6\left(4s\sigma_g 4s\sigma_u^*\right)^2 \tag{6.5}$$

where the superscripts denote the number of electrons in each orbital group. The semi core 3s3p electrons were correlated together with those of $3d_{z^2}, 3d_{xz}$, and $3d_{yz}$ at the GVVPT2 level. For four of the $\delta\delta-\text{states}$, calculations were also performed in which the 3s3p were frozen though out (i.e., at both the MCSCF and GVVPT2 levels). Reference $\kappa(\mathbf{n})$ (6.5) generated: 8 model and 27,891,120 total CSFs for the $1^3\Sigma_u^+$ and $1^3\Gamma_u$ states; 8 model and 15,290,666 total space CSFs for the $1^1\Sigma_u^-, 1^1\Sigma_g^-$, and $1^1\Gamma_u$ states; 10 model and 27,982,592 all space CSFs for the $1^3\Sigma_g^-$ and $1^3\Sigma_u^-$ states; and 12 model versus 15,270,687 all space CSFs for the $1^1\Gamma_g$ and $1^1\Sigma_g^+$ states. Without correlating the 3s3p electrons at the GVVPT2 level, the dimensions were: 12 model versus 3,593,707 total CSFs for the $1^1\Gamma_g$ and $1^1\Sigma_g^+$ states; and 8 model versus 6,434,550 all space CSFs for the $1^3\Sigma_u^+$ and $1^3\Gamma_u$ states. Scalar relativistic calculations on the $1^1\Gamma_g$ and $1^1\Sigma_g^+$ states utilized the same reference $\kappa(\mathbf{n})$ (6.5). A $\delta\delta$ $^3\Gamma_u$ state was computed with only 4 active electrons in 4 orbitals using the reference $\kappa(\mathbf{n})$

$$\left(3d_{x^2-y^2}\delta_g\,3d_{x^2-y^2}\delta_u^*\right)^2\left(4s\sigma_g\,4s\sigma_u^*\right)^2 \tag{6.6}$$

that gave rise to 4 model space and 7518688 all space CSFs.

The $\pi\pi-$ states were computed using a reference $\kappa(\mathbf{n})$ similar to (6.5) but with delta replaced with pi orbitals

$$\left(3d_{xz}\pi_u\,3d_{xz}\pi_g^*\,3d_{yz}\pi_u\,3d_{yz}\pi_g^*\right)^6\left(4s\sigma_g\,4s\sigma_u^*\right)^2 \tag{6.7}$$

This $\kappa(\mathbf{n})$ gave rise to 12 model space and 15,267,629 all space CSFs for the $1^1\Delta_g(\pi\pi)$ and $1^1\Sigma_g^+(\pi\pi)$ states.

The $\delta\pi-$ states were computed from the reference $\kappa(\mathbf{n})$

$$\left(3d_{x^2-y^2}\delta_g\,3d_{x^2-y^2}\delta_u^*\,3d_{xy}\delta_g\,3d_{xy}\delta_u^*\right)^7\left(3d_{xz}\pi_u\,3d_{xz}\pi_g^*\,3d_{yz}\pi_u\,3d_{yz}\pi_g^*\right)^7\left(4s\sigma_g\,4s\sigma_u^*\right)^2 \tag{6.8}$$

Reference $\kappa(\mathbf{n})$ (6.8) led to 16 model space and 27,178,852 total space CSFs for the $1^1\Phi_g(\delta\pi)$ and $1^1\Pi_g(\delta\pi)$ states versus 20 model and 50,736,846 all space CSFs for the $1^3\Phi_g(\delta\pi)$ and $1^3\Pi_g(\delta\pi)$ states.

The $1^1\Sigma_g^+(G:\delta^2\pi^2)$, $1^3\Sigma_g^+(G:\delta^2\pi^2)$, $2^3\Sigma_g^+(G:\delta^2\pi^2)$, $1^3\Delta_u(G:\delta^2\pi^2)$, and $1^3\Sigma_u^+(G:\delta^2\pi^2)$ states (where G is used to denote that the states are derived from the coupling of ground state Ni atoms ($^3F_4 + \,^3F_4$) while superscript 2 implies that two holes of each type exist in the configurations describing the wave functions) were computed using the reference $\kappa(\mathbf{n})$

$$\left(3d_{x^2-y^2}\delta_g\,3d_{x^2-y^2}\delta_u^*\,3d_{xy}\delta_g\,3d_{xy}\delta_u^*\right)^6\left(3d_{xz}\pi_u\,3d_{xz}\pi_g^*\,3d_{yz}\pi_u\,3d_{yz}\pi_g^*\right)^6 \tag{6.9}$$

with the 3s, 3p, $3d_{z^2}$, and 4s electrons kept frozen at the MCSCF level but correlated at

the GVVPT2 level of theory. This $\kappa(\mathbf{n})$ resulted in 40 model versus 55,053,638 total

CSFs for the $1^1\Sigma_g^+\left(G:\delta^2\pi^2\right)$ state; 36 model and 103,306,512 all space CSFs for the

$1^3\Sigma_g^+\left(G:\delta^2\pi^2\right)$ and $2^3\Sigma_g^+\left(G:\delta^2\pi^2\right)$ states; and 40 model versus 103,312,902 all space CSFs

for the $1^3\Delta_u\left(G:\delta^2\pi^2\right)$ and $1^3\Sigma_u^+\left(G:\delta^2\pi^2\right)$ states.

Two states $1^1\Gamma_g\left(G:\delta^2\sigma^2\right)$ and $1^1\Sigma_g^+\left(G:\delta^2\sigma^2\right)$ were computed using reference

$\kappa(\mathbf{n})$

$$\left(3d_{x^2-y^2}\delta_g\,3d_{x^2-y^2}\delta_u^*\,3d_{xy}\delta_g\,3d_{xy}\delta_u^*\right)^6\left(3d_{z^2}\sigma_g\,3d_{z^2}\sigma_u^*\right)^2 \tag{6.10}$$

This $\kappa(\mathbf{n})$ generated 12 model space and 15,270,687 all space CSFs for the computed

states.

The states $1^5\Phi_u\left(G:\delta^2\pi\sigma_{3d}\right)$ and $1^5\Pi_u\left(G:\delta^2\pi\sigma_{3d}\right)$ (where $G:\delta^2\pi\sigma_{3d}$ implies that

the configurations describing the states result from coupled ground state Ni atoms (G) in

which there are two $\delta-\text{holes}$, a $\pi-\text{hole}$, and a $\sigma-\text{hole}$ in a $3d_{z^2}$ -derived MO) were

computed using the reference $\kappa(\mathbf{n})$

$$\left(3d_{x^2-y^2}\delta_g\,3d_{x^2-y^2}\delta_u^*\,3d_{xy}\delta_g\,3d_{xy}\delta_u^*\right)^6\left(3d_{xz}\pi_u\,3d_{xz}\pi_g^*\,3d_{yz}\pi_u\,3d_{yz}\pi_g^*\right)^7\left(3d_{z^2}\sigma_g\,3d_{z^2}\sigma_u^*\right)^3 \tag{6.11}$$

This $\kappa(\mathbf{n})$ led to 12 model versus 69,738,914 total CSFs for the computed quintet states.

Lastly, two quintet states within the $^3D_3\,(3d^94s^1)\ +\ ^3F_4\,(3d^84s^2)$ manifold were

investigated at short bond lengths using the reference $\kappa(\mathbf{n})$

$$\left(3d_{x^2-y^2}\delta_g 3d_{x^2-y^2}\delta_u^* 3d_{xy}\delta_g 3d_{xy}\delta_u^*\right)^7 \left(3d_{xz}\pi_u 3d_{xz}\pi_g^* 3d_{yz}\pi_u 3d_{yz}\pi_g^*\right)^6 \left(4s\sigma_g 4s\sigma_u^*\right)^3 \qquad (6.12)$$

Reference $\kappa(\mathbf{n})$ (6.12) generated 12 model versus 69,740,135 total space CSFs that described the $1\,^5\Delta_g\left(GE:\delta\pi^2\sigma_{4s}\right)$ and $2\,^5\Delta_g\left(GE:\delta\pi^2\sigma_{4s}\right)$ states, where $GE:\delta\pi^2\sigma_{4s}$ implies that the configurations describing the states result from the coupling of a ground (G) and an excited (E) state Ni atom in which there is a $\delta-hole$, two $\pi-holes$, and a $\sigma-hole$ in a 4s-derived MO.

All calculations used the Dunning-type cc-pVTZ basis set [153] in D_{2h} symmetry. In MCSCF calculations, the reference $\kappa(\mathbf{n})$s described above were used as the active space while all other electrons were frozen. Initial MOs for MCSCF calculations were obtained from approximate natural orbitals of second-order restricted Møller−Plesset perturbation (RMP2) calculations from a closed-shell Hartree−Fock (HF) reference. At the GVVPT2 level, 3s, 3p, and all 3d and/or 4s electrons not correlated at the MCSCF level were correlated. A few of the GVVPT2 calculations were performed with the 3s and 3p electrons frozen. Calculations that accounted for scalar relativistic effects employed the sf-X2C technique described in Chapter II. Where indicated, the effective bond order (EBO) was computed using Eqs. (3.11) and (3.12) in Chapter III.

Results and Discussion

To distinguish states of the same symmetry which were computed with different reference $\kappa(\mathbf{n})$s, the following notations are used: 3d-derived MOs (and sometimes 4s-derived MOs) that have vacancies are shown in parentheses after the molecular term symbol of the state; uppercase letters G and E are also included in parentheses after the

molecular terms to indicate that ground ($^3D_3$) or excited ($^3F_4$) atoms are coupled in the Ni_2 molecule, respectively. Thus, the state $1^5\Delta_g\left(GE:\delta\pi^2\sigma_{4s}\right)$ involves $^3F_4$ + $^3D_3$ coupled Ni atoms and the configuration of the state involves one hole in the 3d-delta subspace, two holes in the 3d-pi subspace, and one hole in the 4s-sigma subspace of active MOs. The superscripts on the MOs within parentheses accompanying the molecular term symbols would be used to indicate the number of holes of each kind in the configuration. A single G within parentheses, e.g., in $1^5\Phi_u\left(G:\delta^2\pi\sigma_{3d}\right)$, implies $^3F_4$ + $^3F_4$ atomic coupling. The 4s-derived MO subspace has holes for all computed states and these are not indicated except for the $1^5\Delta_g\left(GE:\delta\pi^2\sigma_{4s}\right)$ and $2^5\Delta_g\left(GE:\delta\pi^2\sigma_{4s}\right)$ states. Where parentheses are absent after the molecular term, the state in question belongs to the $\delta\delta$-hole states of the $^3D_3(3d^94s^1) + {}^3D_3(3d^94s^1)$ manifold. Letter "R" in parentheses following the molecular term implies that scalar relativistic effects were included in the calculations while the expression "no 3s3p" within parentheses after a molecular term symbol implies that 3s and 3p electrons were frozen in GVVPT2 calculations.

The $\delta\delta$-Hole States

PECs of the $\delta\delta$-hole states are shown in Figure 24 and the data describing them are in Table 11. In agreement with results from other high level ab initio methods, the lowest states of Ni_2 were found to be $\delta\delta$-hole states of the $^3D_3\left(3d^94s^1\right) + {}^3D_3\left(3d^94s^1\right)$ manifold. In particular, the ground state was found to be $X^1\Gamma_g$ with the $1^1\Sigma_g^+$ state lying only 16.40 cm^{-1} (0.002 eV) higher at the equilibrium geometry. After including scalar relativistic effects, the energy gap between these states slightly increased to 23.39 cm^{-1} at

equilibrium with the $X^1\Gamma_g$ term having spectroscopic constants: $R_e = 2.20$ Å, $D_e = 1.95$ eV, and $\omega_e = 296$ cm^{-1}. These results are in good agreement with experimental data ($R_e = 2.1545 \pm 0.0004$ Å [279], $D_0^\circ = 2.042 \pm 0.002$ eV [279], and $\omega_e = 280 \pm 20$ cm^{-1} [280]) and with the relativistic CASSCF/CASPT2 results of Pou-Amérigo et al. [278] who also found the $^1\Gamma_g$ and $^1\Sigma_g^+$ terms to be quasidegenerate with $R_e = 2.23$ Å, $D_e = 2.06$ eV, and $\omega_e = 293$ cm^{-1} for the $^1\Gamma_g$ term.
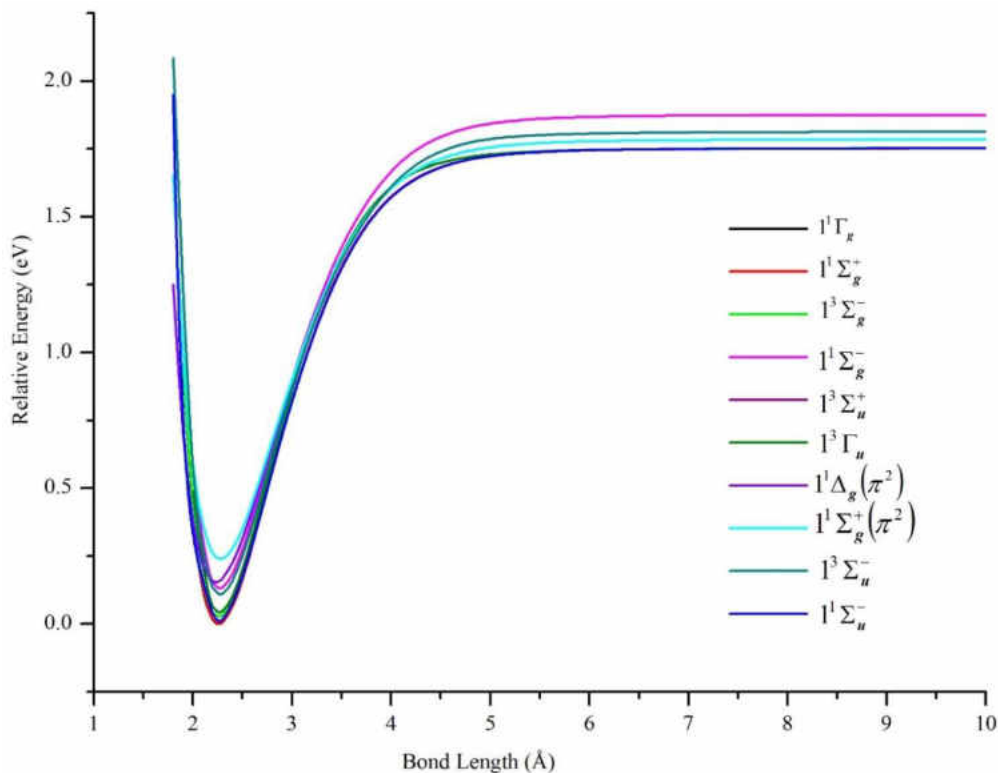
Figure 24. PECs of low-lying electronic states of Ni_2 computed at the GVVPT2 level of theory using the cc-pVTZ basis set. All energies are plotted relative to the lowest energy value of the ground $X^1\Gamma_g$ term. For all states, the holes are in the 3d delta orbitals $(\delta\delta-holes)$ except for the $1^1\Delta_g(\pi^2)$ and $1^1\Sigma_g^+(\pi^2)$ which are $\pi\pi-hole$ states.

Table 11. Equilibrium bond lengths, R_e (Å), binding energies, D_e (eV), harmonic frequencies, ω_e (cm^{-1}), and adiabatic transition energies, T_e (cm^{-1}), of electronic states of Ni_2 calculated at the GVVPT2 level of theory using the cc-pVTZ basis set and reference $\kappa(\mathbf{n})$ (6.5) and (6.6).

Molecular Term	R_e (Å)	D_e (eV)	ω_e (cm^{-1})	T_e (cm^{-1})
$\delta\delta$ – hole states				
computed using $\kappa(\mathbf{n})$ (6.5)				
$X^1\Gamma_g$	2.26	1.75	276.0	
$X^1\Gamma_g$ (no 3s3p)	2.27	1.66	268.5	
$X^1\Gamma_g(R)$	2.20	1.95	296.0	
Experiment	2.1545 ± 0.0004^a	2.042 ± 0.002^a	280 ± 20^b	
$1^1\Sigma_g^+$	2.26	1.75	276.8	16.40
$1^1\Sigma_g^+(R)$	2.20	1.95	297.0	23.39
$1^1\Sigma_g^+$ (no 3s3p)	2.28	1.65	263.3	16.56
$1^1\Sigma_u^-$	2.27	1.74	274.2	91.09
$1^3\Sigma_u^+$	2.27	1.71	274.9	349.60
$1^3\Sigma_u^+$ (no 3s3p)	2.28	1.62	267.4	309.58
$1^3\Gamma_u$	2.27	1.71	274.9	351.11
$1^3\Gamma_u$ (no 3s3p)	2.28	1.62	267.4	310.31
$1^3\Sigma_g^-$	2.26	1.72	275.0	221.98
$1^3\Sigma_u^-$	2.27	1.70	273.9	882.59
$1^1\Sigma_g^-$	2.27	1.74	270.2	1058.87
$2^1\Sigma_u^-$	2.75	0.11	73.5	18575.76
computed using $\kappa(\mathbf{n})$ (6.6)				
$1^3\Gamma_u\left(\delta_{3d_{x^2-y^2}}^2\right)$	2.27	1.71	275.0	2442.21

[a]Ref. [279] (the reported binding energy is for D_0^o), [b]Ref. [280].

The time-delayed resonant two-photon ionization study of Morse et al. [294] predicted either a $^3\Gamma_u$ or $^1\Gamma_g$ state as the ground state of Ni_2. Scalar relativistic calculations due to Cheskidov et al. [282] found the $^1\Gamma_g$ and $^1\Sigma_g^+$ terms to be degenerate at the ACPF and NEVPT2 levels of theory and the $^1\Sigma_g^+$ term to lie very slightly lower

than the $^1\Gamma_g$ at the AQCC, MRCI, and MRCI + Q levels of theory. At 2.25 Å, the EBO was found to be only 0.963 and 0.960 for the $^1\Gamma_g$ and $^1\Sigma_g^+$ states, respectively.

In sf-X2C relativistic GVVPT2 calculations, the EBOs increased slightly to 0.975 for $^1\Gamma_g$ and 0.972 for $^1\Sigma_g^+$. For these two states, the GVVPT2 wave function could be approximated in terms of valence orbital occupancies as

$$
\begin{aligned}
\left|\Psi\right\rangle = 0.445\!\left(3d_{xy}\delta_g^2 3d_{xy}\delta_u^{*2} 3d_{x^2-y^2}\delta_g^2 4s\sigma_g^2 + 3d_{xy}\delta_g^2 3d_{x^2-y^2}\delta_g^2 3d_{x^2-y^2}\delta_u^{*2} 4s\sigma_g^2\right) + \\
0.077\!\left(3d_{xy}\delta_g^2 3d_{xy}\delta_u^{*2} 3d_{x^2-y^2}\delta_u^{*2} 4s\sigma_u^{*2} - 3d_{xy}\delta_u^{*2} 3d_{x^2-y^2}\delta_g^2 3d_{x^2-y^2}\delta_u^{*2} 4s\sigma_u^{*2}\right)
\end{aligned}
\tag{6.13}
$$

Thus, the major configurations describing these singlet states involved the two $\delta-$holes in the same $\delta-$orbital type.

The semi core 3s3p electrons were found to be important in the description of low-lying states of Ni_2. The inclusion of 3s3p electron correlation at the GVVPT2 level increased the binding energies favorably (in comparison with experimental data) by 0.09 eV for $X^1\Gamma_g$, 0.10 eV for $1^1\Sigma_g^+$, 0.09 eV for $1^3\Sigma_u^+$ and $1^3\Gamma_u$ states in non-relativistic calculations. As can be seen in Figure 25 and Table 11, the effects of the 3s3p electrons on the equilibrium bond lengths and harmonic frequencies for these states are minimal whereas inclusion of such core-valence correlation raises, for example, the binding energy of $X^1\Gamma_g$ from 1.66 eV to 1.75 eV compared to a reference D_0^o value of 2.042 ± 0.002 eV [279].
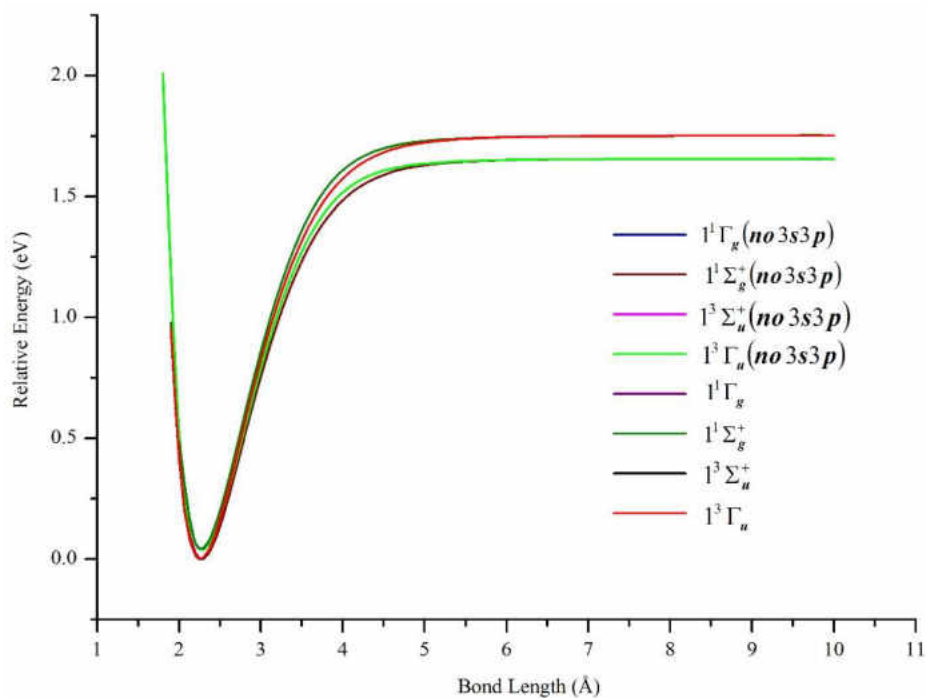
Figure 25. PECs of low-lying $\delta\delta-$hole electronic states of Ni_2 computed at the GVVPT2 level of theory, with and without the correlation of 3s3p semi-core electrons, using the cc-pVTZ basis set. All energies are plotted relative to the lowest energy value of the ground $X^1\Gamma_g$ term.

Scalar relativistic effects shortened the bond length of $X^1\Gamma_g$ by 0.06 Å and further increased the bond energy by 0.20 eV to 1.95 eV in favor of the reference experimental values (see Figure 26 and Table 1). The 3s3p electrons did not have any effect on the EBOs of $X^1\Gamma_g$ and $1^1\Sigma_g^+$; the EBOs were determined as 0.962 and 0.959 at 2.27 Å for $X^1\Gamma_g$ and $1^1\Sigma_g^+$, respectively, when the 3s3p electrons were uncorrelated compared to 0.963 versus 0.960 when they were correlated. Note the quasidenegeracy in the $X^1\Gamma_g$ and $1^1\Sigma_g^+$ states. For example, in Figure 26, the blue and green curves for the $X^1\Gamma_g$ and $1^1\Sigma_g^+$ states, respectively, lie on top of each other (only the green is visible).

Also, the black and red curves for the $X^1\Gamma_g(R)$ and $1^1\Sigma_g^+(R)$ states lie on each other (only the red curve is visible).
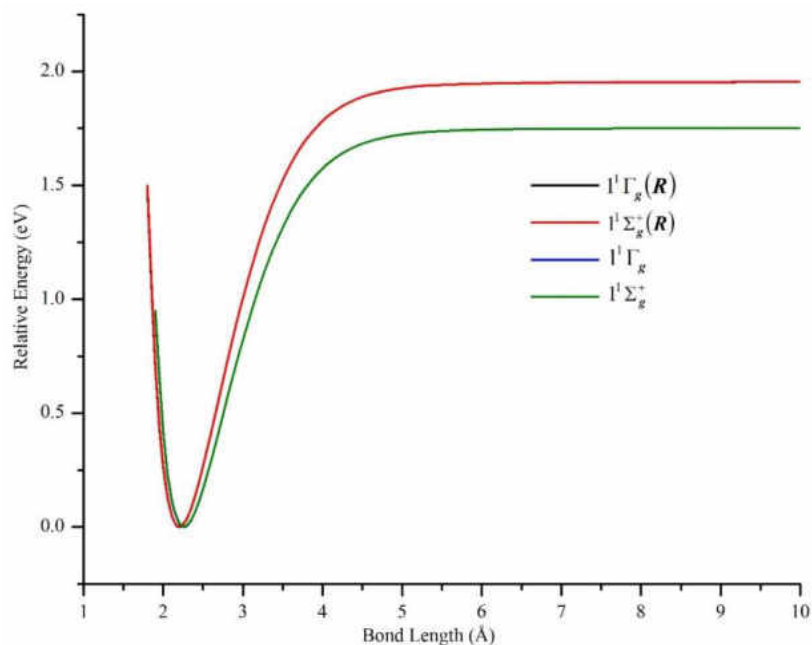
Figure 26. PECs of the lowest-lying $\delta\delta-$hole $X^1\Gamma_g$ and $1^1\Sigma_g^+$ states of Ni_2 computed at the GVVPT2 level of theory, with and without scalar relativity included, using the cc-pVTZ basis set. Non-relativistic energies are plotted relative to the lowest energy value of the ground $X^1\Gamma_g$ term, while relativistic energies are plotted relative to the lowest energy of the $X^1\Gamma_g(R)$ term.

The $1^1\Sigma_u^-$ state that was predicted as the ground state of Ni_2 at the ACPF level of theory [282] and found to lie quite close to a $^1\Sigma_g^+$ ground state in a limited CI study [17] was found at the GVVPT2 level to lie 91.09 cm^{-1} above the $X^1\Gamma_g$ term at equilibrium. The $2^1\Sigma_u^-$ state, however, lay much higher energetically (18575.76 cm^{-1} above the ground state at equilibrium).

As can be seen in Table 11, GVVPT2 predicted the triplet $\delta\delta-$hole states ($1^3\Sigma_g^-$, $1^3\Sigma_u^+$, and $1^3\Gamma_u$) to lie energetically in the order $1^3\Sigma_g^- < 1^3\Sigma_u^+ < 1^3\Gamma_u$. Cheskidov et al.

[282] found this same ordering at the ACPF, AQCC, MRCI and MRCI + Q levels of theory whereas their NEVPT2 calculations predicted $1^3\Sigma_u^+ < 1^3\Gamma_u < 1^3\Sigma_g^-$, with the $1^3\Sigma_g^-$ state lying at least 139 cm^{-1} higher than the other two states. It should be noted that the vertical excitation energies in Ref. [282] were not determined at the equilibrium geometries of the computed states. The $1^3\Sigma_u^+$ state which was predicted as the ground state of Ni_2 in previous wave function [276, 281] and DFT [268, 284] studies was found in the present study to lie at 349.60 cm^{-1} above the $X^1\Gamma_g$ state at the equilibrium geometry. Likewise the $1^3\Sigma_g^-$ state reported in some studies [277] as the ground term of Ni_2 lay at 221.98 cm^{-1} higher at equilibrium. The $1^3\Sigma_u^-$ state was found to have a bond length and bond energy comparable to those of $1^3\Sigma_g^-$, $1^3\Sigma_u^+$, and $1^3\Gamma_u$ but lying at least 531.48 cm^{-1} higher in energy. The EBOs for these triplet states were 0.971 for $1^3\Sigma_g^-$, 0.933 for $1^3\Sigma_u^+$ and $1^3\Gamma_u$, and 0.923 for $1^3\Sigma_u^-$ at the vicinity of their equilibrium geometries. The major configurations for the $\delta\delta-$hole triplet states involved a doubly occupied $4s\sigma_g$ bonding orbital.

The $1^3\Gamma_u\left(\delta_{3d_{x^2-y^2}}^2\right)$ state, in which all two $\delta-$holes were in the $3d_{x^2-y^2}\delta_g\delta_u^*$ orbitals, was computed using reference $\kappa(\mathbf{n})$ (6.6). As can be seen in Table 11, this state was found to have spectroscopic constants comparable to other $\delta\delta-$hole triplet states but lay much higher energetically (2442.21 cm^{-1} above the ground state at equilibrium). The present results suggest that the $3d\delta$ orbitals are indeed split in the bonding interaction. Since they are nondegenerate, the Aufbau principle suggests that low-lying orbitals (the

bonding $3d\delta$ orbitals) be occupied before higher ones. Moreover, Hund's rule suggests that orbitals with similar energies (in this case, $3d\delta_u^*$ orbitals) be singly occupied before electron pairing occurs. This may explain why the $1^3\Sigma_g^-$, $1^3\Sigma_u^+$, and $1^3\Gamma_u$ states in which the $3d_{x^2-y^2}\delta_u^*$ and $3d_{xy}\delta_u^*$ are singly occupied lie lower than the $1^3\Gamma_u\left(\delta_{3d_{x^2-y^2}}^2\right)$ state.

The $\delta\pi$−Hole and $\pi\pi$−Hole States

The PECs of the computed $\pi\pi$−hole states ($1^1\Delta_g\left(\pi^2\right)$ and $1^1\Sigma_g^+\left(\pi^2\right)$) are shown in Figure 24 while those of the $\delta\pi$−hole states ($1^1\Phi_g(\delta\pi)$, $1^1\Pi_g(\delta\pi)$, $1^3\Pi_g(\delta\pi)$, and $1^3\Phi_g(\delta\pi)$) are shown in Figure 27 and compared with the ground state PEC. The data describing these curves are in Table 12. GVVPT2 predicted the $\pi\pi$−hole states to lie higher in energy than the $\delta\pi$−hole states in agreement with previous studies [17, 271, 275]. For the four $\delta\pi$−hole states, the major CSFs involved a doubly occupied $4s\sigma_g$ bonding orbital. Thus, the main configurations of the $1^1\Phi_g(\delta\pi)$ and $1^1\Pi_g(\delta\pi)$ states involved an unpaired alpha spin electron in the $3d\delta$ subspace and an unpaired beta spin electron in the $3d\pi$ subspace (or vice versa), e.g.,

$$3d\delta_g^2\,3d\delta_u^{*2}\,3d\delta_g^2\,3d\delta_u^{*1(\uparrow)}\,3d\pi_u^2\,3d\pi_g^{*2}\,3d\pi_u^2\,3d\pi_g^{*1(\downarrow)}\,4s\sigma_g^2 \qquad (6.14)$$

whereas the major configurations of the $1^3\Pi_g(\delta\pi)$ and $1^3\Phi_g(\delta\pi)$ states were similar to those of the singlet states but with two unpaired alpha spins; one in each of the $3d\delta$ and $3d\pi$ subspaces, e.g.,

$$3d\delta_g^2\,3d\delta_u^{*2}\,3d\delta_g^2\,3d\delta_u^{*1(\uparrow)}\,3d\pi_u^2\,3d\pi_g^{*2}\,3d\pi_u^2\,3d\pi_g^{*1(\uparrow)}\,4s\sigma_g^2 \qquad (6.15)$$

155
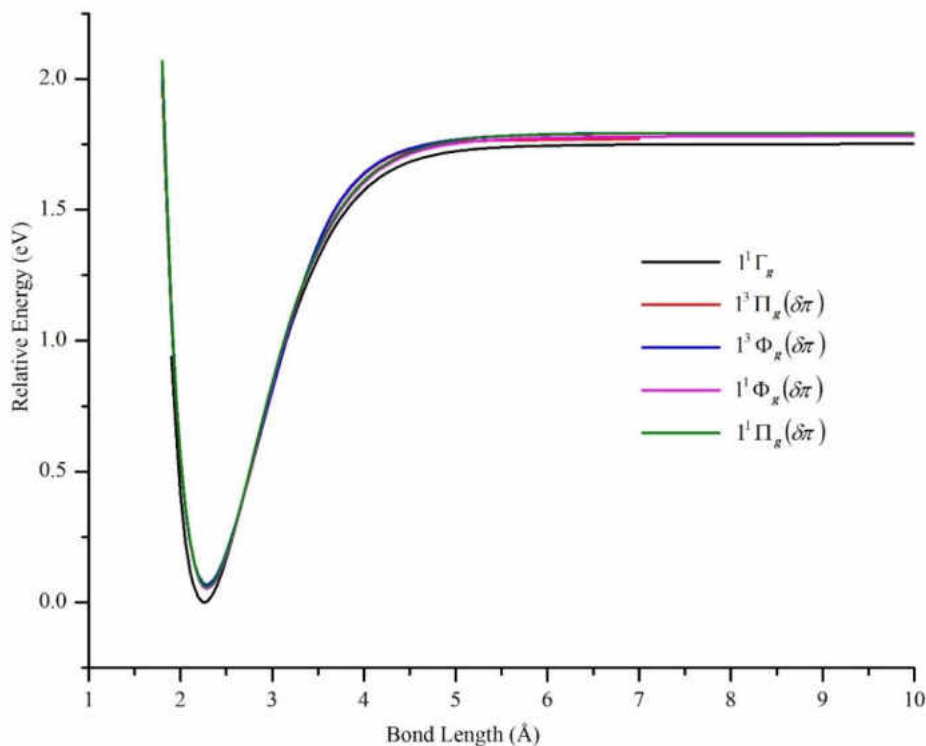
Figure 27. PECs of low-lying $\delta\pi-$hole electronic states of Ni_2 computed at the GVVPT2 level of theory using the cc-pVTZ basis set, compared with the ground $X^1\Gamma_g$ term's PEC. All energies are plotted relative to the lowest energy value of the ground $X^1\Gamma_g$ term.

At the equilibrium geometries, the EBOs were 0.930 for the singlet $1^1\Phi_g(\delta\pi)$ and $1^1\Pi_g(\delta\pi)$ states and 0.933 for the $1^3\Pi_g(\delta\pi)$ and $1^3\Phi_g(\delta\pi)$ states. GVVPT2 predicted the four $\delta\pi-$hole states to lie energetically in the order $1^1\Phi_g(\delta\pi) < 1^1\Pi_g(\delta\pi) < 1^3\Pi_g(\delta\pi) < 1^3\Phi_g(\delta\pi)$ in agreement with the Ref. [282] study at the scalar relativistic ACPF, AQCC, MRCI, and MRCI + Q levels of theory. However, the present calculations found all three states considered in Ref. [282] ($1^1\Pi_g(\delta\pi)$, $1^3\Pi_g(\delta\pi)$, and $1^3\Phi_g(\delta\pi)$) to lie some 500 cm^{-1} lower energetically with respect to the ground state e.g., at the scalar relativistic MRCI + Q level, the $1^3\Phi_g(\delta\pi)$ state was reported [282] as lying 1238 cm^{-1}

156

above the ground state at 2.5 Å while non-relativistic GVVPT2 calculations predicted this state to lye 546.76 cm^{-1} above the ground state at equilibrium (2.26 Å). Based on the observations in the present study that including scalar relativistic effects increased the energy gap between the $^1\Sigma_g^+$ and $X^1\Gamma_g$ states, it is likely that including such effects in GVVPT2 calculations on the $\delta\pi-$hole states may lead to increases in corresponding adiabatic transition energies. It is not anticipated, however, that such effects would lead to any change in the energy ordering of the states.

Although lying higher in energy than the $\delta\pi-$hole states, the $\pi\pi-$hole states were found to have slightly shorter bond lengths and higher bond strengths than the $\delta\pi-$hole states. The $1^1\Delta_g\left(\pi^2\right)$ state was 0.06 Å shorter while the $1^1\Sigma_g^+\left(\pi^2\right)$ state was 0.01 Å shorter in bond length than the $\delta\pi-$hole states. At 2.24 Å, the EBOs of $1^1\Delta_g\left(\pi^2\right)$ and $1^1\Sigma_g^+\left(\pi^2\right)$ were 1.108 and 1.084 respectively; which were slightly higher than the EBOs of all other computed $\delta\delta-$hole and $\delta\pi-$hole Ni$_2$ states. Near the equilibrium, the major configurations of these $\pi\pi-$hole states involved a doubly occupied $4s\sigma_g$ bonding orbital and a configuration of the $3d\pi$ subspace that had the two $\pi-$holes in the same $\pi-$orbital e.g.,

$$3d\pi_u^2 3d\pi_g^{*2} 3d\pi_u^2 3d\pi_g^{*0} 4s\sigma_g^2 \qquad (6.16)$$

States of the $^3F_4 + {}^3F_4$ and $^3F_4 + {}^3D_3$ manifolds

Figure 28 contains PECs of states belonging to the $^3F_4 + {}^3F_4$ manifold. The data describing these curves are in Table 12. Irrespective of how the model space was

partitioned into $\kappa(\mathbf{n})$s, all such states were found to be van der Waals-like with interaction energies ≤ 0.04 eV .

Table 12. Equilibrium bond lengths, R_e (Å), binding energies, D_e (eV), harmonic frequencies, ω_e (cm^{-1}), and adiabatic transition energies, T_e (cm^{-1}), of electronic states of Ni$_2$ calculated at the GVVPT2 level of theory using the cc-pVTZ basis set and Reference $\kappa(\mathbf{n})$ (6.7) to (6.12).

Molecular Term	R_e (Å)	D_e (eV)	ω_e (cm^{-1})	T_e (cm^{-1})
$\delta\pi -$hole states computed with $\kappa(\mathbf{n})$ (6.8)				
$1^1\Phi_g(\delta\pi)$	2.29	1.73	263.7	427.86
$1^1\Pi_g(\delta\pi)$	2.29	1.73	269.7	485.09
$1^3\Pi_g(\delta\pi)$	2.29	1.72	261.9	518.14
$1^3\Phi_g(\delta\pi)$	2.29	1.72	261.3	546.76
$\pi\pi$-hole states computed with $\kappa(\mathbf{n})$ (6.7)				
$1^1\Delta_g(\pi^2)$	2.23	1.63	242.5	1241.68
$1^1\Sigma_g^+(\pi^2)$	2.28	1.55	240.5	1925.85
States computed with $\kappa(\mathbf{n})$ (6.9)				
$1^3\Delta_u(G:\delta^2\pi^2)$	3.96	0.02	26.2	33555.78
$1^3\Sigma_u^+(G:\delta^2\pi^2)$	3.96	0.02	26.2	33555.91
$1^1\Delta_g(G:\delta^2\pi^2)$	3.93	0.03	26.6	34531.63
$1^3\Sigma_g^+(G:\delta^2\pi^2)$	3.95	0.03	26.2	39160.31
$2^3\Sigma_g^+(G:\delta^2\pi^2)$	3.96	0.03	26.0	39162.41
States computed with $\kappa(\mathbf{n})$ (6.10)				
$1^1\Gamma_g(G:\delta^2\sigma_{3d}^2)$	3.73	0.04	26.9	35412.38
$1^1\Sigma_g^+(G:\delta^2\sigma_{3d}^2)$	3.73	0.04	26.9	35412.41
States computed with $\kappa(\mathbf{n})$ (6.11)				
$1^5\Phi_u(G:\delta^2\pi\sigma_{3d})$	3.83	0.03	26.7	33144.35
$1^5\Pi_u(G:\delta^2\pi\sigma_{3d})$	3.84	0.03	26.9	33147.67
States computed with $\kappa(\mathbf{n})$ (6.12)				
$1^5\Delta_g(GE:\delta\pi^2\sigma_{4s})$	2.22		249.1	5123.66
$2^5\Delta_g(GE:\delta\pi^2\sigma_{4s})$	2.54		150.1	9018.57
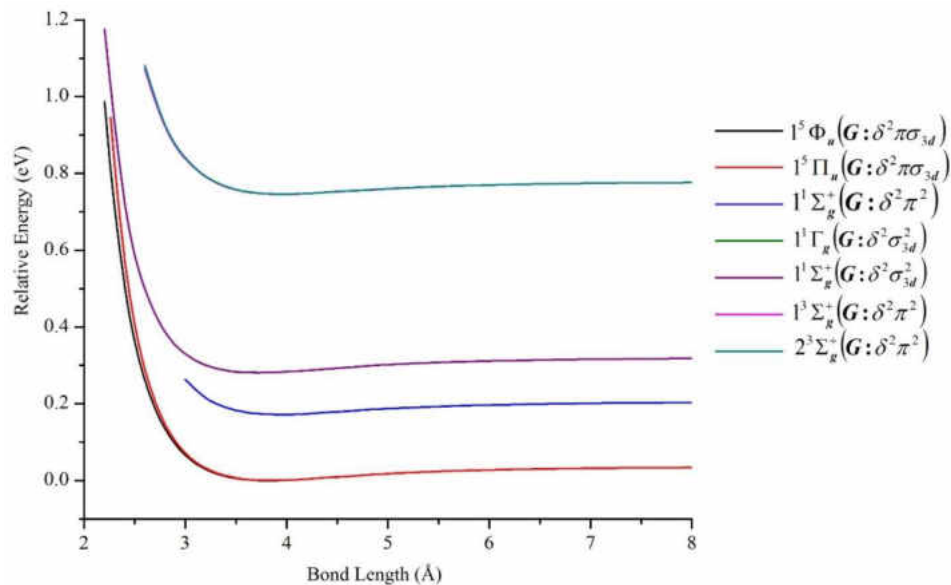
Figure 28. PECs of electronic states of Ni_2, within the $^3F_4(3d^84s^2) + {}^3F_4(3d^84s^2)$ manifold, computed at the GVVPT2 level of theory using the cc-pVTZ basis set in reference $\kappa(\mathbf{n})$s (6.9) to (6.11). All energies are plotted relative to the lowest energy value of the $1^5\Phi_u(G:\delta^2\pi\sigma_{3d})$ term.

For example, near the equilibrium geometry (i.e, at 3.77 Å), the $1^1\Gamma_g(G:\delta^2\sigma^2)$ and $1^1\Sigma_g^+(G:\delta^2\sigma^2)$ states had an EBO of only 0.005 while the $1^5\Phi_u(G:\delta^2\pi\sigma_{3d})$ and $1^5\Pi_u(G:\delta^2\pi\sigma_{3d})$ states had EBOs of 0.003 and 0.00, respectively, at 3.84 Å. These latter quintet states were computed using reference $\kappa(\mathbf{n})$ (11) and found to lie lowest energetically among the computed states of the $^3F_4 + {}^3F_4$ manifold; the $1^5\Pi_u(G:\delta^2\pi\sigma_{3d})$ state being 3.312 cm^{-1} less stable than the $1^5\Phi_u(G:\delta^2\pi\sigma_{3d})$ state at equilibrium. All energies in Figure 28 are plotted relative to the lowest energy value of the $1^5\Phi_u(G:\delta^2\pi\sigma_{3d})$ term. Since the total energies are a function of the nature of partitioning of the active space, the PECs above the $1^5\Phi_u(G:\delta^2\pi\sigma_{3d})$ curve in Figure 28 should not be interpreted as excited state curves since the electronic states were computed using different reference $\kappa(\mathbf{n})$s.

Lastly, the $1^5\Delta_g\left(\text{GE}:\delta\pi^2\sigma_{4s}\right)$ and $2^5\Delta_g\left(\text{GE}:\delta\pi^2\sigma_{4s}\right)$ states of the $^3F_4 + {}^3D_3$

manifold were investigated at short bond lengths using reference $\kappa(\mathbf{n})$ (12). The data for

these states are included in Table 12. Whereas the $^3F_4\left(3d^8\,4s^2\right) + {}^3F_4\left(3d^8\,4s^2\right)$ states are

van der Waals-like, the short bond length (2.22 Å) and high frequency (249.1 cm^{-1}) of the

$1^5\Delta_g\left(\text{GE}:\delta\pi^2\sigma_{4s}\right)$ state is suggestive of significant bonding interaction. At 2.22 Å, the

major configuration for this state was

$$3d_{x^2-y^2}\delta_g^2\,3d_{x^2-y^2}\delta_u^{*2}\,3d_{xy}\delta_g^2\,3d_{xy}\delta_u^{*1}\,3d\pi_u^2\,3d\pi_g^{*1}\,3d\pi_u^2\,3d\pi_g^{*1}\,4s\sigma_g^2\,4s\sigma_u^{*1} \qquad (6.17)$$

contributing 50% by weight to the total wave function. At this geometry, the EBO was

found to be 1.186 (slightly higher than all other computed Ni_2 states).

Concluding Remarks

The GVVPT2 method was used to study low-lying electronic states of Ni_2 as

reported in this Chapter. The results indicate, in general, that bonding in these states

involves predominantly the doubly occupied $4s\sigma_g$ bonding orbital with the 3d-3d

electrons antiferromagnetically coupled. This statement is authenticated by the fact that

EBOs were found to be approximately 1.0 for most of the states and moreover, states

belonging to the $^3F_4\left(3d^8\,4s^2\right) + {}^3F_4\left(3d^8\,4s^2\right)$ manifold were found to be held together

only by weak polarization forces with bond orders close to zero. For computed states of

the $^3D_3\left(3d^9\,4s^1\right) + {}^3D_3\left(3d^9\,4s^1\right)$ dissociation limit, all major configurations involved a

doubly occupied $4s\sigma_g$ bonding orbital and a vacant $4s\sigma_u^*$ antibonding orbital. The

energy ordering of the computed states of the $^3D_3\left(3d^9\,4s^1\right) + {}^3D_3\left(3d^9\,4s^1\right)$ manifold was

in agreement with previous studies [271] that found the $\delta\delta-$hole states to lie lowest in energy followed by the $\delta\pi-$hole and then the $\pi\pi-$hole states. For the investigated $\delta\delta-$hole states, the singlets were more stable than the triplet states at the GVVPT2 level of theory.

In agreement with previous theoretical studies, the present studies found the lowest lying states of Ni_2 to correlate with the $^3D_3 + {}^3D_3$ dissociation limit. In particular, the ground term was determined as $X^1\Gamma_g$ and the $1^1\Sigma_g^+$ excited state of the $^3D_3 + {}^3D_3$ dissociation channel lay at only 16.4 cm^{-1} (0.002 eV) above the ground state at the equilibrium geometry. These states originated from electronic configurations in which the holes in the d-subshells were in the subspace of delta orbitals ($\delta\delta-$states) and had spectroscopic constants: bond length (R_e) = 2.26 Å, harmonic frequency (ω_e) = 276.0 cm^{-1}, and binding energy (D_e) = 1.75 eV for the $X^1\Gamma_g$ state and R_e = 2.26 Å, ω_e = 276.8 cm^{-1}, and D_e = 1.75 for the $1^1\Sigma_g^+$ excited state. Inclusion of scalar relativistic effects through the spin-free exact two component (sf-X2C) method reduced the bond lengths of these two states to 2.20 Å, and increased their binding energies to 1.95 eV and harmonic frequencies to 296.0 cm^{-1} for $X^1\Gamma_g$ and 297.0 cm^{-1} for $1^1\Sigma_g^+$. These values are in good agreement with experimental values of R_e = 2.1545 ± 0.0004 Å [279], ω_e = 280 ± 20 cm^{-1} [280], and D_o = 2.042 ± 0.002 eV [279] for the ground state. As noted before, previous theoretical studies on Ni_2 have seldom reported full PECs on electronic states of the molecule. The present study is one of few in the literature to have constructed full PECs of low-lying states of the Ni_2 molecule.

Core-valence correlation was found to be important in the description of low-lying states of Ni_2 where the inclusion of 3s3p electron correlation at the GVVPT2 level was shown to improve harmonic frequencies and bond energies. Scalar relativistic effects were also shown to be important where spectroscopic constants from relativistic calculations were predicted to be more agreeable with reference data. As was shown in studies of Mn_2 (see Chapter V), relativistic effects were not found to be as important as has been observed for Ni_2. The inclusion of spin-orbit coupling effects was previously found [271, 278, 282] to mix the low-lying states of Ni_2, leading to a $0_g^+ \left[{}^1\Sigma_g^+ (\delta\delta) + {}^3\Sigma_g^- (\delta\delta) \right]$ ground state. It is envisaged that including such effects within the current scalar relativistic GVVPT2 would probably lead to similar mixings of the states.

The states investigated within the ${}^3F_4 (3d^8 4s^2) + {}^3D_3 (3d^9 4s^1)$ manifold suggested significant bonding interaction, giving large harmonic frequencies and short bond lengths in comparison with states correlating with the ${}^3F_4 (3d^8 4s^2) + {}^3F_4 (3d^8 4s^2)$ dissociation limit. Further work on Ni_2 should possibly consider a larger active space that includes orbitals from the 4p subspace in addition to a full treatment of relativistic effects. It should be noted, however, that in the present study, no significant electron excitations were observed from the valence space to 4p-dominated virtual orbitals.

As noted before, the present study showed that Ni does not form strong bonds with atomic configurations in which the 4s subshell is fully filled. This observation seems to be a general rule of tomb for transition elements of the first row. The fully filled 4s-subshell is repulsive and appears to discourage bonding. Bonding in these systems is favored by atomic configurations that involve at least one of the participating atoms in

an excited state ($3d^{n+1}4s^1$) as was illustrated in GVVPT2 studies [158] of electronic states of Sc_2, Cr_2, and Mn_2, where the lowest states of Sc_2 were shown to correlate with the $^2D(3d^1 4s^2) + {}^4F(3d^2 4s^1)$ dissociation asymptote while those of Cr_2 correlated with the $^7S(3d^5 4s^1) + {}^7S(3d^5 4s^1)$ dissociation limit. In the Ref. [158] study, however, the lowest energy results on Mn_2 were obtained with weakly coupled $^5D(3d^5 4s^2) + {}^5D(3d^5 4s^2)$ ground state Mn atoms, similar to the $^3F_4 (3d^8 4s^2) + {}^3F_4 (3d^8 4s^2)$ coupling of ground state Ni atoms. The $3d^n 4s^2 \rightarrow 3d^{n+1} 4s^1$ electronic excitation energy is known [221] to decrease monotonically from Sc to Cr due to increased stabilization of the 3d subshell coupled with the gain in exchange energy. At Mn, however, the situation reverses due to a large loss in exchange energy in the $3d^5 4s^2 \rightarrow 3d^6 4s^1$ excitation [221]. This large loss explains why Mn preferentially bonds through $^5D(3d^5 4s^2)$ ground state atoms. From Fe to Cu, the $3d^n 4s^2 \rightarrow 3d^{n+1} 4s^1$ promotion energy again drops monotonically such that at Ni, the ^3F and ^3D states are quasidegenerate.

CHAPTER VII

DFT-in-DFT EMBEDDING THEORY WITH EXTERNAL ORBITAL
ORTHOGONALITY

Introduction

This Chapter describes the newly developed DFT-in-DFT embedding program [5, 6] that includes external orbital orthogonality. As was noted in Chapter I, many ab initio methods for electronic structure calculations have applicability limited by computational costs that increase polynomially with system size. Due to this limitation, ever-expanding research efforts have considered localization (cf. Refs. [295-298], for example) and embedding [66-70] techniques as a means of extending ab initio methods to the description of larger systems. The problem with most localization techniques, however, is that they involve transformations of orbitals initially obtained in a calculation of a total system. This could be computationally costly for systems of nanosize with several hundreds of atoms. Since embedding schemes use a "divide and conquer" approach, they are particularly attractive. Not only do such schemes avoid calculations of a total system (which can be large and prohibitively expensive even for methods like DFT), but they also allow for the possibility of describing subsystems at different levels of theory. Unfortunately, DFT-in-DFT embedding theory, as currently formulated, is unable to exactly reproduce reference KS-DFT results. Errors in the theory are connected with approximations in the kinetic and exchange-correlation energy functionals. In this Chapter, a new variant of DFT-in-DFT embedding theory is presented that includes an

additional requirement that orbitals of subsystems be orthogonal to each other. This latter constraint of intersystem or external orbital orthogonality was not imposed in previous formulations of DFT-in-DFT embedding theory and led to poor estimates of electron densities particularly at the interface between subsystems and, consequently to heavy reliance on the functionals to correct for the wrong density. In turn this led to poor descriptions of a partitioned system in terms of characterization of interaction strengths between subsystems and other properties. The new embedding scheme described here clearly shows that by enforcing the external orthogonality condition within DFT-in-DFT embedding theory, new embedding equations are realized, which take into account off-diagonal blocks of the KS Fock matrices that couple the subsystems in a natural, density-based way. In this way, electron densities are more accurately represented at all points in space and the overall description of a partitioned system is thus improved. In particular, the new equations do not rely on the use of kinetic functionals since the so-called nonadditive kinetic potential (v_T) is exactly zero in this case. By requiring subsystems orbitals to be orthogonal to each other, the electronic kinetic energy becomes additive and is thus evaluated at the Kohn-Sham (KS) level without further need of a correcting term involving kinetic functionals.

The rationale for the present study was to prepare an accurate embedding theory that will ultimately permit GVVPT2 calculations to be embedded in large systems that are partitioned into small fragments (described at the GVVPT2 level of theory) and larger fragments whose effects on the small fragments of interest are approximated at a lower level of theory such as DFT. Before describing the new embedding protocol, it is

important to review the foundation of the theory, which is conventional KS-DFT [299-301] and the previous formulation of DFT-in-DFT theory [66-74].

Kohn-Sham (KS)-DFT

The present subsection will discuss only the basic KS-DFT equations without providing computational details. KS-DFT is a particular realization of the Hohenberg and Kohn theorem [299]. The Hohenberg and Kohn theorem, based on the constrained-search formulation [300], asserts that for a quantum system of N electrons, there is a functional ($E_v(\rho)$) of the density ($\rho(\vec{r})$) due to these electrons whose minimization, subject to the constraint that the density integrates over all space to give the number of electrons (N), leads to the ground state energy (E_0) for the system,

$$E_0 = \underset{\rho \to N}{\text{Min}} E_v[\rho] \tag{7.1}$$

where the energy functional is defined as

$$E_v[\rho] = F[\rho] + \int v(\vec{r})\rho(\vec{r})d\vec{r} \tag{7.2}$$

$v(\vec{r})$ is the potential due to the nuclei and the functional $F[\rho]$ (involving the kinetic energy, T, and two electron interaction terms, V_{ee}) is

$$F[\rho] = \underset{\Psi \to \rho}{\text{Min}} \langle \Psi | T + V_{ee} | \Psi \rangle \tag{7.3}$$

In Eq. (7.3), the $|\Psi\rangle$ functions are normalized N-electron wave functions constrained to have electron density $\rho(\vec{r})$. The latter is itself required to meet the following constraints:

$$\int \rho(\vec{r})d\vec{r} = N, \qquad \rho(\vec{r}) \geq 0, \qquad \int \left| \nabla \rho^{\frac{1}{2}} \right|^2 d\vec{r} < \infty \tag{7.4}$$

The Euler form of Eq. (7.2) is

$$\frac{\delta T_s[\rho]}{\delta \rho(\vec{r})} + v_s([\rho];\vec{r}) = \mu_s, \qquad (7.5)$$

where the potential $v_s([\rho];\vec{r})$ is defined as

$$v_s([\rho];\vec{r}) = v(\vec{r}) + \int \frac{\rho(\vec{r}')}{|\vec{r} - \vec{r}'|} d\vec{r}' + \frac{\delta E_{xc}[\rho]}{\delta \rho(\vec{r})}, \qquad (7.6)$$

and μ_s is the Lagrange multiplier associated with the electron number conservation constraint on the density in Eq. (7.4); $v(\vec{r})$ is the potential due to the nuclei as stated before; while the last two terms on the right hand side of Eq. (7.6) are the coulomb and exchange-correlation potentials, respectively.

According to Kohn and Sham [301], Eq. (7.5) can be written alternatively as

$$h^{KS}\left|\varphi_m^{KS}\right\rangle = \varepsilon_m^{KS}\left|\varphi_m^{KS}\right\rangle, \qquad (m \in [1, N]) \qquad (7.7)$$

where

$$h^{KS}(\vec{r}) = -\tfrac{1}{2}\nabla^2 + v_s^{KS}([\rho];\vec{r}) \text{ and } \rho(\vec{r}) = \sum_{m=1}^{N}\left|\varphi_m^{KS}(\vec{r})\right|^2, \qquad (7.8)$$

where $\left|\varphi_m^{KS}\right\rangle$ are Kohn-Sham orbitals with corresponding eigenvalues ε_m^{KS}; and $v_s^{KS}([\rho];\vec{r})$ is defined similarly as in Eq. (7.6) and is the Kohn-Sham potential for an auxiliary system of non-interacting electrons. The first term in the definition of $h^{KS}(\vec{r})$ is the usual kinetic energy operator in atomic units. Thus the KS approach approximates a system of interacting electrons in terms of an auxiliary system with the same electron density but with non-interacting electrons.

DFT-in-DFT Embedding Theory

DFT-in-DFT embedding theory [66-74] is based on conventional KS-DFT. As was noted in Chapter I, the approach in DFT-in-DFT embedding is to divide a system

into subsystem A (the embedded subsystem) and subsystem B (the environment subsystem) and to describe these subsystems using KS-DFT. In principle, the environment subsystem may be further subdivided [66]. The ultimate goal of embedding theories is to achieve high accuracy within a local, generally complex, embedded subsystem (A) by describing it at a high level of theory while the effect of the environment is approximated at a lower level of theory such as HF or DFT. This is not the case in DFT-in-DFT embedding (although, in principle, one could use DFT functionals with different degrees of accuracy to describe the subsystems or possibly use time-dependent DFT for subsystem A but KS-DFT for subsystem B). This notwithstanding, DFT-in-DFT is a first step to the goal of being able to partition a system and describe the subsystems at different levels of theory. Besides, an accurate embedding theory could potentially reduce computational costs of large systems since calculations of such systems are reduced to coupled-tasks with smaller numbers of electrons.

As was noted in Chapter I, DFT-in-DFT embedding theory partitions a system's electron density into a sum of fragment densities according to Eq. (1.5) and then minimizes the total energy functional under the constraint of fixed electron number in each subsystem. Such minimization leads to a system of coupled KS-like equations for the subsystems' orbitals, which are referred to as the KS equations with constrained electron density (KSCED) [72].

The basic equations of DFT-in-DFT embedding theory can thus be stated as follows. By partitioning a system into A and B, the energy functional ($E_v[\rho] = E_v[\rho_A + \rho_B]$) also gets partitioned into a sum of subsystem functionals plus a functional term that describes interactions between the subsystems,

$$E_v[\rho_A + \rho_B] = E_{v_A}[\rho_A] + E_{v_B}[\rho_B] + E_{int}[\rho_A, \rho_B], \qquad (7.9)$$

where $E_{v_A}[\rho_A]$ and $E_{v_B}[\rho_B]$ are the functionals for subsystems A and B, respectively (defined as in Eq. (7.2)) while $E_{int}[\rho_A, \rho_B]$ is a functional describing intersubsystem interactions, defined as

$$E_{int}[\rho_A, \rho_B] = F[\rho_A + \rho_B] - F[\rho_A] - F[\rho_B] + \int (v_A \rho_B + v_B \rho_A) dr, \qquad (7.10)$$

where $F[\rho_A + \rho_B]$, $F[\rho_A]$, and $F[\rho_B]$ are defined in the same manner as in Eq. (7.3) whereas $v_A(\vec{r})$ and $v_B(\vec{r})$ are the potentials due to nuclei assigned to the embedded and environment subsystems, respectively. The subsystems' densities ($\rho_A(\vec{r})$ and $\rho_B(\vec{r})$) are required to obey the conditions in Eq. (7.4), viz.

$$\int \rho_I(\vec{r}) d\vec{r} = N_I, \quad \rho_I(\vec{r}) \geq 0, \quad \int \left| \nabla \rho_I^{\frac{1}{2}} \right|^2 d\vec{r} < \infty \qquad (I = A, B) \qquad (7.11)$$

The partitioned energy functional ($E_v[\rho] = E_v[\rho_A + \rho_B]$) is minimized in a two-step procedure subject to the number conservation restrictions of subsystems' densities given in Eq. (7.11),

$$E_0 = \underset{\rho_B \to N_B}{Min} \underset{\rho_A \to N_A}{Min} E_v[\rho_A + \rho_B] = \underset{\rho_B \to N_B}{Min} \left\{ E_{v_B}[\rho_B] + \underset{\rho_A \to N_A}{Min} \left[E_{v_A}[\rho_A] + E_{int}[\rho_A, \rho_B] \right] \right\}, \qquad (7.12)$$

where N_A and N_B are fixed integer numbers of electrons within subsystems A and B, respectively. Such minimization as in Eq. (7.12) results in a pair of coupled Euler-Lagrange equations for the subsystems,

$$\frac{\delta E_{v_A}[\rho_A]}{\delta \rho_A(\vec{r})} + v_A^{eff}([\rho_A, \rho_B]; \vec{r}) = \mu_A, \qquad (7.13)$$

and

$$\frac{\delta E_{v_B}[\rho_B]}{\delta \rho_B(\vec{r})} + v_B^{eff}([\rho_A, \rho_B]; \vec{r}) = \mu_B \qquad (7.14)$$

which are often referred to as Kohn-Sham equations with constrained electron density (KSCED). In Eqs. (7.13) and (7.14), μ_A and μ_B are Lagrangian multipliers associated with the constraints $\int \rho_I(\vec{r})d\vec{r} = N_I$ (I = A or B), whereas the effective potentials describe the effects of the subsystems on each other and are defined as

$$v_A^{eff}\left(\left[\rho_A, \rho_B\right]; \vec{r}\right) = \frac{\delta E_{int}\left[\rho_A, \rho_B\right]}{\delta \rho_A(\vec{r})} = v_B(\vec{r}) + \left.\frac{\delta F[\rho]}{\delta \rho(\vec{r})}\right|_{\rho=\rho_A+\rho_B} - \frac{\delta F[\rho_A]}{\delta \rho_A(\vec{r})}, \qquad (7.15)$$

and

$$v_B^{eff}\left(\left[\rho_A, \rho_B\right]; \vec{r}\right) = \frac{\delta E_{int}\left[\rho_A, \rho_B\right]}{\delta \rho_B(\vec{r})} = v_A(\vec{r}) + \left.\frac{\delta F[\rho]}{\delta \rho(\vec{r})}\right|_{\rho=\rho_A+\rho_B} - \frac{\delta F[\rho_B]}{\delta \rho_B(\vec{r})} \qquad (7.16)$$

The effective potentials defined in Eqs. (7.15) and (7.16) can alternatively be expressed as

$$v_{eff}^I\left(\left[\rho, \rho_I\right]; \vec{r}\right) = v_s^{KS}\left(\left[\rho\right]; \vec{r}\right) + v_T^I\left(\left[\rho, \rho_I\right]; \vec{r}\right), \qquad (I = A, B) \qquad (7.17)$$

differing from the KS potential, $v_s^{KS}\left(\left[\rho\right]; \vec{r}\right)$, by an additional term, called the nonadditive kinetic potential (v_T), defined here for the respective subsystems as

$$v_T^I\left(\left[\rho, \rho_I\right]; \vec{r}\right) = \frac{\delta T_s[\rho]}{\delta \rho(\vec{r})} - \frac{\delta T_s[\rho_I]}{\delta \rho_I(\vec{r})}, \qquad (I = A, B) \qquad (7.18)$$

Eqs. (7.13) and (7.14) are solved iteratively on the assumption of equilibrium between subsystems. In thermodynamic terms, this implies that their chemical potentials or Lagrange multipliers must be equal; that is,

$$\mu_A = \mu_B = \mu \qquad (7.17)$$

KS eigenvalue problems similar to Eq. (7.7) are solved for the subsystems but with the KS potential, $v_s^{KS}\left(\left[\rho\right]; \vec{r}\right)$, replaced with the effective potentials defined in Eq. (7.17) that take into account effects of subsystems on each other. The optimized sets of

KS orbitals for the subsystems are used to obtain their respective densities according to Eq. (7.8). In this process, subsystems' KS orbitals are either expanded over basis functions centered on all nuclei of the system (termed "supermolecular basis" or KSCED(s) [72]) or over basis functions centered on the nuclei of the subsystem in question (termed "monomer basis" or KSCED(m) [302]). The energy functional of the total system is minimized (as in Eq. (7.12)) by optimizing either the density of subsystem A with fixed density of subsystem B or optimizing the densities of both subsystems iteratively to self-consistency. The former approach is termed frozen density embedding (FDE) [302, 303], and has been successfully applied to the study of weak interactions like solvent effects [304, 305]. The latter approach involves fixing (freezing) the density of one subsystem, optimizing the other and vice versa (until self-consistency is achieved) in what is often termed freeze-and-thaw cycles [72]. In these optimizations, however, the final total density is not guaranteed to be the correct one. In particular, the density tends to be underestimated at the interface between subsystems. To overcome this limitation within FDE, Gritsenko and Visscher [306] have recently proposed the density-orbital embedding (DOE) scheme which affords the correct total density, $\rho_{tot}(\vec{r})$, even in regions where $\rho_B(\vec{r})$ may exceed $\rho_{tot}(\vec{r})$, by allowing the so-called density orbital defined for the embedded subsystem to be negative in such situations. This approach is said to broaden the range of admissible $\rho_B(\vec{r})$ in FDE. It remains to be shown how well this proposed scheme reproduces the total density particularly at the interface between subsystems.

Discrepancies in both the FDE and freeze-and-thaw recipes have long been attributed to inaccuracies in the nonadditive kinetic energy potential (v_T) that contributes

to the embedding potential. Different kinetic energy functionals [307, 308] have been used for v_T and have yielded satisfactory results in weakly bound systems [308-311]. These approximations, however, fail for more strongly interacting subsystems [311-314] and can produce counterintuitive results, e.g., for all the complexes considered in Ref. [315], KSCED calculations using generalized gradient approximation (GGA) functionals led to worse molecular geometries than did the KSCED local density approximation (LDA), whereas conventional KS-DFT GGA calculations improved such geometries.

Efforts to improve DFT-in-DFT embedding theory are ongoing. Most of these efforts revolve around obtaining improved approximations to v_T [314], seeking an exact form of v_T [316], or avoiding it completely by resorting to a formalism in which a unique embedding potential is used which is common to interacting subsystems. In this regard, the emb-OEP (optimized effective potential) scheme [69, 70] was realized as well as partition DFT (PDFT) [317]. Both emb-OEP and PDFT seek a unique embedding (or partition) potential that makes subsystems' densities satisfy Eq. (1.5). The emb-OEP scheme uses an extended Wu-Yang functional [318, 319], defined as

$$W[V_{emb}] = \sum_{i=A,B} E_i[\rho_i] + \int V_{emb}(\vec{r})\left(\sum_{i=A,B}\rho_i - \rho_{ref}\right) dr^3 \tag{7.18}$$

where ρ_{ref} is the density of the total system, initially determined in a KS-DFT calculation; ρ_i are densities of subsystems; while V_{emb} is the embedding potential sought for and is the Lagrange multiplier for the density constraint in Eq. (1.5). In PDFT, a partition potential similar to V_{emb} is determined iteratively [317]. Although initial tests of these techniques on small systems were appealing, they appear computationally costly (e.g., both exact embedding [316] and emb-OEP [69, 70] require an initial determination of KS-orbitals

and density for the total system, while PDFT was shown in Ref. [317] to be more expensive than conventional KS-DFT (although the authors stated that their aim was only to reproduce the exact molecular density).

Enforcing External Orthogonality of Orbitals within DFT-in-DFT

The KS orbital sets

$$\left|\overline{\varphi}^A\right\rangle=\left|\varphi_1^A,\varphi_2^A,\cdots,\varphi_{N_A}^A\right\rangle, \text{ and } \left|\overline{\varphi}^B\right\rangle=\left|\varphi_1^B,\varphi_2^B,\cdots,\varphi_{N_B}^B\right\rangle \tag{7.19}$$

which define the subsystem densities

$$\rho_A(\vec{r})=\sum_{a=1}^{N_A}\left|\varphi_a^A(\vec{r})\right|^2, \qquad \rho_B(\vec{r})=\sum_{b=1}^{N_B}\left|\varphi_b^B(\vec{r})\right|^2, \tag{7.20}$$

must be orthogonal to each other (i.e., $\left\langle\overline{\varphi}^A\middle|\overline{\varphi}^B\right\rangle=0$) if the total density of the partitioned system is to be expressed as a sum of fragment densities, $\rho(\vec{r})=\rho_A(\vec{r})+\rho_B(\vec{r})$ (Eq. (1.5)). Although the electron density of a given system may be represented in several alternative ways using any chosen orbital set (see e.g., Ref. [320]), in the particular case where densities of subsystems within DFT-in-DFT embedding theory are described in diagonal quadratic form (Eq. (7.20)) using orthonormalized orbital sets, those orbital sets must be externally orthogonal for the total density to be expressed as a sum of fragment densities [5]. To justify this claim, suppose that the composite orbital set $\left|\overline{\varphi}\right\rangle=\left|\overline{\varphi}^A,\overline{\varphi}^B\right\rangle$ is considered within the total space ($L_{\overline{\varphi}}$), where $\left|\overline{\varphi}^A\right\rangle$ and $\left|\overline{\varphi}^B\right\rangle$ are orthonormalized sets of orbitals of subsystems A and B, respectively (given in Eq. (7.19)). Then, using symmetric orthogonalization [79], an orthonormal orbital set can be constructed within $L_{\overline{\varphi}}$ as

$$\left|\overline{\varphi}^{orth}\right\rangle=\left|\overline{\varphi}\right\rangle\mathbf{S}^{-\frac{1}{2}}, \tag{7.21}$$

where $\mathbf{S}$ is the overlap matrix in terms of the composite set $|\overline{\varphi}\rangle = |\overline{\varphi}^A, \overline{\varphi}^B\rangle$,

$$\mathbf{S} = \langle\overline{\varphi}|\overline{\varphi}\rangle = \begin{pmatrix} \mathbf{I}_{AA} & \mathbf{S}_{AB} \\ \mathbf{S}_{BA} & \mathbf{I}_{BB} \end{pmatrix} \tag{7.22}$$

In terms of the orthonormal set, $|\overline{\varphi}^{\,\mathrm{orth}}\rangle$, the total density can then be expressed as

$$\rho_A(\mathbf{r}) + \rho_B(\mathbf{r}) = \sum_{k,l=1}^{N} \varphi_k^{\mathrm{orth}}(\mathbf{r}) \mathbf{S}_{kl} \varphi_l^{\mathrm{orth*}}(\mathbf{r}) = \sum_{k=1}^{N} \left|\varphi_k^{\mathrm{orth}}(\mathbf{r})\right|^2 + \sum_{k,l=1}^{N} \varphi_k^{\mathrm{orth}}(\mathbf{r})(\mathbf{S}-\mathbf{I})_{kl} \varphi_l^{\mathrm{orth*}}(\mathbf{r}) \tag{7.23}$$

Thus, for any given sets of orbitals, $|\overline{\varphi}^A\rangle$ and $|\overline{\varphi}^B\rangle$, the sum $\rho_A(\mathbf{r}) + \rho_B(\mathbf{r})$ can be represented in diagonal quadratic form only if $\mathbf{S} = \mathbf{I}$; that is, when the orbitals are externally orthogonal (i.e., $\langle\overline{\varphi}^A|\overline{\varphi}^B\rangle = 0$) such that (in Eq. (7.22)), $\mathbf{S}_{AB} = \mathbf{S}_{BA} = \mathbf{0}$. Failure to ensure this external or intersystem orbital orthogonality condition leads to poor estimates of the total density particularly in situations where subsystems' densities interact strongly, which then puts a strong burden on the exchange-correlation and/or kinetic energy functionals to compensate. The new embedding protocol described herein enforces the external orbital orthogonality condition to guarantee that the density is indeed representable as a sum of fragment densities. The next paragraphs describe how this is done.

A Lagrangian is constructed [5] that involves two sets of constraints on subsystems' orbitals: their internal orthonormality and their external orthogonality, viz.

$$\Omega[\overline{\varphi}^A, \overline{\varphi}^B] = E^S[\overline{\varphi}^A, \overline{\varphi}^B] - \sum_{I=A,B}\sum_{c,c'=1}^{N_I} \Theta_{cc'}^I \langle\varphi_c^I|\varphi_{c'}^I\rangle$$
$$- \sum_{a=1}^{N_A}\sum_{b=1}^{N_B} \alpha_{ba} \langle\varphi_a^A|\varphi_b^B\rangle - \sum_{a=1}^{N_A}\sum_{b=1}^{N_B} \beta_{ab} \langle\varphi_b^B|\varphi_a^A\rangle \tag{7.24}$$

The first term on the right hand side of Eq. (7.24) is the energy functional for the total system expressed as a functional of subsystems' orbital sets; the second term is related to

the constraint of internal orbital orthonormality ($\langle \varphi_i^I | \varphi_j^I \rangle = \delta_{ij}$ where I = A or B while δ_{ij} is Kronecker's delta); the last two terms express the constraint of intersystem or external orbital orthogonality; $\Theta_{cc'}, \alpha_{ba}$, and β_{ab} are Lagrange multipliers associated with the constraints. Physically, $\langle \varphi_a^A | \varphi_b^B \rangle$ (or $\langle \varphi_b^B | \varphi_a^A \rangle$) represent the subspace of projected orbitals of subsystem B onto subsystem A (or of A onto B). Such projections equal zero in the case of external orthogonality. Although orbitals of a given system are not required to be orthonormal in order to represent the system's density, internal orthonormality of orbitals is a constraint that is used in deriving both the conventional KS-DFT and DFT-in-DFT embedding equations (i.e., KSCED), and this constraint is used also in constructing the Lagrangian in Eq. (7.24).

Considering small variations in the Lagrangian in Eq. (7.24) with respect to subsystems' orbitals to be zero, leads to the new embedding equations. For example, considering variations with respect to $\langle \varphi_a^A |$ results in

$$\left[h^{KS} + v_T^A \right] \varphi_a^A \rangle = \sum_{a'}^{N_A} | \varphi_{a'}^A \rangle \Theta_{a'a}^A + \sum_{b=1}^{N_B} | \varphi_b^B \rangle \alpha_{ba} \quad \left(a \in \left[1, N_A \right] \right) \tag{7.25}$$

Since the total energy is invariant with respect to unitary orbital transformations within subsystems, a canonical set of orbitals, $|\bar{\varphi}^A\rangle$, may be assumed (for which $\Theta_{aa'}^A = \delta_{aa'} \varepsilon_a^A$. N. B. a canonical set of orbitals, $|\bar{\varphi}^A\rangle$, diagonalizes the Hamiltonian on the left hand side of Eq. (7.25) such that multiplying Eq. (7.25) from the left by $\langle \varphi_{a'}^A |$ gives $\delta_{a'a} \varepsilon_a^A$ on the left hand side and $\Theta_{aa'}^A$ on the right hand side). By assuming canonical orbitals, Eq. (7.25) can be recast as

$$\left[h^{KS} + v_T^A\right]\varphi_a^A\rangle = \left|\varphi_a^A\right\rangle\varepsilon_a^A + \sum_{b=1}^{N_B}\left|\varphi_b^B\right\rangle\alpha_{ba} \quad \left(a \in \left[1, N_A\right]\right) \tag{7.26}$$

Multiplying Eq. (7.26) from the left by $\left\langle\varphi_{b'}^B\right|$ leads to

$$\left\langle\varphi_{b'}^B\right|\left[h^{KS} + v_T^A\right]\varphi_a^A\rangle = \left\langle\varphi_{b'}^B\middle|\varphi_a^A\right\rangle\varepsilon_a^A + \left\langle\varphi_{b'}^B\middle|\sum_{b=1}^{N_B}\middle|\varphi_b^B\right\rangle\alpha_{ba} = 0 + \delta_{b'b}\alpha_{ba}\ , \tag{7.27}$$

where 0 results from the external orthogonality condition (i.e., $\left\langle\varphi_b^B\middle|\varphi_a^A\right\rangle = 0$) while $\delta_{b'b}$

results from the internal orthonormality condition ($\left\langle\varphi_{b'}^B\middle|\varphi_b^B\right\rangle = \delta_{b'b}$). Hence,

$$\alpha_{ab} = \alpha_{ba} = \left\langle\varphi_b^B\middle|h^{KS} + v_T^A\middle|\varphi_a^A\right\rangle \tag{7.28}$$

Substituting Eq. (7.28) in Eq. (7.26) and rearranging leads to

$$\left(I - P^B\right)\left[h^{KS} + v_T^A\right]\varphi_a^A\rangle = \left|\varphi_a^A\right\rangle\varepsilon_a^A \tag{7.29}$$

Similar arguments lead to

$$\beta_{ab} = \beta_{ba} = \left\langle\varphi_a^A\middle|h^{KS} + v_T^B\middle|\varphi_b^B\right\rangle\ , \tag{7.30}$$

and then

$$\left(I - P^A\right)\left[h^{KS} + v_T^B\right]\varphi_b^B\rangle = \left|\varphi_b^B\right\rangle\varepsilon_b^B \tag{7.31}$$

for the complementary subsystem B, where v_T^A and v_T^B are defined in Eq. (7.18) and

$P^B = \left|\overline{\varphi}^B\right\rangle\left\langle\overline{\varphi}^B\right| = \sum_{b=1}^{N_B}\left|\varphi_b^B\right\rangle\left\langle\varphi_b^B\right|$ is the projector on the KS orbitals of subsystem B (P^A is

defined similarly). Since, in general, v_T^A and v_T^B are not equal, Eqs. (7.28) and (7.30)

cannot likewise be equal, in general. The modified one-electron Hamiltonians in Eqs.

(7.29) and (7.31), $\left(I - P^B\right)\left[h^{KS} + v_T^A\right]$ and $\left(I - P^A\right)\left[h^{KS} + v_T^B\right]$, are asymmetric. However,

transforming them to symmetric form is straightforward and accomplished by first noting

that under the external orthogonality constraint, $\left(I-P^B\right)\left|\overline{\varphi}^A\right\rangle=\left|\overline{\varphi}^A\right\rangle$ and $\left(I-P^A\right)\left|\varphi_b^B\right\rangle=\left|\varphi_b^B\right\rangle$. Thus Eqs. (7.29) and (7.31) can be recast (in hermitian form) as

$$\left(I-P^B\right)\left[h^{KS}+v_T^A\right]\left(I-P^B\right)\left|\varphi_a^A\right\rangle=\left|\varphi_a^A\right\rangle\varepsilon_a^A,\tag{7.32}$$

and

$$\left(I-P^A\right)\left[h^{KS}+v_T^B\right]\left(I-P^A\right)\left|\varphi_b^B\right\rangle=\left|\varphi_b^B\right\rangle\varepsilon_b^B\tag{7.33}$$

In Eqs. (7.29) and (7.31) to (7.33), I represents the identity operator within the total one-electron space, and is defined as

$$I=I_T=\left|\overline{\chi}_T\right\rangle S_{TT}^{-1}\left\langle\overline{\chi}_T\right|,\ \ \left(I_T\right)^2=I_T,\tag{7.34}$$

where $\overline{\chi}_T$ is a set of atomic basis functions, that span the total space, with overlap matrix $S_{TT}=\left\langle\overline{\chi}_T\middle|\overline{\chi}_T\right\rangle$.

As shown in Eqs. (7.32) and (7.33), the new embedding equations require the KS orbital sets for subsystems A and B to be eigenvectors of the reduced Hamiltonians $\left(I-P^B\right)\left[h^{KS}+v_T^A\right]\left(I-P^B\right)$ and $\left(I-P^A\right)\left[h^{KS}+v_T^B\right]\left(I-P^A\right)$ unlike in conventional DFT-in-DFT embedding equations where subsystems' orbitals are eigenvectors of the modified Hamiltonians $\left[h^{KS}+v_T^I\right]$ (I = A or B). Eqs. (7.28) and (7.30) indicate that the new equations involve explicit interactions between orbitals of subsystems (this is not required in standard KSCED).

In the case of supermolecular basis expansion, KS orbitals of each subsystem are expanded in terms of the set $\left|\overline{\chi}_T\right\rangle$ as

$$\left|\overline{\varphi}^A\right\rangle=\left|\overline{\chi}_T\right\rangle\mathbf{C}^A,\qquad\left|\overline{\varphi}^B\right\rangle=\left|\overline{\chi}_T\right\rangle\mathbf{C}^B,\tag{7.35}$$

where $\mathbf{C}^A = \mathbf{C}^A_{TN_A} = \left\| C^A_{\mu a} \right\|$ and $\mathbf{C}^B = \mathbf{C}^B_{TN_B} = \left\| C^B_{\mu b} \right\|$ (where indices $a \in [1, N_A]$ and

$b \in [1, N_B]$ enumerate occupied orbitals of the subsystems A and B, respectively, while μ

enumerates atomic orbitals from the set $\bar{\chi}_T$). Multiplying Eqs. (7.32) and (7.33) from the

left by $\langle \bar{\chi}_T |$, and using Eqs. (7.34) and (7.35), leads to the matrix equations

$$\left(\mathbf{R}^B_{TT} \right)^\dagger \mathbf{h}^A_{TT} \mathbf{R}^B_{TT} \mathbf{C}^A = \mathbf{S}_{TT} \mathbf{C}^A \boldsymbol{\varepsilon}^A, \qquad (7.36)$$

$$\left(\mathbf{R}^A_{TT} \right)^\dagger \mathbf{h}^B_{TT} \mathbf{R}^A_{TT} \mathbf{C}^B = \mathbf{S}_{TT} \mathbf{C}^B \boldsymbol{\varepsilon}^B, \qquad (7.37)$$

where

$$\mathbf{R}^L_{TT} = \mathbf{S}^{-1}_{TT} \langle \bar{\chi}_T | I - P^L | \bar{\chi}_T \rangle = \mathbf{I}_{TT} - \mathbf{D}^L_{TT} \mathbf{S}_{TT} \qquad (L = A, B) \qquad (7.38)$$

and

$$\mathbf{D}^L_{TT} = \left[\mathbf{C}^L \left(\mathbf{C}^L \right)^\dagger \right]_{TT} = \left\| D^L_{\mu \nu} \right\|, \qquad D^L_{\mu \nu} = \sum_{i=1}^{N_L} C^L_{\mu i} C^L_{\nu i} \qquad (L = A, B) \qquad (7.39)$$

is the density matrix of the L-th subsystem in the supermolecular atomic basis.

The case of Monomer and Extended Monomer Basis Expansions

In practice, it is computationally more costly to perform embedding calculations

with supermolecular basis set expansions (KSCED(s)) compared with conventional KS-

DFT on the total system. A good embedding scheme should provide a fair cost to

accuracy ratio. Unfortunately, use of monomer basis expansions (KSCED(m)), except

for cases of very weakly interacting systems, often lead to less accurate results than those

from KSCED(s) [6]. In the development of a new variant of DFT-in-DFT embedding

theory, a new way of expanding subsystems' KS orbitals was proposed, referred to as the

"extended monomer basis expansions," (KSCED(e)). In this novel one particle space

approach, KS orbitals of each subsystem are expanded not only over atomic basis

functions centered on atoms of the subsystem (as is done in KSCED(m)) but also over atomic functions centered on atoms in the complementary subsystem close to the boundary or interfacial region. To clarify this, consider the pictorial representation in Figure 29.
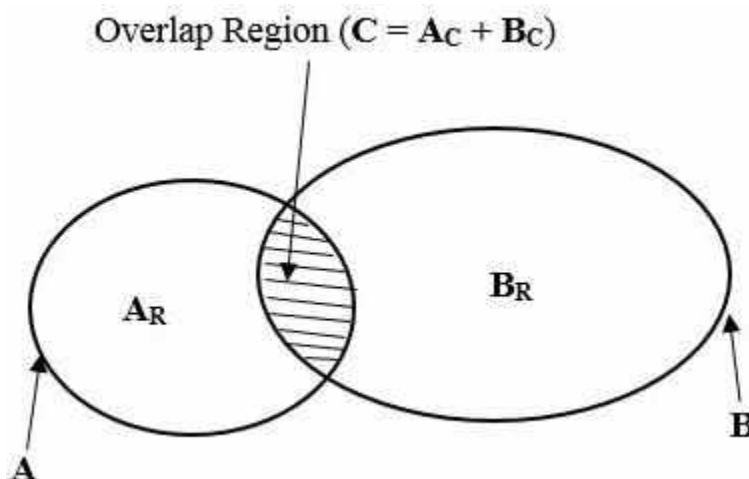
Figure 29. Schematic diagram illustrating extended monomer Bases.

Suppose that nuclei of subsystem A are described as $A = A_R + A_C$ and those of subsystem B as $B = B_C + B_R$ where $C = A_C + B_C$ represents nuclei within the overlap region between A and B whose atomic basis functions are used in the expansion of orbitals of both subsystems. Atomic functions in the supermolecular basis set can be ordered as

$$\left| \bar{\chi}_T \right\rangle = \left| \bar{\chi}_{A_R}, \bar{\chi}_{A_C}, \bar{\chi}_{B_C}, \bar{\chi}_{B_R} \right\rangle = \left| \bar{\chi}_{A_R}, \bar{\chi}_C, \bar{\chi}_{B_R} \right\rangle, \qquad (7.35)$$

while those in the subsystem-specific "extended monomer" basis sets are described as

$$\left| \bar{\chi}_A \right\rangle = \left| \bar{\chi}_{A_R}, \bar{\chi}_C \right\rangle, \quad \left| \bar{\chi}_B \right\rangle = \left| \bar{\chi}_C, \bar{\chi}_{B_R} \right\rangle, \qquad (7.36)$$

where $|\bar{\chi}_C\rangle = |\bar{\chi}_{A_C}, \bar{\chi}_{B_C}\rangle$ is the set of atomic orbitals centered on all nuclei of the overlap region. KS orbitals of the subsystems are expanded over these bases. It should be noted that partitioning of a system (as well as defining an overlap region between subsystems) is arbitrary. Whereas Eqs. (7.32) and (7.33) are suitable for KSCED(s) calculations, in the case of KSCED(m) and KSCED(e) calculations, additional modifications must be made since for such cases, the KS orbitals, $|\bar{\varphi}^A\rangle$ and $|\bar{\varphi}^B\rangle$, belong to different (overlapping) subspaces. For such situations, the sets $|\bar{\varphi}^A\rangle$ and $|\bar{\varphi}^B\rangle$ are now expanded over the newly defined atomic basis sets,

$$|\bar{\varphi}^A\rangle = |\bar{\chi}_A\rangle \mathbf{C}^A, \qquad |\bar{\varphi}^B\rangle = |\bar{\chi}_B\rangle \mathbf{C}^B, \qquad (7.37)$$

These expansions involve the new matrices: $\mathbf{C}^A = \mathbf{C}^A_{AN_A} = \left\| C^A_{\mu_A a} \right\|$, where $a \in [1, N_A]$ and μ_A is the index over atomic orbitals from the set $\bar{\chi}_A$; and $\mathbf{C}^B = \mathbf{C}^B_{BN_B} = \left\| C^B_{\mu_B b} \right\|$, where $b \in [1, N_B]$ and μ_B is the index over atomic orbitals from $\bar{\chi}_B$.

Within the subspaces $L_A = Span\{\bar{\chi}_A\}$ and $L_B = Span\{\bar{\chi}_B\}$, the following operators may be constructed

$$I_A = |\bar{\chi}_A\rangle \mathbf{S}^{-1}_{AA} \langle \bar{\chi}_A| \quad \Leftrightarrow \quad I_A |\bar{\chi}_A\rangle = |\bar{\chi}_A\rangle, \qquad (7.38)$$

and

$$I_B = |\bar{\chi}_B\rangle \mathbf{S}^{-1}_{BB} \langle \bar{\chi}_B| \quad \Leftrightarrow \quad I_B |\bar{\chi}_B\rangle = |\bar{\chi}_B\rangle, \qquad (7.39)$$

where I_A and I_B are projectors onto the subspaces $L_A = Span\{\bar{\chi}_A\}$, spanned by the set $\bar{\chi}_A$, and $L_B = Span\{\bar{\chi}_B\}$, spanned by $\bar{\chi}_B$; $\mathbf{S}_{AA} = \langle \bar{\chi}_A | \bar{\chi}_A \rangle$ and $\mathbf{S}_{BB} = \langle \bar{\chi}_B | \bar{\chi}_B \rangle$ are overlap

matrices associated with $\bar{\chi}_A$ and $\bar{\chi}_B$. The present projectors and that in Eq. (7.34) satisfy the conditions

$$(I_A)^2 = I_A, \qquad (I_B)^2 = I_B, \qquad I_T I_A = I_A I_T = I_A, \qquad I_T I_B = I_B I_T = I_B \qquad (7.40)$$

and additionally,

$$I_A \left| \bar{\varphi}^A \right\rangle = \left| \bar{\varphi}^A \right\rangle, \qquad I_B \left| \bar{\varphi}^B \right\rangle = \left| \bar{\varphi}^B \right\rangle \qquad (7.41)$$

Eqs. (7.32) and (7.33) are rewritten using the new projectors as

$$I_A \left(I - P^B \right) I_T h^A I_A \left| \bar{\varphi}^A \right\rangle = \left| \bar{\varphi}^A \right\rangle \varepsilon^A, \qquad (7.42)$$

$$I_B \left(I - P^A \right) I_T h^B I_B \left| \bar{\varphi}^B \right\rangle = \left| \bar{\varphi}^B \right\rangle \varepsilon^B, \qquad (7.43)$$

considering that, in the general case, $h^L I_L = I_T h^L I_L \;\; (L = A, B)$.

Since the sets $\left| \bar{\varphi}^A \right\rangle$ and $\left| \bar{\varphi}^B \right\rangle$, belong to different (overlapping) subspaces in the case of KSCED(m) and KSCED(e), this implies that not all orbitals from the set $\left| \bar{\varphi}^B \right\rangle$, if any, have a non-zero projection on $L_A = Span\{\bar{\chi}_A\}$ (and vice versa). Consequently the matrix

$$\Delta^B_{N_B N_B} = \left\langle \bar{\varphi}^B \left| I_A \right| \bar{\varphi}^B \right\rangle = \left(C^B_{BN_B} \right)^+ S_{BA} S^{-1}_{AA} S_{AB} C^B_{BN_B} \qquad (7.44)$$

can be singular. To avoid singularity problems and guarantee intersystem orthogonality, only linear combinations of the projected orbitals $I_A \left| \bar{\varphi}^B \right\rangle$ onto the space $L_A = Span\{\bar{\chi}_A\}$, which have non-zero projections, $\left| \bar{\bar{\varphi}}^B \right\rangle$, need be considered

$$\left| \bar{\bar{\varphi}}^B \right\rangle = I_A \left| \bar{\bar{\varphi}}^B \right\rangle = \left| \tilde{\varphi}^B_1, \tilde{\varphi}^B_1, \ldots, \tilde{\varphi}^B_{\tilde{N}_B} \right\rangle \qquad (7.45)$$

If there are such vectors, their number $\tilde{N}_B \left(\text{where } 0 \leq \tilde{N}_B \leq N_B \right)$, would be equal to the number of eigenvectors of the matrix $\left\langle \bar{\varphi}^B \left| I_A \right| \bar{\varphi}^B \right\rangle$. Such vectors would span a subspace

181

$L_A(\bar{\bar{\varphi}}^B) = Span\{\bar{\bar{\varphi}}^B\}$ within $L_A = Span\{\bar{\chi}_A\}$. In this subspace, the following projector may be defined

$$P^{\bar{\bar{\varphi}}^B} = I_A P^{\bar{\bar{\varphi}}^B} I_A = I_A |\bar{\bar{\varphi}}^B\rangle \langle \bar{\bar{\varphi}}^B | I_A | \bar{\bar{\varphi}}^B\rangle^{-1} \langle \bar{\bar{\varphi}}^B | I_A \qquad (7.46)$$

An analogous projector, $P^{\bar{\bar{\varphi}}^A}$, can be defined also for the subspace $L_B(\bar{\bar{\varphi}}^A) = Span\{\bar{\bar{\varphi}}^A\}$

within $L_B = Span\{\bar{\chi}_B\}$ of non-zero projections $I_B|\bar{\varphi}^A\rangle$ of the set $|\bar{\varphi}^A\rangle$ onto

$L_B = Span\{\bar{\chi}_B\}$. These new projectors, $P^{\bar{\bar{\varphi}}^A}$ and $P^{\bar{\bar{\varphi}}^B}$, replace P^A and P^B in Eqs. (7.42) and (7.43).

The orbital set $|\bar{\bar{\varphi}}^B\rangle$ in Eq. (7.45) is obtained by diagonalizing the matrix $\mathbf{\Delta}^B_{N_B N_B}$

and selecting its $\tilde{N}_B$ eigenvectors with non-zero eigenvalues. Thus, one writes

$$\left(\mathbf{V}^B_{N_B N_B}\right)^\dagger \langle \bar{\varphi}^B | I_A | \bar{\varphi}^B \rangle \mathbf{V}^B_{N_B N_B} = \mathbf{d}^B_{N_B}, \qquad (7.47)$$

where $\mathbf{d}^B_{N_B}$ is the diagonal matrix with eigenvalues and $\mathbf{V}^B_{N_B N_B}$ is an orthogonal matrix of

eigenvectors of $\mathbf{\Delta}^B_{N_B N_B}$. If upon diagonalizing $\mathbf{\Delta}^B_{N_B N_B}$, $\tilde{N}_B$ non-zero eigenvalues are

found, $\{d^B_i > 0\}_{i=1}^{\tilde{N}_B}$, then the eigenvectors in $\mathbf{V}^B_{N_B N_B}$ and the corresponding eigenvalues in

$\mathbf{d}^B_{N_B}$ can be reordered such that eigenvectors with non-zero eigenvalues are listed first,

$\mathbf{d}^B_{N_B} = diag\{d^B_1,...,d^B_{\tilde{N}_B},0,...,0\}$. With this reordering, the eigenvectors with zero

eigenvalues (which are listed last) can be ignored and Eq. (7.47) rewritten only in terms

of eigenvectors of $\mathbf{\Delta}^B_{N_B N_B}$ with non-zero eigenvalues, viz.

$$\left(\mathbf{V}^B_{N_B \tilde{N}_B}\right)^\dagger \langle \bar{\varphi}^B | I_A | \bar{\varphi}^B \rangle \mathbf{V}^B_{N_B \tilde{N}_B} = \mathbf{d}^B_{\tilde{N}_B} \qquad (7.48)$$

$\mathbf{V}^B_{N_B \tilde{N}_B}$ now contains only eigenvectors of $\mathbf{\Delta}^B_{N_B N_B}$ with non-zero eigenvalues while $\mathbf{d}^B_{\tilde{N}_B} = diag\{\mathbf{d}^B_1, \ldots, \mathbf{d}^B_{\tilde{N}_B}\}$ are the corresponding positive eigenvalues. Eq. (7.48) leads to the desired orthonormal set,

$$\left| \overline{\overline{\varphi}}^B \right\rangle = I_A \left| \overline{\varphi}^B \right\rangle \mathbf{V}^B_{N_B \tilde{N}_B} \left(\mathbf{d}^B_{\tilde{N}_B} \right)^{-\frac{1}{2}} = \left| \overline{\chi}_A \right\rangle \mathbf{U}^B_{A\tilde{N}_B}, \qquad \left\langle \widetilde{\varphi}^B \middle| \widetilde{\varphi}^B \right\rangle = \mathbf{I}_{\tilde{N}_B \tilde{N}_B} \qquad (7.49)$$

where matrix $\mathbf{U}^B_{A\tilde{N}_B}$ determines the expansion of vectors $\left| \overline{\overline{\varphi}}^B \right\rangle$ within $L_A = Span\{\overline{\chi}_A\}$ and has the form

$$\mathbf{U}^B_{A\tilde{N}_B} = \mathbf{S}^{-1}_{AA} \left\langle \overline{\chi}_A \middle| \overline{\overline{\varphi}}^B \right\rangle = \mathbf{S}^{-1}_{AA} \mathbf{S}_{AB} \mathbf{C}^B_{BN_B} \mathbf{V}^B_{N_B \tilde{N}_B} \left(\mathbf{d}^B_{\tilde{N}_B} \right)^{-\frac{1}{2}} \qquad (7.50)$$

Eq. (7.46) can be rewritten in terms of the definition of $\left| \overline{\overline{\varphi}}^B \right\rangle$ given in Eq. (7.49) as

$$\mathbf{P}^{\overline{\overline{\varphi}}^B} = I_A \mathbf{P}^{\overline{\overline{\varphi}}^B} I_A = I_A \left| \overline{\overline{\varphi}}^B \right\rangle \left\langle \overline{\overline{\varphi}}^B \middle| I_A \qquad (7.51)$$

An analogous definition to that in Eq. (7.49) for projected orbitals $I_B \left| \overline{\varphi}^A \right\rangle$ is

$$\left| \overline{\overline{\varphi}}^A \right\rangle = I_B \left| \overline{\varphi}^A \right\rangle \mathbf{V}^A_{N_A \tilde{N}_A} \left(\mathbf{d}^A_{\tilde{N}_A} \right)^{-\frac{1}{2}} = \left| \overline{\chi}_B \right\rangle \mathbf{U}^A_{B\tilde{N}_A}, \qquad \left\langle \overline{\overline{\varphi}}^A \middle| \overline{\overline{\varphi}}^A \right\rangle = \mathbf{I}_{\tilde{N}_A \tilde{N}_A} \qquad (7.52)$$

where $\mathbf{V}^A_{N_A \tilde{N}_A}$ is the matrix of the eigenvectors of matrix $\mathbf{\Delta}^A_{N_A N_A}$ that have non-zero eigenvalues while $\mathbf{d}^A_{\tilde{N}_A} = diag\{\mathbf{d}^A_1, \ldots, \mathbf{d}^A_{\tilde{N}_A}\} \ \left(0 \leq \tilde{N}_A \leq N_A \right)$ are the corresponding positive eigenvalues. Matrix $\mathbf{U}^A_{B\tilde{N}_A}$ determines the expansion of vectors $\left| \overline{\overline{\varphi}}^A \right\rangle$ within $L_B = Span\{\overline{\chi}_B\}$, where $\mathbf{\Delta}^A_{N_A N_A}$ and $\mathbf{U}^A_{B\tilde{N}_A}$ are defined as

$$\mathbf{\Delta}^A_{N_A N_A} = \left\langle \overline{\varphi}^A \middle| I_B \middle| \overline{\varphi}^A \right\rangle = \left(\mathbf{C}^A_{AN_A} \right)^+ \mathbf{S}_{AB} \mathbf{S}^{-1}_{BB} \mathbf{S}_{BA} \mathbf{C}^A_{AN_A}, \qquad (7.53)$$

and

$$\mathbf{U}^A_{B\tilde{N}_A} = \mathbf{S}^{-1}_{BB} \left\langle \overline{\chi}_B \middle| \overline{\overline{\varphi}}^A \right\rangle = \mathbf{S}^{-1}_{BB} \mathbf{S}_{BA} \mathbf{C}^A_{AN_A} \mathbf{V}^A_{N_A \tilde{N}_A} \left(\mathbf{d}^A_{\tilde{N}_A} \right)^{-\frac{1}{2}} \qquad (7.54)$$

An analogous projector to that in Eq. (7.51) can thus be defined with respect to the set $\left|\overline{\overline{\varphi}}^A\right\rangle$ as

$$P^{\overline{\overline{\varphi}}^A} = I_B P^{\overline{\overline{\varphi}}^A} I_B = I_B \left|\overline{\overline{\varphi}}^A\right\rangle\left\langle\overline{\overline{\varphi}}^A\right| I_B \tag{7.55}$$

These new projectors, $P^{\overline{\overline{\varphi}}^A}$ and $P^{\overline{\overline{\varphi}}^B}$, satisfy the conditions

$$\left|\overline{\varphi}^A\right\rangle = \left(I_A - P^{\overline{\overline{\varphi}}^B}\right)\left|\overline{\varphi}^A\right\rangle \text{ and } \left|\overline{\varphi}^B\right\rangle = \left(I_B - P^{\overline{\overline{\varphi}}^A}\right)\left|\overline{\varphi}^B\right\rangle \tag{7.56}$$

Since $\left(I_A - P^{\overline{\overline{\varphi}}^B}\right)I_T = \left(I_A - P^{\overline{\overline{\varphi}}^B}\right)I_A$ and $\left(I_B - P^{\overline{\overline{\varphi}}^A}\right)I_T = \left(I_B - P^{\overline{\overline{\varphi}}^A}\right)I_B$, Eqs. (7.42) and (7.43)

recast in terms of $P^{\overline{\overline{\varphi}}^A}$ and $P^{\overline{\overline{\varphi}}^B}$ instead of P^A and P^B will have the forms

$$\left(I_A - P^{\overline{\overline{\varphi}}^B}\right)I_A h^A I_A \left|\overline{\varphi}^A\right\rangle = \left|\overline{\varphi}^A\right\rangle \varepsilon^A , \tag{7.57}$$

and

$$\left(I_B - P^{\overline{\overline{\varphi}}^A}\right)I_B h^B I_B \left|\overline{\varphi}^B\right\rangle = \left|\overline{\varphi}^B\right\rangle \varepsilon^B \tag{7.58}$$

Eqs. (7.57) and (7.58) can be written in hermitian form using Eq. (7.56) as

$$\left(I_A - P^{\overline{\overline{\varphi}}^B}\right)I_A h^A I_A \left(I_A - P^{\overline{\overline{\varphi}}^B}\right)\left|\overline{\varphi}^A\right\rangle = \left|\overline{\varphi}^A\right\rangle \varepsilon^A , \tag{7.59}$$

and

$$\left(I_B - P^{\overline{\overline{\varphi}}^A}\right)I_B h^B I_B \left(I_B - P^{\overline{\overline{\varphi}}^A}\right)\left|\overline{\varphi}^B\right\rangle = \left|\overline{\varphi}^B\right\rangle \varepsilon^B \tag{7.60}$$

which involve only the subsystem-specific matrices $h_{AA}^A = \left\langle\overline{\chi}_A\left|h^A\right|\overline{\chi}_A\right\rangle$ and

$h_{BB}^B = \left\langle\overline{\chi}_B\left|h^B\right|\overline{\chi}_B\right\rangle$, and take into account the interactions between the subsystems' orbitals

through the blocks the matrix blocks $\left\langle\overline{\varphi}^B\left|I_A h^A\right|\overline{\varphi}^A\right\rangle$ and $\left\langle\overline{\varphi}^A\left|I_B h^B\right|\overline{\varphi}^B\right\rangle$. It should be

noted that in the limiting case of the supermolecular basis expansion where $\overline{\chi}_A \to \overline{\chi}_T$ and

$\bar{\chi}_B \to \bar{\chi}_T$, the conditions $\left| \bar{\bar{\varphi}}^A \right\rangle \to \left| \bar{\varphi}^A \right\rangle$ and $\left| \bar{\bar{\varphi}}^B \right\rangle \to \left| \bar{\varphi}^B \right\rangle$ hold. Hence, the projectors $P^{\bar{\bar{\varphi}}^A}$

and $P^{\bar{\bar{\varphi}}^B}$ become P^A and P^B in Eqs. (7.32) and (7.33) (i.e., $P^{\bar{\bar{\varphi}}^A} \to P^A$ and $P^{\bar{\bar{\varphi}}^B} \to P^B$).

Projecting Eqs. (7.59) and (7.60) on $\left\langle \bar{\chi}_A \right|$ and $\left\langle \bar{\chi}_B \right|$, respectively, leads to the

matrix Eqs. (7.61) and (7.62) in terms of the expansion matrices, $\mathbf{C}^A = \mathbf{C}^A_{AN_A}$ and

$\mathbf{C}^B = \mathbf{C}^B_{BN_B}$, of Eq. (7.37),

$$\left(\mathbf{R}^B_{AA} \right)^{\dagger} \mathbf{h}^A_{AA} \mathbf{R}^B_{AA} \mathbf{C}^A = \mathbf{S}_{AA} \mathbf{C}^A \boldsymbol{\varepsilon}^A , \tag{7.61}$$

$$\left(\mathbf{R}^A_{BB} \right)^{\dagger} \mathbf{h}^B_{BB} \mathbf{R}^A_{BB} \mathbf{C}^B = \mathbf{S}_{BB} \mathbf{C}^B \boldsymbol{\varepsilon}^B , \tag{7.62}$$

where

$$\mathbf{R}^B_{AA} = \mathbf{S}^{-1}_{AA} \left\langle \bar{\chi}_A \left| I_A - P^{\bar{\bar{\varphi}}^B} \right| \bar{\chi}_A \right\rangle = \mathbf{I}_{AA} - \mathbf{U}^B_{A\tilde{N}_B} \left(\mathbf{U}^B_{A\tilde{N}_B} \right)^{\dagger} \mathbf{S}_{AA} , \tag{7.63}$$

$$\mathbf{R}^A_{BB} = \mathbf{S}^{-1}_{BB} \left\langle \bar{\chi}_B \left| I_B - P^{\bar{\bar{\varphi}}^A} \right| \bar{\chi}_B \right\rangle = \mathbf{I}_{BB} - \mathbf{U}^A_{B\tilde{N}_A} \left(\mathbf{U}^A_{B\tilde{N}_A} \right)^{\dagger} \mathbf{S}_{BB} \tag{7.64}$$

Again, in the limiting case of the supermolecular basis expansion where $\bar{\chi}_A \to \bar{\chi}_T$ and

$\bar{\chi}_B \to \bar{\chi}_T$, the conditions $\boldsymbol{\Delta}^L_{N_L N_L} \to \mathbf{I}_{N_L N_L}$, $\tilde{\mathbf{D}}^L_{LL} \to \mathbf{D}^L_{TT}$ $(L = A, B)$, $\mathbf{R}^B_{AA} \Rightarrow \mathbf{R}^B_{TT}$, and

$\mathbf{R}^A_{BB} \Rightarrow \mathbf{R}^A_{TT}$ hold. Hence, Eqs. (7.63) and (7.64) become equivalent to Eqs. (7.36) and

(7.37).

Decomposition of Subsystem Orbital Spaces: $L_A = Span\{\bar{\chi}_A\}$ *and* $L_B = Span\{\bar{\chi}_B\}$

Since only $\tilde{N}_B$ $\left(0 \le \tilde{N}_B \le N_B \right)$ orbitals of the set of N_B occupied environment

orbitals $\left| \bar{\varphi}^B \right\rangle$ have non-zero projections on the embedded subsystem's atomic orbital

space $L_A = Span\{\bar{\chi}_A\}$, the latter space may be divided into a direct sum of the subspace

spanned by the $\tilde{N}_B$ projected vectors, $L_A \left(\bar{\bar{\varphi}}^B \right)$, and its orthogonal complement, $L_A \left(\bar{\varphi}^A_{\perp} \right)$

$$L_A = L_A\left(\overline{\varphi}_\perp^A\right) \oplus L_A\left(\overline{\widetilde{\varphi}}^B\right), \tag{7.65}$$

Therefore for any given $\left|\overline{\varphi}^B\right\rangle$, the task is to find a set of N_A occupied embedded orbitals within $L_A\left(\overline{\varphi}_\perp^A\right)$ that would be automatically orthogonal to $\left|\overline{\varphi}^B\right\rangle$. This is accomplished as follows. Let the set of environment orbitals that have non-zero projections on the embedded subsystem, $\left|\overline{\widetilde{\varphi}}^B\right\rangle$, be fixed and let a reference set of orthonormal orbitals, $\left|\overline{\varphi}_{ref}^A\right\rangle$, (e.g., eigenvectors of the matrix $\left\langle \overline{\chi}_A \left| h_{core}^A \right| \overline{\chi}_A \right\rangle$ where h_{core}^A is the one-electron core Hamiltonian for subsystem A) within $L_A = Span\{\overline{\chi}_A\}$ be defined as

$$\left|\overline{\varphi}_{ref}^A\right\rangle = \left|\overline{\chi}_A\right\rangle \mathbf{C}_{AA}^{A,ref}, \qquad \left\langle \overline{\varphi}_{ref}^A \middle| \overline{\varphi}_{ref}^A \right\rangle = \mathbf{I}_{AA}, \tag{7.66}$$

where the matrix $\mathbf{C}_{AA}^{A,ref}$ determines the set of reference orthonormal functions in $L_A = Span\{\overline{\chi}_A\}$. Then, the desired set $\left|\overline{\varphi}_\perp^A\right\rangle$ of $M_\perp^A$-vectors orthogonal to $\left|\overline{\widetilde{\varphi}}^B\right\rangle$ can be written as

$$\left|\overline{\varphi}_\perp^A\right\rangle = \left(\mathbf{I}_A - \mathbf{P}^{\overline{\widetilde{\varphi}}^B}\right)\left|\overline{\varphi}_{ref}^A\right\rangle \mathbf{W}_{AM_\perp^A}^B = \left|\overline{\chi}_A\right\rangle \mathbf{R}_{AA}^B \mathbf{C}_{AA}^{A,ref} \mathbf{W}_{AM_\perp^A}^B, \tag{7.67}$$

where matrix $\mathbf{W}_{AM_\perp^A}^B$ is determined by the orthonormality condition

$$\left\langle \overline{\varphi}_\perp^A \middle| \overline{\varphi}_\perp^A \right\rangle = \left(\mathbf{W}_{AM_\perp^A}^B\right)^\dagger \mathbf{T}_{AA}^B \mathbf{W}_{AM_\perp^A}^B = \mathbf{I}_{M_\perp^A M_\perp^A}, \tag{7.68}$$

and

$$\mathbf{T}_{AA}^B = \left\langle \left(\mathbf{I}_A - \mathbf{P}^{\overline{\widetilde{\varphi}}^B}\right)\overline{\varphi}_{ref}^A \middle| \left(\mathbf{I}_A - \mathbf{P}^{\overline{\widetilde{\varphi}}^B}\right)\overline{\varphi}_{ref}^A \right\rangle = \left(\mathbf{R}_{AA}^B \mathbf{C}_{AA}^{A,ref}\right)^\dagger \mathbf{S}_{AA} \mathbf{R}_{AA}^B \mathbf{C}_{AA}^{A,ref} \tag{7.69}$$

If eigenvectors of matrix $\mathbf{T}_{AA}^B$ with zero eigenvalues are neglected, the following equation may be written

$$\left(\mathbf{O}_{AM_\perp^A}^B\right)^\dagger \mathbf{T}_{AA}^B \mathbf{O}_{AM_\perp^A}^B = \mathbf{t}_{M_\perp^A}^B, \tag{7.70}$$

where $\mathbf{O}^B_{AM^A_\perp}$ is the matrix of $M^A_\perp$ eigenvectors of $\mathbf{T}^B_{AA}$ that have positive eigenvalues, contained in the diagonal matrix $\mathbf{t}^B_{M^A_\perp} = diag\{\mathrm{t}^B_1,\ldots,\mathrm{t}^B_{M^A_\perp}\}$. Hence, the matrix $\mathbf{W}^B_{AM^A_\perp}$ appearing in Eq. (7.67) and (7.68), can be written in terms of $\mathbf{O}^B_{AM^A_\perp}$ and $\mathbf{t}^B_{M^A_\perp}$ as

$$\mathbf{W}^B_{AM^A_\perp} = \mathbf{O}^B_{AM^A_\perp}\left(\mathbf{t}^B_{M^A_\perp}\right)^{-\frac{1}{2}}, \tag{7.71}$$

and the desired orthonormal set $\left|\overline{\varphi}^A_\perp\right\rangle$ of the $M^A_\perp$-orbitals orthogonal to $\left|\overline{\overline{\varphi}}^B\right\rangle$ within $L_A = Span\{\overline{\chi}_A\}$ is determined by

$$\left|\overline{\varphi}^A_\perp\right\rangle = \left|\overline{\chi}_A\right\rangle\mathbf{C}^{A,\perp}_{AM^A_\perp}, \tag{7.72}$$

where

$$\mathbf{C}^{A,\perp}_{AM^A_\perp} = \mathbf{R}^B_{AA}\mathbf{C}^{A,\mathrm{ref}}_{AA}\mathbf{O}^B_{AM^A_\perp}\left(\mathbf{t}^B_{M^A_\perp}\right)^{-\frac{1}{2}} \tag{7.73}$$

Similarly, since only $\tilde{\mathrm{N}}_A$ $\left(0 \le \tilde{\mathrm{N}}_A \le \mathrm{N}_A\right)$ orbitals of the set of N_A occupied embedded orbitals $\left|\overline{\varphi}^A\right\rangle$ have non-zero projections on the embedded subsystem's atomic orbital space $L_B = Span\{\overline{\chi}_B\}$, the latter space may be divided into a direct sum of the subspace spanned by the $\tilde{\mathrm{N}}_A$ projected vectors, $L_B\left(\tilde{\overline{\varphi}}^A\right)$, and its orthogonal complement, $L_B\left(\overline{\varphi}^B_\perp\right)$

$$L_B = L_B\left(\overline{\varphi}^B_\perp\right) \oplus L_B\left(\tilde{\overline{\varphi}}^A\right) \tag{7.74}$$

By proceeding in the same manner as was done above in seeking a set of embedded orbitals within $L_A\left(\overline{\varphi}^A_\perp\right)$ orthogonal to projected environment orbitals, a complementary set $\left|\overline{\varphi}^B_\perp\right\rangle$ within the environment subsystem is determined by the equations

$$\left|\overline{\varphi}^B_\perp\right\rangle = \left|\overline{\chi}_B\right\rangle\mathbf{C}^{B,\perp}_{BM^B_\perp}, \tag{7.75}$$

$$\mathbf{C}_{BM_\perp^B}^{B,\perp} = \mathbf{R}_{BB}^A \mathbf{C}_{BB}^{B,ref} \mathbf{O}_{BM_\perp^B}^A \left(\mathbf{t}_{M_\perp^B}^A \right)^{-\frac{1}{2}}, \tag{7.76}$$

where matrix $\mathbf{C}_{BB}^{B,ref}$ determines the set of reference orthonormal functions in $L_B = Span\{\bar{\chi}_B\}$,

$$\left| \bar{\varphi}_{ref}^B \right\rangle = \left| \bar{\chi}_B \right\rangle \mathbf{C}_{BB}^{B,ref}, \qquad \left\langle \bar{\varphi}_{ref}^B \middle| \bar{\varphi}_{ref}^B \right\rangle = \mathbf{I}_{BB}, \tag{7.77}$$

In Eq. (7.76), $\mathbf{t}_{M_\perp^B}^A = diag\left\{ t_1^A, \ldots, t_{M_\perp^B}^A \right\}$ is the diagonal matrix of the $M_\perp^B$ positive eigenvalues and $\mathbf{O}_{BM_\perp^B}^A$ is the matrix of the corresponding eigenvectors of the symmetric and semi-positive definite matrix

$$\mathbf{T}_{BB}^A = \left\langle \left(\mathbf{I}_B - P^{\bar{\varphi}^A} \right) \bar{\varphi}_{ref}^B \middle| \left(\mathbf{I}_B - P^{\bar{\varphi}^A} \right) \bar{\varphi}_{ref}^B \right\rangle = \left(\mathbf{R}_{BB}^A \mathbf{C}_{BB}^{B,ref} \right)^\dagger \mathbf{S}_{BB} \mathbf{R}_{BB}^A \mathbf{C}_{BB}^{B,ref}, \tag{7.78}$$

such that

$$\left(\mathbf{O}_{BM_\perp^B}^A \right)^\dagger \mathbf{T}_{BB}^A \mathbf{O}_{BM_\perp^B}^A = \mathbf{t}_{M_\perp^B}^A \tag{7.79}$$

Conclusions

The above analyses led to modified KSCED equations that explicitly take into consideration the intersystem or external orthogonality of orbitals. This condition is warranted by the very notion of DFT-in-DFT embedding which is to partition a system's electron density into a sum of fragment densities. By enforcing external orbital orthogonality within DFT-in-DFT, the nonadditive kinetic potential in Eq. (7.18), which is largely the cause of errors in DFT-in-DFT embedding theory, is exactly zero. The new embedding protocol presented above therefore completely avoids the use of kinetic functionals. Analyses in Ref. [5] showed that the present protocol is applicable also in the case of wave function theory (WFT)-in-DFT embedding. The next Chapter presents results from test calculations based on this newly developed embedding theory.

It is worth mentioning that the present method is somewhat similar, but not equivalent, to the recently proposed "simple exact DFT embedding scheme" of Manby et al. [321] in that both approaches enforce intersystem or external orbital orthogonality and thereby avoid the use of kinetic energy functionals. However, the present method differs epistemologically from that of Manby et al. in that their method first requires a KS-DFT calculation on the total system, whereas the present scheme derives from traditional DFT-in-DFT embedding in which DFT calculations are only required of individual subsystems. Procedurally, Manby et al. use a level shift projection operator that shifts the energies of KS orbitals of the complementary subsystem to higher values in order to ensure their orthogonality, to desired precision, to those of the other subsystem. Here, intersystem orbital orthogonality is included as an added constraint in the construction of the Langrangian that leads to coupled Euler-Lagrange equations for subsystems.

CHAPTER VIII

PERFORMANCE OF DFT-in-DFT EMBEDDING WITH EXTERNAL ORBITAL
ORTHOGONALITY

Introduction

This Chapter discusses results obtained with the newly developed DFT-in-DFT

embedding theory method that was presented in Chapter VII. As was noted in Chapter

VII, previous formulations of DFT-in-DFT embedding theory (both frozen density

embedding (FDE) [302, 303] and those based on freeze-and-thaw cycles [72]) did not

require explicit consideration of the external orthogonality of subsystems' orbitals,

instead relying on exchange-correlation or kinetic energy functionals to correct

inaccuracies in the electron densities. Although such recipes have been able to adequately

describe systems involving weakly interacting fragments [308-311], yet in the case of

strongly interacting subsystems, these methods have been reported to break down [311-

314] and even lead to illogical results in some cases, e.g., giving worse results with GGA

(than with LDA) functionals whereas KS-DFT improves results for the same studied

systems using the same functionals [315]. Whereas previous efforts at improving DFT-in-

DFT embedding theory have concentrated on obtaining more accurate approximations to

the nonadditive kinetic potential (v_T) [314] or even an exact form [316], such methods

tend to require initial calculations of the total system to obtain an initial orbital guess

and/or electron density. Performing a calculation of the total system at any point of an

embedding   program   seems   to   defeat   the   spirit   of   doing   embedding.

In the present Chapter, electron densities are compared for a number of systems with different interaction strengths, obtained based on the new embedding protocol described in Chapter VII and conventional DFT-in-DFT, with densities based on supermolecular KS-DFT calculations. The results clearly demonstrate that whereas conventional DFT-in-DFT embedding theory underestimates the electron density especially at the artificial boundary between subsystems, the situation is remedied when intersystem or external orbital orthogonality is enforced. Density deformations became negligible when using the new embedding equations. With the new equations, reference KS-DFT total energies were reproduced at least to the 7th decimal place (and exactly at most geometries) for all systems tested. Also included in this Chapter are potential energy curves (PECs) of the separation of some of the tested systems into fragments. PECs, obtained with the new equations, using the usual Kohn-Sham equations with constrained electron density and supermolecular basis expansion (i.e., KSCED(s, Ext. Orth., $v_T = 0$) where s represents "supermolecular basis", Ext. Orth. represents "external orthogonality" as enforced in the new method, and $v_T = 0$ emphasizes that the nonadditive kinetic potential was set to zero), were found to be the same as those from conventional KS-DFT. Equilibrium distances and interaction energies were reproduced exactly for both local density approximation (LDA) and generalized gradient approximation (GGA) functionals. The results presented here were obtained with monomer basis expansions, KSCED(m), supermolecular basis expansions, KSCED(s), and the newly proposed extended monomer basis expansions, KSCED(e) that was also described in Chapter VII.

Since Laricchia et al. [322, 323] had suspected that failures in the current formulation of DFT-in-DFT embedding theory are due to the self-interaction error (i.e.,

the self-energy of the electron) resulting from shortcomings in current LDA and GGA functionals and that this problem could be solved by the use of hybrid functionals, this assertion was investigated within conventional DFT-in-DFT. If Laricchia et al. are correct; the accuracy of embedding results should improve if the fraction of single determinant exchange were increased in hybrid functionals. The present study, however, showed the contrary.

This Chapter is organized as follows. The next subsection provides a description of the way calculations were done; the third subsection presents and discusses the results; while a final subsection summarizes current findings.

Computational Details

Besides the new embedding program that was used in the present studies, a computer program was also developed for computing electron densities in real space given reduced density matrices. Reduced density matrices were obtained from conventional DFT-in-DFT embedding, the new embedding scheme, and from KS-DFT calculations of the studied systems. The obtained density matrices were then used in the new program for computing electron densities in real space. The program was designed to compute densities on a cubic grid with step size 0.01 a_0 (N.B. The isocontour and relief maps of electron density differences included in this Chapter only show densities on chosen planes of the molecules). For each given spatial grid point, the density was the sum of contributions from the fragments in embedding calculations. The electron density difference is defined here as $\Delta\rho$ = electron density from KS-DFT calculation on total system – KSCED(x) [or KSCED(x, Ext. Orth.) or KSCED(x, Ext. Orth. $v_T = 0$)] density (N.B. Henceforth in this Chapter, "x" would represent "m" for monomer, "s" for

192

supermolecular, or "e" for extended monomer"; "Ext. Orth." will be used to denote that "external orthogonality" was enforced in the new program; while "$v_T = 0$" would imply that the "nonadditive kinetic potential" was set to zero, e.g., KSCED(s, Ext. Orth.) designates a calculation that enforced external orthogonality but in which v_T was not set to zero). For density differences of the $H_2O \cdots F^-$ and $Li^+ \cdots H_2O$ complexes (which were previously considered in Ref. [324]), the designations $\Delta\rho^m$ were additionally used , where m represents KS or KSCED(m), to denote definitions of $\Delta\rho$ similar to those used in Ref. [324] (i.e., density difference = density of KS-DFT or KSCED(m) − sum of densities of isolated fragments computed using KS method).

Relief and contour maps of electron density differences ($\Delta\rho$), relative to conventional KS-DFT calculations, were obtained for: the weakly bonded $CH_4 \cdots CH_4$ complex; hydrogen bonded complexes ($H_2O \cdots H_2O, H_2O \cdots F^-$, and $NH_3 \cdots NH_3$); complexes involving charge polarization ($Li^+ \cdots H_2O$, $NH_3 \cdots F_2$, and $C_2H_4 \cdots F_2$); and the parallel-displaced (PD) π-stacked $C_6H_6 \cdots C_6H_6$ complex. All (except $H_2O \cdots F^-$ and $Li^+ \cdots H_2O$) were computed at the same optimized geometries of Zhao and Truhlar [325], which were previously used by Dulak and Wesolowski [326] to determine interaction energies of these complexes using the VWN5 [327] and PW91 [328, 329] functionals with the aug-cc-pVTZ [330] and MG3S [331] basis sets. The VWN5 and PW91 functionals were also used for all complexes in this study and the aug-cc-pVTZ basis set, except for the $H_2O \cdots F^-$ complex where the VWN [327] functional was used with the aug-cc-pVQZ [332] basis set and the $Li^+ \cdots H_2O$ complex where the cc-pVDZ [332]

basis set was used with VWN and PW91 functionals. The density difference maps were obtained using OriginPro 8.6 64Bit [333] while graphical representations of molecular structures were generated from Diamond (version 3) [334] (molecular structures are included with density difference maps).

Potential energy curves (PECs) of the separation of HF···HF into HF molecular fragments were computed using aug-cc-pVTZ with VWN5 and PW91; those of the separation of Li^+···H_2O into Li^+ and H_2O were computed using cc-pVDZ with VWN and PW91; and those of the separation of He···Ne into atoms were computed with VWN and aug-cc-pVTZ. The intent of such calculations was to further clarify the performance of the newly developed KSCED(s, Ext. Orth., $v_T = 0$) and KSCED(e, Ext. Orth., $v_T = 0$) methods in comparison with KSCED(m), KSCED(e), KSCED(s), and KS-DFT.

Lastly, calculations were done of the water dimer (at the same geometry determined by Zhao and Truhlar [325]) using the B1B95 [335], MPW3LYP [336], and BHandHLYP [337] hybrid functionals (and also on the Li^+···Be complex at 2.6 Å using B3LYP [338-340]) while varying the fraction of single determinant exchange in each case in order to investigate the effect of exact exchange on the discrepancy in the embedding energy when compared with that from conventional KS-DFT. Such studies were meant to investigate the suspicion of Laricchia et al. [322, 323] that the use of hybrid orbitals may solve the problems with conventional DFT-in-DFT embedding theory.

Program specifications in all calculations were set as follows: integration threshold = 5.749×10^{-11}, self-consistent field energy convergence criterion = 10^{-6}, maximum number of freeze-and-thaw cycles or macroiterations = 20, gradient

convergence criterion = 10^{-8}, overlapping degeneracy criterion = 2.22×10^{-15}; a Mura-Knowles log3 grid type [341] with 96 radial and 302 angular grid points was used. Where evaluated in the present study, the nonadditive kinetic potential was determined using the Thomas-Fermi (TF) approximation [342] to the kinetic energy functional (when using LDA functionals) or the Lembarki-Chermette [307] kinetic energy functional (LC94) when using the GGA functional (PW91) and the MPW3LYP hybrid functional. The B3LYP, BHandHLYP, and B1B95 hybrid functionals included the LLP kinetic energy functional [343].

Details on how DFT numerical integration was performed in the present work are available in Appendix A, whereas an algorithm of the newly developed DFT-in-DFT embedding theory with external orbital orthogonality is provided in Appendix B.

Results and Discussion

Electron Density Differences

Electron density difference relief and contour maps are shown in Figures 30 to 38 for all systems included in this study. In all relief maps, isocontour lines are shown only for major levels. For each system, the density difference is shown on the plane that has the highest number of atoms, and hence highest electron density, in the system. All density difference values are reported in electrons per cubic bohr ($e/a_{\circ}^{3}$).

The $NH_3 \cdots NH_3$ Complex

The $\Delta\rho$ relief maps for $NH_3 \cdots NH_3$ are shown in Figure 30, obtained using the PW91 functional. The maps are labelled A to D and represent the density differences: A = KS-DFT – KSCED(s); B = KS-DFT – KSCED(s, Ext. Orth., $v_T = 0$); C = KS-DFT –

KSCED(e); and D = KS-DFT − KSCED(e, Ext. Orth., v_T = 0). Each NH_3 molecule was treated as a subsystem in KSCED(x) or KSCED(x, Ext. Orth., v_T = 0) calculations. The density difference, $\Delta\rho$, is shown on the xz-plane.
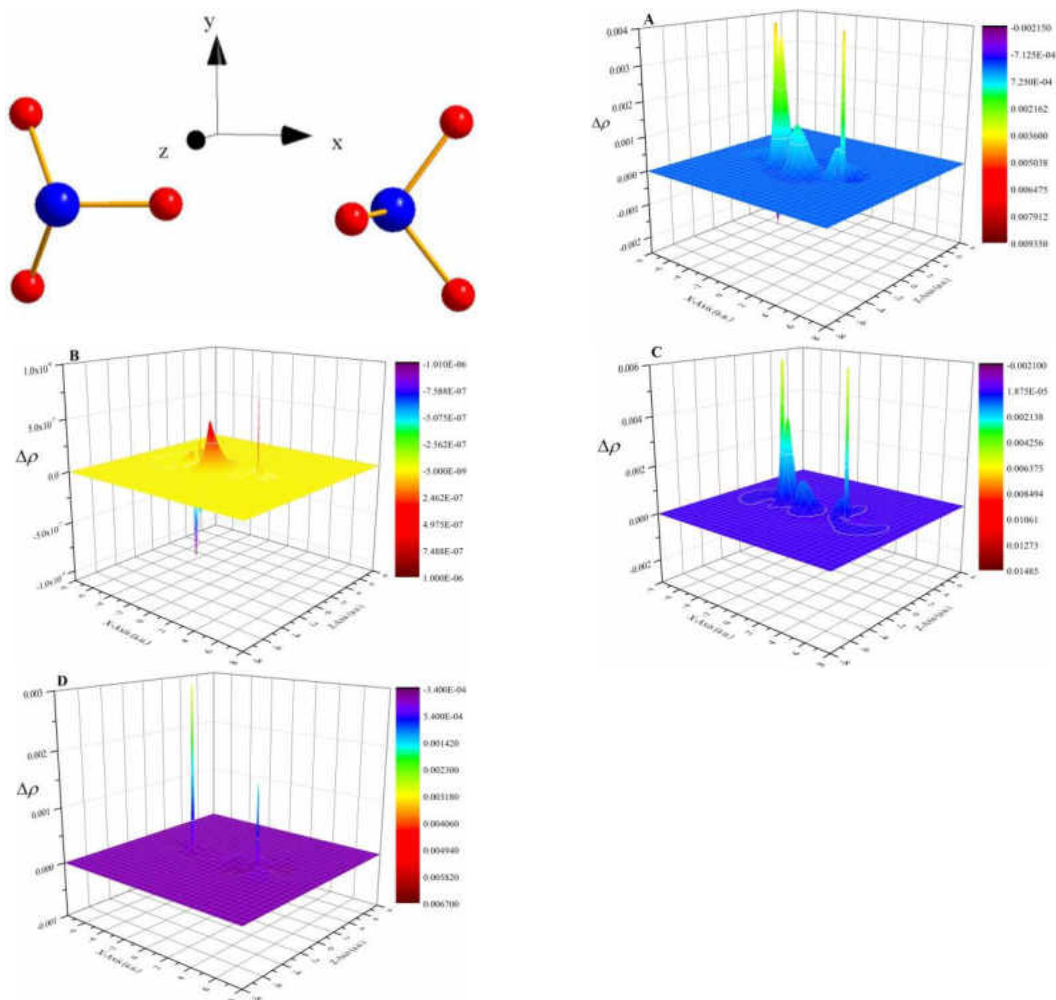
Figure 30. Density difference relief maps of the $NH_3\cdots NH_3$ complex, shown on the xz-plane, obtained using the PW91 functional. The maps display the density differences: A = KS-DFT − KSCED(s); B = KS-DFT − KSCED(s, Ext. Orth., v_T = 0); C = KS-DFT − KSCED(e); and D = KS-DFT − KSCED(e, Ext. Orth., v_T = 0). Coordinates are given in units of Bohr ($a_\circ$) while densities are in electrons per cubic Bohr (e/ $a_\circ^3$).

As can be seen in images A and C, there is an accumulation of electron density at the interfacial region between subsystems and a distortion of subsystems' densities. The

topologies of A and C are quite similar and show density deviations of the order of 10^{-2}

$e/a_{\circ}^3$. This indicates that the extended monomer is a good approximation to the supermolecular basis expansion.

Upon enforcing the external orthogonality constraint, density deviations become negligible; decreasing to the order of 10^{-7} $e/a_{\circ}^3$ in the case of KSCED(s, Ext. Orth., $v_T = 0$) calculations (image B) and 10^{-4} $e/a_{\circ}^3$ in the case of KSCED(e, Ext. Orth., $v_T = 0$) calculations (image D). Thus, accounting for external orthogonality improves embedding densities. Similar plots (shown in Appendix C) were obtained with the VWN5 functional and found to be topologically similar to those presented here from the PW91 functional. The interaction energy of $NH_3 \cdots NH_3$ was computed in Ref. [326] to be 3.74 kcal/mol from KSCED(s) using VWN5 and 4.26 kcal/mol using PW91. The present study predicted 3.71 kcal/mol (with VWN5) and 4.24 kcal/mol (with PW91) using KSCED(s), while the newly developed embedding method, KSCED(s, Ext. Orth., $v_T = 0$), and KS-DFT results agreed exactly (3.34 kcal/mol with VWN5 versus 5.15 kcal/mol with PW91). KSCED(e) calculations, in which the basis functions of the N atom and one H atom of the complementary subsystem were additionally used in expanding KS orbitals of each system, gave 3.70 kcal/mol (with VWN5) and 4.22 kcal/mol (with PW91) whereas KSCED(e, Ext. Orth., $v_T = 0$) calculations predicted an interaction energy that was lower than KS-DFT (and KSCED(s, Ext. Orth., $v_T = 0$)) by only 0.066 kcal/mol when using VWN5 and 0.068 kcal/mol when using PW91. These data indicate, once again, that KSCED(e) is a good approximation of KSCED(s). By accounting for external orbital orthogonality and zeroing out the nonaddititve kinetic potential (Eq. (7.18)), the reference

KS-DFT interaction energies were reproduced exactly in KSCED(s, Ext. Orth., $v_T = 0$) and nearly exactly in KSCED(e, Ext. Orth., $v_T = 0$) calculations of $NH_3 \cdots NH_3$.

<p align="center">The $H_2O \cdots H_2O$ Complex</p>

The $\Delta\rho$ isocontour and relief maps for $H_2O \cdots H_2O$ are shown in Figure 31, obtained using the VWN5 functional. The maps are labelled A to F and represent the density differences: A = KS-DFT – KSCED(s); B = KS-DFT – KSCED(s, Ext. Orth., v_T = 0); C = KS-DFT – KSCED(e); D = KS-DFT – KSCED(e, Ext. Orth., v_T = 0); E = KS-DFT – KSCED(s, Ext. Orth.); and F = superposition of KS-DFT – KSCED(s) surfaces from VWN5 and PW91 calculations, where the surface with the rainbow color palette is that from VWN5. Each H_2O molecule was treated as a subsystem in KSCED(x), KSCED(x, Ext. Orth.), or KSCED(x, Ext. Orth., v_T = 0) calculations. The $\Delta\rho$ is again shown on the xz-plane. Isocontours in A are shown in the range [-0.00465, 0.01245] in steps of 4.275×10^{-4} e/$a_\circ^3$; in C in the range [-0.0046, 0.0111] in steps of 3.925×10^{-4} e/$a_\circ^3$; while in E, they are shown in the range [-0.0314, 0.0372] in steps of 1.715×10^{-3} e/$a_\circ^3$. As can be seen in images A and C, there is a buildup of electron density at the intermolecular region. Inclusion of the Ext. Orth. constraint without zeroing the nonadditive kinetic potential (v_T) in supermolecular basis calculations [KSCED(s, Ext. Orth.)] fails to improve on the density (see image E). However, by zeroing v_T, density deviations become negligible; decreasing to the order of 10^{-6} e/$a_\circ^3$ in the case of KSCED(s, Ext. Orth., v_T = 0) calculations (image B) and 10^{-4} e/$a_\circ^3$ in the case of KSCED(e, Ext. Orth., v_T = 0) calculations (image D).
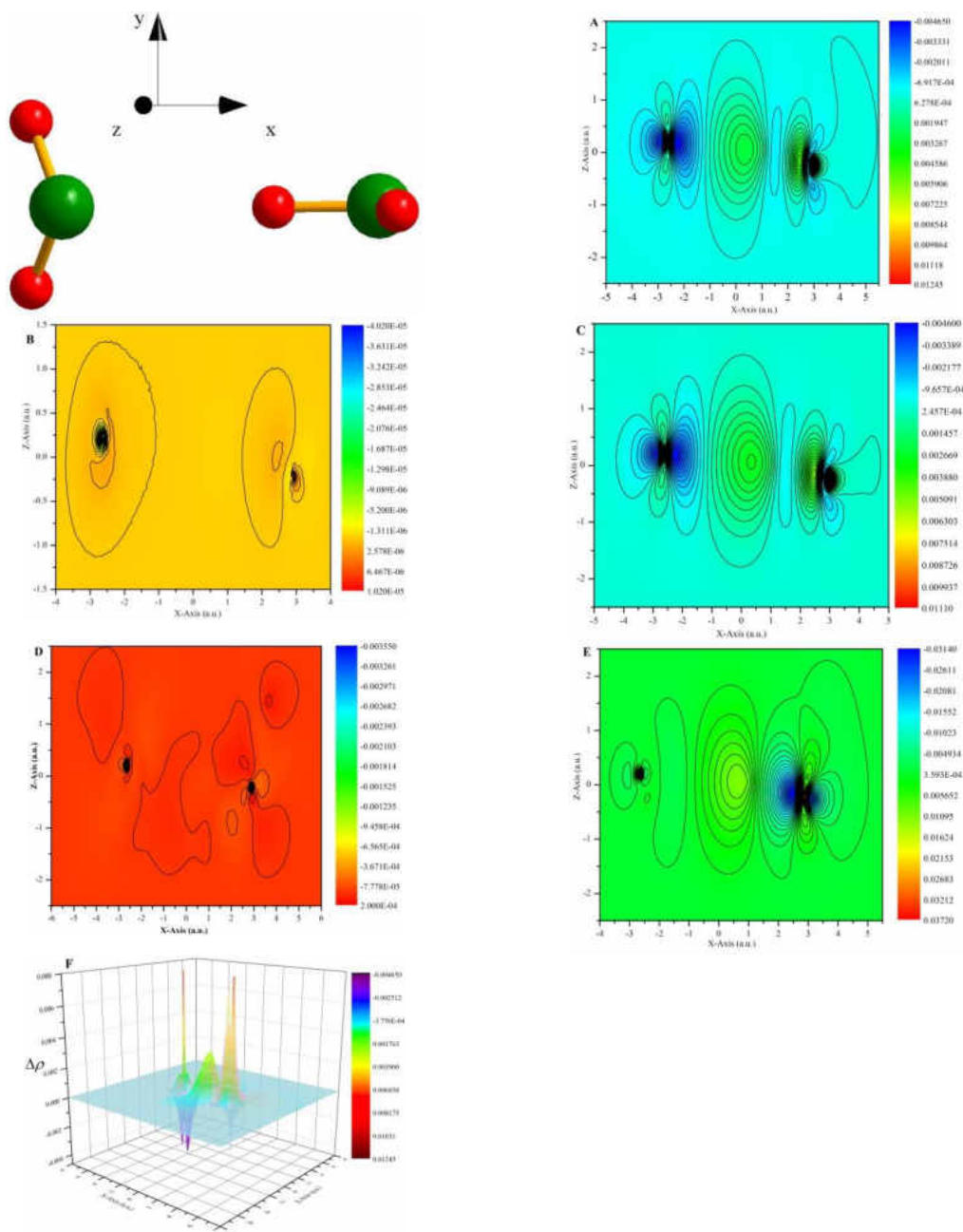
Figure 31. Density difference relief and contour maps of the $H_2O \cdots H_2O$ complex, shown on the xz-plane, obtained using the VWN5 functional. The maps display the density differences: A = KS-DFT – KSCED(s); B = KS-DFT – KSCED(s, Ext. Orth., $v_T = 0$); C = KS-DFT – KSCED(e); D = KS-DFT – KSCED(e, Ext. Orth., $v_T = 0$); E = KS-DFT – KSCED(s, Ext. Orth.); and F = superposition of (KS-DFT – KSCED(s)) surfaces from VWN5 and PW91 calculations, where the surface with rainbow color palette is that from VWN5. Coordinates are given in units of Bohr ($a_\circ$) while densities are in electrons per cubic Bohr (e/$a_\circ^3$).

In image F, relief maps of $\Delta\rho$ = KS-DF – KSCED(s) obtained using VWN5 and PW91 are superimposed (the VWN5 surface is that with a rainbow color palette). As can be seen, the two surfaces are quite similar topologically with the PW91 surface lying slightly above the VWN5 surface at most points but for the intermolecular region. The interaction energy computed in Ref. [326] for this system was 4.92 kcal/mol using VWN5 in KSCED(s). The present study gave 4.90 kcal/mol when using VWN5 in KSCED(s) calculations. Meanwhile KSCED(s, Ext. Orth., v_T = 0) calculations using VWN5 reproduced the KS-DFT interaction energy of 7.29 kcal/mol exactly (to the fifth decimal place) whereas KSCED(e, Ext. Orth., v_T = 0) calculations predicted an interaction energy that was only 0.045 kcal/mol less than the KS-DFT value.

The $F_2\cdots C_2H_4$ Complex

The $\Delta\rho$ relief maps of $F_2\cdots C_2H_4$ are shown in Figure 32, obtained with the VWN5 and PW91 functionals. The maps are labelled A to D and represent the density differences: A = KS-DFT – KSCED(s); B = KS-DFT – KSCED(s, Ext. Orth.); C = KS-DFT – KSCED(s, Ext. Orth., v_T = 0); D = KS-DFT – KSCED(s); and E = KS-DFT – KSCED(s, Ext. Orth., v_T = 0). Images A to C are from VWN5 while D and E are from PW91 calculations. F_2 was the embedded subsystem in KSCED(x), KSCED(x, Ext. Orth.), or KSCED(x, Ext. Orth., v_T = 0) calculations. The $\Delta\rho$ are shown on the yz-plane. As shown in images A, B, and D, $\Delta\rho > 0$ at the F_2 fragment and $\Delta\rho < 0$ at the C_2H_4 fragment. This suggests that there is charge polarization within the supermolecule

from the C_2H_4 to the F_2 moiety. KSCED(x) calculations fail to fully account for such polarization.

Figure 32. Density difference relief maps of the $F_2 \cdots C_2H_4$ complex, shown on the yz-plane, obtained with the VWN5 and PW91 functionals. The maps display the density differences: A = KS-DFT − KSCED(s); B = KS-DFT − KSCED(s, Ext. Orth.); C = KS-DFT − KSCED(s, Ext. Orth., $v_T = 0$); D = KS-DFT − KSCED(s); and E = KS-DFT − KSCED(s, Ext. Orth., $v_T = 0$). Images A to C are from VWN5 while D and E are from PW91 calculations. Coordinates are given in units of Bohr ($a_°$) while densities are in electrons per cubic Bohr (e/ $a_°^3$).

Hence, the density of the F_2 fragment is underestimated while that of C_2H_4 is overestimated in such calculations. However, enforcing external orbital orthogonality and zeroing the nonadditive kinetic potential renders density deviations to become negligibly small (of the order of 10^{-5} $e/a_\circ^3$ with both VWN5 (image C) and PW91 (image E) functionals). Images A, B, and C show that buildup of electron density is minimal in the interfacial region between the fragments. This is not surprising given that a reference binding energy of only 1.06 kcal/mol was reported in Ref. [326] for this system, implying that the electron clouds of the fragments do not interact strongly.

The Ref. [326] study predicted that $F_2 \cdots C_2H_4$ was unbound when using VWN5 and had a binding energy of 0.76 kcal/mol when using PW91 in KSCED(m) calculations. The present study predicted a binding energy of 0.10 kcal/mol (with VWN5) and 0.76 kcal/mol (with PW91) using KSCED(m). On the other hand, KSCED(s, Ext. Orth., $v_T = 0$) calculations using VWN5 reproduced the KS-DFT interaction energy of 4.62 kcal/mol exactly, whereas KSCED(s) gave an interaction energy of 0.33 kcal/mol only, using the same functional.

The $F_2 \cdots NH_3$ Complex

The $\Delta\rho$ relief maps of $F_2 \cdots NH_3$ are shown in Figure 33, obtained with the VWN5 and PW91 functionals. The maps are labelled A to D and represent the density differences: A = KS-DFT – KSCED(s); B = KS-DFT – KSCED(s, Ext. Orth., $v_T = 0$); C = KS-DFT – KSCED(s); and D = KS-DFT – KSCED(s, Ext. Orth., $v_T = 0$). Images A and B are from VWN5 while C and D are from PW91 calculations. F_2 was the embedded subsystem in KSCED(x) or KSCED(x, Ext. Orth., $v_T = 0$) calculations.
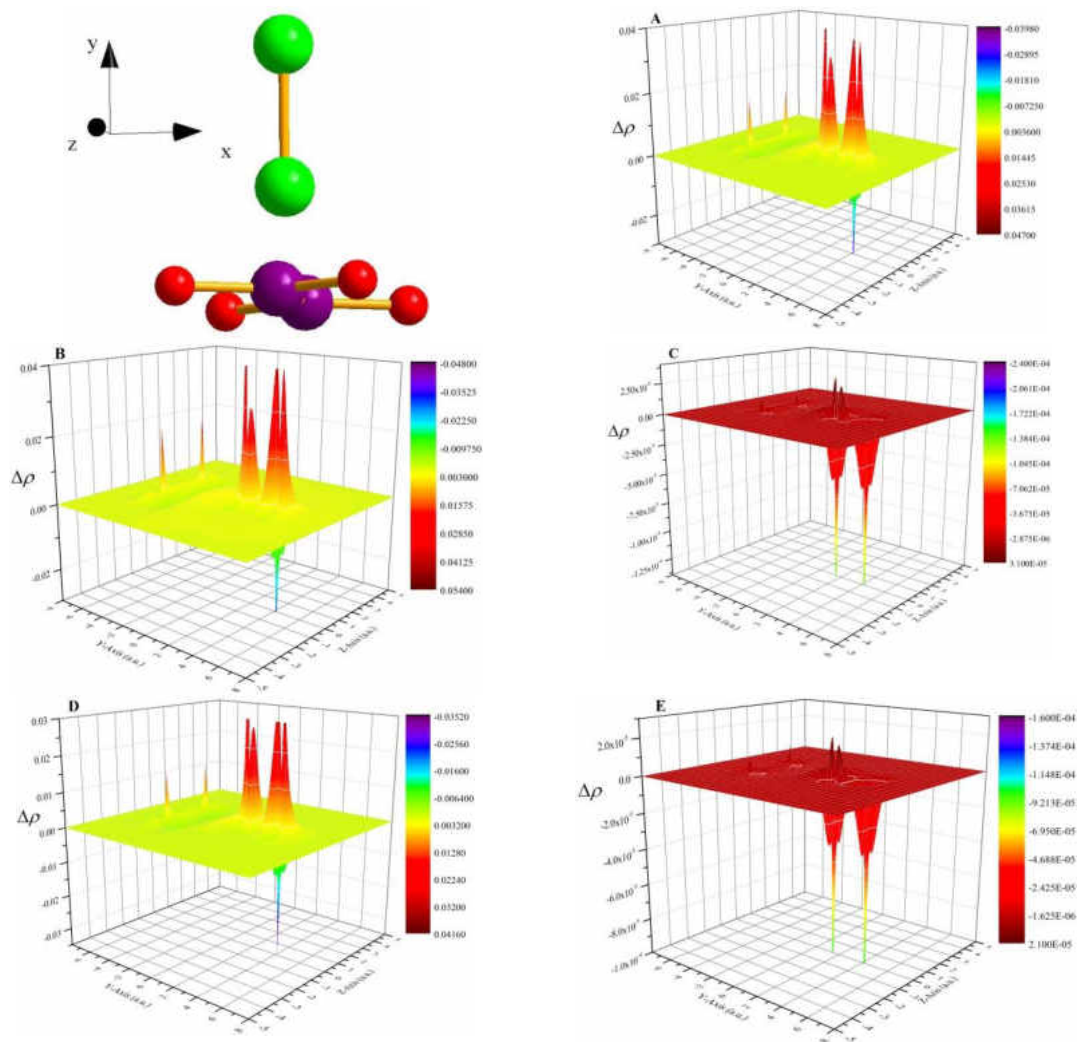
Figure 33. Density difference relief maps of the $F_2 \cdots NH_3$ complex, shown on the yz-plane, obtained with the VWN5 and PW91 functionals. The maps display the density differences: A = KS-DFT − KSCED(s); B = KS-DFT − KSCED(s, Ext. Orth., v_T = 0); C = KS-DFT − KSCED(s); and D = KS-DFT − KSCED(s, Ext. Orth., v_T = 0). Images A and B are from VWN5 while C and D are from PW91 calculations. Coordinates are given in units of Bohr ($a_\circ$) while densities are in electrons per cubic Bohr (e/ $a_\circ^3$).

The $\Delta\rho$ are shown on the yz-plane. Just as for $F_2 \cdots C_2H_4$, the main distortions in electron density are within the F_2 and NH_3 fragments (see images A and C), with the

density of F_2 underestimated and that of NH_3 overestimated in KSCED(s) calculations. There is minimal buildup of electron density at the interfacial region. This suggests charge polarization from NH_3 to F_2 which conventional DFT-in-DFT embedding theory seems unable to capture. Again, it is seen that accounting for external orthogonality within the new embedding scheme and zeroing the nonadditive kinetic potential enables embedding theory densities to be well represented; diminishing density deviations from an order of 10^{-2} e/$a_\circ^3$ to 10^{-6} e/$a_\circ^3$ for both VWN5 (image B) and PW91 (image D) functionals. The interaction energy for this system was found in Ref. [326] to be much lower with VWN5 than with PW91 (0.15 kcal/mol versus 1.26 kcal/mol from KSCED(m)). The present study predicted 0.47 kcal/mol (with VWN5) and 1.31 kcal/mol (with PW91) using KSCED(m). However, calculations with the new embedding program [KSCED(s, Ext. Orth., $v_T = 0$)] using PW91 reproduced the KS-DFT interaction energy (5.368 kcal/mol) exactly.

As seen in these charge polarization systems ($F_2 \cdots C_2H_4$ and $F_2 \cdots NH_3$), density differences are largely positive for the F_2 fragment and largely negative for the C_2H_4 and NH_3 fragments. This suggests that in KS-DFT calculations of the total systems, electron density gets polarized towards the F_2 moiety. Conventional DFT-in-DFT embedding theory appears to be unable to account for such polarization when external orbital orthogonality is neglected. Such failures in turn lead to poor estimates of interaction energies. The new embedding theory corrects these lapses and reproduces the reference interaction energy exactly.

The $\Delta\rho$ isocontour maps of $CH_4 \cdots CH_4$ are shown in Figure 34, obtained with the VWN5 functional. The maps are labelled A and B and represent the density differences: A = KS-DFT – KSCED(s); and B = KS-DFT – KSCED(s, Ext. Orth., $v_T =$ 0). The CH_4 molecules were treated as subsystems in embedding calculations.
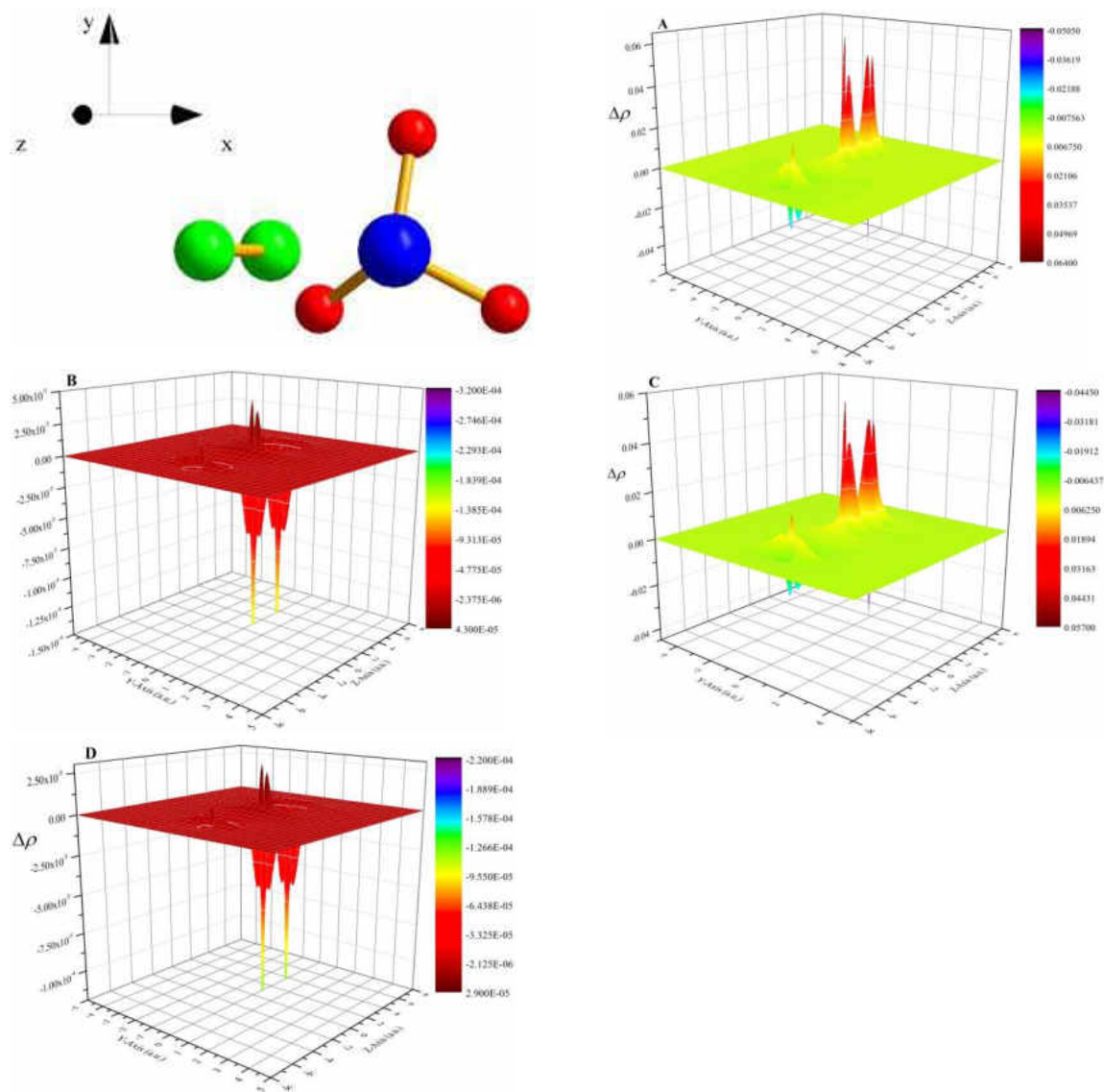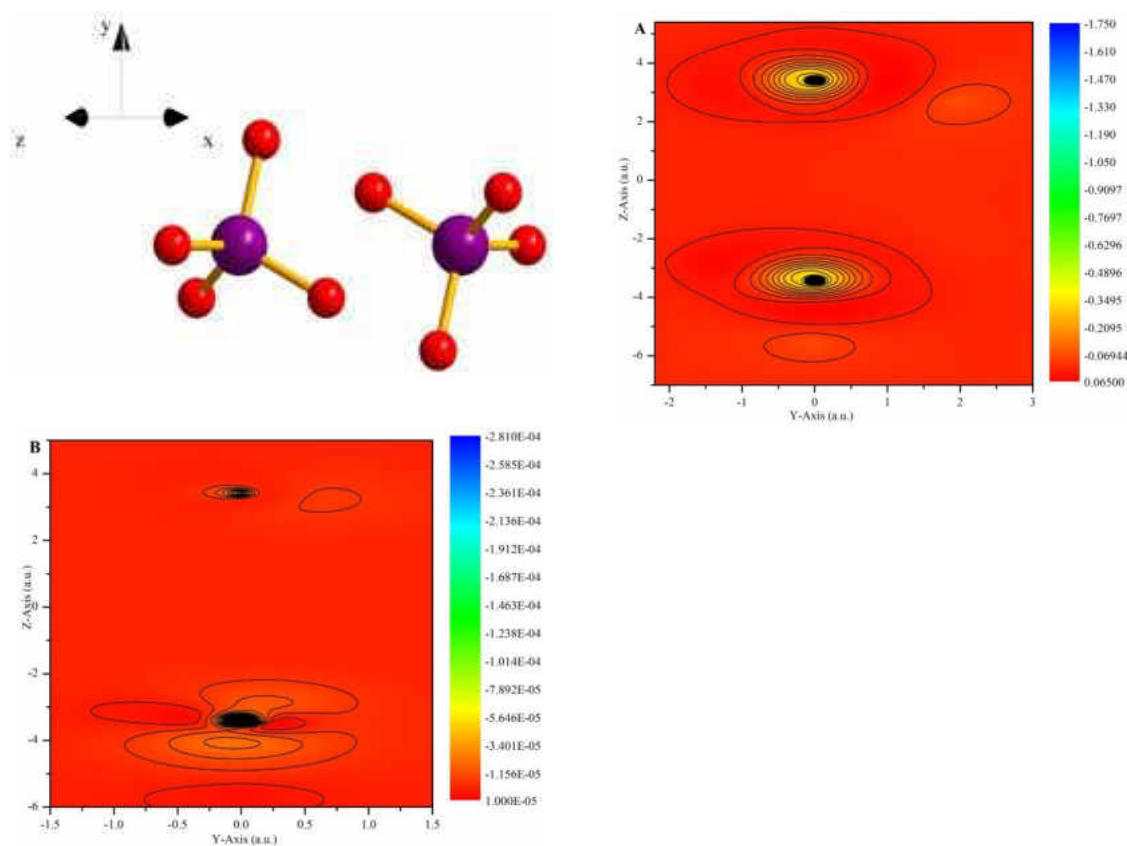

Figure 34. Density difference contour maps of the $CH_4 \cdots CH_4$ complex, shown on the yz-plane, obtained with the VWN5 functional. The maps display the density differences: A = KS-DFT – KSCED(s); and B = KS-DFT – KSCED(s, Ext. Orth., $v_T = 0$). Coordinates are given in units of Bohr ($a_\circ$) while densities are in electrons per cubic Bohr (e/$a_\circ^3$).

The $\Delta\rho$ are shown on the yz-plane. Density deviations can be seen to be largely within molecular regions of each of the subsystems. Charge buildup is minimal at the interface

between the molecular fragments. The $CH_4 \cdots CH_4$ complex involves only weak van der Waals interactions. There is no surprise, therefore, that for this system, no density buildup is observed at the interfacial region.

Comparing images A and B, it is seen that including external orthogonality and setting $v_T = 0$ diminishes density deviations from an order of 10^{-2} e/$a_\circ^3$ in A to 10^{-5} e/$a_\circ^3$ in B. Isocontours in A are shown in the range [-1.75, 0.065] in steps of 4.5375×10^{-2} e/$a_\circ^3$ while those in B are in the range [-2.81$\times 10^{-4}$, 1.00×10^{-5}] in steps of 7.275×10^{-6} e/$a_\circ^3$. The Ref. [326] study predicted an interaction energy of only 0.43 kcal/mol for this complex when using VWN5 in KSCED(m) and the present study obtained 0.42 kcal/mol from the same calculations (i.e., with conventional DFT-in-DFT).

Parallel-Displaced (PD) π-stacked $C_6H_6 \cdots C_6H_6$ complex

The $\Delta\rho$ isocontour and relief maps for the parallel-displaced (PD) π-stacked $C_6H_6 \cdots C_6H_6$ complex are shown in Figure 35. The maps are labelled A to C and represent the density differences: A = KS-DFT – KSCED(m); B = KS-DFT – KSCED(s); and C = KS-DFT – KSCED(s, Ext. Orth., $v_T = 0$). Image A shows $\Delta\rho$ on the yz-plane (which cuts through the benzene rings) while images B and C show $\Delta\rho$ on the xz-plane (which is the plane through the interface between the two benzene rings. The two benzene rings are parallel to each other; one lies on the y = 1.8 Å plane while the other is on the y = -1.8 Å plane. Hence the y = 0 or xz-plane is the interfacial plane). This system, in the considered geometry, involves fairly strong π-π coupling. As can be seen, $\Delta\rho$ values are non-negligible at the intermolecular interface (the y = 0 or xz-plane) and are significant within the subsystems (Image A in Figure 35). No charge polarization as was

predicted in the cases of $F_2\cdots C_2H_4$ and $F_2\cdots NH_3$ is evident for this system. Pi bonding

interaction is, however, evidenced by the fairly significant accumulation of electron

density at the interface between the molecular subsystems, averagely of an order of 10^{-3}

$e/a_\circ^3$ (Image B in Figure 35).
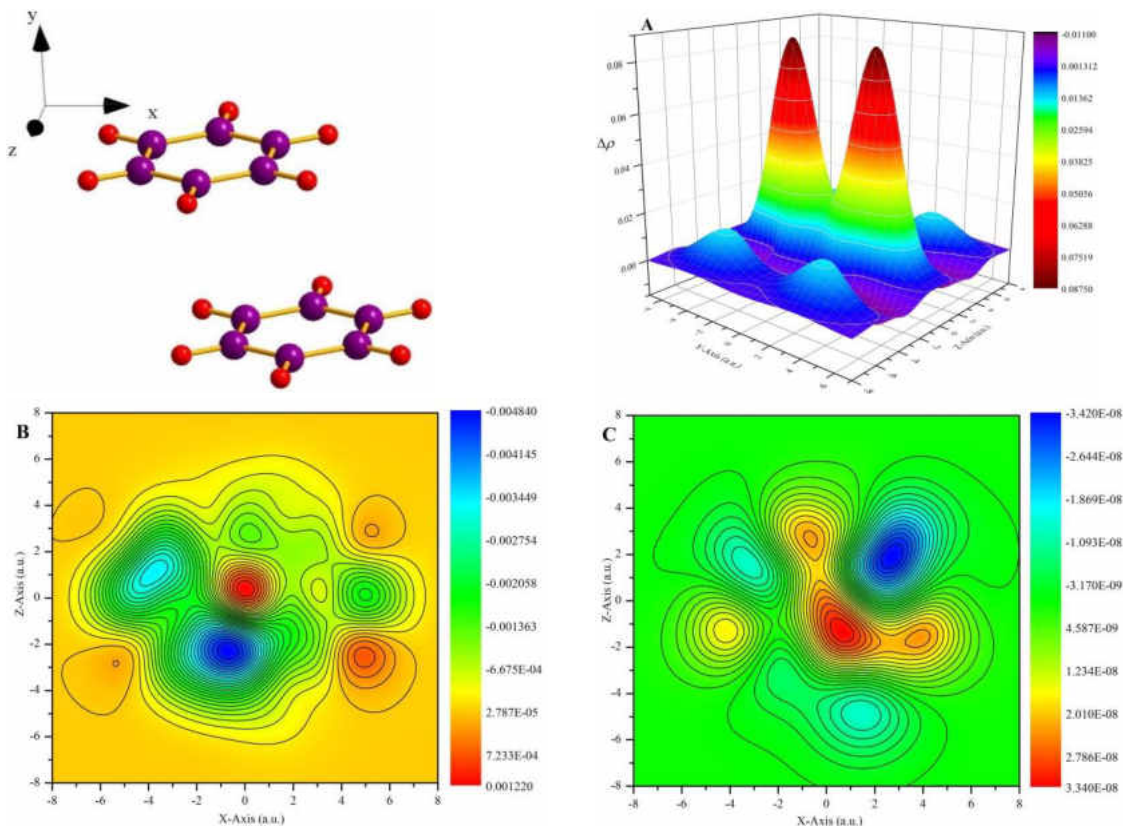
Figure 35. Density difference relief and contour maps of the parallel displaced (PD) π-stacked $C_6H_6\cdots C_6H_6$ complex, shown on the yz-plane (image A) and xz-plane (images B and C), obtained with the VWN5 functional. The maps represent the density differences: A = KS-DFT – KSCED(m); B = KS-DFT – KSCED(s); and C = KS-DFT – KSCED(s, Ext. Orth., v_T = 0). Coordinates are given in units of Bohr ($a_\circ$) while densities are in electrons per cubic Bohr ($e/a_\circ^3$).

Image C of Figure 35 shows that when external orthogonality was enforced within the new embedding program and the nonadditive kinetic potential was set to zero, density deviations became negligible; decreasing from an order of 10^{-3} e/$a_{\circ}^{3}$ in B to an order of 10^{-8} e/$a_{\circ}^{3}$ in C.

The interaction energy of the (PD) π-stacked $C_6H_6 \cdots C_6H_6$ complex was determined in Ref. [326] to be as large as 1.97 kcal/mol less than a reference value of 2.78 kcal/mol, when using the VWN5 functional in KSCED(s) calculations with the aug-cc-pVTZ basis set. In the present study, using the cc-pVDZ basis set and VWN5 in the new embedding program, KSCED(s, Ext. Orth., $v_T = 0$), reproduced the KS-DFT interaction energy of 2.66 kcal/mol exactly to the fifth decimal place.

Density Differences of the $Li^+ \cdots H_2O$ and $F^- \cdots H_2O$ Complexes

Deformation densities for $Li^+ \cdots H_2O$ and $F^- \cdots H_2O$ complexes, similar to those previously reported in Ref. [324] (for $Li^+ \cdots H_2O$) and Ref. [344] (for $F^- \cdots H_2O$), were computed in the present study. As noted before, the intent of such calculations was partly to verify that the newly developed program for computing electron densities was working accurately. Of course, a first test of the code was to verify that it could integrate density over all space to give a value approximately equal to the number of electrons in a system. The $\Delta\rho$ and $\Delta\rho^m$ (m = KS or KSCED(m)) isocontour and relief maps for $Li^+ \cdots H_2O$ are shown in Figure 36 while relief maps of $\Delta\rho$ for $F^- \cdots H_2O$ are in Figure 37. All densities were computed with the VWN functional. The maps in Figure 36 are labelled A to D and represent the density differences: A = KS-DFT – KSCED(s); B = KS-DFT – KSCED(s, Ext. Orth., $v_T = 0$); C = $\Delta\rho^{KS}$ = Full system KS-DFT density – Sum of densities of

isolated Li^+ and H_2O fragments obtained from KS-DFT; and D = $\Delta\rho^{KSCED(m)}$ = KSCED(m) density – Sum of densities of isolated Li^+ and H_2O fragments obtained from KS-DFT. Images A and B in Figure 37 are defined in the same way as A and B in Figure 36.

Images C and D of Figure 36 were a repeat of the first two images in Figure 4 of Ref. [324]. Isocontours in images C and D of Figure 35 are reported in the same range [-0.05, 0.05] and step size (2.5×10^{-3} e/$a_\circ^3$) as in Figure 4 of Ref. [324]. The two sets of images (C and D here and Figure 4 of Ref. [324]) are in good agreement. In all calculations on $Li^+\cdots H_2O$, Li^+ was the embedded subsystem in KSCED(s) or KSCED(s, Ext. Orth., v_T = 0) calculations and the calculations were done at the same geometry as was used in Ref. [324]. Both images A of Figure 36 and A of Figure 37 show a buildup of electron density in the artificial boundary region between Li^+ and H_2O, and between F^- and H_2O, respectively.

Accounting for external orbital orthogonality within the new embedding theory and setting v_T = 0 decreases density deviations significantly to nearly zero for the $Li^+\cdots H_2O$ complex (see Image B of Figure 36) and to the order of 10^{-6} e/$a_\circ^3$ for the $F^-\cdots H_2O$ complex (see Image B of Figure 37). These results again indicate that the new embedding theory corrects embedding densities relative to reference KS-DFT densities.
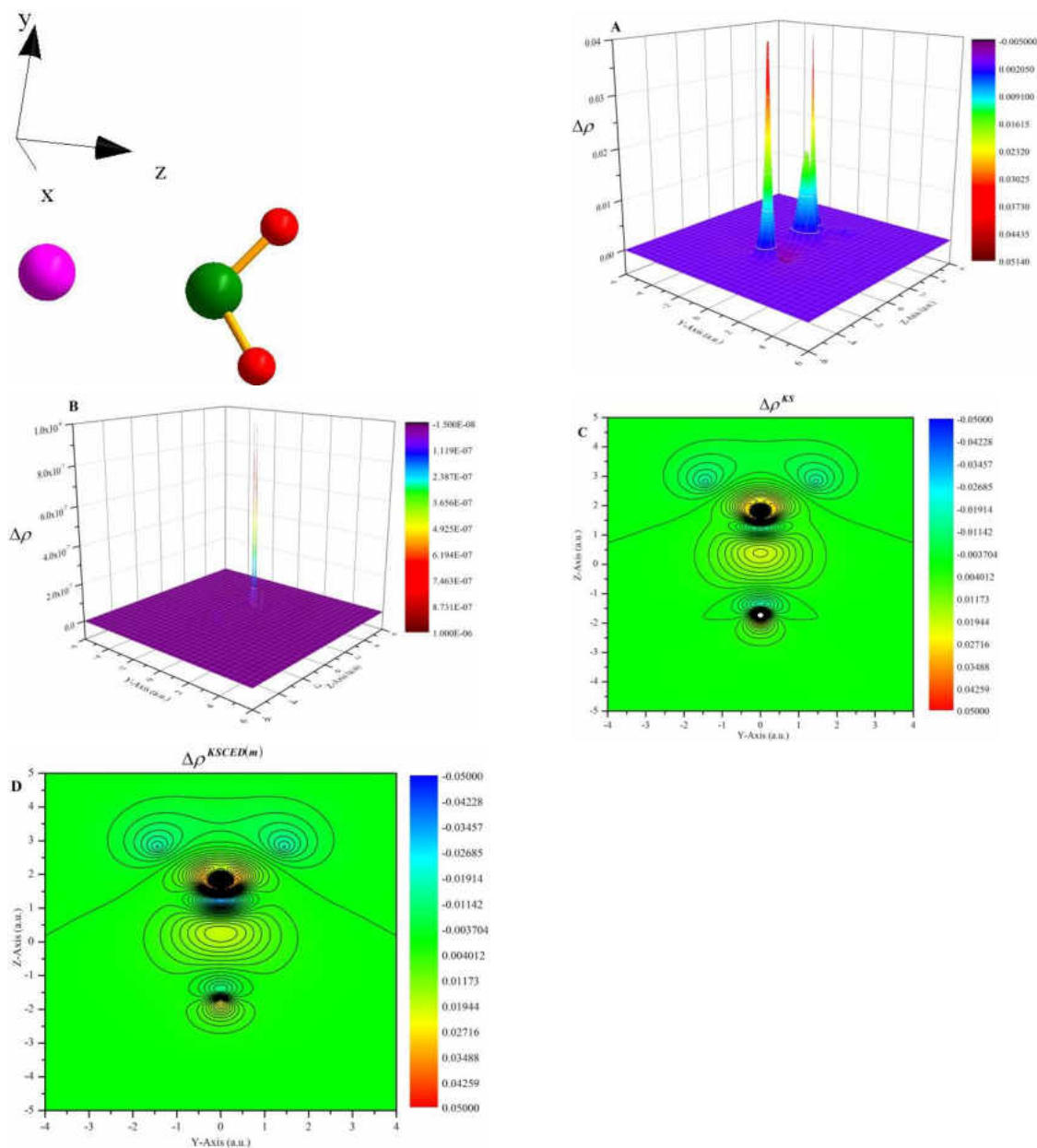
Figure 36. Density difference relief and contour maps of the $Li^+ \cdots H_2O$ complex, shown on the yz-plane, computed with the VWN functional. The maps display the density differences: A = KS-DFT – KSCED(s); B = KS-DFT – KSCED(s, Ext. Orth., $v_T = 0$); C = $\Delta\rho^{KS}$ = Full system KS-DFT density – Sum of densities of isolated Li^+ and H_2O fragments obtained from KS-DFT; and D = $\Delta\rho^{KSCED(m)}$ = KSCED(m) density – Sum of densities of isolated Li^+ and H_2O fragments obtained from KS-DFT. Coordinates are given in units of Bohr (a_0) while densities are in electrons per cubic Bohr (e/ a_0^3). The geometry of Ref. [324] was used in the present calculations.
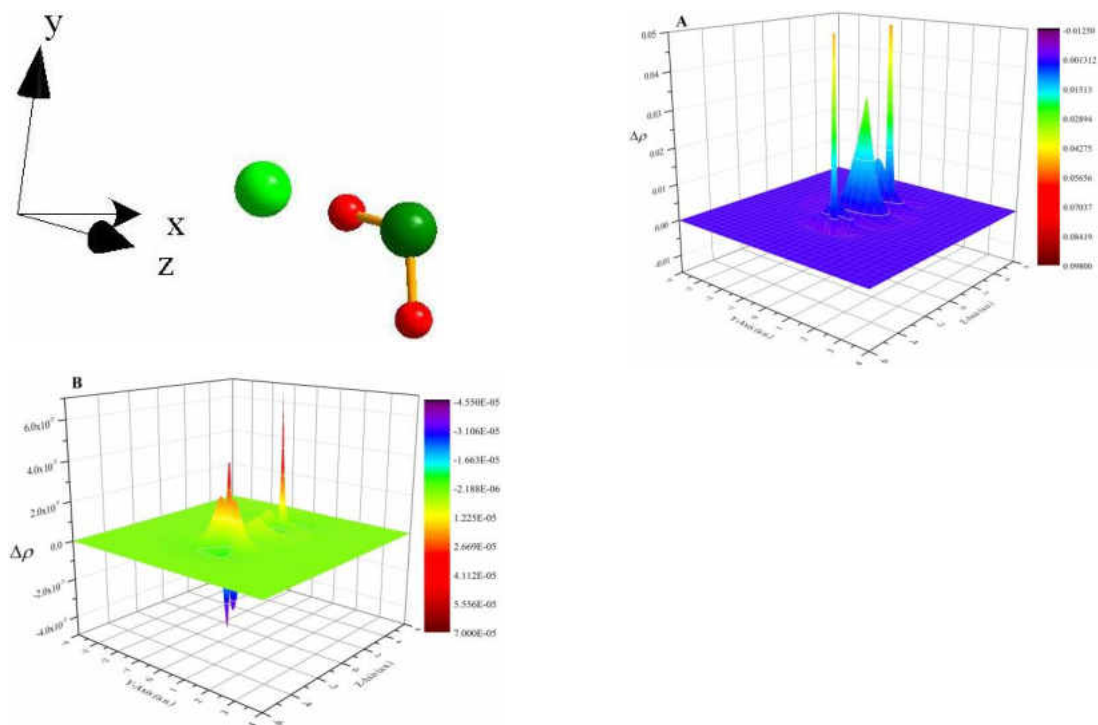
Figure 37. Density difference relief maps of the $H_2O\cdots F^-$ complex, shown on the yz-plane, computed with the VWN functional. The maps display the density differences: A = KS-DFT − KSCED(s) and B = KS-DFT − KSCED(s, Ext. Orth., $v_T = 0$). Coordinates are given in units of Bohr ($a_\circ$) while densities are in electrons per cubic Bohr ($e/a_\circ^3$). The same geometry as was used in Ref. [324] was used here.

Potential Energy Curves of the $Li^+\cdots H_2O$ Complex

Reported in Figures 38 and 39 are the PECs for the separation of $Li^+\cdots H_2O$ into Li^+ and H_2O fragments, computed using the VWN and PW91 functionals, respectively. In both figures, reference KS-DFT curves are marked with symbols to distinguish them from the other curves. The data describing the curves are in Table 13.

Figure 38. PECs of the $Li^+ \cdots H_2O$ complex computed using the VWN functional and cc-pVDZ basis set in the methods shown in the inset. The geometry of Ref. [324] was used and the $Li^+ \cdots O$ intersystem separation (**R**) was varied. Note that the KS-DFT (black), KSCED(s, Ext. Orth., $v_T = 0$) (blue), and KSCED(e, Ext. Orth., $v_T = 0$) (magenta) curves are indistinguishable at the given resolution.

While both Figures suggest a fairly strong interaction between the Li^+ and H_2O fragments (i.e., all methods predict interaction energies of at least 40.00 kcal/mol), there are marked differences in KSCED(m) and KSCED(s) results compared with the reference KS-DFT results. KSCED(m) and KSCED(s), using VWN, predict equilibrium separations that are 0.16 Å and 0.13 Å shorter than KS-DFT, respectively (red and green curves in Figure 38). The KSCED(s) interaction energy is 3.78 kcal/mol more while that from KSCED(m) is 5.34 kcal/mol less than the reference KS-DFT value using VWN. These trends are repeated in the case of PW91 where equilibrium separations are 0.24 Å and 0.22 Å less whereas interaction energies are 0.82 kcal/mol less and 8.54 kcal/mol more than KS-DFT values for KSCED(m) and KSCED(s), respectively (see Table 13 and Figure 39).
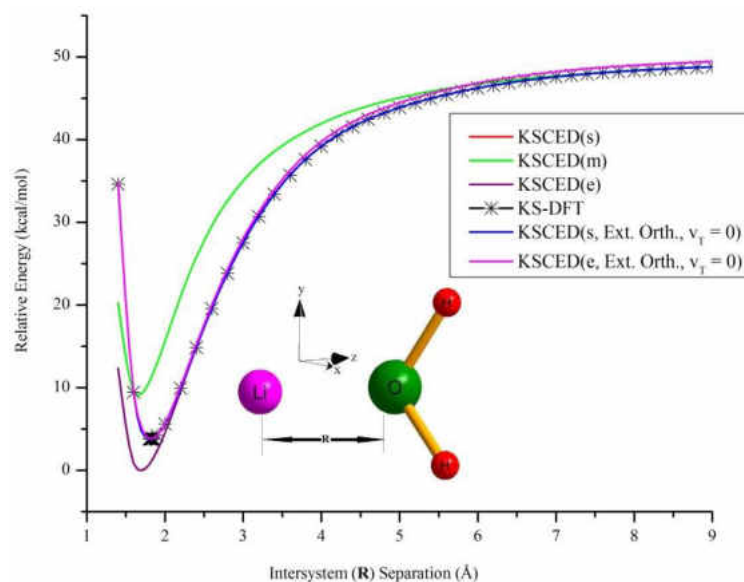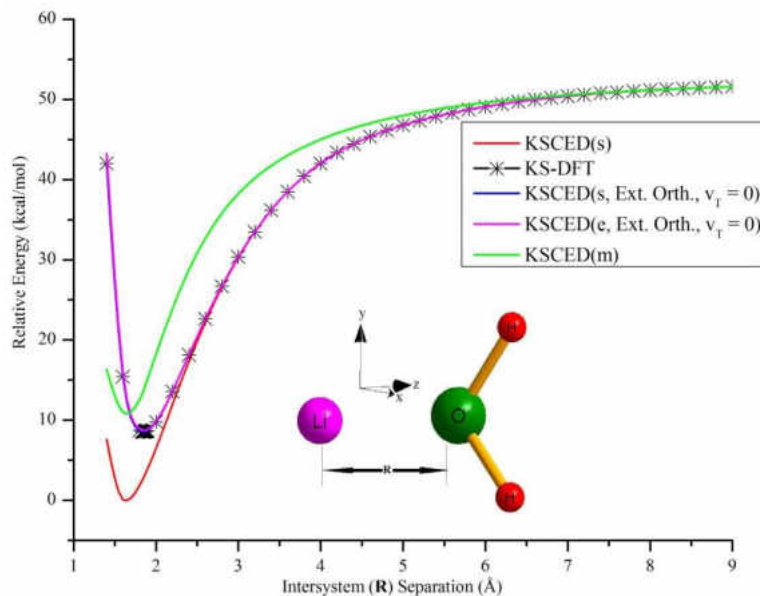
Figure 39. PECs of the $Li^+ \cdots H_2O$ complex computed using the PW91 functional and cc-pVDZ basis set in the methods shown in the inset. The geometry of Ref. [324] was used and the $Li^+ \cdots O$ intersystem separation (**R**) was varied. Note that the KS-DFT (black), KSCED(s, Ext. Orth., $v_T = 0$) (olive), and KSCED(e, Ext. Orth., $v_T = 0$) (magenta) curves are again indistinguishable. Thus, the magenta curve obscures the olive and black curves.

As can be seen in Figure 38, the KSCED(e) curve is very similar to that from KSCED(s) calculations (the purple KSCED(e) and red KSCED(s) curves in Figure 38 are virtually indistinguishable). Irrespective of functional type, enforcing external orbital orthogonality and zeroing the nonadditive kinetic potential ($v_T = 0$) leads, in the present case, to KSCED(s, Ext. Orth., $v_T = 0$) results that are exactly the same as the KS-DFT (compare the blue and black curves in Figure 38 and the olive and black curves in Figure 39 and see Table 13 where equilibrium separations and interaction energies are the same for KSCED(s, Ext. Orth., $v_T = 0$) and KS-DFT).

Table 13. Equilibrium separations (R_e) and interaction energies (D_e) of the $Li^+\cdots H_2O$, $HF\cdots HF$, and $He\cdots Ne$ complexes computed using the VWN, VWN5, and PW91 functionals in the methods shown in the second column.

Complex	Method	Functional Type, Equilibrium Separation, and Interaction Energy			
		VWN		PW91	
		R_e (Å)	D_e (kcal/mol)	R_e (Å)	D_e (kcal/mol)
$Li^+\cdots H_2O$	KSCED(s)	1.69	49.12	1.63	51.66
	KSCED(m)	1.66	40.00	1.61	42.30
	KSCED(e)	1.70	49.11	-	-
	KSCED(e, Ext. Orth., $v_T = 0$)	1.82	45.62	1.86	42.95
	KSCED(s, Ext. Orth., $v_T = 0$)	1.82	45.34	1.85	43.12
	KS-DFT	1.82	45.34	1.85	43.12
		VWN5		PW91	
$HF\cdots HF$					
	KSCED(s)	1.79	4.00	1.78	4.84
	KSCED(m)	1.80	3.71	1.79	4.60
	KSCED(s, Ext. Orth.)	3.00	1.08	2.90	1.25
	KSCED(s, Ext. Orth., $v_T = 0$)	1.58	7.91	1.76	4.93
	KS-DFT	1.58	7.91	1.76	4.93
$He\cdots Ne$				PW91	
	KSCED(s)	-	-	2.53	0.48
	KSCED(s, Ext. Orth.)	-	-	3.22	0.12
	KSCED(s, Ext. Orth., $v_T = 0$)	-	-	2.83	0.29
	KS-DFT	-	-	2.83	0.29

The KSCED(e, Ext. Orth., $v_T = 0$) curve in Figure 38 (magenta colored curve) is also very similar to the reference KS-DFT curve, having exactly the same equilibrium separation (1.82 Å) and an interaction energy that is only 0.28 kcal/mol more than that from KS-DFT (see Table 13). Similar results are obtained with the PW91 functional as shown in Figure 39. These results indicate that the extended monomer basis approach is a good approximation to the more computationally demanding supermolecular basis

expansion. Moreover, it is seen that the new embedding theory method that enforces external orbital orthogonality reproduces reference KS-DFT results of the total system exactly.

Potential energy curves (PECs) of HF⋯HF and He⋯Ne

Figures 40 and 41 show PECs for the separation of the HF⋯HF complex into molecular fragments, computed using the VWN5 and PW91 functionals, respectively. In both figures, reference KS-DFT curves are marked with symbols to distinguish them from the other curves. The data describing the curves are in Table 13. Unlike the Li^+⋯H_2O case for which equilibrium separations of KSCED(s) and KSCED(m) were less than the reference KS-DFT value, the situation is reversed in the case of HF⋯HF where conventional DFT-in-DFT methods (without external orthogonality) are seen to predict longer equilibrium separations than KS-DFT for both VWN5 and PW91 functionals. These observations reveal an acute problem with conventional DFT-in-DFT embedding which is "lack of tendency". For example, the interaction energy obtained from KSCED(s) calculations on Li^+⋯H_2O using PW91 is worse than the KSCED(m) value, using the same functional, in comparison with KS-DFT. The same calculations on HF⋯HF lead to KSCED(s) predicting a better interaction energy than KSCED(m) in comparison with KS-DFT (see Table 13). Moreover, the KSCED(s) interaction energy for Li^+⋯H_2O (with VWN) is rather better than the KSCED(m) value when compared with KS-DFT. Also noteworthy is the fact that deviations in equilibrium separation and interaction energy increase from the LDA (VWN) to the GGA (PW91) functional in the case of Li^+⋯H_2O, using KSCED(s), whereas the opposite effect is seen in the case of HF⋯HF (see Table 13).

Figure 40. PECs of the HF···HF complex computed using the VWN5 functional and aug-cc-pVTZ basis set in the methods shown in the inset. The optimized geometry of Ref. [49] was used and the F···H intermolecular separation (**R**) was varied. Note that the KS-DFT (black) and KSCED(s, Ext. Orth., $v_T = 0$) (olive) curves are degenerate. Thus, the olive curve completely obscures the black curve.

As can be seen in Figures 40 and 41 and in Table 13, enforcing external orbital orthogonality and setting $v_T = 0$ within the new embedding theory leads to KSCED(s, Ext. Orth., $v_T = 0$) results that are exactly the same as those from the reference KS-DFT for both VWN5 and PW91 functionals. Note that the olive and black curves in Figures 40 and 41 obtained from the KSCED(s, Ext. Orth., $v_T = 0$) and KS-DFT methods, respectively, are exactly degenerate such that the olive curve completely obscures the black reference curve. On the other hand, failure to zero out the nonadditive kinetic potential while enforcing external orthogonality within the new embedding theory leads essentially to worse PECs than those from conventional DFT-in-DFT (compare the blue curves in Figures 40 and 41 to the red and green ones).

216
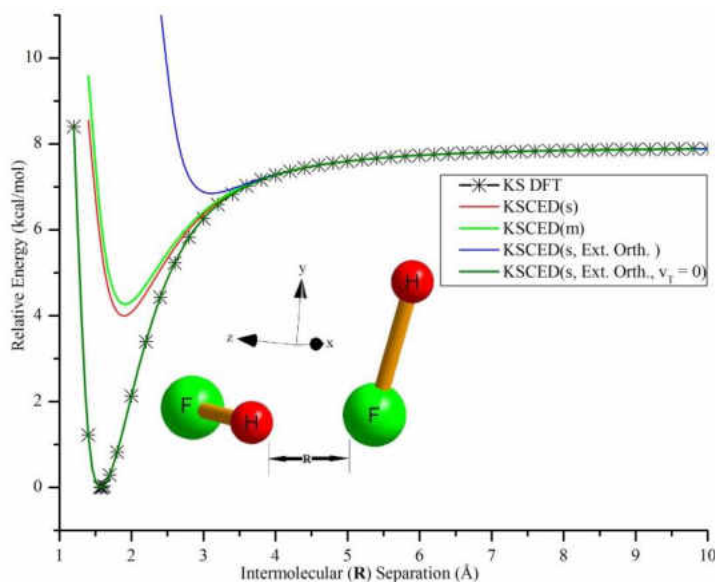
Figure 41. PECs of the HF···HF complex computed using the PW91 functional and aug-cc-pVTZ basis set in the methods shown in the inset. The optimized geometry of Ref. [301] was used and the F···H intermolecular separation (**R**) was varied. Note that the KS-DFT (black) and KSCED(s, Ext. Orth., $v_T = 0$) (olive), curves are degenerate. Thus, the olive curve completely obscures the black curve.

Figure 42 contains PECs of the separation of the He···Ne into atoms, obtained with the PW91 functional. The reference KS-DFT curve is again marked with a symbol. The data describing the curves are in Table 13. As can be seen in Figure 42 and Table 13, KSCED(s) calculations of this complex lead to an equilibrium separation that is 0.30 Å too short and an interaction energy that is 0.19 kcal/mol too high in comparison with KS-DFT. On the other hand, accounting for external orthogonality in KSCED(s) without setting $v_T = 0$ leads to a minimum that is 0.39 Å too long and an interaction energy that is 0.17 kcal/mol too low compared to KS-DFT values obtained with the same functional (compare the blue KSCED(s, Ext. Orth.) curve in Figure 42 to the black KS-DFT curve which is covered by the olive KSCED(s, Ext. Orth., $v_T = 0$) curve). Again, the

KSCED(s, Ext. Orth., $v_T = 0$) and KS-DFT results are indistinguishable, indicating that enforcing external orthogonality and setting $v_T = 0$ within the new embedding theory reproduces reference KS-DFT results exactly.
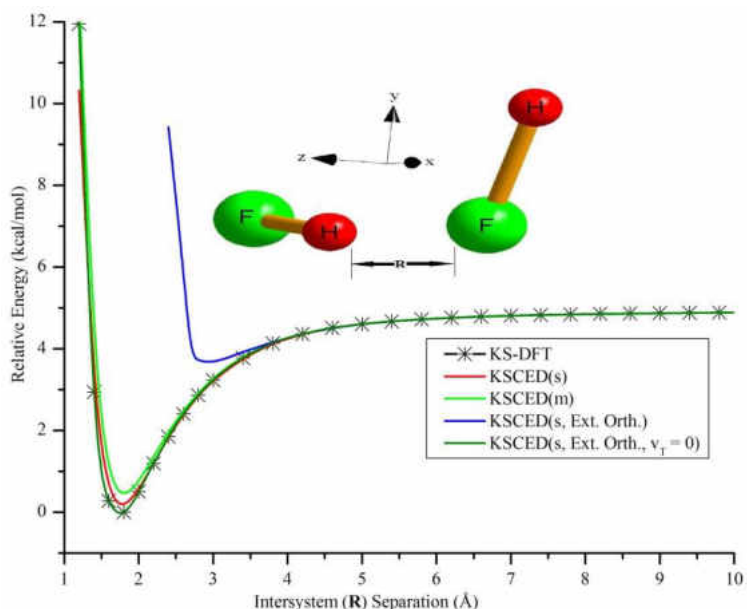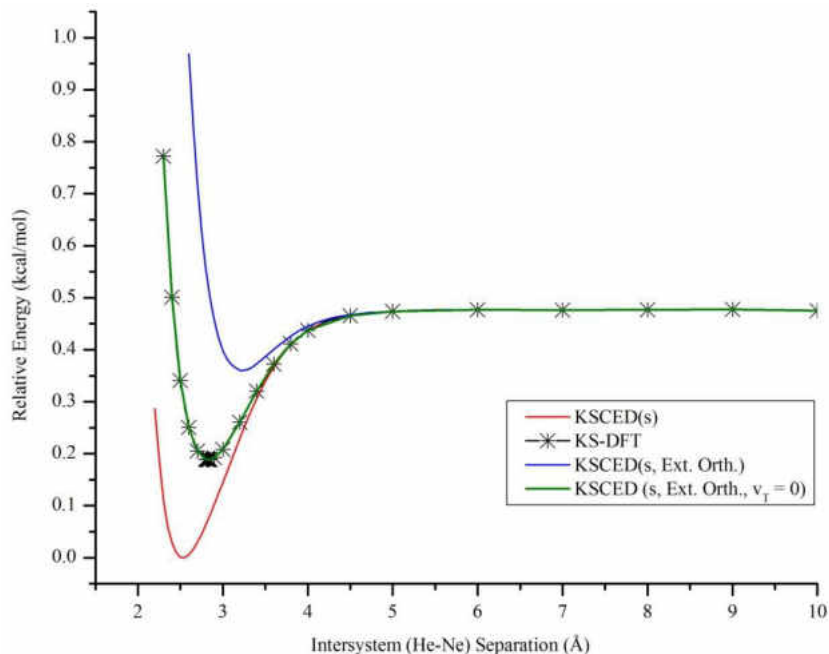

Figure 42. PECs of the He···Ne complex computed using the PW91 functional and aug-cc-pVTZ basis set in the methods shown in the inset. Note that the KS-DFT (black) and KSCED(s, Ext. Orth., $v_T = 0$) (olive) curves are degenerate. Thus, the olive curve completely obscures the black curve.

Fraction of Single Determinant Exchange in Hybrid Functionals

Table 14 shows the effect of varying the fraction of single determinant exchange in hybrid functionals on the disparity between KS-DFT and conventional DFT-in-DFT embedding total energies. The electron's self-energy has been thought to contribute to weaknesses in conventional DFT-in-DFT embedding theory and the use of hybrid functionals was suggested [322, 323] as a means of remedying the situation.

Table 14. Effect of the fraction of single determinant exchange in hybrid functionals on the discrepancy between KSCED(s) compared with KS-DFT energies. All calculations were done with the aug-cc-pVTZ basis; the $Li^+ \cdots Be$ calculations were done at 2.6 Å while those of $H_2O \cdots H_2O$ used the optimized geometry of Ref. [325].

Fraction of Single Determinant Exchange (h_x)	Total Energies (a.u.)		$\Delta E = E(KS\text{-}DFT) - E(KSCED(s))$
	E(KS-DFT)	E(KSCED(s))	
$Li^+ \cdots Be$ (B3LYP)			
0.04	-21.891671360364	-21.910489868010	0.018818507646
0.10	-21.926275975279	-21.946265485470	0.019989510191
0.20	-21.984084155181	-22.006189891727	0.022105736546
0.22	-21.995665672324	-22.018222696085	0.022557023761
0.24	-22.007253768098	-22.030272420481	0.023018652383
0.26	-22.018848422210	-22.042339520133	0.023491097923
0.28	-22.030449614588	-22.054424478564	0.023974863976
0.30	-22.042057325379	-22.066527809243	0.024470483864
0.32	-22.053671534949	-22.078650058669	0.024978523720
0.34	-22.065292223874	-22.090791808693	0.025499584819
0.36	-22.076919372944	-22.102953679274	0.026034306330
0.40	-22.100192975707	-22.127340472416	0.027147496709
$H_2O \cdots H_2O$ (BHandHLYP)			
0.3	-152.871040267362	-152.874371731043	0.003331463681
0.4	-152.860938326125	-152.865550519780	0.004612193655
0.5	-152.851386653639	-152.857334066069	0.005947412430
0.6	-152.842368786515	-152.849728379705	0.007359593190
0.7	-152.833869276532	-152.842747349011	0.008878072479
0.8	-152.825873584780	-152.836416692710	0.010543107930
$H_2O \cdots H_2O$ (B1B95)			
0.28	-152.871301065601	-152.874216293352	0.002915227751
0.38	-152.861562826376	-152.865710111952	0.004147285576
0.48	-152.852373589586	-152.857799215093	0.005425625507
0.58	-152.843716707634	-152.850487127785	0.006770420151
0.68	-152.835576580736	-152.843784118447	0.008207537711
$H_2O \cdots H_2O$ (MPW3LYP)			
0.2	-152.938318737311	-152.941478197217	0.003159459906
0.3	-153.100373174713	-153.104731151947	0.004357977234
0.4	-153.263167359929	-153.268735198459	0.005567838530
0.5	-153.426685309317	-153.433490131835	0.006804822518
0.6	-153.590912114820	-153.599000281007	0.008088166187

If this were indeed the case; then, the accuracy of embedding theory energies should improve if the fraction of single determinant exchange were increased in hybrid functionals. In the present study, calculations of the $Li^+\cdots Be$ and $H_2O\cdots H_2O$ complexes were performed using the hybrid functionals indicated in Table 14 in conventional DFT-in-DFT and KS-DFT methods while varying the fraction of single determinant exchange in the functionals (at the same geometry of the complex). Observing the last column of Table 14, it can be seen that increasing the fraction of single determinant exchange rather increased the discrepancy between the energies of KS-DFT and KSCED(s) for all hybrid functionals tested with the $H_2O\cdots H_2O$ and $Li^+\cdots Be$ systems. This is contrary to the prediction of Laricchia et al. [322, 323] on the use of hybrid functionals as a remedy for DFT-in-DFT.

On the other hand, the newly developed DFT-in-DFT embedding protocol described and implemented in this dissertation was found to be more-or-less insensitive to variations in the fraction of single determinant exchange (hx), virtually reproducing the reference KS-DFT energies for the different values of hx in all tested hybrid functionals.

Concluding Remarks

In this Chapter, the performance of the newly developed variant of DFT-in-DFT embedding that includes external orbital orthogonality as an additional constraint in deriving the coupled Euler-Lagrange equations, which are solved to self-consistency for the subsystems, was assessed. Irrespective of the DFT functional type, the new variant of embedding theory, using supermolecular basis expansions, KSCED(s, Ext. Orth., $v_T = 0$), was found to reproduce reference KS-DFT results exactly, leading to only negligible

density deviations for all the systems tested. It stands to reason, therefore, that the present embedding approach corrects for the inherent limitation of "lack of tendency" in conventional DFT-in-DFT embedding. "Tendency" is used here with respect to the performance of DFT functionals in conventional KS-DFT. There is a general tendency for GGA functionals to improve LDA results in KS-DFT. There is no such general tendency in previous formulations of DFT-in-DFT embedding theory. In some instances, DFT-in-DFT embedding results with GGA functionals are better than those from LDA (in comparison with reference KS-DFT results) and at other instances, they are worse. The present study is not the first to find such problems with conventional DFT-in-DFT. For example, as noted before, the GGA KSCED geometries of all the complexes considered in Ref. [315] were essentially worse than those from LDA KSCED when compared with KS-DFT. In addition, the electronic couplings computed for π-stacked nucleobase dimers in Ref. [345] by KSCED were worsened when semilocal GGA functionals were used in comparison with LDA and reference results. The results presented in this Chapter, however, verify that the new embedding theory is capable of exactly reproducing reference KS-DFT data (at least for the tested systems), irrespective of the DFT functional type. Therefore, instabilities in embedding results due to functional type are completely nullified in the new embedding protocol. Moreover, the new technique completely avoids the use of kinetic functionals that introduce new sources of error within DFT-in-DFT.

Analyses of deformation densities for different systems with varying degrees of interaction strengths between subsystems were presented. The results showed, in general, that, in the absence of external orthogonality, $|\Delta\rho| > 0$ at the artificial boundary between

subsystems introduced in embedding theory. In other words, there is some electron density in the interfacial region between subsystems that conventional embedding theory fails to account for; and this density correlates with the strength of interaction between the subsystems. For example, the buildup of electron density was found in KSCED(x) calculations to be negligible at the interface between CH_4 molecules in the $CH_4 \cdots CH_4$ complex but substantial in complexes such as the parallel displaced (PD) π-stacked $C_6H_6 \cdots C_6H_6$ and hydrogen-bonded complexes considered in this study. A key feature of partitioning a system's density is that of introducing a nodal surface in the system. Although embedding schemes seek to account for interactions between subsystems by including nonadditive terms, such terms depend on subsystems' densities and a total density that is obtained as a sum of subsystems' densities with the inherent limitation of a nodal surface having already been introduced into the system. It is thus not surprising that such added terms fail to exactly compensate for the electron density at the interface in embedding theory. We have, however, shown in this Chapter that partitioning a system's density (as is done in DFT-in-DFT embedding) can be made exact by constraining subsystems' orbitals to be orthogonal to each other and enforcing the vanishing of non-additive kinetic energy. By so doing, total densities and energies are well reproduced, irrespective of DFT functional type or the strength of interaction between the subsystems.

In optimized effective potential embedding (emb-OEP) [69, 70] and partition DFT (PDFT) [317] methods, a unique embedding (partition) potential is introduced as a Lagrange multiplier to the density constraint in Eq. (1.5). It would be of much interest to obtain density difference maps similar to those presented here in such approaches. In particular, it is unclear whether such added potentials correct the problem introduced by

the artificial interface, given that the boundary introduced in embedding theory is essentially a nodal surface that is nonexistent in a normal KS-DFT calculation on the total system. For example, a conventional DFT-in-DFT embedding calculation on the $F^-\cdots H_2O$ complex fixes electron number on F^- and H_2O fragments and consequently estimates a density for F^- that is too high, assumes zero density at the interface between the fragments, and estimates a density around the H of H_2O closest to F^- that is too low compared to KS-DFT densities. This notwithstanding, the new embedding recipe verifies that partitioning a system's density is possible provided strict orthogonality conditions are enforced between the subsystems.

By extending the usual monomer basis expansion, KSCED(m), to include basis functions in the complementary subsystem centered on atoms close to the interface, a less computationally intensive approach was realized, KSCED(e), that gives results close to those obtained with the supermolecular basis, KSCED(s), for the systems tested. KSCED(e, Ext. Orth., $v_T = 0$) calculations were also found to give results that were closely related to those from KSCED(s, Ext. Orth., $v_T = 0$) and reference KS-DFT.

The newly developed computer program for computing electron densities was also verified to be accurate (e.g., comparing Images C and D of Figure 36 to Figure 4 of Ref. [324], besides preliminary tests that found the new program to integrate densities of molecules over all space to give the total number of electrons in the molecules).

CHAPTER IX

GVVPT2 STUDIES OF LITHIUM AND BERYLLIUM TRIMERS

Introduction

This Chapter discusses GVVPT2 studies of Li_3 and Be_3. The study of metal

dimers is but a first step to understanding bonding in clusters and bulk metals. It is only a

first step because the properties of even nanoscale clusters but bulk materials particulatly

can, in general, be quite different from those of their constituents. For example, the force

constants of Sc_2, Cr_2, and Mn_2 are 0.76, 3.54, and 0.09 mdyn/Å, respectively. For the

metal trimers, the values drop to 0.54 and 1.91 mdyn/Å for Sc_3 and Cr_3, respectively, but

increases to 0.37 mdyn/Å for Mn_3 [346]. In addition, Mn_2 is generally known to be

antiferromagnetic [263, 347] whereas both Mn_4 and Mn_5 clusters are ferromagnetic

[237]. Moreover, the Mn_2 bond length has been experimentally determined as 3.4 Å

[347] whereas in the bulk metal, the Mn-Mn distance is only 2.25-2.95 Å [250].

These examples demonstrate how the properties of metals may change on going

from two atoms to small clusters and then to the bulk metals. It is for this reason that after

elucidating the bonding in diatomic metallic molecules, the next step should be to

consider small clusters of metal atoms and such clusters consisting of three atoms are a

natural starting point. Moreover, since the ultimate goal is to be able to embed GVVPT2

calculations in to large systems (that is, being able to carry out GVVPT2 calculations of

small molecules or clusters of interest that are embedded in a larger environment, e.g., a

molecule encapsulated in a C-60 cage or a solvated molecule) where the larger environments are described at lower levels of theory such as at the DFT level, it is necessary to first study small isolated clusters before delving into an embedding procedure involving GVVPT2 and DFT. It was also for this reason that the newly developed accurate DFT-in-DFT embedding theory method was presented prior to the present Chapter. Embedding theory schemes involving wave function theory (WFT) methods embedded in DFT (i.e., WFT-in-DFT embedding) have previously been developed [67, 68, 76]. In such methods, the environment subsystem is often treated at the DFT level, generating an embedding potential which is then included as an external potential in WFT calculations on the embedded subsystem. Such procedures are quite elegant and Khait and Hoffmann [68] showed that such recipes permit high level descriptions of not only the ground states of embedded subsystems but also their low-lying excited states, provided such excited states are indeed localized within the embedded subsystems. The main problem with previous embedding formulations in this regard is the inaccurate description of electron density at the interface of subsystems as was observed in Chapters VII and VIII in the case of conventional DFT-in-DFT embedding theory. However, the newly developed DFT-in-DFT embedding theory method that was presented in Chapter VII was shown [5] to be applicable also in the case of WFT-in-DFT embedding theory. The effort to investigate metal triatomics at the GVVPT2 level of theory was undertaken as a first step towards the ultimate goal of embedding GVVPT2 calculations of small clusters in large environment subsystems.

The rest of this Chapter is organized as follows. In the present subsection, a brief review of previous studies of Li_3 and Be_3 is given; the next subsection describes

computational details; a third subsection presents and discusses results obtained in the present study and makes comparisons with previous theoretical and experimental data on the studied systems; while a final subsection contains concluding remarks.

Previous Studies of Li_3

Small clusters of Li are a natural starting point for studies of metallic clusters since Li is the lightest and simplest of such elements. Li_3 has been the subject of many previous electronic structure and dynamics studies [348]. Geometry optimizations and construction of potential energy surfaces (PESs) of such small trimers are a prerequisite for molecular dynamics studies. PESs of alkali metal trimers provide important information such as pseudorotation barriers, three-fold symmetric wells, as well as D_{3h} Jahn-Teller crossings [349]. Such surfaces have therefore been widely studied [350-356]. Ehara and Yamashita [349] determined the ground state geometry of Li_3 as an isosceles triangle, corresponding to the $^2B_2$ irreducible representation of the C_{2v} point group, through state-averaged CASSCF/MRCI with a triple-ζ quality basis set. The same authors found the 1^2A_1 to be only 0.01 eV less stable than the X^2B_2 state at equilibrium whereas the first excited $^2B_2$ state lay much higher (i.e., at 1.28 eV). In this study, the obtuse isosceles triangular geometry of X^2B_2 with sides $R_{12} = R_{13} = 2.79$ Å, $R_{23} = 3.28$ Å, a symmetric stretching frequency (ω_e) of 325 cm^{-1}, a binding energy (D_e) of 13.73 kcal/mol, and an apex angle of 71.8º was found to be 74 cm^{-1} (0.885 kcal/mol) more stable than the acute isosceles triangular C_{2v} structure with $R_{12} = R_{13} = 3.06$ Å, $R_{23} = 2.68$ Å, symmetric stretching frequency (ω_e) 337 cm^{-1}, and apex angle 52.0º. Meanwhile

226

an equilateral triangular structure for Li_3 with sides $R_{12} = R_{13} = R_{23} = 2.90$ Å lay much higher (i.e., at 2423 cm^{-1} or 6.93 kcal/mol) energetically. On the other hand, a FCI calculation that used the three valence electrons of Li_3 while freezing the 1s electrons through use of an augmented effective core potential (ECP) basis set [357] predicted the lowest spin-aligned quartet state, $1\,^4A_2'$ ($^4B_2$ in C_{2v} symmetry), to be an equilateral triangle (D_{3h} symmetry) with bond length 3.10 Å and binding energy 11.76 kcal/mol [350]. Such an interaction energy is rather large for a spin-aligned Li_3 state given that the spin-aligned Li_2 is a van der Waals species just like Mn_2. Stronger bonds have been reported in smaller clusters of more than two Mn atoms [250, 346] compared to the dimer [347]. The Ref. [350] study suggests a similar scenario for Li_3 in comparison with Li_2. Such stronger interactions in clusters of three and more atoms as seen in the cases of Li_3 [350] and Mn_3 [346] can be explained in terms of contributions from three-body interaction terms [352]. A CCSD(T) study [358] obtained a X^2B_2 for Li_3 corresponding to an obtuse isosceles triangular geometry with $R_{12} = R_{13} = 2.761$ Å, $R_{23} = 3.237$ Å, and an apex angle of 71.8º when using the cc-pwCVQZ basis set. A CASSCF/MRCISD study [359] of the low-lying doublet states of Li_3 that used the technique of macroconfigurations ($\kappa(\mathbf{n})$s) as was used in the present studies, also found a X^2B_2 ground state for Li_3 with $R_{12} = R_{13} = 2.763$ Å, $R_{23} = 3.240$ Å, and an apex angle of 71.8º when using the cc-pwVTZ. A X^2B_2 ground state was also obtained by Ghassemi et al. [360] in MCSCF/MRCI calculations using the aug-cc-pVTZ basis set. For this state, they obtained $R_{12} = R_{13} = 2.77$ Å, $R_{23} = 3.295$ Å, and an apex angle of 73º. These

authors additionally found the 1^2A_1 state of Li_3 to have an acute isosceles triangular C_{2v} structure with $R_{12} = R_{13} = 3.08$ Å, $R_{23} = 2.61$ Å, and an apex angle of 51° and closely associated with the X^2B_2 ground state; the minima of the two states being separated by a conical intersection at the totally symmetric $1^2E'$ configuration of the D_{3h} point group. There are seemingly no experimental data on Li_3 apart from the resonant two-photon ionization (RTPI) spectra of its $2^2E'$ excited state obtained by Wolf et al. [361].

Previous Studies of Be$_3$

Just like Li_3, there appears to be no experimental data on the ground state of Be_3. However, the molecule has been the subject of several theoretical studies [362-377]. Differences exist in terms of bonding in the dimer and trimer of Be. Whereas Be_2 is very weakly bound with the atoms held together mostly by van der Waals forces (e.g., MP4 predicts a binding energy of only 6.0 kcal/mol [363]), Be_3 exhibits significant bonding (e.g., MP4 predicts a binding energy of 56.0 kcal/mol for Be_3 [363]). This relatively strong bonding interaction in comparison with the dimer was attributed to three-body interactions, contributing up to 76% to the bond energy [362]. The binding strength in Be clusters generally increases with cluster size; e.g., whereas Hartree-Fock predicts the dimer and trimer of Be to be virtually unbound [377], the tetramer is bound by 35.0 kcal/mol at this level of theory [375]. Electron correlation effects are particularly important to describing the bonding in Be_3. Without sufficiently accounting for dynamic and non-dynamic electron correlation effects, inadequate results are obtained [366].

Watts et al. [365] found the CCSD results of Be_3 to be substantially different from MRCI and FCI results. The same observation was made by Lee et al. [365] who obtained a bond energy of 24.0 kcal/mol for Be_3 at the MRCI level and concluded that even the best singly-reference approach such as CCSD was incapable of quantitative accuracy in the determination of the binding energy for Be_3.

Many theoretical methods agree on the ground state of Be_3 as a singlet equilateral triangular structure (D_{3h} symmetry) corresponding to the $^1A_1'$ term. For this term, MRCI/[4s2p1d] predicts a bond energy (D_e) of 13.9 kcal/mol and bond length (R_e) of 2.32 Å [364]; MRCI/[7s4p2d] predicts D_e = 19.02 kcal/mol and R_e = 2.23 Å [375]; MRCI/[5s3p2d1f, ANO basis] gives D_e = 22.50 kcal/mol and R_e = 2.22 Å [376]; CCSD(T)/ [5s3p2d1f, ANO basis] obtains D_e = 20.40 kcal/mol and R_e = 2.23 Å [376]; while FCI/[3s2p1d, ANO basis] gives D_e = 17.29 kcal/mol and R_e = 2.27 Å [370] [N.B.: Bond energy here refers to the energy required to dissociate one mole of the trimer into atoms]. These data are summarized in Table 42 together with data from other methods compared with data from the present study. The data from previous MRCI studies with different basis sets [364, 375, 376] indicates a fairly strong basis set effect involved in the description of Be_3; with large basis sets tending to predict larger D_e but smaller R_e values. The same trend was observed at the GVVPT2 level as will be seen in the Results and Discussion subsection of this Chapter. Lee [372] analyzed basis set superposition errors (BSSE) for Be_3 at the MP2 and CCSD(T) levels of theory. Whereas such effects were minimal in calculations for which the core 1s electrons were frozen, they were significant in all-electron-correlated calculations for all tested basis sets. In the former set

of calculations, CBS limit D_e values were 32.63 kcal/mol and 24.28 kcal/mol for MP2 and CCSD(T), respectively (obtained by extrapolating cc-pVDZ and cc-pVTZ energies). In the latter set of calculations, CBS limit D_e values were 31.38 kcal/mol and 24.79 kcal/mol for MP2 and CCSD(T), respectively (obtained by extrapolating cc-pCVDZ and cc-pCVTZ energies).

Computational Details

All calculations were done using the C_{2v} point group. The active spaces used in calculations of Li_3 and Be_3 consisted of 2s- and 2p-derived MOs. These orbitals were partitioned into reference macroconfigurations ($\kappa(\mathbf{n})$s) that were used in MCSCF and GVVPT2 calculations. The partitioning schemes were as follows.

In the case of Li_3, all 2s-derived MOs were placed together in the first valence subspace while 2p-dominated MOs constituted a second subspace. Three reference $\kappa(\mathbf{n})$s were defined as follows,

$$\kappa(\mathbf{n}) \ = \ \left(3a_1 4a_1 2b_2\right)^3 \left(5a_1 6a_1 7a_1 1a_2 1b_1 2b_1 3b_2 4b_2 5b_2\right)^0 \tag{9.1}$$

$$\kappa(\mathbf{n}) \ = \ \left(3a_1 4a_1 2b_2\right)^2 \left(5a_1 6a_1 7a_1 1a_2 1b_1 2b_1 3b_2 4b_2 5b_2\right)^1 \tag{9.2}$$

$$\kappa(\mathbf{n}) \ = \ \left(3a_1 4a_1 2b_2\right)^1 \left(5a_1 6a_1 7a_1 1a_2 1b_1 2b_1 3b_2 4b_2 5b_2\right)^2 \tag{9.3}$$

This set of reference $\kappa(\mathbf{n})$s was used to optimize the structure of Li_3 both at the MCSCF and GVVPT2 levels using cc-pVDZ and cc-pVTZ basis sets. The 1s-derived MOs were frozen in both MCSCF and GVVPT2 calculations. It should be recalled here that studies of low-lying doublet states of Li_3 were previously performed at the MRCISD level of theory that used the technique of $\kappa(\mathbf{n})$s [359]. However, such studies involved a larger

active space in which MRCISD calculations included single and double electron excitations from the subspace of 1s-derived MOs into high-lying orbitals. The large active space consisted of three active subspaces and ten reference $\kappa(\mathbf{n})$s that were used to construct an entire CAS space. The purpose of investigating Li_3 here is two-fold: firstly, to assess the capability of GVVPT2 for describing this system (using smaller active spaces) in comparison with the more computationally demanding MRCISD method; secondly, to assess the importance of the 2p-derived MOs of Li in the active space. In order to investigate the second point, additional calculations of the X^2B_2 ground state of Li_3 were performed with an active space of only 2s-derived MOs (i.e., with the 2p-derived MOs considered as virtual orbitals). A single reference $\kappa(\mathbf{n})$ was used in such calculations viz.

$$\kappa(\mathbf{n}) = \left(3a_1 4a_1 2b_2\right)^3 \tag{9.4}$$

Meanwhile, the spin-aligned 1^4B_2 state of Li_3 was also computed using reference $\kappa(\mathbf{n})$s (9.1) to (9.3).

Calculations of the X^1A_1' ground state of Be_3 partitioned the active orbitals in a way similar to that used to construct reference $\kappa(\mathbf{n})$s (9.1) to (9.3) for Li_3. In the case of Be_3, however, five reference $\kappa(\mathbf{n})$s were specified as follows.

$$\kappa(\mathbf{n}) = \left(3a_1 4a_1 2b_2\right)^6 \left(5a_1 6a_1 7a_1 1a_2 1b_1 2b_1 3b_2 4b_2 5b_2\right)^0 \tag{9.5}$$

$$\kappa(\mathbf{n}) = \left(3a_1 4a_1 2b_2\right)^5 \left(5a_1 6a_1 7a_1 1a_2 1b_1 2b_1 3b_2 4b_2 5b_2\right)^1 \tag{9.6}$$

$$\kappa(\mathbf{n}) = \left(3a_1 4a_1 2b_2\right)^4 \left(5a_1 6a_1 7a_1 1a_2 1b_1 2b_1 3b_2 4b_2 5b_2\right)^2 \tag{9.7}$$

$$\kappa(\mathbf{n}) = \left(3a_1 4a_1 2b_2\right)^3 \left(5a_1 6a_1 7a_1 1a_2 1b_1 2b_1 3b_2 4b_2 5b_2\right)^3 \tag{9.8}$$

$$\kappa(\mathbf{n}) \; = \; \left(3a_1 4a_1 2b_2\right)^2 \left(5a_1 6a_1 7a_1 1a_2 1b_1 2b_1 3b_2 4b_2 5b_2\right)^4 \qquad (9.9)$$

All calculations used the cc-pVDZ and cc-pVTZ basis sets, except for calculations of the $1^4 B_2$ state of Li_3 for which only cc-pVDZ was used. Additional calculations involved the construction of the PEC of the symmetric dissociation of linear Be_3 into atoms. Such calculations were done in D_{2h} symmetry using the cc-pVDZ and cc-pVTZ basis sets.

Results and Discussion

Beryllium Trimer (Be_3)

The equilibrium structure of the $X^1 A_1'$ ground state of Be_3 is an equilateral triangle as shown in the schematic diagram in Figure 43. The Be-Be bond distance and binding energy for this structure, obtained at different levels of theory are shown in Table 15.
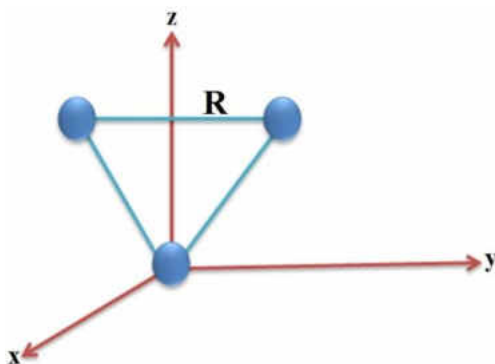

Figure 43. Schematic diagram of the optimized equilateral triangular structure of Be_3.

The data in Table 15 indicate that calculations of Be_3 have a strong basis set dependence. For example, the data in the first three rows of Table 15 were obtained at the same level of theory (MRCI based on a CASSCF reference), yet the binding energies (D_e) are quite

different from each other whereas the bond lengths (R_e) vary only slightly. It is shown that the three sets of data were obtained with different basis sets of increasing size from the first to the third row of the table. The binding energy also increases in this order, with the [4s2p1d] ANO Basis predicting the least D_e (13.84 kcal/mol) and the (12s7p4d3f)/[5s3p2d1f] predicting the largest (22.50 kcal/mol). On the other hand, the bond length decreases only slightly from R_e = 2.32 Å for the [4s2p1d] ANO Basis and R_e = 2.22 Å for the (12s7p4d3f)/[5s3p2d1f] basis set. These trends are repeated for the other methods, with large basis sets tending to predict high binding energies while only slightly decreasing the equilibrium bond distance. For example, GVVPT2 binding energy with cc-pVTZ is nearly double the cc-pVDZ value whereas the bond lengths obtained with the two bases differ by only 0.04 Å.

Table 15. Binding energies (D_e) and equilibrium Be-Be bond distances (R_e) of the equilateral triangular (D_{3h} symmetry) Be_3 molecule obtained from different methods and basis sets.

Method	Basis Set	D_e (kcal/mol)	R_e (Å)
CASSCF/MRCI[a]	[4s2p1d] ANO Basis	13.84	2.32
CASSCF/MRCI[b]	[7s4p2d]	19.02	2.23
CASSCF/MRCI[c]	(12s7p4d3f)/[5s3p2d1f]	22.50	2.22
CCSD(T)[c]	(12s7p4d3f)/[5s3p2d1f]	20.40	2.23
CASSCF/AQCC[d]	aug-cc-pV5Z	28.88 (29.51)[e]	2.17
Active space CCSDt[f]	cc-pVTZ	21.20	2.22
MP4(SDTQ)[g]	6-311 + G(3df)	25.90	2.24
FCI[h]	[3s2p1d] ANO basis	17.20	2.27
GVVPT2[i]	cc-pVDZ	12.91	2.26
GVVPT2[i]	cc-pVTZ	21.68	2.22

[a]Ref. [364], [b]Ref. [375], [c]Ref. [376], [d]Ref. [374], [e]Binding Energy obtained with an active space of 12 electrons in 14 MOs (where one MO of the set of $2p_z$ − derived MOs is removed from the active space of 1s-, 2s-, and 2p-derived MOs), [f]Ref. [377], [g]Ref. [366], [h]Ref. [370], [i]This work.

Other studies have also found calculations of Be_3 to show a strong basis set dependence. For example, when using a small basis set, [4s2p], Watts et al. [364] obtained dissociative energy profiles for Be_3 at different levels of theory (FCI, MRCI, CISD, CISDTQ, MBPT4, CCSD, and CCSDT), whereas a relatively large basis set, [4s2p1d, ANO basis], led to all methods predicting the molecule to be bound (for MRCI, the authors obtained D_e = 13.84 kcal/mol and R_e = 2.32 Å). The GVVPT2 values of D_e = 12.91 kcal/mol and R_e = 2.26 Å obtained with cc-pVDZ are quite close to the MRCI values of Watts et al. [374] and the FCI bond length of R_e = 2.27 Å [370]. Whereas the MRCI results were obtained from a CASSCF reference (that obviously contained more CSFs), the GVVPT2 calculations used the partitioned active space that led to reference $\kappa(\mathbf{n})$s (9.5) to (9.9) for use in the construction of a reference MCSCF wave function.

Since different methods have verified the dependence of these calculations on the basis set used (and particularly, the sensitivity of the binding energy to basis set size and quality) it is thus not surprising that GVVPT2 predicted binding energies differ from those obtained with other methods since those methods used different bases (note that the CCSDt binding energy of 21.20 kcal/mol is quite close to the GVVPT2 value of 21.68 kcal/mol obtained with the same basis set, cc-pVTZ). The AQCC [374] binding energy of 28.88 kcal/mol (obtained with an active space of all 12 electrons of Be_3 in 13 MOs derived from 1s, 2s, and 2p minus two $2p_z$ − derived MOs and using the aug-cc-pV5Z basis set) is about 7 kcal/mol larger than the GVVPT2 value with cc-pVTZ although the GVVPT2 bond length is only 0.05 Å longer. By adding one more $2p_z$ − derived MO into the active space leading to a space of 12 electrons and 14 orbitals (12e, 14o), a slightly

higher binding energy (29.51 kcal/mol) was obtained in the AQCC study [374]. These authors oriented the Be_3 molecule to lie on the xy-plane in their study such that the $2p_z$−derived MOs were the least important. In the present study (and as shown in Figure 43), the Be_3 molecule was placed on the yz-plane and 1s electrons were frozen in all calculations. The AQCC study correlated the 1s electrons. In GVVPT2 calculations of Be_3, the leading configuration was $3a_1^2 4a_1^2 2b_2^2$ contributing 74% to the overall wave function with both double and triple-ζ basis sets (N.B. The occupied orbitals in the indicated configuration are 2s-derived MOs). This weight percent was the same at the equilibrium geometry and at the dissociation limit.
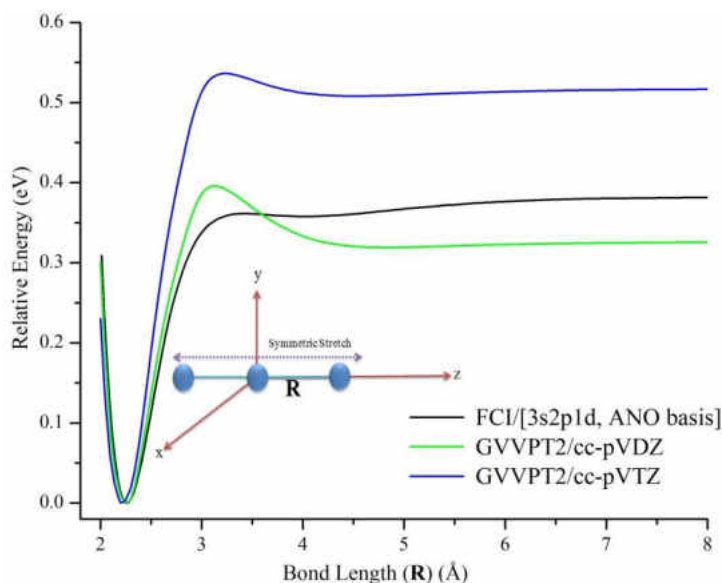

Figure 44. PECs of the symmetric dissociation of linear Be_3 (D_{2h} symmetry) computed at the GVVPT2 level of theory using the cc-pVDZ and cc-pVTZ basis sets, compared with the FCI curve (Ref. [370]) that used the [3s2p1d] ANO basis set.

Figure 44 contains PECs of the symmetric dissociation of linear Be_3, obtained at the GVVPT2 level using the cc-pVDZ and cc-pVTZ basis sets, and compared with a

previous FCI curve. In these calculations (done in D_{2h} symmetry), the central atom was held fixed while the edge atoms were gradually pulled apart.

As can be seen in Figure 44, the GVVPT2 PEC obtained with cc-pVDZ is quite similar to the FCI curve at short bond lengths. The FCI curve predicted an inner deep minimum and an outer shallow van der Waals minimum. GVVPT2 calculations reproduce these essential features of the curve including the hump between the deep inner minimum and outer van der Waals minimum. Again, given that the FCI calculations were done with a different basis set than was used in the present studies, it is not surprising that the binding energies are not in agreement. As was observed in the case of the triangular molecule, binding energies of the linear species are also found to depend fairly strongly on the basis set used. This fact was observed also by Vetere et al. [378] who found the potential well depths for Be_2 and linear Be_3 to correlate with basis set size, with small basis sets leading to completely dissociative energy profiles. Their calculations of linear chains of Be_4 and Be_5 also predicted double minima as observed here for linear Be_3.

Table 16. Binding energies (D_e) and equilibrium Be-Be bond distances (R_e) of the symmetric dissociation of linear (D_{2h} symmetry) Be_3 molecule obtained at the GVVPT2 level of theory, compared with previous FCI results.

Method	Basis Set	R_e (minimum) (Å)	R (maximum) (Å)	R (Van der Waals min.) (Å)	Binding Energy (D_e) (kcal/mol)
GVVPT2	cc-pVDZ	2.25	3.14	4.84	7.61
GVVPT2	cc-pVTZ	2.21	3.23	4.53	11.99
FCI[a]	ANO [3s2p1d]	2.26	3.55	4.02	8.76
FCI[b]	ANO [5s3p2d]	2.23	-	-	11.40

aRef. [370], [b]Ref. [378].

Table 16 contains data describing the curves in Figure 44. It can be seen that GVVPT2 results with cc-pVDZ compare well with FCI results with the [3s2p1d] ANO basis set [370] whereas GVVPT2 results with cc-pVTZ are also close to the FCI studies of Vetere et al. [378] with a slightly larger basis set, [5s3p2d] ANO basis set. However, GVVPT2 predicts the maximum to occur at a slightly shorter bond length and the outer van der Waals minimum to occur at a slightly longer bond length than does FCI [370].

Lithium Trimer (Li_3)

Parameters describing the optimized geometry of Li_3 are shown in Table 17. Its X^2B_2 ground state is found to be an obtuse isosceles triangle. Also included is data on the computed 1^4B_2 state of the molecule.

Table 17. Equilibrium Li-Li bond distances (R_e and R'_e) and apex angle (Θ) of the optimized geometries of X^2B_2 and 1^4B_2 states of the Li_3 molecule obtained at the GVVPT2 level of theory, compared with previous results.

Method	Basis Set	R_e (Å)	R'_e (Å)	Θ (degrees)
		X^2B_2		
CASSCF/MRCI[a]	cc-pVTZ	2.79	3.21	71.8
MCSCF/MRCI[b]	aug-cc-pVTZ	2.77	3.30	73.0
CCSD(T)[c]	cc-pwVQZ	2.76	3.24	71.8
CASSCF/MRCISD[d]	cc-pwVTZ	2.76	3.24	71.8
GVVPT2[e]	cc-pVDZ	2.83	3.34	72.5
GVVPT2[e]	cc-pVTZ	2.79	3.27	72.0
GVVPT2[f]	cc-pVDZ	2.83	3.28	70.9
GVVPT2[f]	cc-pVTZ	2.79	3.25	71.1
		1^4B_2		
GVVPT2[e]	cc-pVDZ	3.18	3.17	59.89

[a]Ref. [349], [b]Ref. [360], [c]Ref. [358], [d]Ref. [359], [e]This work, [f]This work (small active space of only three 2s-derived active MOs as indicated in reference $\kappa(\mathbf{n})$ (9.4)).

The data in Table 17 show general agreement between GVVPT2 results in comparison with those from other high level ab initio methods. GVVPT2 results with a partitioned active space of 2s- and 2p-derived MOs and cc-pVTZ gave the same R_e (2.79 Å) and nearly the same R'_e (3.27 vs 3.21 Å) and apex angle (72.0° vs 71.8°) compared with MRCI calculations that used a CASSCF reference [349]. Interestingly, GVVPT2 results that used a small active space of only 2s-derived MOs and cc-pVTZ gave results in very good agreement with MRCISD calculations [359] that used all 1s-, 2s-, and 2p-derived MOs and correlated all 12 electrons of Li. GVVPT2 bond lengths of $R_e = 2.79$ Å and $R'_e = 3.25$ Å and apex angle of $\Theta = 71.1°$ agree with the MRCISD values of $R_e = 2.76$ Å and $R'_e = 3.24$ Å and apex angle of $\Theta = 71.8°$. These results suggest that the 1s electrons (as well as the 2p-derived MOs) of Li may not play a major role in the bonding in the X^2B_2 state of Li_3. This fact is supported by comparing GVVPT2 results obtained with cc-pVTZ using an active space of 2s- and 2p-derived MOs with those obtained with an active space of only 2s-derived MOs. The data compare as follows: $R_e = 2.79$ vs 2.79 Å, $R'_e = 3.27$ vs 3.25 Å and $\Theta = 72.0°$ vs 71.1° for large and small active spaces, respectively. Including the 2p-derived MOs into the active space slightly increases R'_e by 0.02 Å and Θ by 0.9 Å. It is quite interesting also that GVVPT2 results obtained with cc-pVDZ compare fairly well with MCSCF/MRCI results [360] obtained with a large basis set (aug-cc-pVTZ). The data compare as follows: $R_e = 2.83$ vs 2.77 Å, $R'_e = 3.34$ vs 3.30 Å and $\Theta = 72.5°$ vs 73.0° for GVVPT2 and MCSCF/MRCI, respectively. These results suggest that basis set effects may be small in the description of Li_3. This fact was

noted in the Ref. [359] study where different basis sets used to study low-lying doublet states of Li_3 led to similar results.

The GVVPT2 data obtained for the $1^4 B_2$ state of Li_3 suggests an equilateral geometry as was obtained also by Colavecchia et al. [350] at the FCI level of theory.

Concluding Remarks

This Chapter presented studies of low-lying states of Be_3 and Li_3 as were done at the GVVPT2 level of theory. Overall, GVVPT2 was found to predict geometries that were in good agreement with results from previous studies that used other high level methods, including FCI. In particular, the present study demonstrated that small active spaces partitioned into reference $\kappa(\mathbf{n})$s are sufficient for accurately describing, at least, the ground states of the studied molecules. In the case of Li_3, this study suggests that correlating 1s electrons of Li does not change results significantly. Although the present work did not include calculations that correlated 1s electrons of Li, yet comparison of results from the present work with a previous MRCISD study [359] that had considered such core-valence correlation supports the conclusion that 1s electrons may not be important in the description of the bonding.

Calculations of Be_3 revealed a strong dependence of the quality of results on the type and size of the basis set used. This dependence was shown mostly in binding energies as evidenced in e.g., the PECs in Figure 44 for the symmetric dissociation of linear Be_3 (D_{2h} symmetry) into atoms. GVVPT2 predicted the $1^1 \Sigma_g^+$ state of linear Be_3 to lie 0.42 eV higher than the $X^1 A_1'$ ground state of triangular Be_3 at the equilibrium geometry when using the cc-pVDZ basis set. This is in fairly good agreement with a

previous FCI study [370] that had found these two states to be separated by about 0.36 eV using the [3s2p1d] ANO basis set.

Calculations on the supposedly simple Li and Be triatomics are expected to provide insight into studies on trimmers of transition metals. From the present study, it is clear that much is still to be learned about Li_3 and Be_3.

CHAPTER X

OVERVIEW AND FUTURE DIRECTIONS

Overview

This dissertation presented results of GVVPT2 studies of ground and low-lying excited electronic states of selected dimers of the first and second row of transition elements. Also included were GVVPT2 studies of triatoms of lithium and beryllium. The transition metal molecules considered in this work were investigated at the GVVPT2 level of theory for the first time. Transition metal systems are not easy targets for theoreticians since these systems often involve many low-lying electronic states occurring within narrow energy ranges (as was particularly illustrated in the case of Ni_2). Such situations pose numerous challenges to theoretical calculations varying from discontinuities in PECs [238, 239] to convergence crises [232]. For example, a previous study due to Camacho et al. [18] that used the MCQDPT method to investigate Mn_2, observed over 5000 intruders (or discontinuities in the PEC) within an internuclear distance of only 2.1 Å. Contrary to the conclusion drawn by Camacho et al. [18] that multireference perturbation theory (MRPT) methods were incapable of describing challenging systems like those of transition metal molecules, the present study found the GVVPT2 method to produce smooth and continuous PECs of both ground and low-lying excited electronic states of all the molecules investigated.

The work in this dissertation is also the first to have applied a version of GVVPT2 that includes scalar relativistic effects through the spin-free exact two component (sf-X2C) method [119-124]. Such effects were found in the present study to significantly change the chemistry of second row transition metal molecules relative to their first row counterparts. Examples of such changes include: the large effective bond order (EBO) of the ground state of Y_2 compared to its isovalent Sc_2 counterpart (with the same ground state symmetry); the absence of an outer shelf in the ground state PEC of Mo_2 whereas one was found in its isovalent Cr_2 counterpart (with the same ground state symmetry); and the existence of significant bonding interaction in the ground state of Tc_2 whereas its isovalent Mn_2 was found to be a weak van der Waals species. The present work therefore underscored the importance of including relativistic effects particularly in the theoretical investigation of electronic states of molecules of second row transition elements (and of course, molecules of other heavier elements).

The present work verified the capability of GVVPT2 for describing challenging transition metal systems not just in terms of smoothness of PECs but also in terms of accuracy. The spectroscopic data obtained at the GVVPT2 level for all studied molecules were in good agreement with data obtained from previous studies that had employed other high level ab initio techniques and also to experimental data where available. Moreover, the predicted ground state symmetries of the investigated molecules were in agreement with generally held views on those molecules.

Although the technique of macroconfigurations $\kappa(\mathbf{n})$s [22] has been used within GVVPT2 for many years, there is a uniqueness worth mentioning in the present work. This uniqueness relates to the way active spaces were chosen and partitioned into

242

reference κ(**n**)s for MCSCF and GVVPT2 calculations. The partitioning scheme mostly started from a valence-bond-style approach in which bonding orbitals were grouped together in the same valence subspaces with their corresponding antibonding counterparts. Prior active spaces for GVVPT2 tended to be truncations (e.g., singles and doubles) of CASSCF spaces. It took quite some experimentation with molecules like Cr_2 and Mn_2 to arrive at such a partitioning scheme. It was shown in the work reported herein that such partitioning of the active space led, in many cases, to only one reference κ(**n**) that proved to be sufficient for describing the investigated states. For example, all investigated states of Cr_2 used the same single reference κ(**n**) as well as those of its isovalent Mo_2 counterpart.

The present work included electronic states that have not previously been characterized in the literature, notably the $2^1\Sigma_g^+$ and $3^1\Sigma_g^+$ states of Y_2 as well as the $1^5\Sigma_g^+$ and $1^9\Sigma_g^+$ states of Tc_2. In particular, GVVPT2 studies of the three lowest $^1\Sigma_g^+$ states of Y_2 were the first to find that those states correlate with the ground state atoms' dissociation limit, as expected theoretically. Moreover, the present study is the first to have obtained full PECs of these states of Y_2, which prove to be critical in understanding the dissociation channels. Calculations of the $1^5\Sigma_g^+$ and $1^9\Sigma_g^+$ states of Tc_2 found them to be significantly nondegenerate at short bond lengths contrary to Mn_2 where states of the same symmetry were found to be quasidegenerate with the $1^1\Sigma_g^+$ state at all bond lengths. This scenario begs an explanation from relativistic effects. Since such effects are minimal in Mn_2 with the result that the 3d and 4s subshells are substantially different in

spatial extent, the 4s electrons remain nonbonding such that the Mn_2 molecule is held together only by weak antiferromagnetic coupling of the 3d electrons. Therefore, the 3d-derived MOs are not strongly perturbed energy-wise. Thus, different distributions, and spin orientations, of electrons within such nearly degenerate orbitals (leading e.g., to a $1^1\Sigma_g^+$ or $1^5\Sigma_g^+$ or $1^9\Sigma_g^+$ state) produce electronic states that are quasidegenerate. In Tc_2, however, the situation is different. Fairly strong relativistic effects contract the outer 5s subshells such that both the 4d and 5s orbitals participate in bonding. Since the 4d- and 5s-derived MOs get strongly perturbed energy-wise in the process of bond formation, different distributions of electrons within these orbitals lead to nondegenerate electronic states.

Studies of electronic states of Ni revealed what seems to be a general rule of thumb for transition elements of the first row; that these elements seldom form strong bonds involving participating atoms in a ground state configuration with a fully filled 4s subshell. It seems that the fully filled 4s-subshell is repulsive and hence, discourages bonding. Bonding in these systems appears to be favored by atomic configurations that involve at least one of the participating atoms in an excited state ($3d^{n+1}4s^1$). Calculations of states of Ni_2 that involved states within the $^3F_4(3d^8 4s^2) + \,^3F_4(3d^8 4s^2)$ dissociation channel of ground state Ni atoms, as well as those of Mn_2 within the $^5S(3d^5 4s^2) + \,^5S(3d^5 4s^2)$ asymptote, were found to be van der Waals-like electronic states. On the other hand, all calculations of the studied molecules of first row transition elements that involved the coupling of atoms with a partially filled 4s subshell predicted strong bonding interactions; e.g., the investigated states within the $^3D_3(3d^9 4s^1) + \,^3D_3(3d^9 4s^1)$

manifold of the Ni_2 molecule. On the other hand, Tc_2 was found to form strong bonds in electronic states within the $^5S(4d^55s^2) + {}^5S(4d^55s^2)$ dissociation channel. This again, is due to relativistic effects as explained previously.

This dissertation also presented a novel DFT-in-DFT embedding theory protocol that was found to accurately reproduce reference KS-DFT results for all systems tested and DFT functionals used. Worthy of special note in this new variant of DFT-in-DFT is the fact that by enforcing intersystem orbital orthogonality, the nonadditive kinetic potential (v_T), believed to be a major cause of errors in DFT-in-DFT embedding and to which many previous research efforts have been devoted, can be set exactly to zero. Thus, for the first time, an accurate DFT-in-DFT embedding theory has been developed that neither relies on kinetic functionals nor requires a supermolecular KS-DFT calculation. This new embedding technique was found to reproduce reference supermolecular KS-DFT total energies to at least the 7th decimal place for all studied systems, irrespective of their intersystem interaction strengths or the type of DFT functionals used. To my knowledge, no previous version of freeze-and-thaw DFT-in-DFT, that does not require a supermolecular KS-DFT calculation, matches the accuracies of the data reported in the present work from the new DFT-in-DFT embedding theory protocol. Since the accuracies of results obtained with the new embedding protocol did not depend on the DFT functionals used, it stands to reason that this novel embedding approach successfully addresses the inherent problem in previous formulations of DFT-in-DFT embedding theory which is "lack of tendency" or counterintuitive predictions in certain circumstances but not others; e.g., GGA functionals performing better than LDA functionals in some cases but vice versa in others.

It was shown within the new embedding scheme that extending the usual monomer basis expansion to include a few basis functions of the complementary subsystem near the interface between subsystems (a new technique referred to as the "extended monomer expansion") led to accuracies in results that were comparable to those obtained from the more computationally demanding supermolecular basis expansions. This suggested that the newly proposed extended monomer expansion approach is a good approximation to the supermolecular basis expansion.

The difference electron density maps included in this dissertation were obtained using a code that was written to compute electron densities in real space given reduced one particle density matrices. The code was verified to work accurately through repeat calculations of densities of compexes like $F^- \cdots H_2O$ that are available in the literature. Moreover, preliminary tests of the code involved verifying that it could integrate the density of a given molecule over all space to give approximately the total number of electrons in the molecule. The present work has therefore realized a new computer program that can be used to perform analyses of electron densities of systems. It should be noted that the program was written to support both embedding and other computer codes. All that is needed as input is the one particle density matrix and geometry of the studied molecule. Analyses of densities obtained with this new program revealed that whereas conventional DFT-in-DFT embedding theory underestimates the electron density particularly at the interface between subsystems, the newly developed embedding scheme remedies the situation and leads to only negligible density distortions in all regions in space. Such negligible density distortions did not significantly impact the energies of the studied systems as already discussed above.

Future Directions

The present work sets the stage for calculations of small clusters of transition metals. The investigation of Be_3 and Li_3, as detailed in Chapter IX, is a step in this direction. Moreover, the development of an accurate DFT-in-DFT embedding theory protocol was also a first step to the ultimate goal of embedding GVVPT2 calculations of small clusters in large environments whose effects are approximated at the DFT level of theory. Since the newly developed DFT-in-DFT embedding scheme has been demonstrated to work accurately, the stage is set for the development of an embedding protocol (using the same ideas of the new DFT-in-DFT scheme) that will enable embedding of GVVPT2 calculations. Protocols of this sort are termed wave function theory (WFT)-in-DFT embedding recipes as was mentioned in Chapter VIII.

Although GVVPT2 calculations of transition metal dimers gave results that generally agreed with those from other high level methods, the predicted bond lengths were found to be slightly longer in some instances; e.g., the ground state of Cr_2. It is suspected that this is possibly due to the simplified reference Hamiltonian (H_0) that GVVPT2 currently relies on. Future research should probably investigate the effects of using a modified reference Hamiltonian as is done in e.g., the CASPT2 method. Studies of the $1^1\Sigma_g^+$, $2^1\Sigma_g^+$, and $3^1\Sigma_g^+$ states of Y_2 suggested that $5p_z$-derived MOs participated in the bonding. Future research on electronic states of second row transition metal molecules should possibly investigate the effects of larger active spaces that include high lying 5p-derived MOs. Also, a consideration of complete manifolds of low-lying states within such studies could be very valuable and lead to more definitive answers.

As mentioned earlier, this dissertation involves the first application of a version of the GVVPT2 program that includes scalar relativistic effects through the spin-free exact two component (sf-X2C) method. Although the results presented herein were good in comparison with those from other high level methods, spin-orbit coupling effects were ignored. Future work on systems for which relativity is believed to be important should possibly incorporate spin-orbit coupling effects after the new scalar relativistic variant of GVVPT2.

APPENDICES

Appendix A

Numerical Integration in DFT

In numerical integrations, molecular integrals ($\mathbf{I}$) are expressed as a sum over atomic centers ($\mathbf{I_A}$) [379, 380],

$$\mathbf{I} = \sum_A \mathbf{I_A} \tag{A-1}$$

Each atomic center is associated with a partition (or nuclear weight) function, w_A, such that

$$\mathbf{I} = \int F(\vec{r})d\vec{r} = \sum_A \mathbf{I_A} = \sum_A \int w_A(\vec{r})F(\vec{r})d\vec{r} = \sum_A \int w_A(\vec{r}_A + \vec{R}_A)F(\vec{r}_A + \vec{R}_A)d\vec{r}_A , \tag{A-2}$$

where $F(\vec{r})$ is the function to be integrated. Vectors $\vec{r}$, $\vec{r}_A$, and $\vec{R}_A$ are shown in Figure 45, where $\mathbf{0}$ is the origin, $\mathbf{A}$ is the position of the nucleus of atom A, while $\mathbf{e}$ is the position of a given electron.
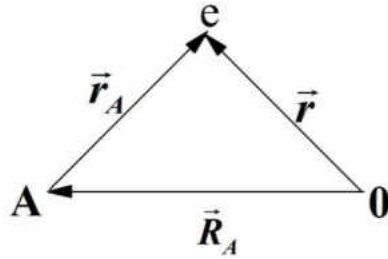
Figure 45. Schematic diagram showing the position vectors of an electron and an associated nucleus.

The partition functions, $w_A(\vec{r})$, satisfy the conditions [380]

$$w_A(\vec{r}) \geq 0 , \quad \sum_A w_A(\vec{r}) = 1 \text{ at any } \vec{r} \in \mathbb{R}^3 \tag{A-3}$$

Additionally, $w_A(\vec{r})$ must be close to unity near nucleus **A**, close to zero near all other nuclei, and must be as smooth as possible to in order to guarantee the smoothness of the functions $w_A(\vec{r})F(\vec{r})$ to be integrated.

Each integral at atomic centers is approximated as a sum of shell integrals over a series of concentric spheres centered at the nucleus of the atom. To illustrate this, consider a sphere of radius $|\vec{r}_A|$ around atom A with nucleus at $|\vec{R}_A|$ relative to the origin **(0)** as shown in Figure 46.
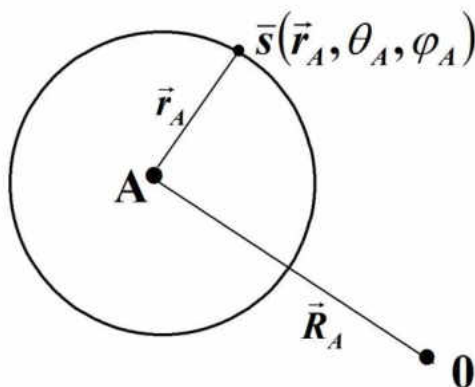
Figure 46. Schematic diagram showing a sphere of radius $|\vec{r}_A|$ about atomic center **A**.

The molecular integral in Eq. (A-2) may then be written as

$$I = \sum_A 4\pi \int_0^\infty F_A(\vec{r}_A)\vec{r}_A^2 d\vec{r}_A \, , \tag{A-4}$$

where

$$F_A(\vec{r}_A) = \frac{1}{4\pi} \int_{\Omega_A} f_A(\vec{r}_A(\vec{s})) d\vec{s} \tag{A-5}$$

is the integration over the shell of radius $\left|\vec{r}_A\right|$, centered at nucleus **A** with $d\bar{s}$ being the surface element given in spherical coordinates as

$$d\bar{s} = \sin(\theta_A) d\theta_A d\varphi_A \tag{A-6}$$

The function $f_A(\vec{r}_A(\bar{s}))$, given in Eq. (A-5) is expressed as

$$f_A(\vec{r}_A(\bar{s})) = w_A(\vec{R}_A + \vec{r}_A(\bar{s})) F(\vec{R}_A + \vec{r}_A(\bar{s})) \tag{A-7}$$

where $w_A(\vec{R}_A + \vec{r}_A(\bar{s}))$ and $F(\vec{R}_A + \vec{r}_A(\bar{s}))$ denote the partition function and the function to be integrated, respectively.

The nuclear weight or partition function $w_A(\vec{r}) = w_A(\vec{R}_A + \vec{r}_A(\bar{s}))$ at a point $\vec{r}$ is given as

$$w_A(\vec{r}) = \frac{p_A(\vec{r})}{\sum_B p_B(\vec{r})} = \frac{p_A(\vec{r})}{z(\vec{r})}, \tag{A-8}$$

where $p_A(\vec{r})$ is an unnormalized cell function of atom A, composed of independent pair contributions, $s(\mu_{AB}(\vec{r}))$,

$$p_A(\vec{r}) = \prod_{B \neq A} s(\mu_{AB}(\vec{r})), \tag{A-9}$$

and the $\mu_{AB}(\vec{r})$ are hyperbolic coordinates defined as

$$\mu_{AB}(\vec{r}) = \frac{\left|\vec{r} - \vec{R}_A\right| - \left|\vec{r} - \vec{R}_B\right|}{\left|\vec{R}_{AB}\right|} = \frac{r_A - r_B}{R_{AB}}, \tag{A-10}$$

with the condition that

$$\mu_{AB}(\vec{R}_A) = -1, \ \mu_{AB}(\vec{R}_B) = 1, \text{ and } \left|\mu_{AB}(\vec{r})\right| \leq 1 \ \forall \vec{r} \in \mathbb{R}^3 \tag{A-11}$$

where $\vec{R}_A$ and $\vec{R}_A$ are position vectors of atoms A and B, respectively, whereas $\left|\vec{R}_{AB}\right|$ is the separation between A and B as shown in Figure 47.
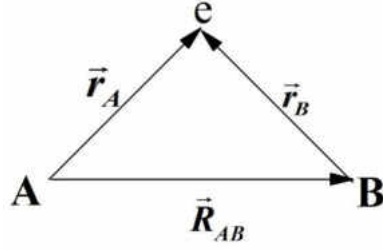
Figure 47. Schematic diagram showing atomic centers **A** and **B** and an electron (**e**) at $\vec{r}_A$ with respect to nucleus **A** and $\vec{r}_B$ with respect to nucleus **B**.

The cell function $p_A(\vec{r})$ in Eq. (A-9) must be close to unity near nucleus **A** and close to zero near any other nucleus. Thus, the contribution $s(\mu_{AB}(\vec{r}))$ between atoms A and B must be a monotonically decreasing function of the form given in Figure 48.
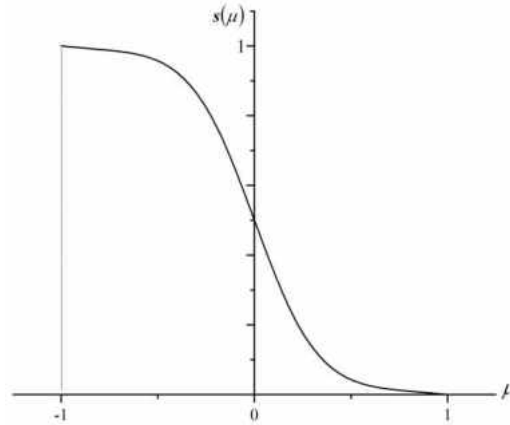

Figure 48. Schematic diagram showing the variation of $s(\mu_{AB}(\vec{r}))$ between atomic centers **A** and **B**.

The following restrictions are imposed on the cell function contribution, $s(\mu_{AB}(\vec{r}))$,

$$0 \le s(\mu) \le 1 \quad \forall \, |\mu| \le 1, \tag{A-12}$$

$$s(-1)=1, \; s(1)=0, \tag{A-13}$$

$$\frac{ds}{d\mu} \le 0, \; \left.\frac{ds}{d\mu}\right|_{\mu=\pm 1} = 0 \tag{A-14}$$

Becke [380] proposed the following form for the cell function contribution, $s(\mu_{AB}(\vec{r}))$,

$$s(\mu) = \frac{1}{2}[1 - p_k(\mu)] ,$$ (A-15)

where the polynormials $p_k(\mu)$ and $p_{k+1}(\mu)$ are related as follows

$$p_{k+1}(\mu) = p[p_k(\mu)] \text{ with } p_1(\mu) = \frac{3}{2}\mu - \frac{1}{2}\mu^3$$ (A-16)

Becke [380] found k = 3 to be the optimum value for a sufficiently well behaved $s(\mu)$.
Since $p_3(-\mu) = -p_3(\mu)$, it follows that

$$s(-\mu) = \frac{1}{2}[1 + p_3(\mu)] = 1 - s(\mu)$$ (A-17)

Properties of the hyperbolic coordinates $\mu_{AB}(\vec{r})$

Figure 47 is to be referenced in the analysis of the properties of $\mu_{AB}(\vec{r})$. The figure is redrawn below (Figure 49) to include the angle φ_A between vectors $\vec{r}_A$ and $\vec{R}_{AB}$, and the properties of $\mu_{AB}(\vec{r})$ between atomic centers **A** and **B**.
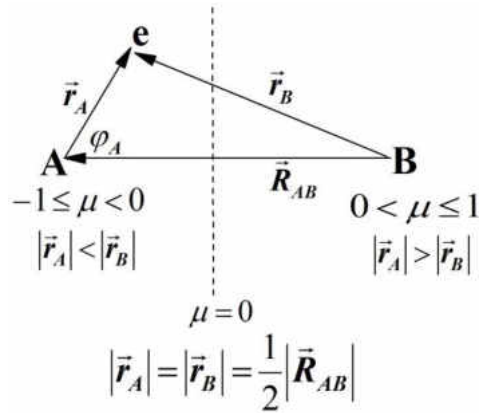

Figure 49. Schematic diagram showing the variation of $\mu_{AB}(\vec{r})$ between atomic centers **A** and **B**.

From Eqs. (A-10) and (A-11), the following inequality holds

$$-1 \leq \mu_{AB}(\vec{r}) = \frac{r_A - r_B}{R_{AB}} \leq 1 \ , \tag{A-18}$$

where r_A, r_B and R_{AB} are the absolute values of the respective vectors. From the cosine rule (based on Figure 49),

$$r_B^2 = \left| \vec{r}_A - \vec{R}_{AB} \right|^2 = r_A^2 + R_{AB}(R_{AB} - 2r_A \cos(\varphi_A))$$
$$\Updownarrow \tag{A-19}$$
$$(r_A - r_B)(r_A + r_B) = R_{AB}(2r_A \cos(\varphi_A) - R_{AB})$$

The function $\mu_{AB}(\vec{r})$ obeys the relation

$$\mu_{AB}(\vec{r}) = \frac{r_A - r_B}{R_{AB}} = \frac{2r_A \cos(\varphi_A) - R_{AB}}{r_A + r_B} \leq \frac{2r_A - R_{AB}}{r_A + r_B} \tag{A-20}$$

Thus, $\mu_{AB}(\vec{r}) \leq 0$ only inside a sphere of radius $r_A < \frac{1}{2} R_{AB}$. That is

$$\mu_{AB}(\vec{r}) \leq 0 \text{ if } \left| \vec{r} - \vec{R}_A \right| < \frac{1}{2} R_{AB} \tag{A-21}$$

At a fixed radius r_A of a given sphere around atom A, r_B and $\mu_{AB}(\vec{r})$ are even functions of the angle φ_A

$$r_B = r_B(\varphi_A) = r_B(-\varphi_A) \text{ and } \mu_{AB} = \mu_{AB}(\varphi_A) = \mu_{AB}(-\varphi_A) = \frac{r_A - r_B(\varphi_A)}{R_{AB}} \tag{A-22}$$

From Eqs. (A-19) and (A-20),

$$\frac{dr_B}{d\varphi_A} = \frac{r_A R_{AB}}{r_B} \sin(\varphi_A), \ \frac{d^2 r_B}{d\varphi_A^2} = \frac{r_A R_{AB}}{r_B} \cos(\varphi_A) \tag{A-23}$$

and

$$\frac{d\mu_{AB}}{d\varphi_A} = -\frac{2r_A}{r_A + r_B} \sin(\varphi_A), \ \frac{d^2 \mu_{AB}}{d\varphi_A^2} = -\frac{2r_A}{r_A + r_B} \cos(\varphi_A) \tag{A-24}$$

Thus, $r_B(\varphi_A)$ has its maximum at $\varphi_A = \pi$ and minimum at $\varphi_A = 0$, whereas $\mu_{AB}(\varphi_A)$ has

its maximum on the sphere $s_A\left(r_A < \dfrac{1}{2}R_{AB}\right)$ when $\varphi_A = 0$ and minimum when $\varphi_A = \pi$.

Eqs. (A-23) and (A-24) also imply that the curvatures of $r_B(\varphi_A)$ and $\mu_{AB}(\varphi_A)$ change at

$\varphi_A = \dfrac{\pi}{2}$. Since $s(\mu)$ is a monotonically decreasing function of $\mu_{AB}(\varphi_A)$, it can be stated

that, at the point $(r_A, \varphi_A = \pi)$, $s(\mu)$ achieves its minimum value among all the points of

the ball $B_A(r_A) \equiv \left\{ \vec{r} \in R^3, \left| \vec{r} - \vec{R}_A \right| \le r_A \right\}$.

Alternative form of cell function contribution $s(\mu)$

Although the present work employed the Becke definition of $s(\mu)$, the following

alternative form due to Stratmann et al. [381] could otherwise be used. Stratmann et al.

define $s(\mu)$ as

$$s(\mu) = \frac{1}{2}\left[1 - g_a(\mu)\right] , \tag{A-25}$$

where $g_a(\mu)$ is a piece-wise odd function defined as

$$g_a(\mu) = \begin{cases} -1 & \mu \le -a \\ z_a(\mu) & \mu \in (-a, a) \\ +1 & \mu \ge a \end{cases} , \qquad 0 < a < 1 \tag{A-26}$$

where $z_a(\mu)$ is defined as

$$z_a(\mu) = \frac{1}{16}\left[35\left(\frac{\mu}{a}\right) - 35\left(\frac{\mu}{a}\right)^3 + 21\left(\frac{\mu}{a}\right)^5 - 5\left(\frac{\mu}{a}\right)^7 \right] \tag{A-27}$$

Within the limits $\mu \in (-a, a)$, the function $z_a(\mu)$ is subject to the constraints

$$z_a(-\mu) = -z_a(\mu), \quad \frac{dz_a}{d\mu} \ge 0, \tag{A-28a}$$

$$z_a(-a)=-1, \; z_a(a)=1, \; \left.\frac{dz_a}{d\mu}\right|_{\mu=\pm a}=0 \qquad \text{(A-28b)}$$

The function $z_a(\mu)$ has zeroth second and third order derivatives at $\mu=\pm a$ and leads to

$$s(0)=\frac{1}{2}, \; \left.\frac{ds}{d\mu}\right|_{\mu=0}=-\frac{35}{32a} \qquad \text{(A-29)}$$

Contrary to the Becke function in Eq. (A-15), the Stratmann et al. [381] function satisfies the conditions

$$s(\mu)=\begin{cases}1 & \text{if } \mu \leq -a \\ 0 & \text{if } \mu \geq \;\; a\end{cases} \qquad \text{(A-30)}$$

A requirement that the first derivatives of the Becke and Stratmann et al. cell functions coincide at $\mu=0$ leads to the following value for the parameter a in Eqs. (A-26) to (A-30)

$$a=\frac{35}{2\times 27}=0.648148148, \qquad \text{(A-31)}$$

which is nearly the same as the value of a = 0.64 determined empirically as the best one by Stratmann et al.

Assuming that N is the nearest atomic neighbor to atom A and considering a sphere around center **A**, which is determined by the condition

$$\mu_{AN}^{max}(r_A^*)=\frac{2r_A^*}{R_{AN}}-1=-a \quad , \qquad \text{(A-32)}$$

for any point $\vec{r}$ inside this sphere,

$$r_A=\left|\vec{r}-\vec{R}_A\right| < r_A^*=\frac{1}{2}(1-a)R_{AN}, \qquad \text{(A-33)}$$

the nuclear weight is unity, $w_A(\vec{r})=1$. This implies that if a given radial grid, r_{Ai}, is such that $r_{Ai} < r_A^*$, then all angular grid points on the sphere of radius r_{Ai} will lie inside the ball (Eq. (A-33)) and, hence, $w_A(\vec{r})=1$ for those points.

Selection of significant functions

The partitioning in Eq. (A-2) decomposes the three-dimensional molecular integral in Eq. (A-1) into a sum over atomic-like integrals which are easier to evaluate. Each of these atomic centers is further separated into radial and angular integrations, giving rise to individual grid points which are naturally associated with the respective atoms. In carrying out the integrations, advantage is taken of the fast decaying nature of Gaussian atomic orbitals such that for each grid point, only such functions that are numerically significant (according to a user-specified criterion) are considered. It is considered that each basis function is enclosed by a sphere, with a threshold radius ε, beyond which its influence is deemed negligible. Thus, for the basis function $\chi_\mu^A(i)$ centered at $\vec{R}_A$, the requirement is that $\left|\chi_\mu^A(i)\right| \leq \varepsilon$ for every point outside the sphere enclosing $\chi_\mu^A(i)$. Hence, for any grid point ($\vec{r}_g$), a set (s_g) of significant basis functions (χ_μ^A) is selected which fulfill the condition

$$\chi_\mu^A \in s_g, \text{ if } \left|\vec{r}_g - \vec{R}_A\right| \leq \lambda_\mu^A(\varepsilon), \tag{A-34}$$

where $\lambda_\mu^A(\varepsilon)$ is the radius of the sphere. Thus, for every grid point, a list of basis functions whose spheres include the point is considered. Of course, this list of significant basis functions is different for each grid point. Nevertheless, the number of basis functions in each set s_g becomes independent of the size of the system for sufficiently

large molecules. By employing test (A-34), the creation of the s_g is computationally insignificant even for molecules approaching 1000 atoms. If all basis functions centered at a given atom A are not significant for a given grid point, then the atom is considered insignificant at that point. In particular, an atom is not significant if its most diffuse orbital is not included in the set s_g for a given grid point. To maximize computational efficiency, blocks or batches of grid points are used rather than individual grids. Each block of points is represented by a set of significant basis functions, $S_G = \bigcup_{g \in G} s_g$ with $G = \{\vec{r}_g\}_g$, which includes all basis functions that are significant at least for some grid point in the set G:

$$\chi_\mu^A \in S_G, \text{ if } \left| \vec{r}_g - \vec{R}_A \right| \leq \lambda_\mu^A(\varepsilon) \text{ for some } \vec{r}_g \in G \tag{A-35}$$

The work described herein used a block scheme in which blocks are chosen to be spheres of grid points. In this case, condition (A-35) is verified only once for each sphere (block).

Consider a sphere, $s_A(r_A)$, of radius r_A, centered at nucleus **A** as shown in Figure 50. All spherical grid points $\{\vec{r}_g\}_g$ lying on the sphere define a block G_A; that is,

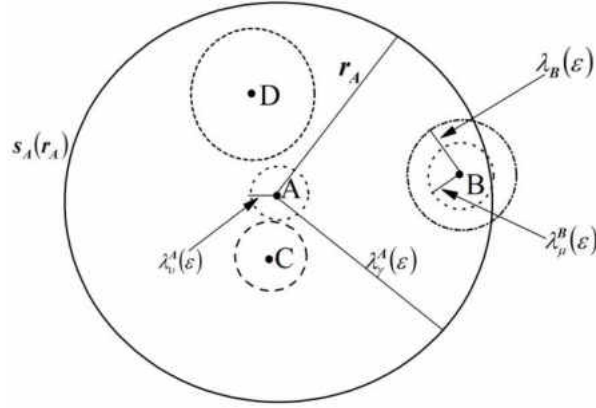$$\left| \vec{r}_g - \vec{R}_A \right| = r_A \quad \forall \vec{r}_g \in G_A \tag{A-36}$$

Figure 50. Given sphere $s_A(r_A)$, atoms C and D are not significant and their basis functions are not included in the list $L_{G_A(r_A)}$. Atom B is significant and its $\chi_\mu^B(\vec{r})$ is included into the set $L_{G_A(r_A)}$. For atom A, enclosed by $s_A(r_A)$, basis function $\chi_\gamma^A(\vec{r})$ is significant but $\chi_\upsilon^A(\vec{r})$ is not (i.e., $\chi_\gamma^A(\vec{r}) \in L_{G_A(r_A)}$, $\chi_\upsilon^A(\vec{r}) \notin L_{G_A(r_A)}$).

Given a threshold, ε, each atom B is assumed to be enclosed by a sphere of radius $\lambda_B(\varepsilon)$ and each of its functions $\chi_\mu^B(\vec{r}_B)$ by a sphere of radius $\lambda_\mu^B(\varepsilon)$. The list $L_{G_A(r_A)}$ of significant functions, associated with the block G_A, includes only those basis functions whose spheres (centered at corresponding atoms) are intersected by $s_A(r_A)$. An atom B is "not significant" and none of its functions is included into the list $L_{G_A(r_A)}$, if the following inequality holds,

$$|r_A - R_{AB}| > \lambda_B(\varepsilon) \qquad \text{(A-37)}$$

In particular, if $r_A > \lambda_A(\varepsilon)$, then the parent atom (A) itself is insignificant. If atom B is significant, as indicated in Figure 50 (that is, if its maximum sphere is crossed by $s_A(r_A)$), then at least some of its basis functions will be included into the list $L_{G_A(r_A)}$:

$$\chi_\mu^B \in L_{G_A(r_A)}, \text{ if } |r_A - R_{AB}| \leq \lambda_\mu^B(\varepsilon) \tag{A-38}$$

Where used, all basis functions included into a block $L_{G_A(r_A)}$ would be labelled with a tilde: $L_{G_A(r_A)} = \{\chi_{\tilde\mu}\}_{\tilde\mu}$.

In order to obtain radii of basis functions to be used in determining the grid points at which the functions are significant, it is convenient to use their spherical average forms. For Gaussian basis sets, the spherical average of a basis set $\chi_\mu^A(\vec{r})$, with orbital quantum number l, is

$$\bar\chi_l(r) = C_l r^l e^{-\alpha_l^{min} r^2}, \tag{A-39}$$

where r is the distance from the host atomic center A of the function, α_l^{min} is the exponent of the most diffuse primitive function (the one with minimum exponent), and

$$C_l = \sqrt{\frac{(2\alpha_l^{min})^{l+3/2}}{2\pi\Gamma(l+3/2)}} \tag{A-40}$$

The radius $\lambda_\mu^A(\varepsilon)$ of the function $\bar\chi_l(r)$ is determined by the equation

$$\bar\chi_l(\lambda_l(\varepsilon)) = \varepsilon, \tag{A-41}$$

where ε is defined here as

$$\varepsilon = e^{-\beta}, \; \beta = -\ln(\varepsilon) > 0, \tag{A-42}$$

e.g., if $\varepsilon = 10^{-10}$ (this is the value that was used in the present work), then $\beta = 10\ln(10) \approx 23$. In the case of s-functions ($l = 0$), $\lambda_\mu^A(\varepsilon)$ becomes

261

$$\lambda_s = \sqrt{\frac{\gamma_s}{\alpha_s}} \ , \tag{A-43}$$

where the following notations have been introduced

$$\alpha_l = \alpha_l^{min} \ , \quad \gamma_l = \beta + \ln(C_l) = \ln(C_l/\varepsilon) \tag{A-44}$$

For functions with $l > 0$, the solution of Eq. (A-41) is more complicated. In this case, the derivative of $\bar{\chi}_l(r) = C_l r^l e^{-\alpha r^2}$ with respect to r is

$$\bar{\chi}_l'(r) = C_l (l - x) r^{l-1} e^{-\alpha r^2} \ , \quad x = 2\alpha r^2 \tag{A-45}$$

In the region of interest (i.e., where $r > 0$), $\bar{\chi}_l(r)$ has one stationary point (maximum)

$$r_l^{max} : \quad \bar{\chi}_l'(r_l^{max}) = 0 \Leftrightarrow x = l \quad \Rightarrow \left. r_l^{max} \right|_{x=l} = \sqrt{\frac{l}{2\alpha}} \tag{A-46}$$

If ε is sufficiently small, then the root λ_l must satisfy the conditions

$$r_l^{max} < r_l^* < \lambda_l , \tag{A-47}$$

where r_l^* is the point where $\chi_l(r)$ changes its curvature; that is,

$$r_l^* : \quad \bar{\chi}_l''(r_l^*) = 0 \tag{A-48}$$

If $l = 1$, then

$$\bar{\chi}_1'' = C_1(-2\alpha r)[l - x + 2] e^{-\alpha r^2} \Rightarrow \left. r_1^* \right|_{l+2} = \sqrt{\frac{l+2}{2\alpha}} = \sqrt{\frac{3}{2\alpha}} \ (l=1) \tag{A-49}$$

If $l > 1$, then

$$\bar{\chi}_l'' = C_l \left[(l-x)(l-x-1) - 2x \right] r^{l-2} e^{-\alpha r^2} , \tag{A-50}$$

and r_l^* is determined by the equation

$$(l-x)(l-1-x) - 2x = 0 \quad \Leftrightarrow \quad x^2 - (2l+1)x + l(l-1) = 0 , \tag{A-51}$$

with desired root

$$r_l^* = \frac{1}{2} \sqrt{\frac{2l+1+\sqrt{8l+1}}{\alpha}} \quad (l>1) \tag{A-52}$$

As expected, $r_l^* > r_l^{max}$.

The simplest Newton scheme [382] leads to an iterative process to localize λ_l from Eq. (A-41),

$$\Delta r = -\frac{\chi_l(r) - \varepsilon}{\chi_l'(r)} \tag{A-53}$$

Starting from the initial point, $r = r_l^*$ guarantees that each iteration $\Delta r > 0$ since in this region, $\chi_l(r) > \varepsilon$ and $\chi_l'(r) < 0$, and the convergence occurs monotonically,

$$\Delta r = \frac{1}{2\alpha\alpha - l/r} \left(1 - e^{\alpha r^2 - l \ln(r) - \gamma} \right) \Big|_{r \to \lambda_l} \to +0 \tag{A-54}$$

Radii $\{\lambda_\mu^A(\varepsilon)\}$ are determined for all basis functions $\{\chi_\mu^A\}$ with $l \geq 1$ and determine the effective radius $\lambda^A(\varepsilon)$ of the atom A as

$$\lambda^A(\varepsilon) = \max \lambda_\mu^A(\varepsilon) \Big|_{\forall \chi_\mu^A \in A} \tag{A-55}$$

Integration Scheme

Two integration schemes have been used in this work: the Legendre quadrature [383] and the Lebedev quatrature [384-386] methods. Murray et al. [383] express the integral in Eq. (A-4) as

$$\int_0^\infty F(r)r^2 dr \Bigg|_{\substack{r=r(q),\\ q\in[0,1]}} = \int_0^1 F(r(q))r^2(q)\frac{dr}{dq}dq = \int_0^1 G(q)dq \ , \qquad \text{(A-56)}$$

where

$$G(q) = F(r(q))r^2(q)\frac{dr}{dq}, \qquad \text{(A-57)}$$

and employs the following Euler-Maclaurin scheme with equally spaced points ($i = 1, 2, \ldots, n-1$)

$$\int_0^1 G(q)dq = \frac{1}{n}\left\{\sum_{i=1}^{n-1} G\left(\frac{1}{n}\right) + \frac{1}{2}[G(0) + G(1)]\right\} - \sum_{k=1}^{m}\frac{B_{2k}}{n^{2k}(2k)!}\left[G^{(2k-1)}(1) - G^{(2k-1)}(0)\right]$$
$$- \frac{B_{2m+2}}{n^{2m+1}(2m+2)!}G^{(2m+2)}(\xi), \quad \xi \in [0,1] \qquad \text{(A-58)}$$

where B_{2k} are Bernoulli numbers. The goal is to find functions $r = r(q)$ that render $G(q)$ and its derivatives to be zero at the ends $q = 0, 1$. The assumptions are that $F(r)$ and its derivatives are zero at $r = \infty$ ($q = 1$), while $F(r)r^2$ and its first derivative are zero at $r = 0$ ($q = 0$). The function r has the following form

$$r = \text{const}\left(\frac{q}{1-q}\right)^m \quad (m \geq 1) \qquad \text{(A-59)}$$

Hence,

$$\frac{dr}{dq} = \text{const}.m.\frac{q^{m-1}}{(1-q)^{m+1}} \,, \tag{A-60}$$

and

$$G(q) = m.(\text{const})^3 \frac{q^{3m-1}}{(1-q)^{3m+1}} F(r(q)) \,, \tag{A-61}$$

with $G(0) = G(1) = 0$ since $F(\infty) \to 0$ exponentially. $G^{(k)}$ is expressed as

$$G^{(k)} = \sum_{i=1}^{k} \binom{k}{i} \frac{d^{k-i}F[q]}{dq^{k-i}} \frac{d^{i}\left(r^2 \frac{dr}{dq}\right)}{dq^{i}} = (\text{const})^3.m\sum_{i=0}^{k} \frac{d^{k-i}F[q]}{dq^{k-i}} \frac{d^{i}}{dq^{i}}\left[\frac{q^{3m-1}}{(1-q)^{3m+1}}\right] \tag{A-62}$$

At $q = 0$, $G^{(k)}(0) \equiv 0 \;\; \forall k < 3m-1$, and at $q = 1$, $G^{(k)}(1) \equiv 0 \;\; \forall k$ since all derivatives of F are zero at $r = \infty$.

The const in Eqs. (A-59) to (A-62) is assumed to be R = the Bragg-Slater radius for atoms (for atomic radii, see Ref. [387]). With this, the integral of $F(r)r^2$ is written as

$$\int_{0}^{\infty} F(r)r^2 dr = \sum_{i=1}^{n} W_i F(r_i) \,, \tag{A-63}$$

where

$$r_i = r\left(\frac{i}{n}\right) = \text{const}.\left(\frac{q_i}{1-q_i}\right)^2 = R\frac{i^2}{(n-i)^2} \,, \tag{A-64}$$

and

$$W_i = \frac{1}{n}\left(r^2 \frac{dr}{dq}\right)_{q=\frac{i}{n}} = \frac{m}{n}(\text{const})^3 \frac{q_i^5}{(1-q_i)^7} = 2n.R^3 \frac{i^5}{(n-i)^7} \tag{A-65}$$

265

In the case of N^r radial points, the integral is

$$I = 4\pi \sum_A \int_0^\infty F_A(r_A) r_A^2 dr_A \approx 4\pi \sum_A \sum_{i=1}^{N^r} W_{Ai}^r F_A(r_{Ai}), \qquad \text{(A-66)}$$

where

$$W_{Ai}^r = 2R_A^3(N^r+1)\frac{i^5}{(N^r+1-i)^7}, \quad r_{Ai} = R_A \frac{i^2}{(N^r+1-i)^2}, \qquad \text{(A-67)}$$

and

$$F_A(r_A) = \frac{1}{4\pi} \int_{S(r_A)} W_A(\vec{r}_A + \vec{R}_A) F(\vec{r}_A + \vec{R}_A) d\bar{s} \qquad \text{(A-68)}$$

is the integral on the surface of a sphere of radius r_A, centered at $\mathbf{A}$ ($\vec{R}_A$ is the position vector of $\mathbf{A}$).

In the case of using Cartesian basis functions, the Lebedev quadrature [384-386] is preferably used because it is suited to the treatment of such functions in molecular systems with Abelian symmetry. Lebedev's quadrature for the surface integral on a unit sphere, $S(f) = \frac{1}{4\pi}\int f(\bar{s}) d\bar{s}$, is

$$\frac{1}{4\pi}\int f(\bar{s}) d\bar{s} = \sum_{j=1}^{N^\Omega} W_j^\Omega f(\bar{\bar{s}}_j), \qquad \text{(A-69)}$$

where each grid point $\bar{\bar{s}}_j = (a_j, b_j, c_j)$ lies on the unit sphere: $a_j^2 + b_j^2 + c_j^2 = 1 \quad \forall j \in [1, N^\Omega]$.

Based on Eqs. (A-66), (A-68) and (A-69), the integral has the final form

$$I = \int F(\vec{r})d\vec{r} = \sum_A \sum_{i=1}^{N^r} \tilde{W}_{Ai}^r F_A(r_{Ai}) = 4\pi \sum_A \sum_{i=1}^{N^r} W_{Ai}^r \sum_{j=1}^{N^\Omega} W_j^\Omega w_A(\vec{r}_{ij}) F(\vec{r}_{ij}) , \qquad \text{(A-70)}$$

where

$$\tilde{W}_{Ai}^r = 4\pi W_{Ai}^r = (8\pi)R_A^3(N^r+1)\frac{i^5}{(N^r+1-i)^7} , \qquad \text{(A-71)}$$

$$F_A(r_{Ai}) = \frac{1}{4\pi} \int_{S_A(r_{Ai})} w_A(\vec{R}_A + \vec{r}_{Ai}) F(\vec{R}_A + \vec{r}_{Ai}) d\bar{s}_A = \sum_{j=1}^{N^\Omega} [W_j^\Omega w_A(\vec{R}_A + r_{Ai}\bar{\vec{s}}_j)] F(\vec{R}_A + r_{Ai}\bar{\vec{s}}_j), \quad \text{(A-72)}$$

$$\vec{r}_{ij} = \vec{R}_A + r_{Ai}\bar{\vec{s}}_j = (X_A + r_{Ai}a_j, Y_A + r_{Ai}b_j, Z_A + r_{Ai}c_j), \qquad \text{(A-73)}$$

and

$$r_{Ai} = R_A \frac{i^2}{(N^r+1-i)^2} \qquad \text{(A-74)}$$

Appendix B

Algorithm for DFT-in-DFT Embedding with External Orbital Orthogonality

1) Specify subsystem parameters: Numbers of atoms, electrons, spin multiplicities, one-particle spaces for Kohn-Sham (KS) orbital expansions

2a) If KSCED(m) and no previous KS orbitals, construct and orthonormalize hcore-orbitals of subsystems in monomer bases

2b) If KSCED(e) or KSCED(s) and no previous KS orbitals, construct and orthonormalize hcore-orbitals in extended one-particle spaces

3a) If Ext. Orth. is required in KSCED(m), construct $Z_{AB} = S_{AA}^{-1}*S_{AB}$ and $Z_{BA} = S_{BB}^{-1}*S_{BA}$ matrices (A-emb., B-env.), else proceed

3b) If Ext. Orth. is required, construct $Z_{AB} = S_{AA}^{-1}*S_{AB}$ and $Z_{BA} = S_{BB}^{-1}*S_{BA}$ matrices (A-emb., B-env.), else proceed

4a) Construct R-matrices (Eq. (7.38)) and optimize env. subsystem orbitals at given emb. subsystem orbitals

4b) Do step 4a)

5a) If Ext. Orth., verify orthogonality of occupied env. to emb. orbitals, else proceed

5b) Do step 5a)

6a) Construct subsystem and total densities

6b) Do step 6a)

7a) Compute SCF part of total energies, $E_{scf}[tot]$

7b) Do step 7a)

8a) If Ext. Orth., compute exchange correlation energy ($E_{xc}[tot]$); else, Compute $E_{xc}[tot]$ and nonadditive kinetic potential (v_T). Total energy = $E_{scf}[tot] + E_{xc}[tot] + v_T$

8b) Do step 8a)

9a) Iteratively optimize subsystem densities via freeze-and-thaw cycles or macroiterations. At each step, repeat 4a) to 8a) till self-consistency is achieved

9b) Do step 9a)

10a) Analyze spin and space symmetries of subsystems

10b) Do step 10a)

Additional Density Difference Relief and Contour Maps of the Systems Studied Herein

N.B. The letters A to J labelling the different maps represent the density differences: A = KS-DFT – KSCED(s) relief map; B = KS-DFT – KSCED(s) contour map; C = KS-DFT – KSCED(s, Ext. Orth.) relief map; D = KS-DFT – KSCED(s, Ext. Orth.) contour map; E = KS-DFT – KSCED(m) relief map; F = KS-DFT – KSCED(m) contour map; G = KS-DFT – KSCED(m, Ext. Orth.) relief map; H = KS-DFT – KSCED(m, Ext. Orth.) contour map; I = KSCED(s) – KSCED(s, Ext. Orth.); J = KSCED(m) – KSCED(m, Ext. Orth.).
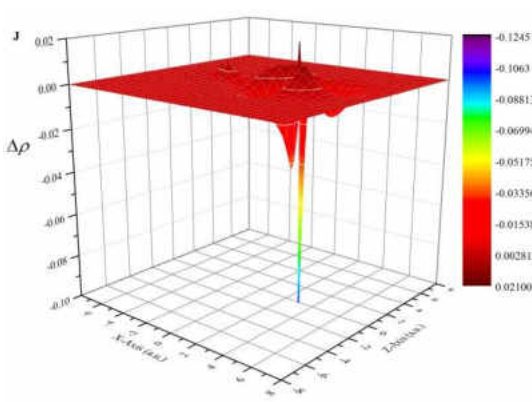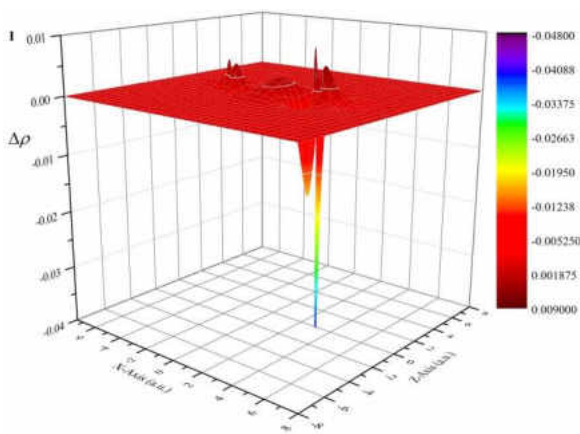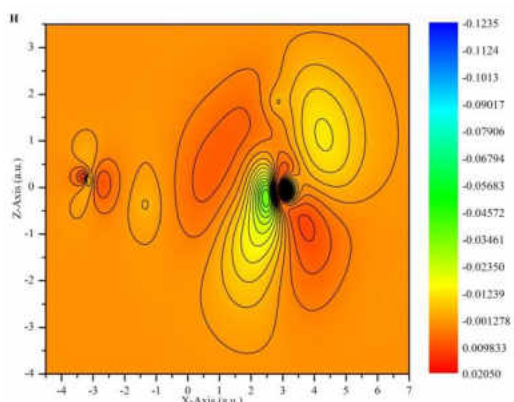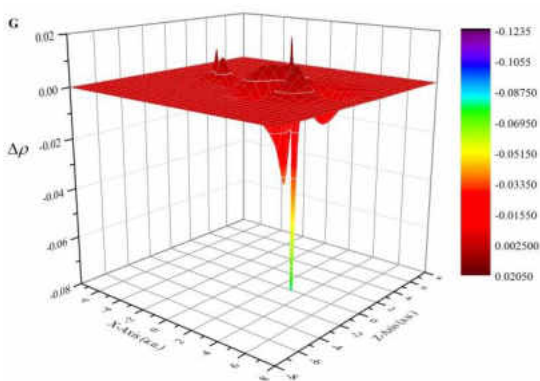
The $NH_3 \cdots NH_3$ Complex

Maps obtained with the VWN5 functional
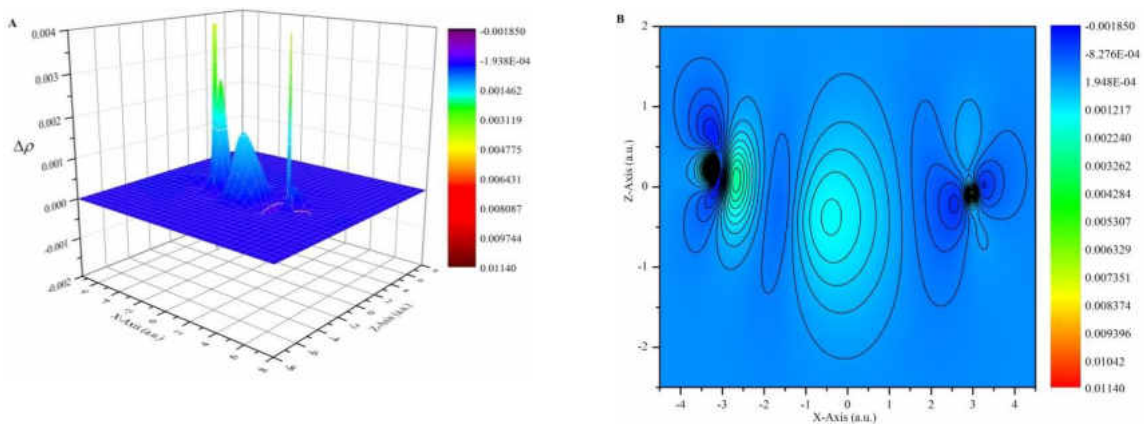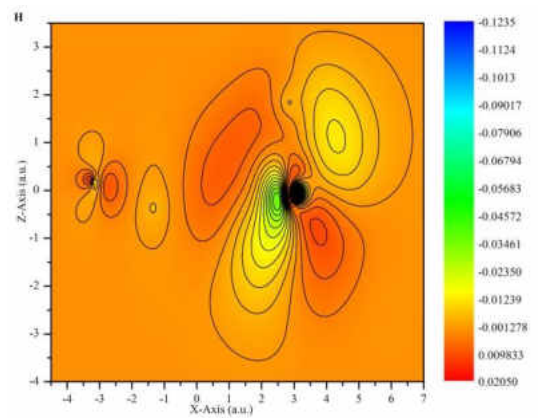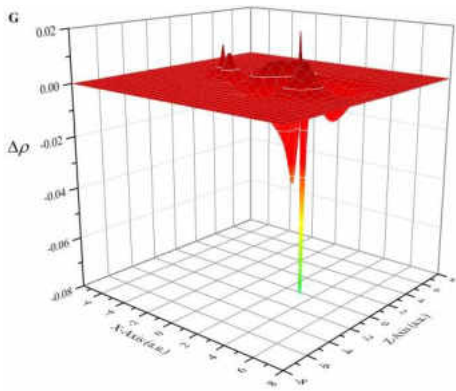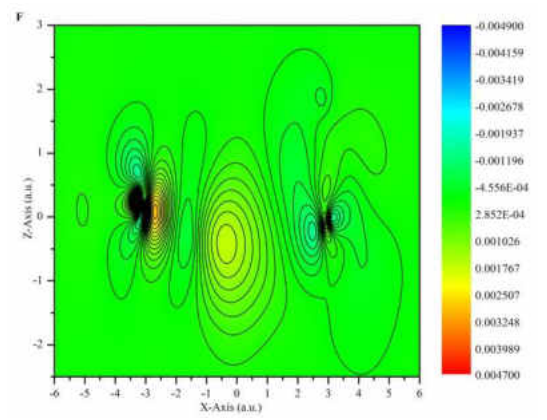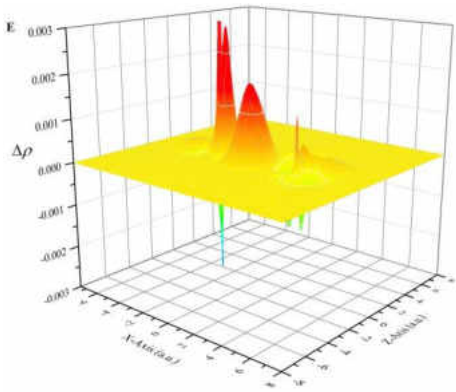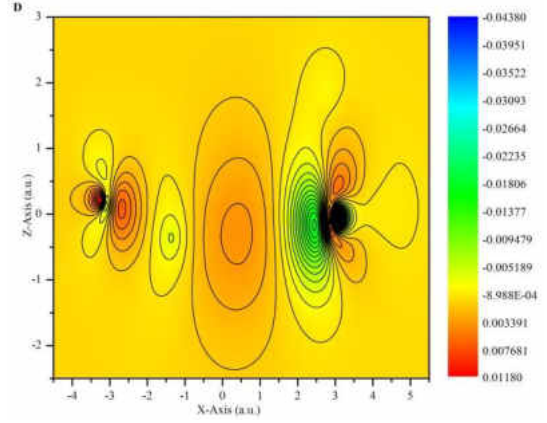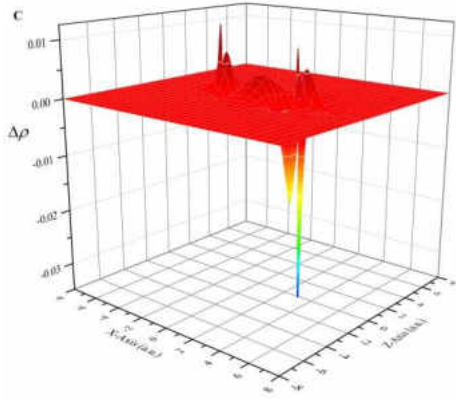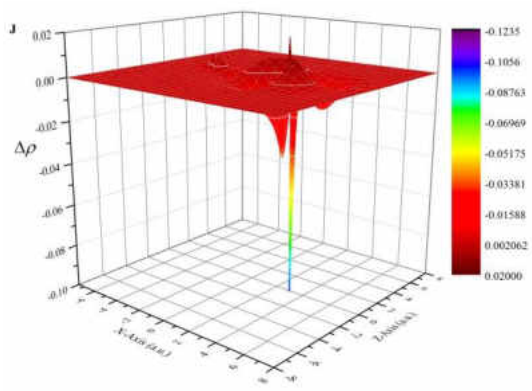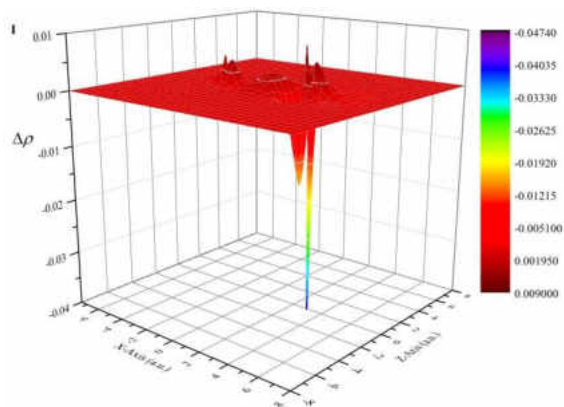
Maps obtained with the PW91 functional

Maps obtained with the VWN5 functional

Maps obtained with the PW91 functional

The $F_2 \cdots C_2H_4$ Complex

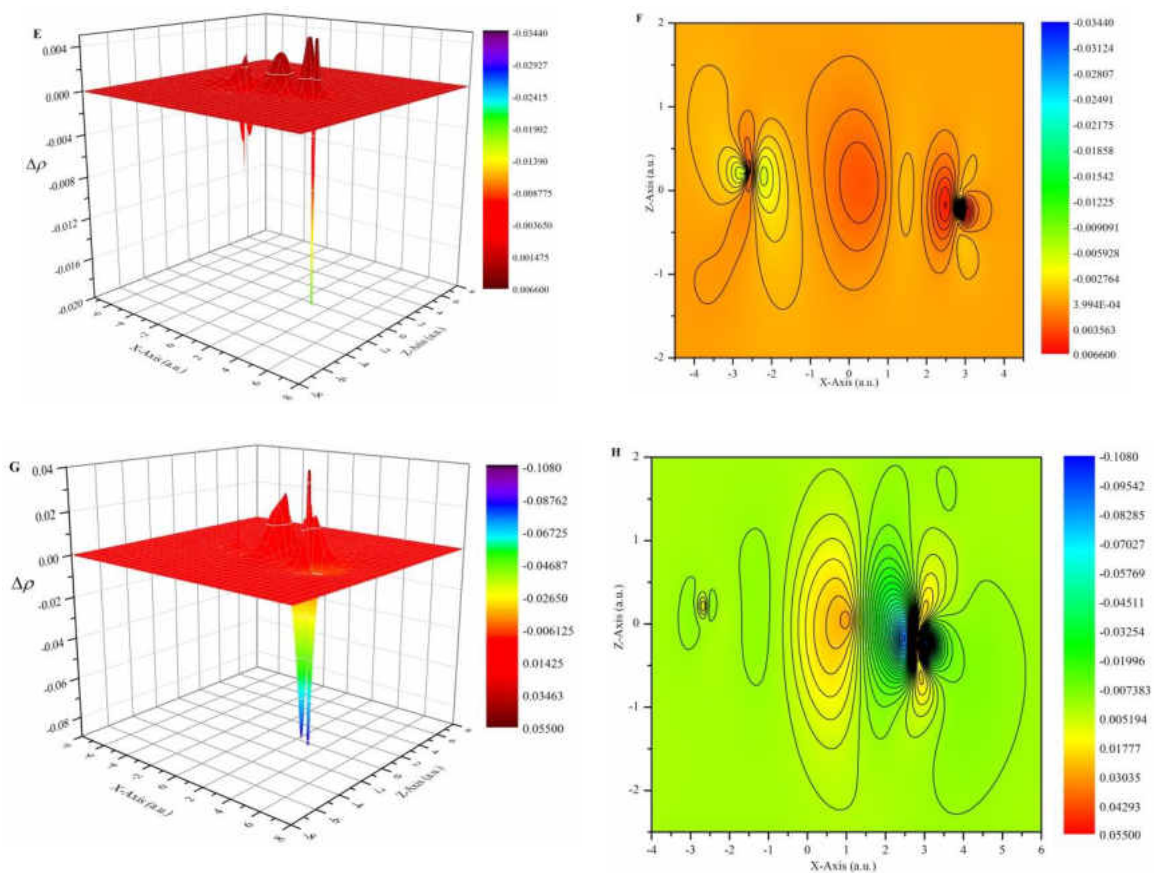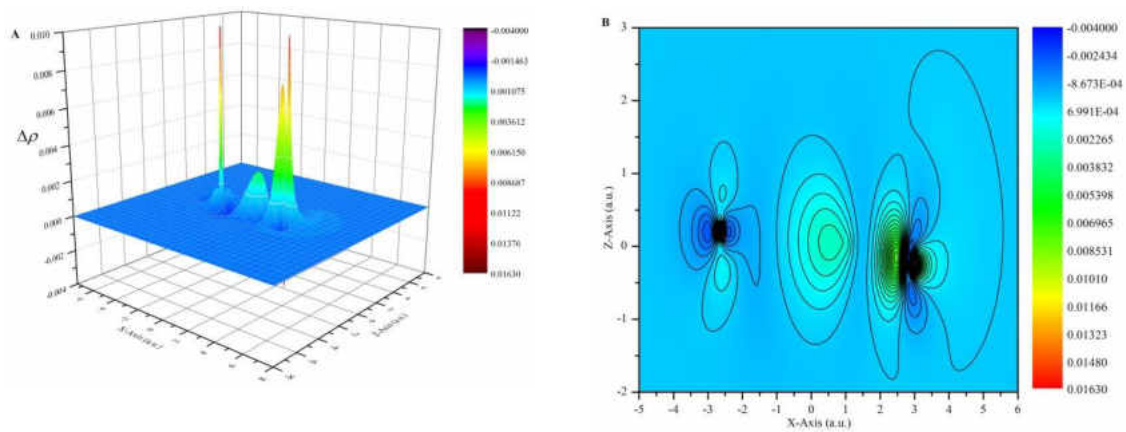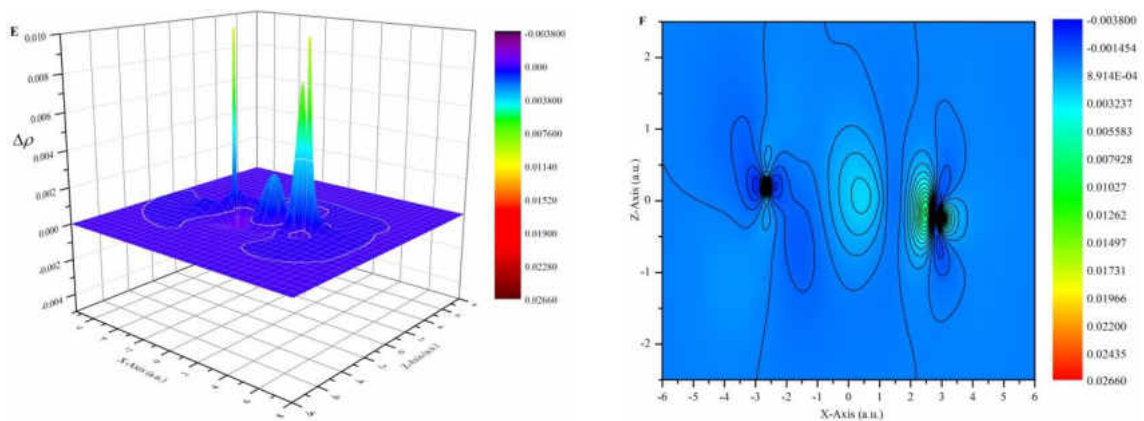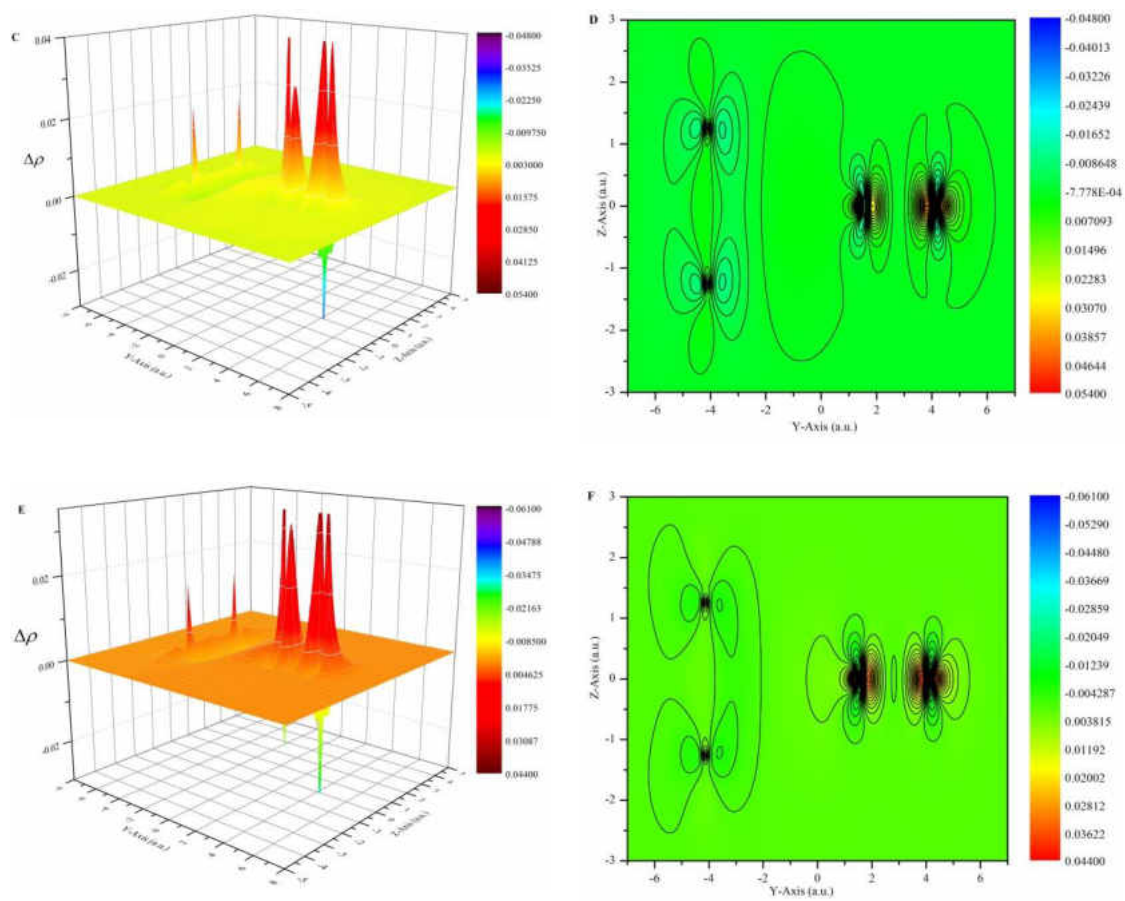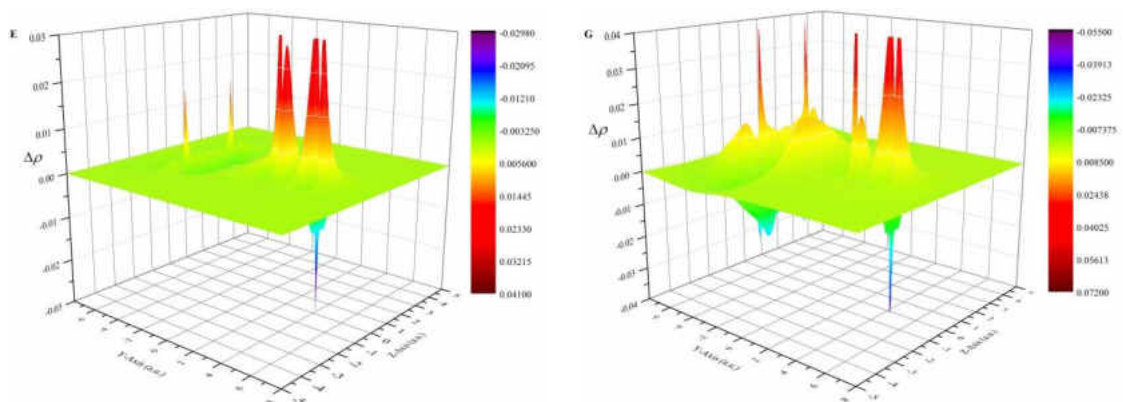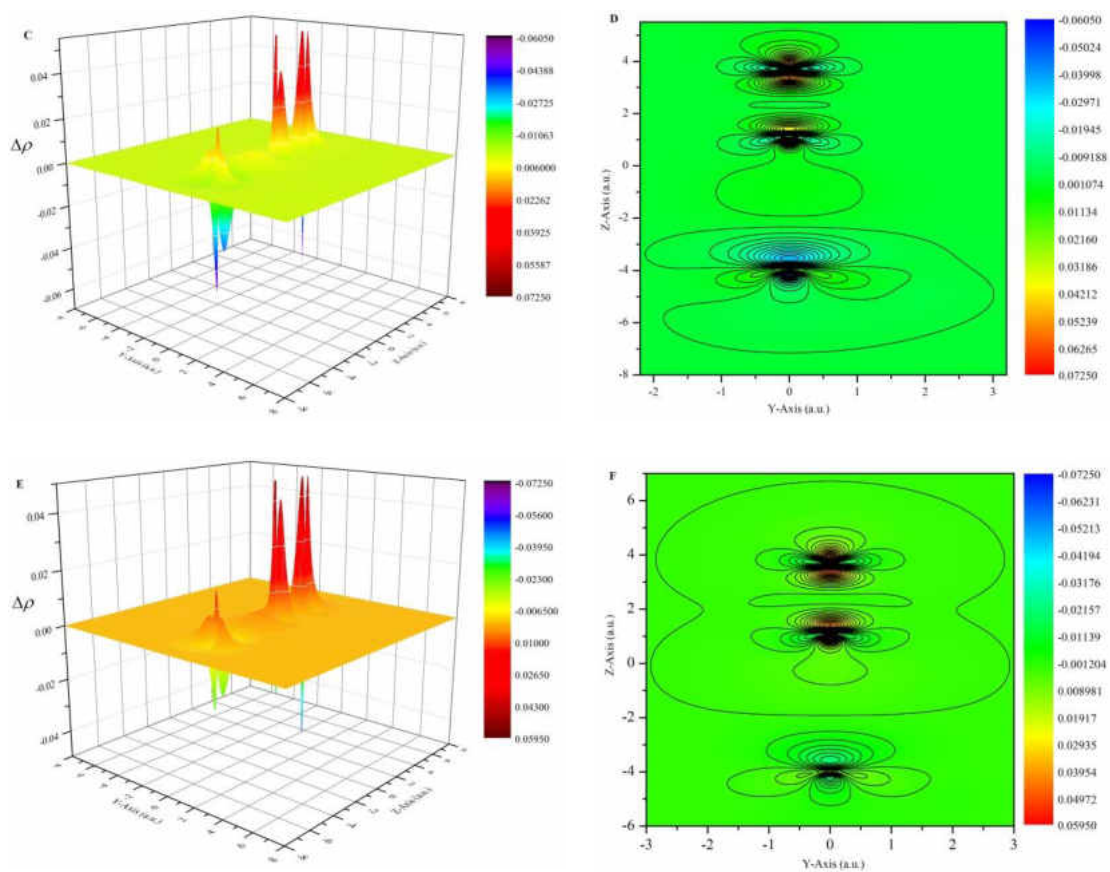Maps obtained with the VWN5 functional

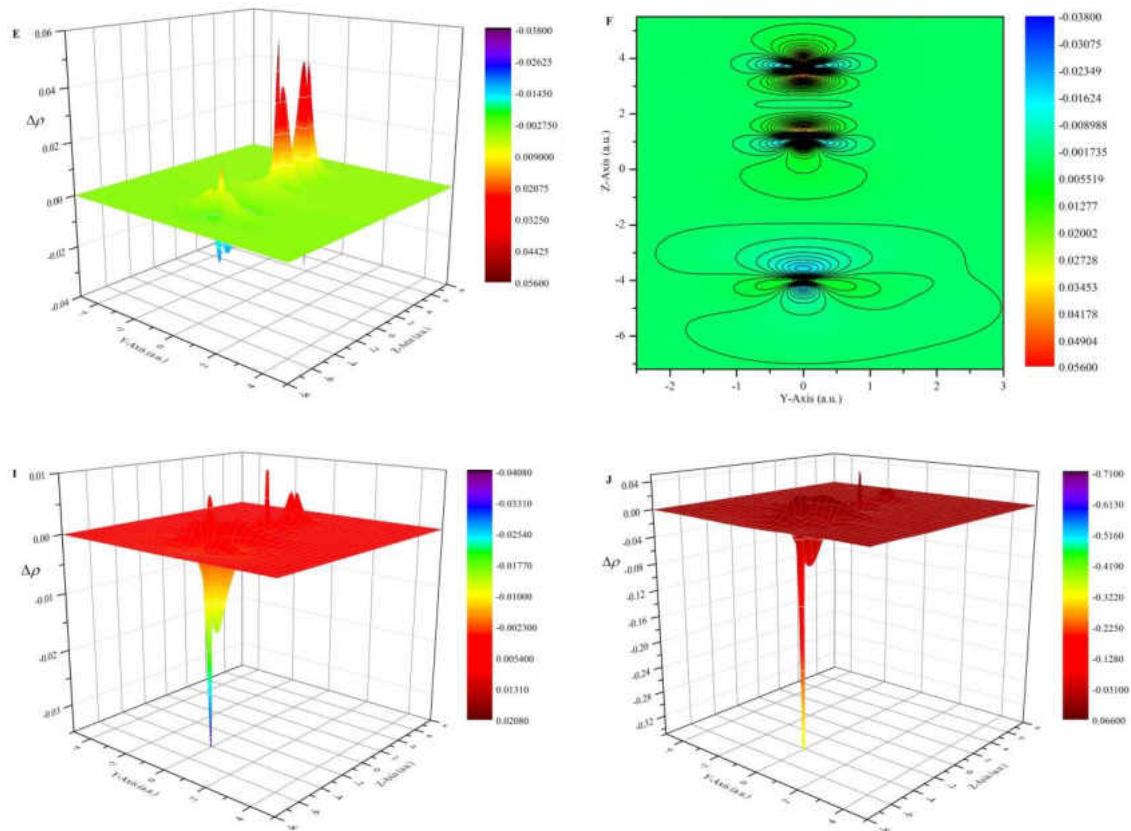Maps obtained with the PW91 functional

The $F_2 \cdots NH_3$ Complex

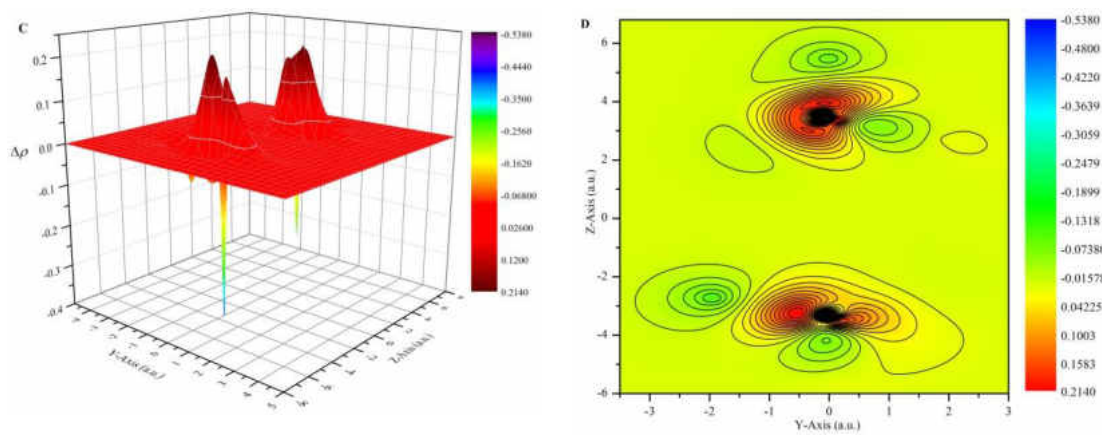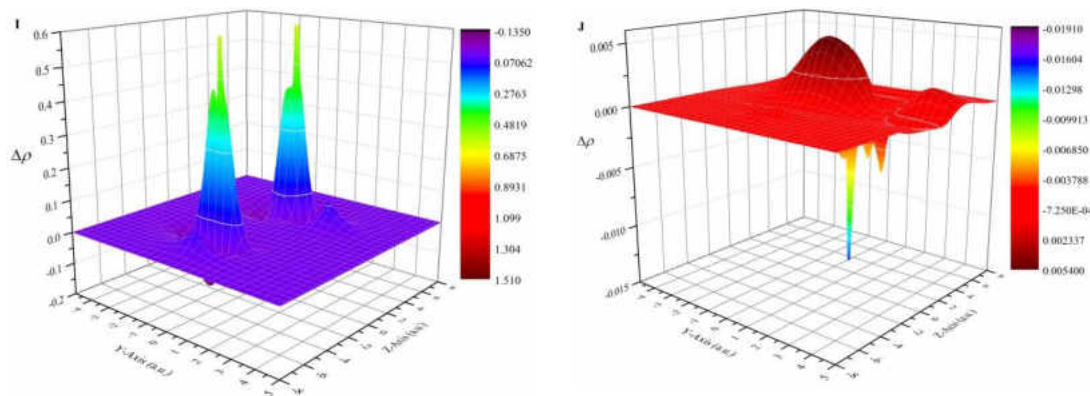Maps obtained with the VWN5 functional

274

Maps obtained with the PW91 functional

The $CH_4 \cdots CH_4$ *Complex*
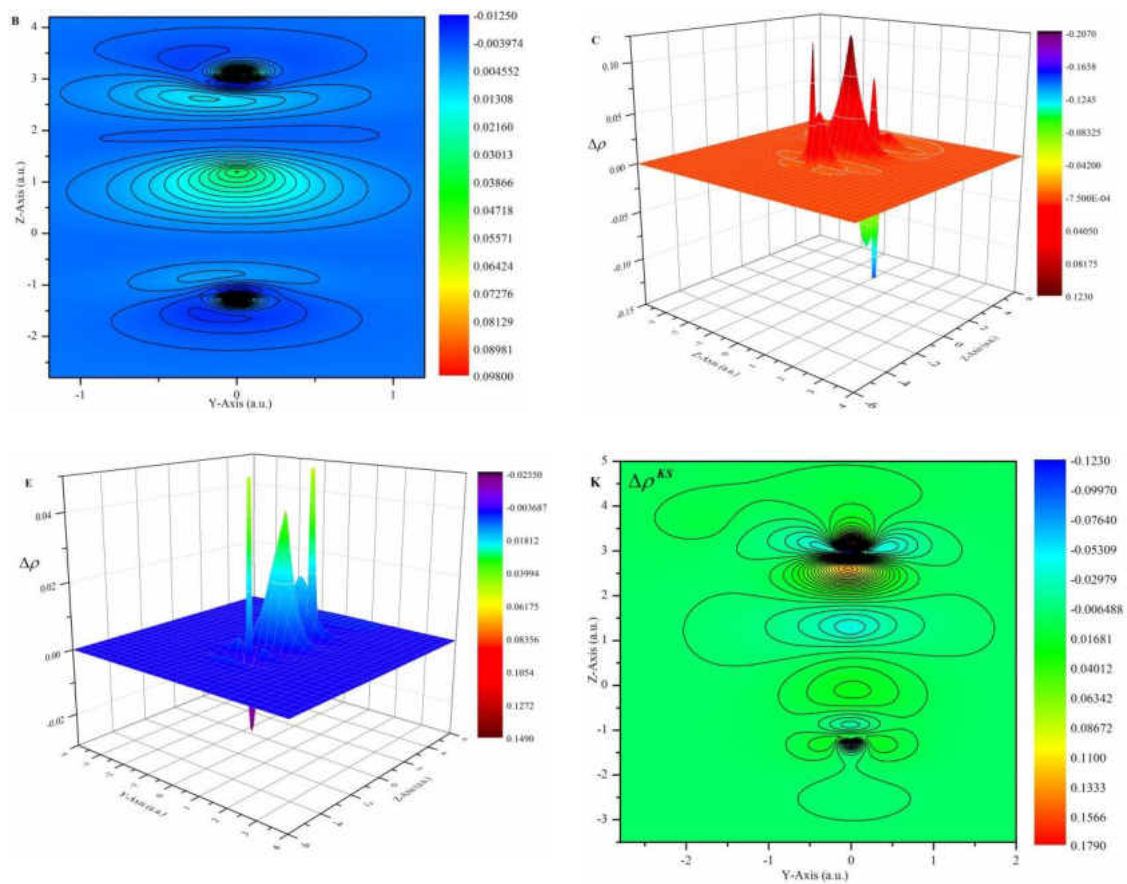
Maps obtained with the VWN5 functional

275

The $F^- \cdots H_2O$ Complex

Maps obtained with the VWN functional
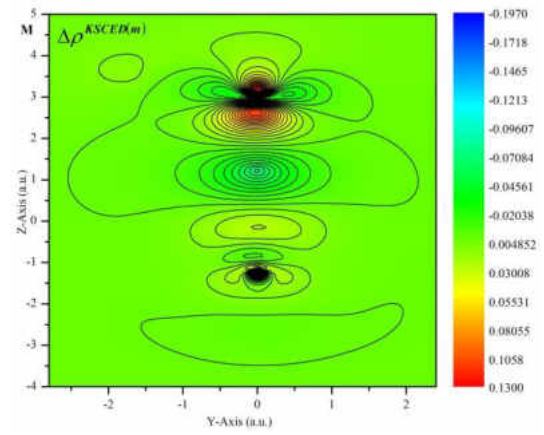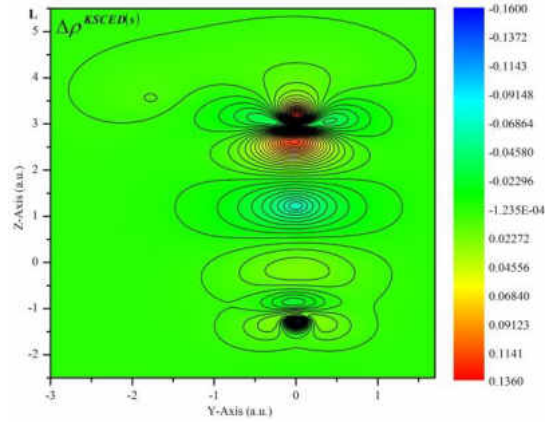
REFERENCES

1. Knowles, P.; Schütz, M.; Werner, H.-J. in *Modern Methods and Algorithms of Quantum Chemistry*, J. Grotendorst (Ed.), John von Neumann Institute for Computing, Jülich, NIC Series, 2000, Vol. 1, ISBN 3-00-005618-1, p. 69.

2. Gordon, F. S. *Using Multiconfiguration Methods to Treat Electron Correlation in PES Calculations*, Department of Chemistry, Hope College, Holland, Michigan 49423. (http://www.chem.hope.edu/~discus/muccc/muccc10/MUCCC10-Gordon.pdf).

3. Khait, Y. G.; Song, J.; Hoffmann, M. R. *J. Chem. Phys*. **2002**, *117*, 4133.

4. Jiang, W.; Khait, Y. G.; Hoffmann, M. R. *J. Phys. Chem. A* **2009**, *113*, 4374.

5. Khait, Y. G.; Hoffmann, M. R. *Annu. Rep. Comput. Chem*. **2012**, *8*, 53.

6. Tamukong, P. K.; Khait, Y. G.; Hoffmann, M. R. *J. Phys. Chem. A* **2014** (submitted).

7. Liu, M.; de Leon Snapp, N.; Park, H. *Chem. Sci*. **2011**, *2*, 80.

8. Najafpour, M. M.; Rahimi, F.; Aro, E. M.; Lee, C. H.; Allakhverdiev, S. I. *J. R. Soc. Interface* **2012**, *9*, 2383.

9. Hocking, R. K.; Brimblecombe, R.; Chang, L. Y.; Singh, A.; Cheah, M. H.; Glover, C.; Casey, W. H.; Spiccia, L. *Nat. Chem.* **2011**, *3*, 461.

10. Osterloh, F. E.; Parkinson, B. A. *MRS Bull* **2011**, *36*, 17.

11. Anxolabéhère-Mallart, E.; Costentin, C.; Fournier, M.; Nowak, S.; Robert, M.; Savéant, J. M. *J. A. Chem. Soc.* **2012**, *134*, 6104.

12. Bogani, L., Wernsdorfer, W. *Nat. Mat.* **2008**, *7*, 179.

13. Park, M. S.; Min, B. I. *Phys. Rev. B* **2003**, *68*, 224436.

14. Yagi, Y.; Briere, T. M.; Sluiter, M. H.; Kumar, V.; Farajian, A. A.; Kawazoe, Y. *Phys. Rev. B* **2004**, *69*, 075414.

15. Infante, I.; Andrews, L.; Wang, X.; Gagliardi, L. *Chem. Eur. J.* **2010**, *16*, 12804.

16. Kalemos, A.; Kaplan, I. G.; Mavridis, A. *J. Chem. Phys*. **2010**, *132*, 024309.

17. Shim, I.; Dahl, J. P.; Johansen, H. *Int. J. Quantum Chem*. **1979**, *15*, 311.

18. Camacho, C.; Witek, H. A.; Yamamoto, S. *J. Comput. Chem*. **2009**, *30*, 468.

19. Ruipérez, F.; Aquilante, F.; Ugalde, J. M.; Infante, I. *J. Chem. Theory Comput.* **2011**, *7*, 1640.

20. Angeli, C.; Pastore, M.; Cimiraglia, R. *Theor. Chem. Acc.* **2007**, *117*, 743.

21. Dyall, K. G. *J. Chem. Phys*. **1995**, *102*, 4909.

22. Khait, Y. G.; Song, J.; Hoffmann, M. R. *Int. J. Quantum Chem*. **2004**, *99*, 210.

23. Moore, C. E. Atomic Energy Levels. *National Bureau of Standards*, Washington, DC, **1958**.

24. Hotop, H.; Lineberger, W. C. *J. Phys. Chem. Ref. Data* **1975**, *14*, 731.

25. Pyykkö. P. *Adv. Quantum Chem*. **1978**, *11*, 353.

26. Fricke, B. *Struct. Bonding (Berlin)* **1975**, *21*, 89.

27. Bauschlicher Jr., C. W.; Walch, S. P.; Partridge, H. *Chem. Phys. Lett*. **1984**, *103*, 291.

28. Schwerdtfeger, P.; Bowmaker, G. A. *J. Chem. Phys*. **1994**, *100*, 4487.

29. Neogrády, P.; Kellö, V.; Urban, M.; Sadlej, A. J. *Int. J. Quant. Chem*. **1997**, *63*, 557.

30. Douglas, M.; Kroll, N. M. *Ann. Phys*. **1974**, *82*, 89.

31. Hess, B. A. *Phys. Rev. A* **1986**, *33*, 3742.

32. Kupratakuln, S. *J. Phys. C: Solid State Phys*. **1970**, *3*, S109.

33. Christensen, N. E.; Seraphin, B. 0. *Phys. Rev. B* **1971**, *4*, 3321.

34. Pyykkö, P.; Desclaux, J. P. *Acc. Chem. Res*. **1979**, *12*, 276.

35. Desclaux, J. P.; Kim, Y. K. *J. Phys. B At. Mol. Opt. Phys*. **1975**, *8*, 1177.

36. Pyykkö, P. *Chem. Rev*. **1988**, *88*, 563.

37. Pou-Amerigo, R.; Merchán, M.; Nebot-Gil, I.; Widmark, P. O.; Roos, B. O. *Theor. Chim. Acta* **1995**, *92*, 149.

38. Roos, B. O.; Malmqvist, P.-Å. *Phys. Chem. Chem. Phys*. **2004**, *6*, 2919.

39. Illiaš, M.; Kellö, V.; Urban, M. *Acta Phys. Slov*. **2010**, *60*, 259.

40. Einstein, A. *Ann. Phys.-Berlin* **1905**, *17*, 891.

41. Bohr, N. *Philos. Mag*. **1913**, *26*, 1.

42. Yung, Y. C. *Mod. Chem. Appl*. **2013**, *1*, e107.

43. Bar-On, I.; Ryaboy, V. *Siam J. Sci. Comput.* **1997**, 18, 1412.

44. Tichavský, P.; Yeredor, A. *IEEE Trans. Sig. Proc.* **2009**, *57*, 878.

45. Kendall, R. A.; Aprà, E.; Bernholdt, D. E.; Bylaska, E. J.; Dupuis, M.; Fann, G. I.; Harrison, R. J.; Ju, J.; Nichols, J. A.; Nieplocha, J.; Straatsma, T. P.; Windus, T. L. Wong, A. T. *Comput. Phys. Commun.* **2000**, *128*, 260.

46. Aquilante, F.; De Vico, L.; Ferré, N.; Ghigo, G.; Malmqvist, P.-Å.; Neogrády, P.; Pedersen, T. B.; Pitoňak, M.; Reiher, M.; Roos, B. O.; Serrano-Andrés, L.; Urban, M.; Veryazov, V.; Lindh. R. *J. Comput. Chem*. **2010**, *31*, 224.

47. de Jong, W. A.; Bylaska, E.; Govind, N.; Janssen, C. L.; Kowalski, K.; Müller, T.; Nielsen, I. M. B.; van Dam, H. J. J.; Veryazov, V.; Lindh, R. *Phys. Chem. Chem. Phys*. **2010**, *12*, 6896.

48. Vancoillie, S.; Delcey, M. G.; Lindh, R.; Vysotskiy, V.; Malmqvist, P.-Å.; Veryazov, V. *J. Comput. Chem*. **2013**, *34*, 1937.

49. Motamarri, P.; Nowak, M. R.; Leiter, K.; Knap, J.; Gavini, V. *J. Comput. Phys*. **2013**, *253*, 308.

50. Pask, J. E.; Sterne, P. A. *Model. Simul. Mater. Sci. Eng.* **2005**, *13*(3), R71.

51. Thom A. J. W.; Alavi, A. *Phys. Rev. Lett*. **2007**, *99*, 143001.

52. Ohtsuka, Y.; Nagase, S. *Chem. Phys. Lett*. **2008**, *463*, 431.

53. Booth, G. H.; Thom, A. J. W.; Alavi, A. *J. Chem. Phys*. **2009**, *131*, 054106.

54. Thom, A. J. W. *Phys. Rev. Lett*. **2010**, *105*, 263004.

55. Booth, G. H.; Alavi, A. *J. Chem. Phys*. **2010**, *132*, 174104.

56. Werner, H.-J.; Manby, F. R.; Knowles, P. J. *J. Chem. Phys*. **2003**, *118*, 8149.

57. Fe-dorov, D. G.; Ishida, T.; Kitaura, K. *J. Phys. Chem. A* **2005**, *109*, 2638.

58. Füsti-Molnár, L.; Kong, J. *J. Chem. Phys*. **2005**, *122*, 074108.

59. Ozaki, T. *Phys. Rev. B* **2006**, *74*, 245101.

60. Zhao, Z.; Meza, J.; Lee, B.; Shan, H.; Shrohmaier, E.; Bailey, D.; Wang, L.-W. *J. Phys. Conf. Ser*. **2009**, *180*, 012079.

61. Bowler, D. R. Miyazaki, T. *Rep. Prog. Phys*. **2012**, *75*, 036503.

62. Schütz, M.; Hetzer, G.; Werner, H.-J. *J. Chem. Phys*. **1999**, *111*, 5691.

63. Yang, W. *Phys. Rev. Lett*. **1991**, *66*, 1438.

64. Yang, W.; Lee, T. –S. *J. Chem. Phys*. **1995**, *163*, 5674.

65. Khandogin, J.; Musier-Forsyth, K.; York, D. M. *J. Mol. Biol.* **2003**, *330*, 993.

66. Jacob, C. R.; Neugebauer, J.; Visscher, L. *J. Comput. Chem.* **2008**, *29*, 1011.

67. Wesolowski, T. A. *Phys. Rev. A* **2008**, *77*, 012504.

68. Khait, Y. G.; Hoffmann, M. R. *J. Chem. Phys*. **2010**, *133*, 044107.

69. Huang, C.; Pavone, M.; Carter, E. A. *J. Chem. Phys*. **2011**, *134*, 154110.

70. Huang, C.; Carter, E. A. *J. Chem. Phys*. **2011**, *135*, 194104.

71. Wesolowski, T. A.; Warshel, A. *J. Phys. Chem.* **1993**, *97*, 8050.

72. Wesołowski, T. A.; Weber, J. *Chem. Phys. Lett*. **1996**, *248*, 71.

73. Cortona, P. *Phys. Rev. B* **1991**, *44*, 8454.

74. Senatore, G.; Subbaswamy, K. R. *Phys. Rev. B* **1986**, *34*, 5754.

75. Johnson, M. D.; Subbaswamy, K. R.; Senatore, G. *Phys. Rev. B* **1987**, *36*, 9202.

76. Govind, N.; Wang, Y. A.; da Silva, A. J. R.; Carter, E. A. *Chem. Phys. Lett*. **1998**, *295*, 129.

77.   Govind, N.; Wang, Y. A.; Carter, E. A. *J. Chem. Phys*. **1999**, *110*, 7677.

78.   Schrödinger, E. *Ann. d. Phys*. **1926**, *79*, 734.

79.   Szabo, A.; Ostlund, N. S. *Modern Quantum Chemistry*, Dover Publications, Inc.: NewYork, 1996.

80.   Born, M.; Oppenheimer, R. *Ann. Phys. (Leipzig)* **1927**, *84*, 457.

81.   Cramer, C. J. *Essentials of Computational Chemistry, Theories and Models*, John Wiley & Sons, Chichester, 2002.

82.   Helgaker, T.; Jørgensen, P.; Olsen, J. *Molecular Electronic-Structure Theory*, John Wiley & Sons, The Atrium, Southern Gate, Chichester, 2000.

83.   http://en.wikipedia.org/wiki/Lagrange_multiplier (Accessed: 05/10/2014).

84.   Echenique, P.; Alonso, J. L. *Mol. Phys*. **2007**, *105*, 3057.

85.   Hartree, D. R. *Proc. Camb. Philos. Soc*. **1927**,*24*, 89.

86.   Fock, V. *Z. Phys*. **1930**, *61*, 126.

87.   Slater, J. C. *Phys. Rev*. **1930**, *35*, 210.

88.   Roothaan, C. C. J. *Rev. Mod. Phys*. **1951**, *23*, 69.

89.   Löwdin, P.-O. *J. Chem. Phys*. **1950**, *18*, 365.

90.   Huzinaga, S.; Arnau, C. *Phys. Rev. A* **1970**, *1*, 1285.

91.   Møller, C.; Plesset, M. S. *Phys. Rev*. **1934**, *46*, 618.

92.   Shephard, R. *Adv. Chem. Phys*. **1987**, *69*, 63.

93.   Roos, B. O. *Adv. Chem. Phys*. **1987**, *69*, 399.

94.   Schmidt, M. W.; Gordon, M. S. *Annu. Rev. Phys. Chem*. **1998**, *49*, 233.

95.   Roos, B. O.; Taylor, P. R.; Siegbahn, P. E. M. *Chem. Phys*. **1980**, *48*, 157.

96.   Olsen, J.; Roos, B. O.; Jørgensen, P.; Jensen, H. J. Aa. *J. Chem. Phys*. **1988**, *89*, 2185.

97.   Malmqvist, P.-Å.; Rendell, A.; Roos, B. O. *J. Phys. Chem*. **1990**, *94*, 5477.

98.   Khait, Y. G.; Song, J.; Hoffmann, M. R. *Int. J. Quantum Chem*. **2004**, *99*, 210.

99.   Gelfand, I. M.; Tsetlin, M. L. *Dokl. Akad. Nauk SSSR* **1950**, *71*, 825.

100.   Pauncz, R. *Spin Eigenfunctions: Construction and Use* (Plenum: New York, 1979).

101.   Matsen, F. A. *Int. J. Quantum Chem*. **1976**, *10*, 525.

102.   Paldus, J. *Int. J. Quantum Chem*. **1975**, *9*, 165.

103.   Shavitt, I. In *The Unitary Group for the Evaluation of Electronic Energy Matrix Elements, Lecture Notes in Chemistry*; Hinze, J., Ed. Springer: Berlin, 1981; Vol. 22, p 51.

104.   Jiang, W. *Applications of a Configuration-Driven Unitary Group Approach to Electronic Structure Theory*. Ph.D. Dissertation, University of North Dakota, Grand Forks, ND, 2009.

105.   Theis, D. *Theoretical Development and Application of GVVPT2 Gradients and Nonadiabatic Coupling Terms*. Ph.D. Dissertation, University of North Dakota, Grand Forks, ND, 2011.

106.   Douady, L. G. J.; Ellinger, Y.; Subra, R.; Levy, B. *J. Chem. Phys*. **1980**, *72*, 1452.

107.   Yeager, D. L.; Jørgensen, P. *J. Chem. Phys*. **1979**, *71*, 755.

108.   Werner, H. J.; Meyer, W. *J. Chem. Phys*. **1980**, *73*, 2342.

109.   Eade, R. H. A.; Robb, M. A. *Chem. Phys. Lett*. **1981**, *83,* 362.

110.   Golab, J. T.; Yeager, D. L.; Jørgensen, P. *Chem. Phys*. **1983**, *78*, 175.

111.   Hoffmann, M. R.; Sherrill, C. D.; Leininger, M. L.; Schaefer III, H. F. *Chem. Phys. Lett*. **2002**, *355*, 183.

112.   Hoffmann, M. R.; Fox, D. J.; Gaw, J. F.; Osamura, Y.; Yamaguchi, Y.; Grev, R. S.; Fitzgerald, G.; Schaefer III, H. F.; Knowles, P. J.; Handy, N. C. *J. Chem. Phys*. **1984**, *80*, 2660.

113.   Khait, Y. G.; Song, J.; Hoffmann, M. R. *Chem. Phys. Lett*. **2003**, *372*, 674.

114.   Hoffmann, M. R.; Datta, D.; Das, S.; Mukherjee, D.; Szabados, Á.; Rolik, Z.; Surján, P. R. *J. Chem. Phys.* **2009**, *131*, 204104.

115.   Epstein, P. S. *Phys. Rev*. **1925**, *28*, 695.

116. Nesbet, R. K. *Proc. R. Soc. London, Ser. A* **1955**, *230*, 312.

117. Nakano, H. *J. Chem. Phys*. **1993**, *99*, 7983.

118. Khait, Y. G.; Hoffmann, M. R. *J. Chem. Phys*. **1998**, *108*, 8317.

119. Liu, W. *Mol. Phys.* **2010**, *108*, 1679.

120. Cheng, L.; Gauss, J. *J. Chem. Phys.* **2011**, *135*, 084114.

121. Li, Z.; Suo, B.; Zhang, Y.; Xiao, Y; Liu, W. *Mol. Phys.* **2013**, *111*, 3741.

122. Li, Z.; Xiao, Y.; Liu, W. *J. Chem. Phys*. **2012**, *137*, 154114.

123. Dyall, K. G. *J. Chem. Phys.* **1997**, *23*, 9618.

124. Liu, W.; Peng, D.; *J. Chem. Phys.* **2009**, *131*, 031104.

125. Arnoldi, W. E. *Appl. Math.* **1951**, *9*, 17.

126. Lanczos, C. *J. Res. Nat. Bur. Standards* **1950**, *45*, 255.

127. Davidson, E. R. *J. Comput. Phys.* **1975**, *17*, 87.

128. Jacobi, C. G. J. *J. Reine Angew. Math*. **1846**, 51.

129. Vetterling, W. T.; Teukolsky, S. A.; Press, W. H.; Flannery, B. P. *Numerical Recipes Example Book (C)*, Second Edition (Cambridge University Press, New York, 1992), p. 185.

130. Obara, S.; Saika, A. *J. Chem. Phys*. **1986**, *84*, 3963.

131. Head-Gordon, M.; Pople, J. A. *J. Chem. Phys*. **1988**, *89*, 5777.

132. Hamilton, T. P.; Schaefer III, H. F. *Chem. Phys*. **1991**, *150*, 163.

133. Witzig, T. E.; White, C. A.; Wiseman, G. A.; Gordon, L. I.; Emmanouilides, C.; Raubitschek, A.; Janakiraman, N.; Gutheil, J.; Schilder, R. J.; Spies, S.; Silverman, D. H. S.; Parker, E.; Grillo-López, A. J. *J. Clin. Oncol.* **1999**, *17*, 3793.

134. Ansell, S. M.; Ristow, K. M.; Habermann, T. M.; Wiseman, G. A.; Witzig, T. E. *J. Clin. Oncol.*, **2002**, *20*, 3885.

135. Morschhauser, F., Illidge, T., Huglo, D., Martinelli, G., Paganelli, G., Zinzani, P. L.; Rule, S.; Liberati, A. M.; Milpied, N.; Hess, G.; Stein, H.; Kalmus, J.; Marcus, R. *Blood* **2007**, *110*, 54.

136. Knight, L. B.; Van Zee, J. R.; Weltner, W. *Chem. Phys. Lett.* **1983**, *94*, 296.

137. Singer, R. J.; Grinter, R. *Chem. Phys.* **1987**, *113*, 99.

138. Moskovits, M.; Lella, D. P.; Limm, W. *J. Chem. Phys*. **1984**, *80*, 626.

139. Verhaegen, G.; Smoes, S.; Drowart, J. *J. Chem. Phys*. **1964**, *40*, 239.

140. Matxain, J. M.; Rezabal, E.; Lopez, X.; Ugalde, J. M.; Gagliardi, L. *J. Chem. Phys*. **2008**, *128*, 194315.

141. Matxain, J. M.; Rezabal, E.; Lopez, X.; Ugalde, J. M.; Gagliardi, L. *J. Chem. Phys.* **2010**, *132*, 139901.

142. Kaplan, I. G.; Miranda, U. *AIP Adv*. **2011**, *1*, 022108.

143. Brackett, E.; Brewer, L. *University of California Radiatio Laboratory Rept. UCRL-3712*, **1957**.

144. Knight, L. B.; Woodward, R. W.; Van Zee, R. J.; Weltner, W. *J. Chem. Phys*. **1983**, *79*, 5820.

145. Yang, D. S.; Simard, B.; Hackett, P. A.; Bréces, A.; Zgierski, M. Z. *Int. J. Mass Spectrom. Ion Processes* **1996**, *159*, 65.

146. Fang, L.; Shen, C.; Liu, Y.; Lindsay, D. M.; Lombardi, J. R. *Low Temp. Phys.* **2000**, *26*, 752.

147. Badger, R. M. *J. Chem. Phys.* **1934**, *2*, 128.

148. Walch, S. P.; Bauschlicher Jr., C. W., in *Comparison of ab initio Quantum Chemistry with Experiment for Small Molecules*; Barlett, R. J., Ed.; Riedel: Amsterdam, Holland, 1985; p. 17.

149. Dai, D.; Balasubramanian, K. *J. Chem. Phys*. **1993**, *98*, 7098.

150. La John, L. A.; Christiansen, P. A.; Ross, R. B.; Atashroo, T.; Ermler, W. C. *J. Chem. Phys.* **1987**, *87*, 2812.

151. Gutsev, G. L.; Bauschlicher Jr., C. W. *J. Phys. Chem. A* **2003**, *107*, 4755.

152. Yanagisawa, S.; Tsuneda, T.; Hirao, K. *J. Comput. Chem.* **2001**, *22*, 1995.

153.   Balabanov, N. B.; Peterson, K. A. *J. Chem. Phys.* **2005**, *123*, 064107.

154.   Peterson, K. A.; Figgen, D.; Dolg, M.; Stoll, H. *J. Chem. Phys.* **2007**, *126*, 124101.

155.   Camacho, C.; Witek, H. A.; Cimiraglia, R. *J. Chem. Phys.* **2010**, *132*, 244306.

156.   Gingerich, K. A. *Faraday Symp. Chem. Soc.* **1980**, *14*, 109.

157.   Wu, Z. J. *Chem. Phys. Lett.* **2004**, *383*, 251.

158.   Tamukong, P. K.; Theis, D.; Khait, Y. G.; Hoffmann, M. R. *J. Phys. Chem. A* **2012**, *116*, 4590.

159.   Tamukong, P. K.; Hoffmann, M. R. Li, Z.; Liu, W. *J. Phys. Chem. A* **2014**, *118*, 1489.

160.   Sugar, J.; Corliss, C. *J. Phys. Chem. Ref. Data* **1985**, *14*, 264.

161.   Sugar, J.; Musgrove, A. *J. Phys. Chem. Ref. Data* **1988**, *17*, 155.

162.   Roos, B. O.; Borin, A. C.; Gagliardi, L. *Angew. Chem. Int. Ed.* **2007**, *46*, 1469.

163.   Kant, A.; Strauss, B. J. *J. Chem. Phys.* **1966**, *45*, 3161.

164.   Kündig, E.P.; Moskovits, M.; Ozin, G.A. *Nature* **1975**, *254,* 503.

165.   Salahub, D.R. *Adv. Chem. Phys.* **1987**, *69,* 447.

166.   Bauschlicher Jr., C. W.; Patridge, H. *Chem. Phys. Lett.* **1994**, *231*, 277.

167.   Thomas III, E. J.; Murray, J. S.; O'Connor, C. J.; Politzer, P. *J. Mol. Struct.* **1999**, *487*, 177.

168.   Michalopoulos, D.L.; Geusic, M.E.; Hansen, S.G.; Powers, D.E.; Smalley, R.E. *J. Phys. Chem.* **1982**, *86*, 3914.

169.   Bondybey, V.E.; English, J. H. *Chem. Phys. Lett.* **1983**, *94*, 443.

170.   Simard, B.; Lebeault-Dorget, M.-A.; Marijnissen, A.; ter Meulen, J. *J. Chem. Phys.* **1998**, *108*, 9668.

171.   Hilpert, K.; Ruthardt, K. *Ber. Bunsenges. Phys. Chem.* **1987**, *91*, 724.

172.   Su, C. X.; Hales, D. A.; Armentrout, P. B. *Chem. Phys. Lett.* **1993**, *201*, 199.

173.   Casey, S. M.; Leopold, D. G. *J. Phys. Chem*. **1993**, *97*, 816.

174.   Rydberg, R. *Z. Phys*. **1931**, *73*, 376.

175.   Klein, O. *Z. Phys*. **1932**, *76*, 226.

176.   Rees, A. L. G. *Proc. Phys. Soc*. **1947**, *59*, 998.

177.   Scuseria, G. E.; Schaefer III, H. F. *Chem. Phys. Lett*. **1990**, *174*, 501.

178.   Mitrushenkov, A. O.; Palmieri, P. *Chem. Phys. Lett*. **1997**, *278*, 285.

179.   Dachsel, H.; Harrison, R. J.; Dixon, D. A. *J. Phys. Chem. A* **1999**, *103*, 152.

180.   Andersson, K.; Roos, B. O.; Malmqvist, P. A.; Widmark, P. O. *Chem. Phys. Lett*. **1994**, *230*, 391.

181.   Andersson, K.; Roos, B. O. *Chem. Phys. Lett*. **1995**, *245*, 215.

182.   Roos, B. O. *Collect. Czech. Chem. Commun*. **2003**, *68*, 265.

183.   Andersson, K. *Theor. Chim. Acta* **1995**, *91*, 31.

184.   Celani, P.; Stoll, H.; Werner, H. J.; Knowles, P. J. *Mol. Phys*. **2004**, *102*, 2369.

185.   Müller, T. *J. Phys. Chem. A* **2009**, *113*, 12729.

186.   Hess, B. A.; Jansen, G. *Phys. Rev. A* **1989**, *39*, 6016.

187.   Hongo, K.; Maezono, R. *Int. J. Quantum Chem*. **2012**, *112*, 1243.

188.   Kurashige, Y.; Yanai, T. *J. Chem. Phys*. **2011**, *135*, 094104.

189.   Efremov, Y. M.; Samoilova, A. M.; Kozhukhovsky, V. B.; Gurvich, L. V. *J. Mol. Spectrosc*. **1978**, *73*, 430.

190.   Gupta, S. K.; Atkins, R. M.; Gingerich, K. A. *Inorg. Chem*. **1978**, *17*, 3211.

191.   Pellin, M.; Foosnaes, T.; Gruen, D. M. *J. Chem. Phys*. **1981**, *74*, 5547.

192.   Hopkins, J. B.; Landridge-Smith, P. R. R.; Morse, M. D.; Smalley, R. E. *J. Chem. Phys*. **1983**, *78*, 1627.

193.   Kraus, D.; Lorenz, M.; Bondybey, V. E. *Phys. Chem. Commun*. **2001**, *4*, 44.

194.   Feng, L.; Davis, B.; Lu, H.; Chen, X.; Shen, X.; Lombardi, J. R. *Chem. Phys. Lett*. **2002**, *352*, 70.

195.   Andzelm, J.; Radzio, E.; Salahub, D. R. *J. Chem. Phys*. **1985**, *83*, 4573.

196.   Atha, P. M.; Hillier, I. H.; Guest, M. F. *Chem. Phys. Lett*. **1980**, *75*, 84.

197.   Bursten, B. E.; Cotton, F. A.; Hall, M. B. *J. Am. Chem. Soc*. **1980**, *102*, 6349.

198.   Goodgame, M. M.; Goddard III, W. A. *Phys. Rev. Lett*. **1982**, *48*, 135.

199.   Goodgame, M. M.; Goddard III, W. A. *Phys. Rev. Lett*. **1985**, *54*, 661.

200.   Balasubramanian, K.; Zhu, X. *J. Chem. Phys*. **2002**, *117*, 4861.

201.   Borin, A. C.; Gobbo, J. P.; Roos, B. O. *Chem. Phys*. **2008**, *343*, 210.

202.   Roos, B. O.; Lindh, R.; Malmqvist, P.-Å.; Veryazov, V.; Widmark, P. O. *J. Phys. Chem. A* **2005**, *109*, 6575.

203.   Bergner, A.; Dolg, M.; Kuechle, W.; Stoll, H.; Preuss, H. *Mol. Phys*. **1993**, *80*, 1431.

204.   Kaupp, M.; Schleyer, P. R.; Stoll, H.; Preuss, H. *J. Chem. Phys*. **1991**, *94*, 1360.

205.   Dolg, M.; Stoll, H.; Preuss, H.; Pitzer, R. M. *J. Phys. Chem*. **1993**, *97*, 5852.

206.   Hay, P. J.; Wadt, W. R. *J. Chem. Phys*. **1985**, *82*, 270.

207.   Hay, P. J.; Wadt, W. R. *J. Chem. Phys*. **1985**, *82*, 284.

208.   Roy, L. E.; Hay, P. J.; Martin, R. L. *J. Chem. Theory Comput.* **2008**, *4*, 1029.

209.   Bauschlicher, Jr., C. W. *Theor. Chim. Acta* **1995**, *92*, 183.

210.   Feller, D. *J. Chem. Phys*. **1993**, *98*, 7059.

211.   Feller, D. *J. Chem. Phys*. **1992**, *96*, 6104.

212.   Halkier, A.; Helgaker, T.; Jørgensen, P.; Klopper, W.; Olsen, J. *Chem. Phys. Lett*. **1999**, *302*, 437.

213.   Williams, T. G.; De Yonker, N. J.; Wilson, A. K. *J. Chem. Phys*. **2008**, *128*, 044101.

214.   Jiang, W.; Khait, Y. G.; Hoffmann, M. R. *Mol. Phys*. **2009**, *107*, 889.

215. Helgaker, T.; Klopper, W.; Koch, H.; Noga, J. *J. Chem. Phys*. **1997**, *106*, 9639.

216. Halkier, A.; Helgaker, T.; Jørgensen, P.; Klopper, W.; Koch, H.; Olsen, J.; Wilson, A. K. *Chem. Phys. Lett*. **1998**, *286*, 243.

217. Schwartz, C. *Phys. Rev. A* **1962**, *126*, 1015.

218. Xu, X. ; Truhlar, D. G. *J. Chem. Theory Comput*. **2012**, *8*, 80.

219. Brynda, M.; Gagliardi, L.; Roos, B. O. *Chem. Phys. Lett*. **2009**, *471*, 1.

220. Andersson, K. *Chem. Phys. Lett*. **1995**, *237*, 212.

221. Harrison, J. F. *Chem. Rev*. **2000**, *100*, 679.

222. Morse, M. D. *Chem. Rev*. **1986**, *86*, 1049.

223. Ruipérez, F.; Piris, M.; Ugalde, J. M.; Matxain, J. M. *Phys. Chem. Chem. Phys*. **2013**, *15*, 2055.

224. Angeli, C. ; Cavallini, A. ; Cimiraglia, R. *J. Chem. Phys*. **2007**, *127*, 074306.

225. *Kirk-Othmer Encyclopedia of Chemical Technology*, 4th Ed. Vol. 15, Interscience, New York, 1995, p. 963.

226. Poineau, F.; Sattelberger, A. P.; Czerwinski, K. R. *J. Coord. Chem.* **2008**, *61*, 2356.

227. Noddack, W.; Tacke, I.; Berg, O. *Naturwis.* **1925**, *13*, 567.

228. de Jonge, F. A. A.; Pauwels, E. K. J. *Eur. J. Nucl. Med.* **1996**, *23*, 336.

229. Armstrong, J. T. *Chem. Eng. News* **2003**, *8*, 110.

230. Borin, A. C.; Gobbo, J. P.; Roos, B. O. *Mol. Phys*. **2009**, *107*, 1035.

231. Buchachenko, A. A.; Chalasinski, G.; Szczęśniak, M. M. *J. Chem. Phys*. **2010**, *132*, 024312.

232. Van Zee, R. J.; Baumann, C. A.; Weltner Jr, W. *J. Chem. Phys*. **1981**, *74*, 6977.

233. Cheeseman, M.; Van Zee, R. J.; Weltner Jr, W. *J. Chem. Phys*. **1989**, *91*, 2748.

234. Bier, K. D.; Haslett, T. L.; Kirkwood, A. D.; Moskovits, M. J. *J. Chem. Phys*. **1988**, *89*, 6.

235. Kirkwood, A. D.; Bier, K. D.; Thompson, J. K.; Haslett, T. L.; Huber, A. S.; Moskovits, M. *J. Phys. Chem.* **1991**, *95*, 2644.

236. Haslett, T. L.; Moskovits, M.; Weitzman, A. L. *J. Mol. Spectrosc.* **1988**, *135*, 259.

237. Baumann, C. A.; Van Zee, R. J.; Bhat, S. V.; Weltner Jr., W. *J. Chem. Phys.* **1983**, *78*, 190.

238. Camacho, C.; Yamamoto, S.; Witek, H. A. *Phys. Chem. Chem. Phys.* **2008**, *10*, 5128.

239. Yamamoto, S.; Tatewaki, H.; Moriyama, H.; Nakano, H. *J. Chem. Phys.* **2006**, *124*, 124302.

240. Koga, T.; Tatewaki, H.; Matsuyama, H.; Satoh, Y. *Theor. Chem. Acc.* **1999**, *102*, 105.

241. Tatewaki, H.; Koga, T.; Yamamoto, S. *Theor. Chem. Acc.* **2000**, *105*, 55.

242. Sekiya, M.; Noro, T.; Osanai, Y.; Koga, T.; *Theor. Chem. Acc.* **2001**, *106*, 297.

243. Angeli, C.; Cavallini, A.; Cimiraglia, R. *J. Chem. Phys.* **2008**, *128*, 244317.

244. Nayak, S. K.; Jena, P. *Chem. Phys. Lett.* **1998**, *289*, 473.

245. Briere, T. M.; Sluiter, M. H. F.; Kumar, V.; Kawazoe, Y. *Phys. Rev. B* **2002**, *66*, 064412.

246. Jellinek, J.; Acioli, P. H.; Garcia-Rodeja, J.; Zheng, W.; Thomas, O. C.; Bowen Jr., K. H. *Phys. Rev. B* **2006**, *74*, 153401.

247. Bobadova-Parvanova, P.; Jackson, K. A.; Srinivas, S.; Horoi, M. *J. Chem. Phys.* **2005**, *122*, 014310.

248. Yamanaka, S.; Ukai, T.; Nakata, K.; Takeda, R.; Shoji, M.; Kawakami, T.; Takada, T.; Yamaguchi, K. *J. Quantum Chem.* **2007**, *107*, 3178.

249. Kabir, M.; Mookerjee, A.; Kanhere, D. G. *Phys. Rev. B* **2006**, *73*, 224439.

250. Tzeli, D.; Miranda, U.; Kaplan, I. G.; Mavridis, A. *J. Chem. Phys.* **2008**, *129*, 154310.

251. Cotton, F. A.; Fanwick, P. E.; Gage, L. D. *J. Am. Chem. Soc.* **1980**, *102*, 1570.

252. Cotton, F. A.; Shive, L. W. *Inorg. Chem.* **1975**, *14*, 2032.

253. Poineau, F.; Mausolf, E.; Jarvinen, G. D. Sattelberger, A. P.; Czerwinski, K. R. *Inorg. Chem.* **2013**, *52*, 3573.

254. Cotton, F. A.; Walton, R. A. *Multiple Bonds Between Metal Atoms*; Wiley: New York, 1982.

255. Hareland, W. A.; Ebersole, E. R.; Ramachandran, T. P. *Anal. Chem.* **1972**, *44*, 520.

256. Palmeri, P.; Wyart, J. *J. Quant. Spect. Rad. Trans.* **1999**, *61*, 603.

257. Miedema, A. R.; Gingerich, K. A. *J. Phys. B: Atom. Molec. Phys.* **1979**, *12*, 2081.

258. Brewer, L.; Winn, J. S. *Faraday Symp. Chem. Soc*. **1980**, *14*, 126.

259. Klyagina, A. P.; Fursova, V. D.; Levin, A. A.; Gutsev, G. L. *Zh. Strukt. Khim.* **1985**, *28*, 39.

260. Sekine, R.; Kondo, R.; Yamamoto, T.; Onoe, J. *Radiochem.* **2003**, *45*, 233.

261. Yang, S.-Y.; Zhu, Z.-H. *Chin. Phys*. B **2004**, *13*, 2053.

262. Bunge, C. F.; Barrientos, J. A.; Bunge, A. V. *At. Data Nucl. Data Tables* **1993**, *53*, 113.

263. Negodaev, I.; de Graaf, C.; Caballol, R. *Chem. Phys. Lett.* **2008**, *458*, 290.

264. Moore, C. E. Atomic Energy Levels. Natl. Bur. Stand. (U.S.) Circ. 467, Vol. I and II (**1952**); reprinted as Natl. Stand. Ref. Data Ser., Natl. Bur. Stand. (U.S.) 35 (**1971**).

265. Bauschlicher, C. W., Jr.; Walch, S. P.; Partridge, H. *J. Chem. Phys*. **1982**, *76*, 1033.

266. Raghavachari, K.; Trucks, G. W. *J. Chem. Phys*. **1989**, *91*, 1062.

267. Schultz, N. E.; Zhao, Y.; Truhlar, D. G. *J. Phys. Chem. A*. **2005**, *109*, 4388.

268. Murphy, R. B.; Messmer, R. P. *J. Chem. Phys.* **1992**, *97*, 4974.

269. Andersson, K.; Roos, B. O. *Chem. Phys. Lett*. **1992**, *191*, 507.

270. Upton, T. H.; Goddard III, W. A. *J. Am. Chem. Soc*. **1978**, *100*, 5659.

271. Melius, C. F.; Moskowitz, J. W.; Mortola, A. P.; Baillie, M. B.; Ratner, M. A. A. *Surf. Sci*. **1976**, *59*, 279.

272. Cooper, W. F.; Clarke, G. A.; Hare, C. R. *J. Phys. Chem*. **1972**, *76*, 2268.

273. Rösch, N.; Rhodin, T. N. *Phys. Rev. Lett*. **1974**, *32*, 1189.

274. Wood, C.; Doran, M.; Hillier, I. H.; Guest, M. F. *Faraday Symp. Chem. Soc*. **1980**, *14*, 159.

275. Noell, J. O.; Newton, M. D.; Hay, P. J.; Richard L. Martin, R. L.; Bobrowicz, F. W. *J. Chem. Phys*. **1980**, *73*, 2360.

276. Basch, H.; Newton, M. D.; Moskowitz, J. W. *J. Chem. Phys*. **1980**, *73*, 4492.

277. Harris, J.; Jones, R. O. *J. Chem. Phys*. **1979**, *70*, 830.

278. Pou-Amérigo, R.; Merchán, M.; Nebot-Gil, I.; Malmqvist, P.-Å.; Roos, B. O. *J. Chem. Phys*. **1994**, *101*, 4893.

279. Pinegar, J. C.; Langenberg, J. D.; Arrington, C. A.; Spain, E. M.; Morse, M. D. *J. Chem. Phys*. **1995**, *102*, 666.

280. Ho, J.; Polak, M. L.; Ervin, K. M.; Lineberger, W. C. *J. Chem. Phys*. **1993**, *99*, 8542.

281. Dong, C. D.; Lefkidis, G.; Hübner, W. *J. Supercond. Nov. Magn*. **2013**, *26*, 1589.

282. Cheskidov, A. V.; Buchachenko, A. A.; Bezrukov, D. S. *J. Chem. Phys*. **2012**, *136*, 214304.

283. Balabanov, N. B.; Peterson, K. A. *J. Chem. Phys*. **2005**, *123*, 064107.

284. Yanagisawa, S.; Tsuneda, T.; Hirao, K. *J. Chem. Phys*. **2000**, *112*, 545.

285. Diaconu, C. V.; Cho, A. E.; Doll, J. D.; Freeman, D. L. *J. Chem. Phys*. **2004**, *121*, 10026.

286. Dolg, M.; Wedig, U.; Stoll, H.; Preuss, H. *J. Phys. Chem*. **1987**, *86*, 866.

287. Kamal, C.; Banerjee, A.; Ghanty, T. K.; Chakrabarti, A. *Int. J. Quantum Chem*. **2012**, *112*, 1097.

288. Du, J.; Sun, X.; Wang, H. *Int. J. Quantum Chem*. **2008**, *108*, 1505.

289. Yan, S.-Y.; Zhu, Z.-H. *Chin. Phys. B* **2008**, *17*, 4498.

290. De Vore, T. C.; Ewing, A.; Franzen, H. F.; Calder, V. *Chem. Phys. Lett*. **1975**, *35*, 78.

291. Ahmed, F.; Nixon, E. R. *J. Chem. Phys*. **1979**, *71*, 3547.

292. Rasanen, M.; Heimbrook, L. A.; Bondybey, V. E. *J. Mol. Struct*. **1987**, *157*, 129.

293. Kant, A. *J. Chem. Phys*. **1964**, *41*, 1872.

294. Morse, M. D.; Hansen, G. P.; Langridge-Smith, P. R. R.; Zheng, L.-S.; Geusic, M. E.; D. L. Michalopoulos, D. L.; Smalley, R. E. *J. Chem. Phys*. **1984**, *80*, 5400.

295. Foster, J. M.; Boys, S. F. *Rev. Mod. Phys*. **1960**, *32*, 300.

296. Boys, S. F. in *"Quantum Theory of Atoms, Molecules and the Solid State"* P. O. Lowdin ed. Academic Press, New York, **1966**, p. 253.

297. Edmiston, C.; Ruedenberg, K. *Rev. Mod. Phys*. **1963**, *35*, 457.; *J. Chem. Phys*. **1965**, *43*, S97.

298. Reed, A. E.; Weinhold, F. *J. Chem. Phys*. **1985**, *83*, 1736.

299. Hohenberg, P.; Kohn, W. *Phys. Rev. B* **1964**, *136*, 864.

300. Levy, M. *Proc. Natl. Acad. Sci. U.S.A.* **1979**, *76*, 6062.

301. Kohn, W.; Sham, L. J. *Phys. Rev. A* **1965**, *140*, 1133.

302. Wesołowski, T. A. in *Computational Chemistry: Reviews of Current Trends*, **2006**, Vol. 10 (ed. J. Leszczynski), World Scientific, Singapore, p.1.

303. Wesolowski, T. A.; Warshel, A. *J. Phys. Chem.* **1993**, *97*, 8050.

304. Neugebauer, J.; Jacob, C. R.; Wesołowski, T. A.; Baerends, E. J. *J. Phys. Chem. A* **2005**, *109*, 7805.

305. Jacob, C. R.; Neugebauer, J.; Jensen, L.; Visscher, L. *Phys. Chem. Chem. Phys.* **2006**, *8*, 2349.

306. Gritsenko, O. V.; Visscher, L. *Phys. Rev. A* **2010**, *82*, 032519.

307. Lembarki, A.; Chermette, H. *Phys. Rev. A* **1994**, *50*, 5328.

308. Wesolowski, T. A. *J. Chem. Phys*. **1997**, *106*, 8516.

309. Jacob, C. R.; Wesolowski, T. A.; Visscher, L. *J. Chem. Phys.* **2005**, *123*, 174104.

310. Götz, A. W.; Beyhan, S. M.; Visscher, L. *J. Chem. Theory Comput.* **2009**, *5*, 3161.

311. Wesolowski, T. A.; Ellinger, Y.; Weber, J. *J. Chem. Phys.* **1998**, *108*, 6078.

312. Fux, S.; Kiewisch, K.; Jacob, Ch. R.; Neugebauer, J.; Reiher, M. *Chem. Phys. Lett.* **2008**, *461*, 353.

313. Beyhan, S. M.; Götz, A. W.; Jacob, Ch. R.; Visscher, L. *J. Chem. Phys.* **2010**, *132*, 044114.

314. Fux, S.; Jacob, C. R.; Neugebauer, J.; Visscher, L.; Reiher, M. *J. Chem. Phys.* **2010**, *132*, 164101.

315. Dułak, M.; Kamiński, J. W.; Wesolowski, T. A. *J. Chem. Theory Comput.* **2007**, *3*, 735.

316. Goodpaster, J. D.; Ananth, N.; Manby, F. R.; Miller, T. F. *J. Chem. Phys.* **2010**, *133*, 084103.

317. Elliott, P.; Burke, K.; Cohen, M. H.; Wasserman, A. *Phys. Rev. A* **2010**, *82*, 024501.

318. Wu, Q.; Yang, W. *J. Chem. Phys.* **2003**, *118*, 2498.

319. Wu, Q.; Yang, W. *J. Theor. Comput. Chem.* **2003**, *2*, 627.

320. Harriman, J. E. *Phys. Rev. A* **1981**, *24*, 680.

321. Manby, F. R.; Stella, M.; Goodpaster, J. D.; Miller III, T. F. *J. Chem. Theory Comput.* **2012**, *8*, 2564.

322. Laricchia, S.; Fabiano, E.; Della Sala, F. *J. Chem. Phys.* **2010**, *133*, 164111.

323. Laricchia, S.; Fabiano, E.; Della Sala, F. *J. Chem. Phys.* **2013**, *138*, 124112.

324. Dułak, M.; Wesolowski, T. A. *J. Chem. Phys.* **2006**, *124*, 164101.

325. Zhao, Y.; Truhlar, D. G. *J. Chem. Theory Comput.* **2005**, *1*, 415.

326. Dułak, M.; Wesolowski, T. A. *J. Mol. Model.* **2007**, *13*, 631.

327. Vosko, S. H.; Wilk, L.; Nusair, M. *Can. J. Phys.* **1980**, *58*, 1200.

328. Perdew, J. P.; Chevary, J. A.; Vosko, S. H.; Jackson, K. A.; Pederson, M. R.; Singh, D. J.; Fiolhais, C. *Phys. Rev. B* **1992**, *46*, 6671.

329. Perdew, J. P.; Chevary, J. A.; Vosko, S. H.; Jackson, K. A.; Pederson, M. R.; Singh, D. J.; Fiolhais, C. *Phys. Rev. B* **1993**, *48*, 4978.

330. Kendall, R. A.; Dunning, T. H.; Harrison, R. J. *J. Chem. Phys*. **1992**, *96*, 6796.

331. Lynch, B. J.; Zhao, Y.; Truhlar, D. G. *J. Phys. Chem. A* **2003**, *107*, 1384.

332. Dunning, Jr. T. H. *J. Chem. Phys*. **1989**, *90*, 1007.

333. OriginPro Version 8.6 64Bit, Data Analysis and Graphing Software (OriginLab Corporation, One Roundhouse Plaza, Northampton, MA 01060. www.OriginLab.com).

334. Putz, H.; Brandenburg, K.; Kreuzherrenstr, B. G. Diamond -Crystal and Molecular Structure Visualization Crystal Impact. 102, 53227 Bonn, Germany. http://www.crystalimact.com/diamond.

335. Becke, A. D. *J. Chem. Phys*. **1996**, *104*, 1040.

336. Zhao, Y.; Truhlar, D. G. *J. Phys. Chem. A* **2004**, *108*, 6908.

337. Becke, A. D. *J. Chem. Phys*. **1993**, *98*, 1372.

338. Becke, A. D. *J. Chem. Phys*. **1993**, *98*, 5648.

339. Lee, C.; Yang, W.; Parr, R. G. *Phys. Rev. B* **1988**, *37*, 785.

340. Stephens, P. J.; Devlin, F. J.; Chabalowski, C. F.; Frisch, M. J. *J. Phys. Chem.* **1994**, *98*, 11623.

341. Mura, M. E.; Knowles, P. J. *J. Chem. Phys*. **1996**, *104*, 9848.

342. Thomas, L. H. *Proc. Camb. Philos. Soc*. **1927**, *23*, 542.; Fermi, E. *Rend. Acad. Maz. Lancei* **1927**, *6*, 602.

343. Lee, H.; Lee, C.; Parr, R. G. *Phys. Rev. A* **1991**, *44*, 768.

344. Kiewisch, K.; Eickerling, G.; Reiher, M.; Neugebauer, J. *J. Chem. Phys*. **2008**, *128*, 044114.

345. Pavanello, M.; Neugebauer, J. *J. Chem. Phys*. **2011**, *135*, 234103.

346. Lombardi, J. R.; Davis, B. *Chem. Rev*. **2002**, *102*, 2431.

347. Cheeseman, M.; Van Zee, R. J.; Flanagan, H. L.; Weltner Jr., W. *J. Chem. Phys.* **1990**, *92*, 1553.

348. Rousseau, R.; Marx, D. *Phys. Rev. A* **1997**, *56*, 617.

349. Ehara, M.; Yamashita, K. *Theor. Chem. Acc.* **1999**, *102*, 226.

350. Colavecchia, F. D.; Burke Jr., J. P.; Stevens, W. J.; Salazar, M. R.; Parker, G. A.; Pack, R. T. *J. Chem. Phys.* **2003**, *118*, 5484.

351. Cvitaš, M. T.; Soldán, P.; Hutson, J. M.; Honvault, P.; Launay, J. M. *J. Chem. Phys.* **2007**, *127*, 074302.

352. Higgins, J.; Hollebeek, T.; Reho, J.; Ho, T.-S.; Lehmann, K. K.; Rabitz, H.; Scoles, G.; Gutowski, M. *J. Chem. Phys.* **2000**, *112*, 5751.

353. Simoni, A.; Launay, J. M.; Soldán, P. *Phys. Rev. A* **2009**, *79*, 032701.

354. Quéméner, G.; Honvault, P.; Launay, J.-M.; Soldán, P.; Potter, D. E.; Hutson, J. M. *Phys. Rev. A* **2005**, *71*, 032722.

355. Guérout, R.; Soldán, P.; Aymar, M.; Deiglmayr, J.; Dulieu, O. *Int. J. Quantum Chem.* **2009**, *14*, 3387.

356. Larson, J.; Ghassemi, E. N.; Larson, A. *Europhys. Lett.* **2013**, *101*, 43001.

357. Stevens, W. J.; Basch, H.; Kraus, M. *J. Chem. Phys.* **1984**, *81*, 6026.

358. Wheeler, S. E.; Sattelmeyer, K. W.; Schleyer, P. v. R.; Schaefer III, H. F. *J. Chem. Phys.* **2004**, *120*, 4683.

359. Azenkeng, A. *Theoretical Studies of Low-Lying Electronic States of Lithium, Titanium, and Mercury Compounds*. Ph.D. Dissertation, University of North Dakota, Grand Forks, ND, 2007.

360. Ghassemi, E. N.; Larson, J.; Larson, A. *J. Chem. Phys.* **2014**, *140*, 154304.

361. Wolf, J.-P.; Delacrétaz, G.; Wöste, L. *Phys. Rev. Lett.* **1089**, *63*, 1946.

362. Daudey, J. P.; Novaro, O.; Kolos, W.; Berrondo, M. *J. Chem. Phys.* **1979**, *71*, 4297.

363. Whiteside, R. A.; Krishnan, R.; Pople, J. A.; Krogh-Jespersen, M. B.; Von Ragúe Schleyer, P.; Wenke, G. *J. Comput. Chem.* **1980**, *1*, 307.

364. Watts, J. D.; Cernusak, I.; Noga, J.; Bartlett, R. J.; Bauschlicher Jr, C. W.; Lee, T. J.; Rendell, A. P.; Taylor, P. R. *J. Chem. Phys.* **1990**, *93*, 8875.

365. Lee, T. J.; Rendell, A. P.; Taylor, P. R. *J. Chem. Phys.* **1990**, *92*, 489.

366. Kaplan, I. G.; Roszak, S.; Leszczynski, J. *J. Chem. Phys.* **2000**, *113*, 6245.

367. Kolchin, A. M.; Hall, R. W. *J. Chem. Phys.* **2000**, *113*, 4083.

368. Lee, J. S. *Phys. Rev. A* **2003**, *68*, 043201.

369. Srinivas, S.; Jellinek, J. *J. Chem. Phys.* **2004**, *121*, 7243.

370. Junquera-Hernández, J. M.; Sanchez-Marin, J.; Bendazzoli, G. L.; Evangelisti, S. *J. Chem. Phys.* **2004**, *120*, 8405.

371. Cerowski, V.; Rao, B. K.; Khanna, S. N.; Jena, P.; Ishii, S.; Ohno, K.; Kawazoe, Y. *J. Chem. Phys.* **2005**, *123*, 074329.

372. Lee, J. S. *J. Chem. Phys.* **2005**, *109*, 11927.

373. Heaven, M. C.; Merritt, J. M.; Bondybey, V. E. *Annu. Rev. Phys. Chem.* **2011**, *62*, 375.

374. Amaro-Estrada, J. I.; Scemama, A.; Caffarel, M.; Ramírez-Solís, A. *J. Chem. Phys.* **2011**, *135*, 104311.

375. Harrison, R. J.; Handy, N. C. *Chem. Phys. Lett*. **1986**, *123*, 321.

376. Rendell, A. P.; Lee, T. J.; Taylor, P. R. *J. Chem. Phys.* **1990**, *92*, 7050.

377. Klos, J.; Zuchowski, P. S.; Rajchel, L.; Chalasinski, G.; Szczesniak, M. M. *J. Chem. Phys.* **2008**, *129*, 134302.

378. Vetere, V.; Monari, A.; Scemama, A.; Bendazzoli, G. L.; Evangelisti, S. *J. Chem. Phys.* **2009**, *130*, 024301.

379. Gräfenstein, J.; Cremer, D. *J. Chem. Phys.* **2007**, *127*, 164113.

380. Becke, A. D. *J. Chem. Phys.* **1988**, *88*, 2547.

381. Stratmann, R. E.; Scuseria, G. E.; Frisch, M. J. *Chem. Phys. Lett*. **1996**, *257*, 213.

382. Ypma, T. J. *SIAM Rev.* **1995**, *37*, 531.

383. Murray, C. W.; Handy, N. C.; Laming, G. J. *Mol. Phys*. **1993**, *78*, 997.

384. Lebedev, V. I. *Zh. Vӯchisl. Mat. Mat. Fiz.* **1976**, *16*, 293.

385. Lebedev, V. I. *Siberian Math. J.* **1977**, *18*, 99.

386. Lebedev, V. I. *Russian Acad. Sci. Dokl. Math.* **1995**, *50*, 283.

387. Gill, P. M. W.; Johnson, B. G.; Pople, J. A. *Chem. Phys. Lett*. **1993**, *209*, 506.